Real-time imaging through fog over long distance

Swapnesh Panigrahi

▶ **To cite this version:**

Swapnesh Panigrahi. Real-time imaging through fog over long distance. Optique [physics.optics]. Université de Rennes, 2016. Français. NNT : 2016REN1S041 . tel-01421843

HAL Id: tel-01421843
https://theses.hal.science/tel-01421843

Submitted on 23 Dec 2016

HAL is a multi-disciplinary open access archive for the deposit and dissemination of scientific research documents, whether they are published or not. The documents may come from teaching and research institutions in France or abroad, or from public or private research centers.

L'archive ouverte pluridisciplinaire **HAL**, est destinée au dépôt et à la diffusion de documents scientifiques de niveau recherche, publiés ou non, émanant des établissements d'enseignement et de recherche français ou étrangers, des laboratoires publics ou privés.

THÈSE / UNIVERSITÉ DE RENNES 1
sous le sceau de l'Université Bretagne Loire

pour le grade de
DOCTEUR DE L'UNIVERSITÉ DE RENNES 1
Mention: Physique
Ecole doctorale SDLM

présntée par

Swapnesh Panigrahi

Préparée à l'unité de recherche UMR-CNRS 6251
Institut de Physique de Rennes
Université de Rennes 1

Real-time imaging through fog over long distances

Thèse rapportée par:

Anne SENTENAC
DR CNRS, Institut Fresnel
Bernard LE JEUNE
PR, Université Bretagne Occidentale
et soutenue à Rennes le 13 Juillet 2016
devant le jury composé de :
Bernard LE JEUNE
PR, Université Bretagne Occidentale / *rapporteur*
Anne SENTENAC
DR CNRS, Institut Fresnel / *rapporteur*
Sylvain GIGAN
PR, Université Pierre et Marie Curie / *examinateur*
Philippe RÉFRÉGIER
PR, Ecole Centrale de Marseille / *examinateur*
Hema RAMACHANDRAN
PR, Raman Research Institute / *examinateur*
Mehdi ALOUINI
PR, Université de Rennes 1 / *directeur de thèse*
Julien FADE
MCF, Université de Rennes 1 / *co-encadrant*

Dedicated to Bou and Bapa.

Contents

List of Figures

List of Tables

0 Introduction

0.1 Imaging through turbid media: An introduction

Interaction of light with randomly scattering media is a subject of interest due to its relation to fundamental physics and its various applications in real-life situations. Scattering of light is a ubiquitous phenomena and is responsible for blueness of the clear sky or the reddish sunrise/sunset. It is also responsible for the soothing 'diffused' reflectance from stones like marbles, which is presumably the reason behind their usage in architecture since ages. These stones attain their visual properties due to the scattering of light near their surface which diffuses the information of objects and inhomogeneities present inside them with minimum specular reflection. Similarly, it is also the reason why some paints are more soothing to eyes than others. The study of light in such nebulous media has given rise to various fields of study like disordered photonics and optical biomedical imaging which have helped grow our understanding of some interesting physical phenomena [3] and also helped in medical diagnosis [4, 5]. The familiarity of these concepts and at the same time their underlying complexity make it an enticing topic for research.

The knowledge gained from studying the scattering of light in turbid media has also helped in imaging through turbid media like colloids [6], fog [7] and tissues [8]. These imaging problems, which are still under active research can be addressed using technology, information theory and a deep understanding of properties of light through scattering media. Theoretical and experimental advances in understanding the transport of light in such random media has already helped the field to transit from research stage to application in real-life situations. The technological advances in recent years have seen use of signal processing strategies to optimally use the raw data for the purpose of imaging through randomly scattering media. These advancements can be exploited to engineer

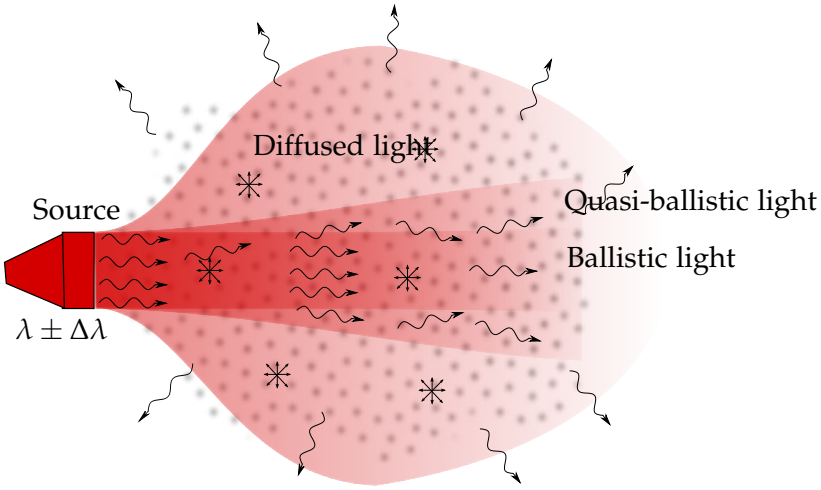

Figure 1: The drawing represents the transport of light through a boundary-less scattering medium. The dots represent the scatterers and the source represents a narrow band collimated light source. Ballistic photons reaching a detector at the other end of the source, travel in line-of-sight without scattering and absorption. However, the number of such photons decrease exponentially with the distance traveled in the medium. The quasi-ballistic photons (or snake photons) undergo mostly forward scattering, thereby retaining some information about the source. Finally, the diffuse photons lose directional information as they travel in the medium due to multiple scattering and can be seen as isotropically scattered from the medium.

devices and signal processing strategies that optimally solve real-life problems, reaching close to the physical limitations of the detection systems used.
To attain imaging through turbid media, it is first necessary to have a minimum understanding of the behavior of light as it traverses through a scattering medium. A brief description of light transport in turbid medium , important terminology and methodology are introduced in the next section.

0.2 Light transport in a turbid medium

In the course of this thesis, the words *light* and *photons* will be used interchangeably to mean the concept of light, which cannot be considered as only electromagnetic waves or classical particles. The properties of light, in general, are well-studied and quite well understood. However, the transport of light in complex media is still an active subject both theoretically and experimentally. When the incoming light is scattered by a single scatterer, the probability of the exit direction of scattered light in space depends on the properties of the scatterer itself. In the presence of many scatterers that have randomly distributed refractive indexes, positions and shapes, the behavior of transport of light becomes quite unpredictable. However, macroscopically, the system gives rise to emergent length scales along with the fundamentally associated length scales like, the wavelength of light λ_0 and

average size of the scatterers. A length scale that indicates the amount of scattering and absorption is given by the mean free path (MFP) and is denoted by l. For light with a wave vector k inside a turbid medium, an extreme case arises when $kl < 1$. In this case, photons are scattered before they can travel a wavelength giving rise to interesting fundamental phenomena like localization of light [9] which are not of concern in this thesis.

However, in most real life scenarios, only *weak scattering* is encountered where $kl >> 1$. In this regime, a few photons may predominantly encounter forward scattering to exit out of the medium, these photons are termed as *ballistic photons* and they retain the spatio-temporal information of the source/emitter. If a detection system could only detect ballistic photons, then one can achieve diffraction limited resolution imaging through turbid medium. Unfortunately in highly scattering media, the ballistic photons are much fewer in number compared to the photons that are multiply scattered. The photons that undergo multiple scattering events are termed as *diffuse photons* and they loose most of the information about the source as a result of the random scattering they encounter. Since they undergo the most scattering, their transport is dominated by the properties of the medium, which can be exploited to extract information about the medium itself. This fact is utilized in diffuse optical imaging through tissues in the context of medical imaging, where they can produce absorption maps for the tissue under consideration [10]. Another class of photons that lie in between ballistic and diffuse photons are called quasi-ballistic or *snake photons*. They undergo mostly forward scattering and thus retain some information. The *snake photons* show better photon budget than ballistic photos, providing a possible trade-off between resolution and the signal-to-noise ratio. The transport properties of the snake photons are difficult to model compared to ballistic or diffused light. As a result, a general practice at least in imaging schemes is to include the quasi-ballistic photons (snake photons) in the description of the ballistic photons unless specified [8]. An exhaustive theory may provide a continuous understanding of all the photons in such scattering media. In the classical physics regime, the Boltzmann transport equation provides an accurate description of the light transport in scattering media [8]. However, this transport theory is analytically difficult to solve but remains tractable using simulations and Monte-Carlo techniques [8]. The Monte-Carlo simulations have proved to be in-line with experiments and have been the benchmark for other theories for validation [11].

The understanding of the light transport through scattering media has led to implementations and solutions of the problem of imaging through such media. There are a few techniques that utilize diffuse light for imaging. Frequency-domain modulation imaging [12], where the effect of the scattering medium on the modulation index and phase of an input light signal are exploited to attain scattering and absorption inhomogeneity maps within the medium. Another method relies on the *memory effect* of speckle through a static random medium. In this case, the complex transfer function of the medium is 'learned' and imaging through turbid media is treated as an inverse problem [13]. This field of research is presently very intense for spatio-temporal focusing/imaging through static turbid media, with a variety of approaches to 'learn' the turbid media prior to the image reconstruction [13]. These techniques are efficient but cannot be applied in scenarios

where real-time, direct imaging through a non-stationary scattering medium is required and, therefore, will not be considered in this thesis. In such situations, ballistic photons imaging has the potential to provide images with resolution only limited by the diffraction. Various methods exist that essentially allow a detection system to selectively capture the low signal-to-noise ratio (SNR) ballistic photons by filtering out the diffuse photons. In the next section some of these techniques are reviewed.

0.3 Ballistic discrimination: review of techniques

Selective detection of ballistic photons is sought when the spatial resolution of objects embedded in scattering media is of interest [14, 15]. For instance, in industrial applications where it is required to image objects embedded in colloidal system, or in navigation where vision through fog can be efficiently achieved with ballistic filtering. The problem of imaging through such media has been addressed using various techniques that essentially rely on discriminating forward scattered photons from multiply scattered (diffuse) photons traversing through a turbid medium. The strategies envisaged for ballistic photons discrimination imaging can be classified as described below in brief.

Spatial discrimination Since ballistic photons travel through the medium in the forward direction with minimum scattering, they can be selectively discriminated by spatially filtering out the diffused light which are scattered in multiple directions before reaching the detector [16, 17]. It has been used in confocal imaging for ballistic photon imaging, where appropriate pinhole sizes, depending on the scattering parameters of the medium, can be designed to discriminate ballistic photons from the diffuse photons [18]. The advantage of this method is that its quite simple and productive. It does not require changing the imaging setup drastically and thus, quite useful in confocal microscopy [18]. However, the pinhole size must be changed if the scattering properties differ from sample to sample. Moreover, the small size of the aperture reduces the amount of light received by the detector.

Temporal discrimination The most commonly used technique for selective imaging of ballistic light is by temporal filtering. The ballistic photons that travel straight through the scattering medium reach the detector earlier than the multiply scattered light which undertake longer path lengths and hence longer times to reach the detector. Time gated imaging and coherence gated imaging take advantage of this difference in arrival time of the ballistic photons and non-ballistic photons to attain imaging through scattering media [8].
Time gated imaging at time scales of hundreds of femto-seconds is achieved by using Kerr gate shutters [19], streak cameras [20] or intensifier cameras systems [21]. Such temporal discrimination has found applications in medical imaging through tissues as well [22].
Coherence-gated holographic imaging also takes advantage of the difference in arrival time of ballistic and diffuse photons. In this case, an image plane hologram is recorded on

a camera by interfering the appropriately delayed reference beam with the light received through the turbid medium. Multiple images are averaged upon to reduce speckle noise which are assumed to be uncorrelated from frame to frame [23, 24, 8].
The low SNR of ballistic photons requires averaging over large number of images to achieve ballistic photon imaging. Owing to this limitation, such a method have not found application in real-time imaging. However, effort have been made to attain single shot ballistic imaging by exploiting optical Kerr effect for fast shuttering [19]. The quality of image obtained, in this case, depends on the the gating delay and imaging scheme employed [8, 25].

Discrimination based on light property In a turbid medium, polarized light is known to preserve its polarization properties deeper into the medium [26]. The depolarization length scales are longer than the mean free path of photons in the medium. Further, it has been well-established that the circularly polarized light has deeper penetration with respect to linearly polarized light [27, 28]. The preservation of polarization properties of light in scattering media has been used to achieve ballistic photon imaging [29].

Modulation or frequency domain imaging Modulation techniques have been utilized to enhance the SNR of the ballistic photons. For example, in polarization gated imaging a source with rotating linear polarization at a certain frequency is passed through a turbid medium and is detected by a synchronized analyzer locked-in with the source modulation [6, 30, 31, 32]. This way, the polarization modulation method takes advantage of the polarization memory effect of ballistic photons in turbid media. Another strategy is to use intensity modulated light through turbid media. This strategy has been used in medical imaging widely [8]. However, it is commonly used for diffuse optical imaging where the scattering parameters of the medium are estimated so as to create inhomogeneity maps using only diffuse light. The mapping principle is based on the fact that the intensity modulated light in a diffused medium behaves as photon density waves whose dispersion relation is dependent on the scattering properties of the medium [8].
There is limited literature on the ballistic photon imaging using intensity modulated light. However, it has been used with scanning laser systems for underwater imaging [33] and to enhance the SNR of ballistic photons through colloids [34].

0.4 Motivation and objective

The thesis is an outcome of a collaboration between Institut de Physique de Rennes, Université de Rennes 1 in Rennes, France and Raman Research Institute in Bangalore, India. The project, named “Real-time image through fog over long distances” (RITFOLD) is funded through Indo-French Centre for the Promotion of Advance Research (Centre Franco-Indien pour la Promotion de la Recherche Avancée) (IFCPAR/CEFIPRA). The project aims at exploring imaging of active sources through fog by using two imaging modalities that were identified by the collaborating partners. The two imaging modalities,

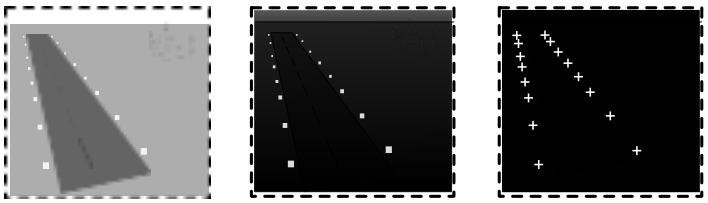

[a] [b] [c]

Figure 2: Schematic of potential application of long distance imaging of active sources through fog. [a] A drawing of a landing strip with active runway lights as may be imaged by an intensity camera. [b] Optimal estimation of the active sources through fog (or in clear sky) may provide visual aide to a pilot by isolating runway lights from the background. [c] Detection strategies may be developed for auto-detection of the active runway lights to assist in automated landing or taxiing or for visual estimation of orientation of the aircraft with respect to the landing strip.

namely polarimetric imaging and intensity modulated imaging, present various advantages like potential for real-time imaging and possibility of developing relatively simple and compact camera systems. These imaging systems may also be designed such that they can be mearged together into a single system to take advantages of both the systems. Accordingly, imaging through fog in real-time by developing advanced, but portable and cost-effective imaging systems with robust signal processing is the primary motivation behind the studies performed during the course of thesis.

An imaging system which can provide visual aide through fog may have many application in transport safety and navigation. One of the application envisaged for a such a system is aircraft landing and taxiing in degraded weather conditions. In small airports that do not have instrument landing systems, the pilot needs to have a visual confirmation of the runway a few hundred meters away before it is allowed to land. Even in large airports which have instrument landing systems of various categories that allow the planes to land in zero visibility conditions, the pilot has no visual clue about the runway. With active sources placed along side the runway lights and a specialized imaging system capable of imaging through degraded weather, it is possible to auto-detect the runway lights and provide as visual aide to the pilot or even for automatic landing. Such a scenario is illustrated in Fig. 2. Implementation of such system in a real-life scenario may drastically reduce the minimum distance for visual confirmation required for aircraft landing. Even a small decrease in this minimum required visual distance can have tremendous effect on the traffic control during degraded weather conditions, thus, reducing delays. The safety standards are also enhanced when the pilot has visual aide while landing or taxiing in degraded weather conditions. Owing to this, there is interest for implementation of novel imaging systems that are cost-effective, real-time and portable.

In light of the above mentioned considerations, the thesis is divided into two parts. The first part deals with implementation of a polarimetric imaging scheme over a long range of a kilometer for imaging of a polarized beacon through fog under real atmospheric

conditions. The imaging system is, further, tied together with image processing schemes that optimally enhance the contrast of the polarized sources through fog and are rigorously derived by proposing a noise model and using estimation techniques. The second part deals with an intensity modulated light imaging modality, where the prototype of a novel quadrature demodulation camera is developed, which is capable of demodulating light modulated at radio frequencies in real-time. Further, the optimal operating frequencies for ballistic imaging through fog are derived using diffusion theory of photon transport. The two different imaging modalities are implemented to explore the possibility and efficiency of realizing such an imaging system and are briefly introduced below.

0.4.1 Polarimetric imaging

As mentioned in section 0.3, polarized light has a deeper penetration into a turbid media. The random scattering of polarized light in turbid media attenuates the intensity but the polarization properties are preserved for longer depths. Thus, a polarization sensitive device capable of recording the polarization information of received light may provide a simple solution for enhancing visibility through a turbid medium. This methodology is studied in the first part of the thesis. In chapter 1, the basics of polarization of light is discussed, followed by a description of a snapshot polarimetric camera capable of simultaneously recording two images of a scene in two orthogonal polarization directions. The camera is, then, used in a long range outdoor experiment to obtain data in degraded weather conditions. The chapter details this original experiment and quantitatively compares the performance of various simple polarimetric image representations for contrast imaging of a polarized source through fog in various visibility conditions. Then, chapter 2 deals with deriving a contrast maximizing optimal polarimetric representation using a correlated Gaussian noise model, as deducted from experimental data, and Maximum-likelihood estimation principle. Using this optimal representation, a detection scheme is envisaged and its real-time implementations are also presented.

0.4.2 Intensity modulation imaging

In the second part of the thesis, real-time imaging of modulated light through turbid mediums is studied. Modulation-demodulation techniques are known to provide an enhancement of the SNR of a small signal embedded in intense background by spectral filtering of the noise. They have clear advantages in efficiently rejecting background which is either not modulated or modulated at a frequency far from the modulation frequency of the signal. This is indeed very well understood and full-field implementation of such a technique in the context of imaging is sought. However, in case of imaging through turbid media, the ballistic photons constitute the signal embedded in a background of diffuse light which creates a halo around the source. With intensity modulated light, both the ballistic and diffuse light will be modulated at the same frequency, thus it is not apparent that a spectral noise filtering by modulation techniques can provide true ballistic discrimination. In light of this, after an introduction to diffusion theory of photon transport in turbid media

in chapter 3, an information theoretical analysis parametrized by the diffusion model is derived in chapter 4 to gain insight into scattering parameters dependent operating frequencies that may provide true ballistic filtering using modulated light. Finally, one of the major challenges in modulated light imaging is the lack of full-field demodulation cameras that can work at radio frequencies. In chapter 5, this challenge is addressed by developing a novel full-field, all-optical demodulation camera capable of working at high frequencies in real time.

The two approaches are independent of each other but serve the same goal using different physical approach. The imaging systems corresponding to the two approaches are also designed so that they may be merged together to take advantage of both the system. In addition to the common application goal of the two parts of the thesis, various scientific methodologies used for theoretical and experimental analysis or system design and calibration, recur throughout the thesis remaining coherent with the overall research strategy followed in this thesis. For example, in both the cases, along with experiments and instrumentation, similar information theoretical tools have been used to quantify the efficiency of the imaging system. Especially, a quantity called Fisher information (introduced in Appendix A) is relied upon to quantify the information content in a detected data stream for estimation of a parameter describing the source properties. The efficiencies of the detection systems are quantified using the corresponding expression for Fisher information derived for each imaging modality. Furthermore, concepts like principal component analysis (PCA) recur, both as a signal processing strategy and for calibration of imaging systems.

The similarity of the instrumental design choices made for developing the imaging systems will also be apparent, as they aim at achieving the design considerations like real-time imaging, modularity, robustness and inexpensiveness.

In fact, the basic ideologies followed in developing this thesis, for the both the imaging modalities, can be summarized into the following list:

- Development of unconventional imaging systems. Using and developing novel and advanced imaging systems capable of performing real-time imaging and are cost effective, modular, robust and flexible enough to be transferred to real-field application with minimum cost and time.
- Deriving noise model for such imaging systems for imaging through turbid media to quantify the efficiency of the imaging systems and identification of optimal operating points and representations.
- Experiments using the imaging systems and validation of the theoretical models with experimental data.
- Using information theoretical tools to develop algorithms for optimal estimation techniques with real-time processing capabilities.
- Using the processing algorithms on real experimental data for validation and proof of concept.

Overall, the thesis provides an extensive study of the polarization sensitive imaging and modulated light imaging for achieving imaging through turbid media. The research spans development of imaging systems, experimental design and acquisition, information theoretical analysis and signal processing and optimal estimation and detection strategies.

Part i

Polarimetric contrast imaging

1

Long range polarimetric imaging through fog

Polarization of light is one of its fundamental properties alongside its frequency and coherence. It has been studied long before [35] the theories of electromagnetism were unified by Maxwell in 1865. The first huge leap in the understanding of polarization of light is due to Stokes, who proposed four parameters that define the state of polarization of light under consideration in 1852 [36]. These parameters, now, named after him as Stokes parameters are still in wide use. Another representation valid for totally polarized was provided by Jones in 1941 [37]. The Jones vector and Stokes parameters describe the state of polarization of light, but do not provide insight into its origin. After the unification of electromagnetism by Maxwell, polarization was defined with respect to the oscillation plane of the electric field vector. A further leap in understanding in the polarization of light comes from another unification theory due to Wolf et. al. [38]. The theory unifies coherence and polarization of light by considering the inherent fluctuations in electric fields and their covariance as the fundamental element that give rise to both coherence and polarization. In the following sections the polarization of light is revisited from the above mentioned perspectives.

1.1 Light as electromagnetic wave

Light as an electromagnetic wave was first unified by Maxwell in 1865 [39]. The theory states that light in free space (or in an isotropic dielectric medium) is a transverse propagating electromagnetic wave, where the electric field $\boldsymbol{E}$ and magnetic field $\boldsymbol{H}$ oscillate in mutually perpendicular directions and in phase, for a monochromatic wave. For light of angular frequency ω, wave number k and propagating in z direction, the electric field may oscillate in the xy plane such that it can be represented as a vector in the rectangular

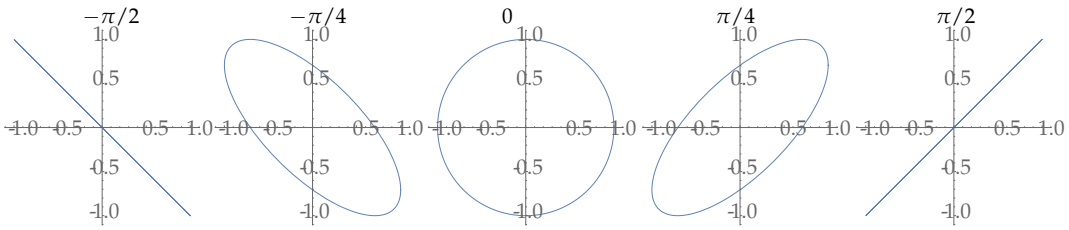

Figure 1.1: States of polarization.

coordinate as

$$\boldsymbol{E} = E_x \, cos\,[kz - \omega t]\,\hat{\boldsymbol{x}} + E_y \, cos\,[kz - \omega t + \phi]\,\hat{\boldsymbol{y}}, \tag{1.1}$$

where t represents time and $\hat{\boldsymbol{x}}$ and $\hat{\boldsymbol{y}}$ are unit vectors in x and y directions respectively. Polarization of light is regarded as the result of the orientation of the electric field in the electromagnetic wave. In Fig. 1.1, the locus of the tip of the electric field is traced out in the xy plane for various values of ϕ. The locus generally describes an ellipse with rotated axis with two degenerate cases: for $\phi = m\pi$ ($m = 0, \pm1, \pm2, ..$), where it describes a straight line and is conveniently called 'linearly polarized' and for $E_x = E_y$ with $\phi = \frac{1}{2}m\pi$ ($m = \pm1, \pm3, \pm5, ..$), where it forms a circle and is called 'circularly polarized' with appropriate handedness. Viewed along the direction of propagation of light, the tip of the electric field may rotate clockwise (or anti-clockwise) and is named as right-handed (or left-handed) elliptically polarized. A complete description of this polarization ellipse can be figured out by obtaining the information about the amplitudes E_x, E_y and the phase ϕ. However, for experimental determination of the state of polarization, four parameters are identified and are named as Stokes parameters, named after Stokes who had first introduced them [36].

The Stokes parameters are used to determine the amplitudes and the phase by measuring four parameters that have same physical dimensions as the intensity. In the case of plane monochromatic and deterministic wave, the four Stokes parameters are then defined as,

$$S_0 = E_x^2 + E_y^2 \tag{1.2a}$$

$$S_1 = E_x^2 - E_y^2 \tag{1.2b}$$

$$S_2 = 2E_xE_y \, cos\,[\phi] \tag{1.2c}$$

$$S_3 = 2E_xE_y \, sin\,[\phi] \tag{1.2d}$$

Three of these parameters are independent, since $S_0^2 = S_1^2 + S_2^2 + S_3^2$ for the fully polarized light under consideration. The Stokes parameters are important and widely used because they provide complete information of polarization state of light using simple experiments that measure the time-averaged intensity of the waves.

Table 1.1: Optical components and their matrix representation for Jones calculus.

Component	Matrix representation
Horizontal Polarizer (P_H)	$\begin{bmatrix} 0 & 0 \\ 0 & 1 \end{bmatrix}$
Vertical Polarizer (P_V)	$\begin{bmatrix} 1 & 0 \\ 0 & 0 \end{bmatrix}$
Quarter-wave plate (QWP)	$\begin{bmatrix} 1 & 0 \\ 0 & -i \end{bmatrix}$

1.2 Modern theories of light polarization

The treatment of polarized light was carried forward by Mueller [40] who introduced a matrix based calculi to describe the linear interaction of the polarized light with optically anisotropic medium (both in transmission and reflection modes). The 4×4 Mueller matrices, describe the relation of output Stokes vector to the input Stokes vector. This method will not be used in this thesis and, thus, it is not reviewed further. Another matrix based calculi to describe fully polarized light was proposed by Jones [37]. Jones calculus, works in the space of two-dimensional complex vectors that represent the electric field. The Jones vector for a general fully polarized light as described in Eq. (1.1) (elliptically polarized state) is written by omitting the space and time varying phase factor $kz - \omega t$, as

$$E = \begin{pmatrix} E_x \\ E_y \end{pmatrix} = \begin{pmatrix} E_x \\ E_y \, e^{i\phi} \end{pmatrix}. \tag{1.3}$$

In this formalism, a linearly polarized light along x axis may be written as $E = E_0[1, 0]^T$ and a right-handed circularly polarized beam is $E = E_0[1, i]^T$. The interaction of light with a non-depolarizing birefringent material is represented by a 2×2 complex matrix. Jones matrix for common polarization sensitive optical components are given in Table 5.1.

The Jones calculus, as originally developed by Jones for deterministic electromagnetic waves, *per se* does not allow description of partially polarized light or depolarized light, which are the most commonly encountered states of light in nature.

The 'modern' or alternative theory for polarization was developed with active contribution due to Emil Wolf [38]. The theory is based on considering electromagnetic field as stochastic in nature and goes on to unify the polarization and coherence properties of light [38]. Invariance descriptions of polarization and coherence have been reported [41], adding to the general acceptability of the relatively new way of thinking about properties of light. In the description below, only the polarization properties are considered and briefly described. Considering a quasi-monochromatic plane electromagnetic wave with mean angular frequency ω traveling in the z direction and the field at position $\boldsymbol{r}$ and time

t in the x and y axes are $E_x(\boldsymbol{r},t)$ and $E_y(\boldsymbol{r},t)$, respectively. Then, the second-order covariance properties of the electric field at the location $\boldsymbol{r}$ is called the polarization matrix (or coherency matrix) and is written as

$$\Gamma(\boldsymbol{r},t) = \begin{pmatrix} \langle E_x^*(\boldsymbol{r},t)E_x(\boldsymbol{r},t)\rangle & \left\langle E_x^*(\boldsymbol{r},t)E_y(\boldsymbol{r},t)\right\rangle \\ \left\langle E_x^*(\boldsymbol{r},t)E_y(\boldsymbol{r},t)\right\rangle & \left\langle E_y^*(\boldsymbol{r},t)E_y(\boldsymbol{r},t)\right\rangle \end{pmatrix} = \begin{pmatrix} I_{xx}(\boldsymbol{r},t) & c(\boldsymbol{r},t) \\ c^*(\boldsymbol{r},t) & I_{yy}(\boldsymbol{r},t) \end{pmatrix}, \tag{1.4}$$

where, $\langle\rangle$ denotes the expectation over ensembles of field values, the $*$ denotes the complex conjugate and shorthands ($I_x x$, $I_y y$ and c) for the ensemble averages are used, which are self evident in the above equation.
The diagonal elements of the polarization matrix represent the average intensities for each component of the electric field and the off-diagonal component represents the correlation between the two components of the electric fields. The polarization matrix is Hermitian and non-negative. The classical Stokes vectors can be written in terms of the elements of the polarization matrix as

$$\begin{aligned} S_0 = &\quad \Gamma_{xx} + \Gamma_{yy} = &\quad I_{xx} + I_{yy} = I_T, \\ S_1 = &\quad \Gamma_{xx} - \Gamma_{yy} = &\quad I_{xx} - I_{yy}, \\ S_2 = &\quad \Gamma_{xy} + \Gamma_{yx} = &\quad 2Re[c], \\ S_3 = &\quad i(\Gamma_{yx} + \Gamma_{xy}) = &\quad 2Im[c], \end{aligned} \tag{1.5}$$

where, the dependency on $\boldsymbol{r}$ and t are omitted for the sake of clarity. The use and applications of the polarization matrix is well presented in modern books dedicated to polarized light [42]. For partially polarized light, a degree of polarization (DOP) can be defined as the ratio of intensity of part of the light that is fully polarized to the intensity of unpolarized component. Under the above formalism, the polarization matrix of the partially polarized light can be expressed as a sum of polarization matrices of the fully polarized component (termed "principal polarization state") and unpolarized component of light [38] as

$$\Gamma = \mathcal{P}\,\widetilde{\Gamma}_P + \frac{1-\mathcal{P}}{2}\begin{pmatrix} 1 & 0 \\ 0 & 1 \end{pmatrix}$$

with $\left|\widetilde{\Gamma}_P\right| = 0$ and where the degree of polarization (DOP) (denoted by $\mathcal{P}$) can be written as

$$DOP = \mathcal{P} = \sqrt{1 - \frac{4det\left[\Gamma\right]}{(tr\left[\Gamma\right])^2}} \tag{1.6}$$

Also, using the stokes vector, the DOP can be expressed as

$$DOP = \frac{\sqrt{S_1^2 + S_2^2 + S_3^2}}{S_0} \tag{1.7}$$

The DOP along with the angles that define the polarization ellipse present the complete information about the principle polarization state of light.

1.3 Polarization vision

Clearly, in many scenarios, polarization vision can provide additional information about an object compared to polarization insensitive cameras. It may enable clear vision through nebulous media and can help distinguish between different materials and identify structural non-uniformity at a comparatively low processing cost [43, 44]. Despite the advantages, it is worth noting that the human eye has not evolved to acquire true polarization vision. The human eye has a tiny polarization sense [45] but it seems rather a consequence of the structure of the cones than an alternative vision. This may be due to the fact that on an ordinary day, polarization does not bring any drastic information for survival. In contrast some insects like the honey bees [46] have polarization vision to assist in navigation. They use the polarization of the blue sky to have an idea about the location of the sun. However, polarization vision is most important when seeing through nebulous media and to efficiently 'see' transparent objects. In the whole spectrum of species on earth, polarization vision has developed mostly in marine animals. Some of the spectacular animals with polarization vision are the mantis shrimp [47] and octopus [48]. Most fishes [49] have polarization vision as well. In marine conditions, preys have developed transparency as means of defense from visual predators, and it is hypothesized that polarization vision provides evolutionary advantages for a predator to efficiently detect such transparent prey [50].

Therefore, polarization vision may prove useful in variety of areas. Let us list a few of these areas, some inspired from nature itself, to have an overall view. (1) In detection of transparent objects, which is used in industrial machine vision applications for 3D shape estimation [51]. (2) In navigation, this provides the only way for terrestrial navigation using only a vision and no other equipment and (3) For imaging through turbid media like colloids [32, 6], tissues [52], and degraded weather conditions [7, 53].

1.4 Polarimetric contrast imaging

The application of polarization sensitive imaging to the fields described in the previous section has led to implementation and invention of polarization sensitive cameras. These cameras, that will be briefly reviewed in section 1.5 provide polarimetric information about the scene being imaged. Such cameras usually, measure the Stokes vector at each pixel. Thus, a Stokes camera may provide a four-dimensional image $S = [S_0, S_1, S_2, S_3]$. The Stokes images are obtained by taking a minimum of four images of the scene [54]. Commonly, six images of the scene are recorded where, I_x is the image taken using a polarizer with polarization axis parallel to x axis, I_y,is the image taken with y axis oriented polarizer, I_{+45° and I_{-45°, with polarizers oriented at $\pm 45^\circ$ and I_R, I_L are images of the scene in right and left circular polarization states respectively. Then, the four-dimensional Stokes image is calculated as,

$$S = \begin{pmatrix} S_0 \\ S_1 \\ S_2 \\ S3 \end{pmatrix} = \begin{pmatrix} I_x + I_y \\ I_x - I_y \\ I_{+45^\circ} - I_{-45^\circ} \\ I_R - I_L \end{pmatrix} \tag{1.8}$$

In cases where the degree of polarization is to be estimated at each pixel, a DOP image can be obtained by $DOP = \sqrt{S_1^2 + S_2^2 + S_3^2}/S_0$. Then, the DOP image can be used to distinguish between materials that have the same reflectivity but may have different polarimetric properties [43, 44]. DOP imaging has been used widely in various fields of polarimetry, like, industrial machine vision where three dimensional inspection of reflective metals is required [55], or in biomedical imaging for diagnosis of skin pathology [56] and for tissue imaging [52].

The Stokes imager requires four images to be stored, whereas, often this complete information about the state of polarization at each pixel of a scene is reduced to a single scalar image (polarization contrast image) to be displayed to an end user or used as input for a higher segmentation or detection algorithm. As a result this may be an overkill, especially, in applications where the birefringence of materials constituting the image can be neglected. Indeed, in those cases, the first two components of the stokes vector are enough to provide polarimetric information of the scene as $S_2 = S_3 = 0$ under active illumination with linear polarization along x or y direction. An image analogous to the DOP image can be obtained by neglecting the last two components of the Stokes vector and computing the so-called 'orthogonal-states contrast' (OSC) image as

$$OSC = \frac{S_1}{S_0} = \frac{I_x - I_y}{I_x + I_y}. \tag{1.9}$$

The DOP and the orthogonal-states contrast (OSC) image are identical when the materials constituting the scene are all non-birefringent, under active illumination with linear polarization along x or y directions.

Such simplified two-channel polarimetric imager not only require minimal computation and smaller memory space, they can be made portable and real-time with relatively low cost of production. In the next section, an original long-range polarimetric imaging experiment is described where a simultaneous two channel, real-time polarimetric camera is utilized. In this part of the thesis, polarization sensitive detection is used to enhance the signal-to-noise ratio of polarized signals through fog. As mentioned in the introduction chapter, the ballistic photons retain the polarization properties of the source as they traverse through a turbid medium. However, conventional cameras are not polarization sensitive and new full-field, real-time polarization sensitive cameras are needed to take advantage of the polarization properties of light when used in imaging. In the following section, polarimetric cameras are reviewed and then a modular snapshot polarimetric camera, built, in-house, is described and used for long range imaging.

1.5 Brief review of some polarimetric cameras

Let us first review the various techniques that have been used for polarimetric sensitive imaging. All conventional polarimetric cameras use polarization sensitive optical filters to obtain four images and then estimate the Stokes vector at each pixel, as described in the previous chapter. Various methods are used to realize such a camera and they involve Savart plates [57, 58], polarization gratings [59, 60, 61] or liquid crystal variable retarders (LCVR) [62] to obtain polarimetric images serially. However, to obtain simultaneous polarization information, micro-grid division-of-focal-plane polarimetric imagers [63] and Wollaston prism-based simplified polarimetric cameras [64] have proved efficient, robust and capable of attaining real-time polarimetric image of a scene. Moreover, recently some alternative approaches have been proposed to obtain polarization contrast imaging with completely different measurement paradigms [65, 66] which remain out of context with respect to this thesis. However, the conventional polarimetric sensitive imaging systems are briefly reviewed in the following paragraphs.

Division of time One of the simplest methodology to attain polarimetric sensitive imaging is where various images of a scene are taken sequentially using different polarization filters. These methods are efficient only for static scenes or in situations where real-time imaging is not necessary. A LCVR can be used to speed up the imaging but still remain far from real-time [62].

Division of focal plane Division of focal plane is an imaging scheme where four pixels (or more) form a super pixel, thus dividing the focal plane. Each pixel in the super pixel is integrated with a nano-wire polarization filter to estimate the Stokes vector at each super pixel [67, 68]. This method is similar to the Bayer filter patterns used in color cameras where wavelength filters are used to obtain a color image at each super pixel. This recent variation of polarimetric camera has its own limitation. One of the main concerns is the non-uniformity in optical properties of the nano wire polarization filter which can vary as much a 20% [69, 70].

Division of amplitude Another scheme for attaining real-time polarimetric imaging is based on division of amplitude. In this methodology, the incoming beam of light is divided into two or more beams by specialized prism and then passed through polarimetric filters to obtain polarization sensitive images. Commercially available imagers based on this methodology are becoming popular [71]. They use a three-way prism which splits the incoming light into three channels which are then independently filtered and recorded on three separate synchronized camera sensors. This technique is simple and provides real-time polarimetric images, however, it requires three different sensors. This makes it expensive and less flexible to be used in varied situations. In this part of the thesis, the division of amplitude method is used to develop a snapshot polarimetric camera by using a Wollaston prism to separate the beams and image with a single sensor. A prototype

of the Wollaston-prism based snapshot polarimetric camera is detailed in the next section and used for contrast enhanced imaging through fog.

Alternative non-conventional approaches Other interesting approaches for polarimetric imaging have been reported in literature that are worth mentioning. Depolarization sensing by orthogonality breaking is such an approach where a dual-frequency orthogonal polarization field is used to measure depolarization of light without any addition polarimetric component [72]. In another approach, imaging degree of polarization is achieved by analysis of speckle characteristics [73, 74, 75]. One method exploits illumination of the sample with large diversity of polarization states and specific processing to attain endoscopic polarization measurement [76]. Wavelength polarization coding has also been used to attain snapshot polarimetric imaging [77]. Finally, co-designed imaging systems capable of generating any polarization state have been proposed to adaptively provide polarimetric contrast optimization [78].

1.6 Wollaston prism-based snapshot polarimetric camera

In the course of this thesis, a two-channel snapshot polarimetric camera is utilized. The camera is designed to record two simultaneous images of a scene in two orthogonal polarization directions using only a single intensity camera and optical components. The resulting two images can then be used to produce two components of the Stokes vector that may be used to obtain polarimetric contrast map of the scene being imaged. Even such a simple construct that only provides partial polarimetric information, can be used efficiently in various scenarios where a simple intensity detector may fall short. In the following sections, the construction and calibration of such a snapshot camera is detailed. The design of this Wollaston-prism based snapshot polarimetric camera mainly relies on an anterior thesis work by A. Benieŕe [64] in which the design is shown to minimize optical aberrations.

1.6.1 Design

At the core of the snapshot polarimetric camera considered here, lies a Wollason prism (WP) . The WP usually consists of two cemented prisms made from birefringent material like calcite, α-BBO or quartz. This allows for variability in operating wavelength and angular separation in the output polarized beams. The birefringent material has an ordinary axis and extra-ordinary axis that introduce different refractive index for light having polarization axis along these axes. As a result, the incident beam of light is divided into two angularly separated, orthogonally polarized beams. The angle of separation depends on the birefringence of the prism and commercially available WPs may have angular separation ranging from 1° - 20° with operating wavelength ranging from 190 nm to 3500 nm. The angle of separation is also wavelength dependent, therefore, in many cases the WP may be used in a Fourier-transform spectrometer [79]. Compared to other polarizers, the

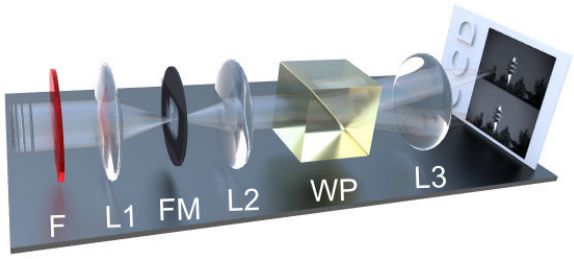

Figure 1.2: A schematic showing the working principle of the Wollaston-based snapshot polarimetric camera.

WP has a high extinction ratio of the order of 100000:1. The WP is also used in production of entangled polarization states of single photons for applications in quantum optics [80]. In the context of imaging, the Wollaston prism can be used to form two images of the scene, each taken at orthogonal direction of polarization. The two images will provide simultaneous polarimetric images of the scene and they can be recorded by a single intensity camera, thus making the system modular and real-time. This is the principle underlying the imaging system used in this part of the thesis and a design of the polarimetric camera is shown in Fig. 1.2.
The design of the Wollaston prism-based snapshot polarimetric camera was studied, implemented and reported in [64]. Let us list out the constraints and design considerations that were taken into account during the development of the Wollaston prism-based snapshot polarimetric camera.

- Wavelength dependence of angle of separation: The angle of separation of the two images formed by the Wollaston prism depends on the wavelength of the incoming light. Therefore, to obtain a proper image on an intensity camera, it is necessary to use a narrow band filter (F) as shown in the Fig. 1.2.

- Modularity: Keeping in mind a modular and flexible design such that the optical components can be fit onto any traditional camera, objectives L1 and L2 are introduced. The lens L1 makes an intermediate image and L2 makes a parallel beam of light that is angularly split by the WP and can be imaged by lens L3 on any intensity camera.

- Overlapping of two images: The two images formed by the WP will have considerable overlap due to the small angular separation of the input beam of light. This is overcome by placing a rectangular field-mask (FM) of appropriate size at the intermediate image to limit the field of view such that the two final images are well separated.

- Geometric aberrations due to the WP: The images formed through the Wollaston prism are prone to asymmetric geometric distortion. The addition of lenses L1 and L2 produce a parallel beam of light and this help is minimizing asymmetric geometric distortion in the final images [64].

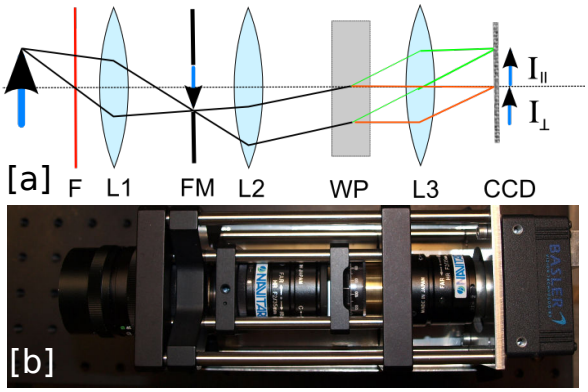

Figure 1.3: Snapshot polarimetric camera: The Wollaston prism(WP) angularly separates the incident beam into two orthogonal polarization components forming two images $I_{\parallel}$ and $I_{\perp}$ on the CCD. The illustration in [a] geometrically indicates the working principle of the imaging setup. A top view of the prototype imaging setup is shown in [b].

- Intensity mismatch: The average intensities received at each corresponding pixel of the two images may not be the same even when the imaging system is illuminated uniformly with depolarized light. This mismatch can easily be corrected with appropriate calibration.

Based on the above design of a snapshot polarimetric camera, a prototype was created to be used in an outdoor experiment for imaging a polarized beacon of light through fog. As shown in the Fig. 1.3, the incoming beam of light is spectrally filtered by a narrow band filter (F) centered at 612 nm and with a width of 12 nm. An intermediate image formed by the lens L1 (50 mm , F/2.8 camera objective) is then masked using a steel mask with a rectangular opening of size 3 mm $\times$ 18 mm. The mask was painted black to reduce any reflection from it. The lens L2 (25 mm , F/2.1 camera objective) is used to form a collimated beam of light which passes through the Wollaston prism. The WP used has a separation angle of 5° at wavelength 630 nm. Finally, any conventional intensity camera could be used to record two images at each frame. In this part of the thesis, two different intensity cameras were used without changing the optical apparatus, which shows the flexibility of such design. For the preliminary results presented in this chapter, the camera used was a 12 bit, 780 $\times$ 582 pixels resolution camera (Basler A312f) CCD camera with pixel size of 8 μm and average dark count of 23 e^-/pixel/s and standard deviation of 0.6 e^-/pixel/s. In light of the preliminary results and conclusions, the camera was later upgraded to a 16-bit, 2560 $\times$ 2160 pixels, Peltier cooled, low-noise CMOS camera (Andor Neo - sCMOS) with pixel size of 6.5 μm and a dark count of 0.015 e^-/pixel/second at -30° cooling. Further results shown in chapter 2 uses the data taken with the CMOS camera.
The system allows one to obtain two simultaneous images of the scene on the same intensity camera as shown in Fig. 1.3. The camera described above has the advantages of being modular in design, without moving parts and hence robust enough to be used in the field. It takes simultaneous polarimetric images of the scene and with simple computation it can provide various polarimetric information not available to intensity camera. However, the

system has its own limitations, most of which can be corrected by an appropriate calibration step. These imperfections are listed below and the calibrations are detailed in the next section.

- Spectral range: One of the main disadvantage of this optical setup is the spectral range of operation. When a gray-scale intensity camera is used, the polarimetric camera can provide sharp images only when operated within a limited range of the central wavelength of light by introducing a filter F in the optical path. The incoming light need not be coherent but the limited spectral range reduces the amount of light entering the system.

- Geometric distortion and image registration: Any imaging system that forms two or more images on different sets of pixels has to be calibrated to obtain a set of images that are matched to each other pixel-wise. This is called pixel registration. In case of imaging systems with similar geometric distortion in all the imaging channels, this task requires a simple calibration step, where a translation parameter may be saved for extraction of pixel registered set of images from a single frame. However, in the case of such a Wollaston prism-based polarimetric camera, the WP introduces asymmetric geometric distortion on the two images. To correct for this aberration, a calibration method may be used where the asymmetric wavefront distortion is corrected by a non-linear interpolation technique. This calibration method is described in detail in the next section of this chapter.

- Field of view and resolution: Another minor limitation of this imaging system is the reduced field of view due to the requirement of the field mask to eliminate overlapping images and the loss in resolution incurred by splitting the detector area in to two halves. The field-of-view limitation is not very important when considering long range imaging, and the resolution constraint can be easily balanced by using very high pixel density cameras that are easily available. Thus, both the limitations can be ignored given the benefits of the system.

The calibration steps employed to correct for most of the above limitations are detailed below and also reported in [7].

1.6.2 Calibration

Due to the modularity of the system, the camera and the optical components can be calibrated independently from each other. The various calibration for the snapshot polarimetric camera is detailed below.

Detector calibration

For a camera sensor there are mainly three calibrations to be performed in order to record an image that closely corresponds to the scene being imaged, namely dark pattern calibration, non-uniformity of pixel gain and removal of hot and dead pixels. Each pixel

has different dark noise properties at a particular temperature and exposure time. After averaging over a number of dark frames acquired in total darkness, one obtains the fixed pattern noise frame (I_{FPN}) that can be subtracted from the images of interest. It must be noted that this correction depends on the exposure time when the detector is not cooled. Thus, 500 dark frames were averaged to obtain the I_{FPN} for different exposure times. Another important correction to be made is the non-uniformity in pixel gain. Owing to the fabrication process, each pixel in the sensor may not have the same sensitivity. This non-uniformity is estimated by illuminating the sensor with spatially uniform white light and recording the resulting pattern. The correction image is obtained by dividing this recorded pattern by the mean gray level to create a gain non-uniformity image I_{GNU}. Using the above two calibration images, any recorded raw image (I_{raw}) is corrected using $I_{corr} = (I_{raw} - I_{FPN})/I_{GNU}$.

The calibrations of the effects of the optical components can be obtained irrespective of the camera properties. The calibration methodology employed for this camera is detailed below.

With the camera calibrated according to the above mentioned procedure, the next step is to extract the two images corresponding to the two orthogonal polarization directions from a single frame. It is necessary that the two extracted images have a one-to-one correspondence between pixels such that they map the same scene. This image registration method is an integral part of any imaging system that acquires two or more images of the scene. The image registration process is straightforward if both the images share the same geometrical distortion (or no geometric distortion). However, the WP used in the polarimetric imaging setup does introduces astigmatism and anamorphic distortion in the resulting images [81]. The distortion is non-symmetrical with respect to the two image channels and hence a perfect image registration of pixels over the entire field of view is not possible by merely translating one of the image to match the other. The difference in distortion in the two images can be corrected by a non-linear coordinates transformation on $I_{\perp}$ to match the distortion in $I_{\parallel}$.

A grid of equally spaced dots (printed black dots on white paper illuminated with light having no specific polarization orientation) was used as a calibration scene and imaged through the system to obtain image registration parameters. First, a translation parameter was manually chosen to be provide an approximate image registration. The resulting difference image ($I_{\parallel}$-$I_{\perp}$) of the calibration scene is shown in Fig. 1.4a.[a]. A further correction in translation parameters was obtained by searching for the maximum correlation between the two polarimetric images over a grid of 21 $\times$ 21 pixels. The correlation values for the grid-search is shown in the inset of Fig. 1.4a. The translation parameters acquired by searching for the maximum correlation was applied to attain image registration. The difference image of the two extracted images, for the calibration scene is shown in Fig. 1.4a.[b]. This method already shows a great improvement in comparison to uncorrected images (Fig. 1.4a.a), but it can be observed that pixel registration is imperfect in the outer regions of the image.

To correct for the residual mismatch over the entire field of view caused by the non-

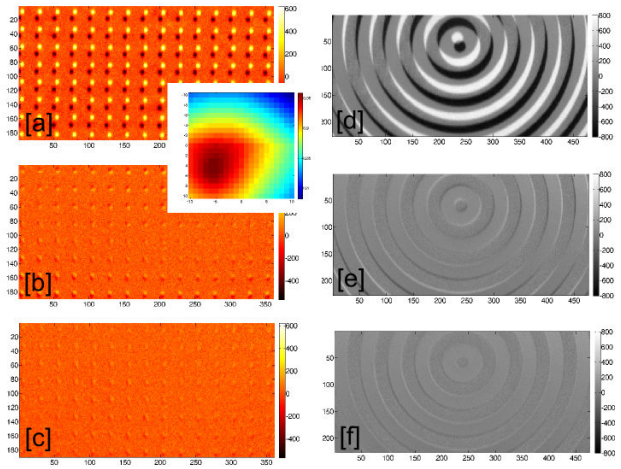

(i)

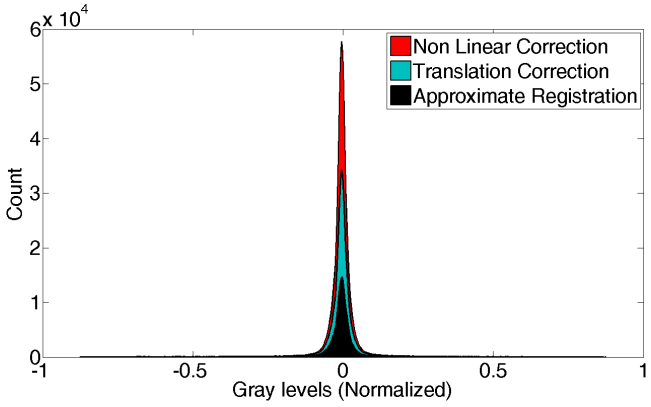

(ii)

Figure 1.4: (i) The figure shows three methods of image registration process (row-wise) on Balser A312 camera. A grid of black dots over a white background was used as calibration scene and concentric circles where used as a test image to which the calibration process was applied. For each process the difference the two extracted images ($I_{\parallel}$ - $I_{\perp}$) is shown for calibration scene (left column) and test scene (right column). Images [a] and [d] show the difference image for calibration and test scenes, respectively, for an approximate, manual translation. After the approximate translation, new translation parameters were computed by searching for maximum correlation between the two images over 21 $\times$ 21 pixels (the search map is shown in the inset). The corresponding difference image for calibration and test scene are shown in image [b] and [e], respectively. Finally, a non-linear geometric distortion correction was performed and the corresponding difference image for calibration and test scene are shown in [c] and [f], respectively. (ii) The graph shows the histogram of difference image for the test scene for the three image registration methods for the 16-bit Andor Neo SCMOS camera.

symmetrical aberration in both channels, a non-linear coordinates transformation on $I_{\perp}$ to match the distortion in $I_{\parallel}$ was sought. This was performed by extracting the coordinates of the centroids of the dots in two thresholded polarimetric images and finding the coefficients of a 2D polynomial of degree 3 for the X-Y coordinate transformation. The coefficients of the polynomial are found using least squares optimization procedure. A polynomial of degree three was found to be sufficient to describe the non-linear transformation as the higher order coefficients of the polynomial are negligible compared to the lower order coefficients. This transformation, along with bi-cubic interpolation of intensity values, was then used to create a transformed image ($I'_{\perp}$) such that both the $I_{\parallel}$ and $I'_{\perp}$ share the same geometrical distortion, as can be observed in the difference image after correction given in Fig. 1.4a[c].

A comparison of effectiveness of image registration using simple translation and non-linear correction is given in Fig. 1.4.i.(d-f) on a test scene (plain white paper with circular pattern in black). In comparison to approximate extraction shown in Fig. 1.4.i.(d), a simple translation allows for a better difference image by reducing the number of pixels with intensity far from 0, by 63 % (shown in Fig. 1.4.i.(e)). Further, with the non-linear distortion correction, a further reduction by 30 % is obtained (see Fig. 1.4.i.(f)).

The image calibration was performed for both the cameras, Balser A312 and Andor Neo, which were used in the course of the thesis. The intensity histogram of the difference image of the test scene, obtained by the three image registration methods is also shown Fig. 1.4.ii, for completeness.

It must be noted that the non-linear correction method is computationally slower than finding linear translation parameters by maximum correlation method. The calculation of parameters for non-linear correction is a one-time calibration procedure that takes about a minute for completion on a standard computer (Matlab on 2.60GHz processor). This time is acceptable even though it is 25 times slower than finding maximum correlation in a small neighborhood of (20×20 pixels) because of its one time use. However, the computational time becomes important when taking into account the time required to correct each acquired image. In this case, the simple translation is four orders of magnitude faster than the non-linear correction, which takes about 2 seconds to process because of interpolation of large number of pixels values. For applications requiring high processing speed and where only an image with limited size is considered, the interpolation should be operated on a smaller amount of pixel for fast processing. However, if the region of interest is chosen near the central region of the field of view, it is sufficient to use only linear translation. Thus, in the remainder of this chapter, a small region of interest around the source pixel is considered which remains well registered with only simple translation. This reduces the computational cost of the analysis performed in this chapter which deals with the local contrast of the source with respect to its immediate background.

Intensity Asymmetry It is important to take note of any transmission asymmetry in the two image channels introduced by the WP. In our case a 2.7% asymmetry in intensity was

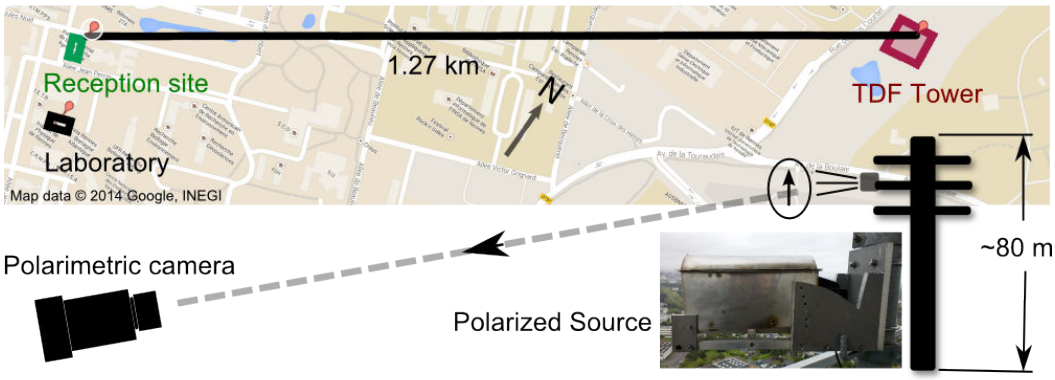

Figure 1.5: Long range polarimetric imaging experimental setup: [a] shows the source and the camera separated by 1.3 km with the camera placed in the University of Rennes 1 campus and the source placed on the TDF Tower. [b] and [c] show the polarized light source on the telecommunication tower and the GSM switch respectively.

observed after imaging a uniformly illuminated depolarizing object (plain white paper) through the system. The measured average intensity ratio ($I_{\parallel}/I_{\perp}$ = 1.027) was used to correct this asymmetry. This ratio was seen to be constant over a large central region including the region of interest. The average OSC measured for the depolarized object was measured to be -0.0127.

1.7 Long-range polarimetric imaging through fog

1.7.1 Description of experiment

As mentioned in the introduction chapter, the driving aim of this part of the thesis is to explore the possibility and quantify the efficiency of detecting a polarized beacon of incoherent light through fog. For applications in transport safety, like landing and taxiing of aircrafts in degraded weather, active light sources may be used along the runway and specialized cameras may be used on-board to provide visual aide to the pilot. During landing, the runway lights need to be detected from a long distance, preferably over few 100 meters. To test the polarimetric vision over such distances and in real foggy conditions, an outdoor experiment spanning over a kilometer was envisaged. Such experiment allows us to assess the benefits of using polarized light for improved visibility of a polarized beacon of light through foggy atmosphere over long distances that may be used in maritime, areal or road transport applications.

In this section, the outdoor experimental setup for imaging of a polarized light beacon through fog is described along with its interfacing and control. Then, an analysis is

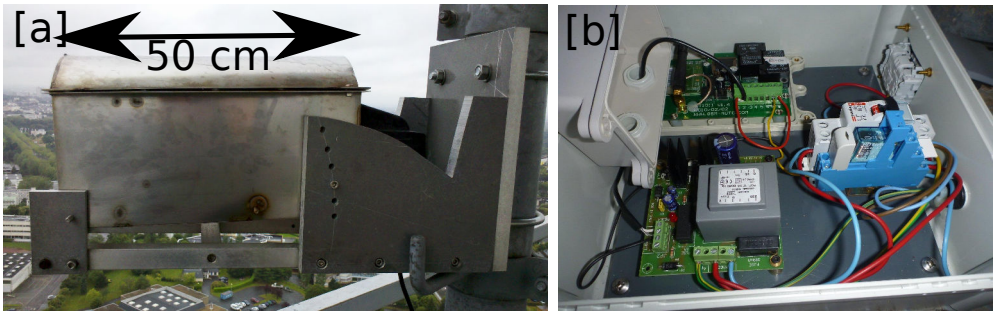

Figure 1.6: [a] The source placed inside a weather proof metal housing. [b] Picture of the remote GSM switch used to control the source with a standard mobile phone.

performed to quantitatively compare the contrast of the source obtained by various polarimetric image representations commonly used in literature under varying weather and visibility conditions. The results presented here were reported in [7]. The experimental setup which is shown in schematic in Fig. 1.5, mainly consists of a polarized light source and a snapshot polarimetric imaging system that simultaneously acquires two images of a scene corresponding to the two orthogonal directions of polarization. The polarimetric camera and acquisition computer are placed on the mezzanine floor of the mechanical building within the University of Rennes 1 campus, Beaulieu, in Rennes (France). The mechanical building is about a 100 m away from the laboratory in Institute de Physique de Rennes (IPR) and the acquisition computer is connected to a local area network for remote acquisition. The remote acquisition capability was essential due to relative unpredictability of foggy conditions and to allow all-time, world-wide access to experiment via secure network to the collaborators in India. The polarized source of light is placed in line-of-sight with respect to the polarimetric camera, nearly 1.3 kilometers away on a telecommunication tower operated by the TDF company. Since the source needed to be placed in open air exposed to wind, rain, humidity and rapid temperature variations due to the weather and the incandescent lamp, the mechanical design and stability of the source was of utmost importance. The main engineering considerations for the source are detailed in the next subsection.

Light source

The source used is a 300 W halogen incandescent lamp with a linear polarizer, both placed inside a weatherproof steel housing as shown in Fig. 1.6.a. Keeping in mind the cost of installation and ease of mass production, the light from the incandescent lamp is polarized using an adhesive dichroic polymer polarizing sheet glued to a glass plate placed 20 cm away from the lamp and oriented such that the polarization axis is vertical. Such polarizing sheets provide a practical solution as they are available at low cost and have a polarizing efficiency of about 99.5 % for wavelengths ranging from 400 nm to 700 nm. It is worthwhile to note that, according to test on the standard polarizer sheets, they were found to be susceptible to deterioration by heat induced by the source and/or by rapid temperature fluctuations that are encountered in outdoor conditions during winter. Taking these factors

into consideration, polarizing sheets specifically designed for LCD projector industry were used, thus ensuring high durability and high power operation conditions. To further test such polarizing sheets to suit our experimental conditions, durability tests were conducted in indoor conditions using a 300 W lamp.
A polarizing sheet was placed at a distance of 20 cm away and the lamp was allowed to run continuously during day times. In these conditions, it was noticed that the polarimetric contrast of the sheet was reduced by 57.4% in a period of 5 days with continuous daytime usage. In light of this, the weather-proof steel housing was designed with a vent pipe and the polarizer was placed sufficiently far (20 cm) from the lamp, allowing the hot air generated by the incandescent lamp to be removed by convection, thus providing an efficient heat dissipation. Such mechanical design ensures a reasonable operating life of the polarizing sheet before requiring replacement in around a years time.
The telecommunication tower over which the source is installed is about 80 m in height and provides a suitable location for the source. The distance of the tower from the laboratory site in the University of Rennes-1 is optimal for various applications where a long-range imaging through fog may be crucial. The tower is also the tallest structure in the surrounding area and is in line-of-sight from university buildings. Finally, once installed, accessing the source is limited due to the necessary access authorization required by the TDF company. It is necessary to ensure remote switching capabilities for the source. Taking various factors into consideration, a GSM switch was installed to enable easy and secure remote control of the experiment.

Polarimetric camera and acquisition

The polarimetric camera was setup to be controlled by an acquisition system programmed in LabView. A graphical control was programmed with the following features to make easy and robust acquisition of data in day and night conditions. A screen-shot of the control program is shown in Fig. 1.7 and the features are listed below.

- Pixel registration by linear translation: The control program included inputs to provide the translation parameters required to obtain pixel registered central image. The translation parameters were obtained during the calibration step.

- Real-time display: The interface included a real-time display for the raw image obtained from the polarimetric camera. The intensity values at two pixels of choice were also displayed with respect to time. Usually, one of the pixels (and its counterpart in the orthogonal polarization image) corresponds to the location of the source and the other corresponds to a pixel representing the ambient light. Using the data from these pixels, orthogonal-states contrast (OSC) (defined in Eq. (1.9)) was calculated and (optionally) shown in real-time.

- Automatic exposure control (AEC): One of the important features of the acquisition system is the ability to change the exposure automatically to avoid saturation or under exposure of the source and its immediate surrounding. The illumination levels

(a)

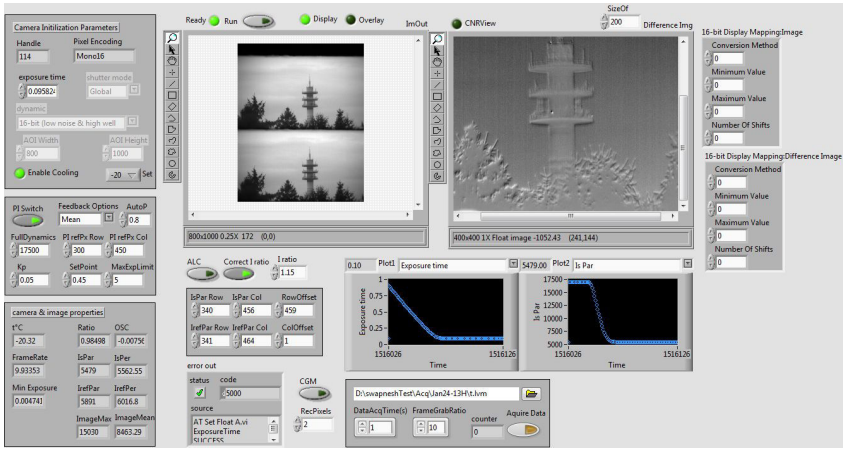

(b)

Figure 1.7: Evolution of the control and acquisition program developed in LabView for the two cameras.

may vary drastically, during foggy conditions, especially, during dawn or dusk. The implementation of AEC was necessary to take advantage of the camera beyond its dynamics over the entire dataset and to gather 'clean' data, which are not saturated or under exposed. This was implemented by programming a proportional feedback loop over the intensities at the pixel containing the source and a neighboring pixel. The changing exposure time was also recorded for each time stamp to finally normalize the recorded image with respect to its corresponding exposure time during post-processing.

- Data and image saving with predefined time interval: The time interval with which the image and the data at the specified pixels could be chosen independently. This was implemented for long acquisitions where saving images too frequently was constrained by the available memory in the acquisition computer.

- Cumulative grab mode (CGM): When the ambient light is sufficient, like during day time, the exposure time may be very small. In this case, the camera may be able to sample the AC line, 100 Hz frequency of the light source. To avoid this, a cumulative

grab mode was implemented, where time series data corresponding to the maximum source intensity over a few frames (number of frames depending on the exposure time) was only saved.

In-situ calibration of the polarimetric camera

Along with the calibration procedures detailed in section 1.6.2, further alignment of the detection system with the polarization direction of the source is required while mounting the detection system with respect to the polarized source. The polarimetric camera setup and the control/acquisition computer are settled in a mezzanine floor of a building facing the telecommunication tower. The whole setup is placed on a stable mechanical mount with adjustable angle (pitch) so that the imaging system can be aligned in line-of-sight with the source on the tower. In addition, the tilt angle (roll) must be well aligned so that the polarization axis of the imager is strictly aligned with the polarization direction of the source. This calibration is preferably done during night time in clear sky with the source turned on. It is indeed easier to minimize and even null the intensity at the source location in the perpendicular polarization image ($I_{\perp}$) in dark background. After such calibration, an OSC of 0.97 for the source pixel was observed which increased to a value of 1.00 when the low intensity neighborhood background intensities were subtracted from each polarimetric channel before computing the OSC.

Indeed, this calibration step is not required if circular polarization states are used instead of linear polarization. In fact, it has been shown that the penetration depth of the circularly polarized light in a turbid media is longer than that of linearly polarized light [27, 28] and may be more suitable for application in aircraft landing assistance. The versatility of the design of the imaging system allows to obtain images in orthogonal circular polarization with minimal change to the system (i.e. addition of a quarter wave plate). In this thesis, circular polarization is not used, instead all the results shown correspond to linearly polarized source and detection in orthogonal linear polarizations. However, all the core concepts presented can be directly translated to the use of circular polarization.

During these preliminary acquisitions to test the calibration of the system, it was checked on the acquired frames that the daytime clear sky is polarized to some extent, depending on location of the sun in the sky, and that the ambient light backscattered on the tower structures and imaged on the camera can partly retain polarization. However, it was observed that the imaged scene is almost totally unpolarized as soon as a thin layer of fog or haze is present in the atmosphere, or when the weather is covered by (even very thin) clouds. As a result, the difference image of the two image channels is expected to provide an obvious advantage over intensity imaging due to its ability to cancel the unpolarized background and isolate the polarized source.

1.7.2 Principle of the measurement

All weather acquisition

Once settled, optimized and calibrated the imaging system described in previous sections, and using the above mentioned control program, numerous time series of data were taken during different times of the day (dawn, daytime, dusk and nighttime) with varying atmospheric conditions (clear sky, thin haze, fog, cloud, rain). The corresponding time-series acquisitions were recorded during years 2011-2014 with various time periods (10 images/minute to 6 images/hour) over long time spans of several hours or tens of hours. During these long term acquisitions, the dynamically varying exposure time in AEM was recorded for each acquisition and the frames were normalized to their respective exposure times during post-acquisition analysis.
These acquisitions made in various weather conditions (including rain and snow) and during various times of the day to quantitatively reveal the effectiveness of using polarimetric imaging for detecting a polarized light beacon through fog. The analysis of the experimental results led us to retain four main different scenarios, associating clear-sky / foggy conditions and day/night time. The conditions in daytime with fog are indeed such that, the intensity of the pixels around the source are nearly uniform making it difficult to identify the source from the background in a simple intensity image. In clear sky conditions, the background consists of the telecommunication tower structures and installations. On the other hand, in night time one has the conditions where the source is brighter and the background is dark with unpolarized and localized bright light sources (for instance, the red aircraft warning lights on the tower) or sometimes, during heavy fog, a uniformly lit background because of scattering of city lights.

Standard polarimetric representation compared

In all these condition, a polarimetric image representation is sought, that maximizes the contrast of the polarized source with respect to its background. Since, the polarimetric imager provides us with two images ($I_{\parallel}$ and $I_{\perp}$), a generic polarimetric representation may be denoted by γ, where γ is an image that is a function of the pixels in the two images $I_{\parallel}$ and $I_{\perp}$. For example, two of the most common candidate for a polarimetric image representation are the difference image, $\gamma_{\Delta} = I_{\parallel} - I_{\perp}$ and the OSC image $\gamma_{OSC} = (I_{\parallel} - I_{\perp})/(I_{\parallel} + I_{\perp})$. To quantitatively compare the various common representations used in literature, two more representations were chosen, i.e. the intensity summed image $\gamma_{\Sigma} = I_{\parallel} + I_{\perp}$ and the polarization filtered image $\gamma_{\parallel} = I_{\parallel} / \langle I_{\perp} \rangle$, where $\langle I_{\perp} \rangle$ denotes the mean intensity values in the neighborhood of the source in image $I_{\perp}$. These four representations, their symbol and definitions are tabulated in Table 1.2.

Polarimetric images, region of interest and contrast measure

A typical frame recorded from the imaging system is shown in Fig. 1.8a. From each such acquired frame in the time series, two sub images were extracted as indicated by the yellow

Signal representation	Symbol	Definition
Intensity summed image	γ_Σ	$I_\parallel + I_\perp$
Polarimetric difference image	γ_Δ	$I_\parallel - I_\perp$
OSC image	γ_{OSC}	$\frac{I_\parallel - I_\perp}{I_\parallel + I_\perp}$
Polarization filtered image	$\gamma_\parallel$	$\frac{I_\parallel}{\langle I_\perp \rangle}$

Table 1.2: Simple signal representations of polarimetric data, with $\langle I_\perp \rangle$ denoting spatial average performed on $I_\perp$ over a square neighborhood of pixels surrounding the source.

rectangles in the Fig. 1.8a using the image registration method described in section 1.6.2. For the analysis that follows this chapter, the source pixel was identified and an ROI of 21 $\times$ 21 pixels in its immediate neighborhood was chosen as shown by the square region in cyan in Fig. 1.8a [1]. Thus, the ROI from the polarimetric image of the scene taken parallel to the direction of polarization of source, denoted by $I_\parallel$, contains the source information. Meanwhile, the ROI from the polarimetric image of the scene taken in orthogonal direction of polarization, denoted by $I_\perp$, has no information of the source on a clear day. These two images $I_\parallel$ and $I_\perp$ can be used to form various standard polarimetric representations and the contrast of the source obtained from each representation can be compared.

Two regions in the 21 $\times$ 21 pixels ROI are identified as shown in the Fig. 1.8b. The 3 $\times$ 3 central pixels shown in red in Fig. 1.8b are identified as 'source/signal' pixel and the set of pixels is denoted by S. The set of pixels shown in blue in Fig. 1.8b are identified as 'background' pixels and denoted by B. The background pixels constitute all the pixels in the ROI excluding a central region of size 11 $\times$ 11.

For any single polarimetric representation γ obtained from the two polarimetric images $I_\parallel$ and $I_\perp$, a contrast measure of the 'signal' with respect to the 'background' can be defined using the ROI presented above. The image representations presented in Table 1.2 clearly will have different intensity scaling at each pixel, rendering it difficult to infer a direct quantitative comparison of the source contrast presented by each representation. To fairly compare the visual contrast of the source with respect to its background, it is necessary to obtain a statistical contrast measure akin to the signal-to-noise ratio. In light of this, a contrast-to-noise ratio (CNR) is used to quantify the absolute contrast of the source with respect to its immediate background, and is defined as

$$\mathcal{C}(\gamma) = \frac{\langle \gamma \rangle_S - \langle \gamma \rangle_B}{\sqrt{\frac{1}{N-1} \sum_{i \in B}^{N} \left(\gamma_i - \langle \gamma \rangle_B\right)^2}} \tag{1.10}$$

where $\langle \gamma \rangle_B = \sum_{i=0}^{N} \gamma_i / N$ is the spatial average over pixels in B and N is the number of pixels in set B.

The CNR, similar to the signal-to-noise ratio, is a measure of how many standard deviations away does the signal pixel lie from the mean of its surrounding pixels. The CNR value is thus independent of the intensity scaling in each representation and provides us

[1] The red square shown in the image was a region from where the ambient light properties were derived, whenever necessary.

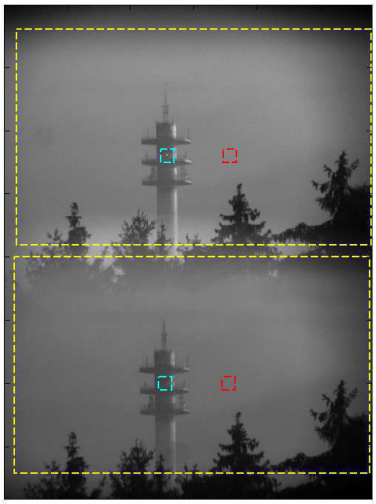

(a)

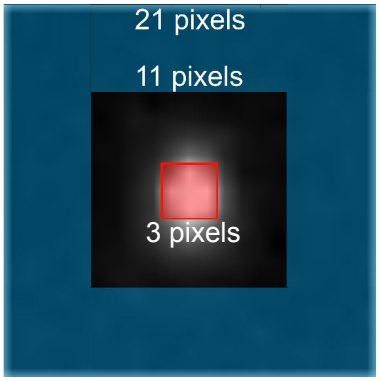

(b)

Figure 1.8: (a) A raw frame captured by the polarimetric camera. The yellow rectangular overlay shows the two pixel-registered sub images, with the top rectangle forming the image $I_{\parallel}$ and the bottom rectangle forming the image $I_{\perp}$. The cyan box is a 21 $\times$ 21 pixels ROI and the red box shows the ambient exposure. The ROI from the two images can then be used to obtain a single polarimetric representation γ. (b) In the ROI of the polarimetric representation γ, two sets of pixels are identified. The region in blue is denoted by B for background and the region in red is denoted by S for source pixels. The pixels in the two regions are used to define a statistical contrast measure.

with the means of quantifying and fairly comparing the contrast obtained by various representations. Such a contrast measure is well adapted to our data which has been checked to be Gaussian distributed. More generally, the metric is well suited for additive noise, which is expected and checked in the considered imaging scheme. It can be noted that alternative definitions of contrasts may be better suited if other types of noise were to be considered.

The estimated CNR, of course, would depend on the choice of ROI. In this study, a 21 $\times$ 21 pixels ROI was chosen keeping in mind the size of the source and fair uniformity of the background. The central 3 $\times$ 3 pixels within the ROI was identified by taking into account the fluctuation of the maximum source intensity from frame to frame due to turbulence in the intervening air/fog. Finally, the exclusion region of 11 $\times$ 11 was chosen according to the spread of the source. The CNR for the optimal representation described in the next chapter was calculated over various sizes of exclusion region (for a data set with varying visibility as presented in the next chapter) and the exclusion region of 11 $\times$ 11 was chosen accordingly. The histogram of the occurrence of maximum CNR for each frame for various exclusion region is shown in Fig. 1.9.

In the following subsections, a thorough data analysis is performed on two particular time-series acquisitions allowing one to observe clear sky and foggy conditions in day time (section 1.7.3) and night time (section 1.7.3). These two experimental data series are

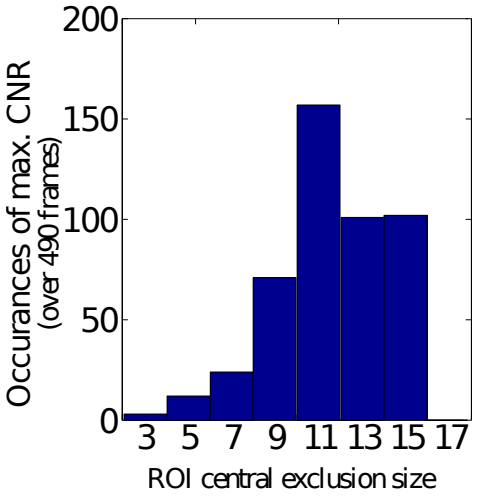

Figure 1.9: The CNR was calculated as a function of various exclusion sizes for each frame in a data set encompassing varied visibility conditions. The occurrence of maximum CNR at each exclusion size is plotted, demonstrating that a 11 $\times$ 11 pixels exclusion region is the appropriate ROI shape to consider for contrast maximization in the experimental conditions at hand.

representative of the wide variability of environmental conditions that were made possible to address with the experiment described in this chapter.

1.7.3 Results

Day time measurement

On of the first data acquisition series was recorded on the 17-10-2011, between 9.45 am and 10.53 am. During this 68-minutes acquisition, a frame was recorded every 10 seconds which enabled us to record the fading of thick fog around the 30 minutes into the acquisition. This data set was chosen among many as it encompasses various visibility conditions. In Fig. 1.10 the experiment results are plotted. In Fig. 1.10.a, the curve in red shows the time evolution of the intensity of the pixel corresponding to the location of the polarized source in the image. The curve in black represents the evolution of the ambient light intensity which was estimated from a spatial averaging of the total intensity $I = I_{\parallel} + I_{\perp}$ in a homogeneous 21 $\times$ 21 pixels sky region, marked in Fig. 1.8a with a red square. The camera exposure time during the whole experiment was controlled by the LabView program in Auto Exposure Mode, so as to prevent underexposure or saturation of the signal pixel. The evolution of the exposure time is also provided in Fig. 1.10.a in dotted blue curve, revealing the smooth evolution of the fog density and background illumination during the experiment.

Across this experimental dataset of 408 images, four instants are shown in Fig. 1.10, labeled H, I, J and K. The corresponding images are respectively shown in Fig. 1.10.c. They correspond to different situations of visibility of the source through fog. The time frame labeled H corresponds to high fog density where the source is completely embedded in

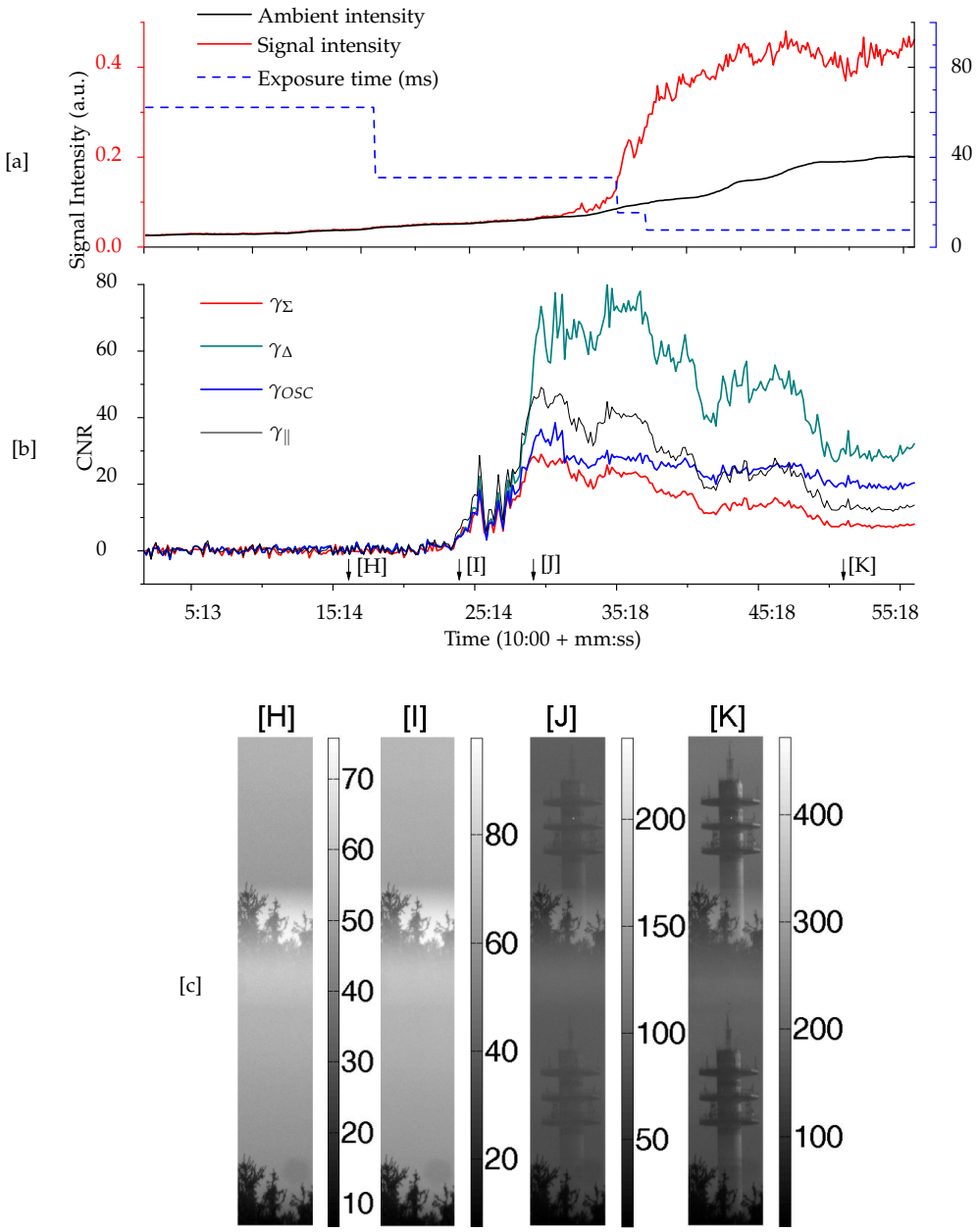

Figure 1.10: Comparison of contrast of the source with respect to the background for intensity image and polarimetric images after manipulation. The raw image corresponding to the frame number indicated by the arrow is shown in the inset. The plot indicates that in foggy conditions in day time the OSC image, γ_{OSC} always has more contrast than the simple intensity image. Its is also observed that the difference image γ_Δ has higher contrast in thin fog situations. During heavy fog, the polarization filtered image $\gamma_\parallel$ has highest contrast.

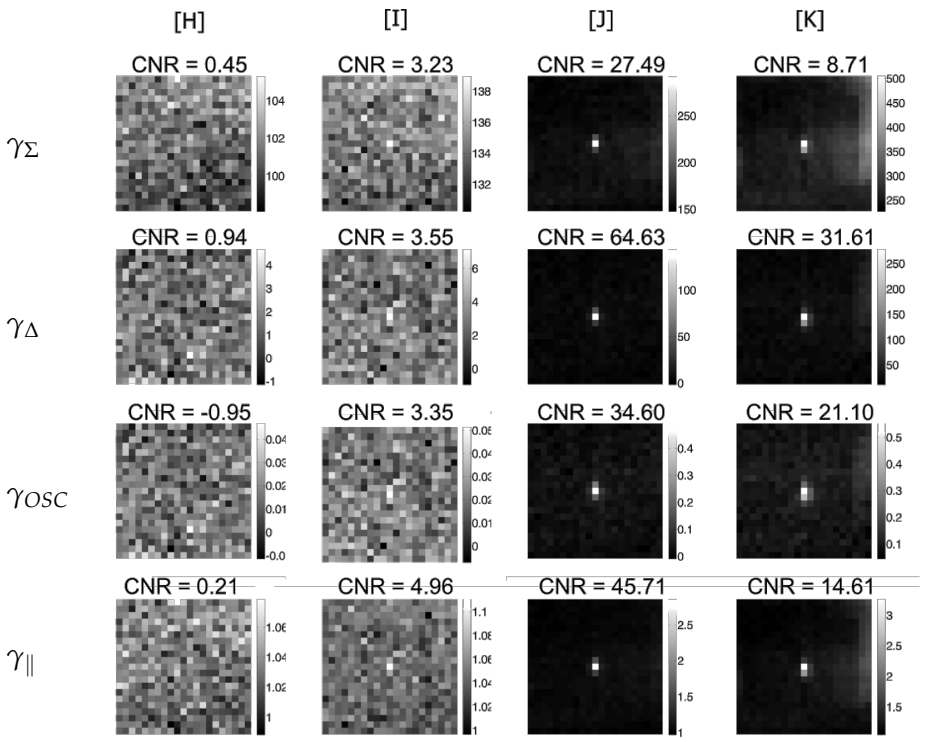

Figure 1.11: The image of the source extracted at times indicated by I, J and K in fig. 1.10. Row 1 to 4 correspond to intensity-summed image, difference image, OSC image and polarization filtered image respectively. The corresponding CNRs are also given for comparison.

the background illumination, as can be checked in Fig. 1.10.a by comparing the levels of the signal and background intensities. Frame I is the first image on which the light source begins to be detectable over the background (see Fig. 1.10.a) due to thinning of fog. Then, acquisition J corresponds to an intermediate situation of a light haze limiting the visibility of the source whereas the last measurement K has been acquired in clear sky, but with a background illumination significantly higher than in the frame J.

Let us now analyze the CNRs associated to the four signal representations considered in this section and defined in Table 1.2 (in pg. 49). The evolution of the CNRs across the whole dataset is given in Fig. 1.10.b. In Fig. 1.11, the contrast images computed for each signal representation and for each situation H-K, on a 21×21 pixels neighborhood of the central signal pixel is also provided. The numerical values indicated in Fig. 1.11 correspond to the CNR of the central pixel estimated on this neighborhood. As it can be seen from these results, the source is hidden behind heavy fog until 10.23 am and all CNR values remain close to zero in this situation.

Measurements performed after 10.23 am are more interesting. Indeed, they first allowed us to observe that, as soon as the light emitted by the source is visible over the background, it retains a very high polarization degree, with no detectable depolarization induced by the turbid atmosphere. This can be interpreted as follows: due to long working distances, light can be almost totally absorbed even by a very thin fog, while the latter cannot be

considered as a strongly diffusive medium, and hence no strong depolarization can be expected from it. Then, the results given in Figs. 1.10 and 1.11 reveal that as soon as intensity coming from the source is detectable, all polarimetric signal representations (γ_Δ, γ_{OSC} and $\gamma_\parallel$) provide CNR values significantly higher than the CNR obtained with an intensity-summed measurement (γ_Σ). This general result thus confirms the interest of polarimetric measurement for enhanced vision in poor visibility conditions. The analysis can be however refined so as to identify the best signal representation in a given situation. In very low visibility conditions (acquisition I), it appears that $\gamma_\parallel$ gives the best improvement in terms of CNR (60% increase) w.r.t. an intensity measurement γ_Σ.

On the other hand, when visibility increases, the best signal representation corresponds to a difference image γ_Δ allowing the CNR to be enhanced up to a factor of almost 4 (acquisition J). The efficiency of the difference image is due to its ability to suppress the background contribution. This enhancement is either due to diffused light in the turbid atmosphere, as in acquisition J, or due to the surrounding scene, as in acquisition K on which elements of the telecommunication tower can be identified on the intensity image. Indeed, as it has been noticed in section 1.7.1, the ambient light does not exhibit noticeable polarization as soon as the sky is covered by clouds or when a thin layer of haze or fog is obscuring the atmosphere. Hence, the contributions of this ambient background on the two polarimetric images $I_\parallel$ and $I_\perp$ are strictly identical, and can thus be suppressed on a difference image. Interestingly, the representation that provides the best contrast varies with the visibility conditions. Identification of a contrast maximizing representation may provide a better detection of the source embedded in a foggy background. However, to comment on the detection efficiency of any representation, one should analyze jointly the probability of detection and the probability of false alarm in each representation. The identification of an adaptive, contrast-maximizing representation and preliminary detection strategies will be further explored in the next chapter.

Lastly, it is interesting to note that γ_{OSC} never appears to be the best representation: this is understandable since OSC implies a normalization of γ_Δ by the total intensity γ_Σ, which increases the relative noise in the final image and thus decreases the CNR. In the next subsection, it will be shown that such normalization can be much more detrimental to signal quality in night time conditions. Though necessary for assessing the DOP of a target, this normalization can however be avoided when it comes to locating or detecting a target in poor visibility conditions.

Night time measurement

A similar experiment was conducted during night time. For illustration, an acquisition taken on the 14-10-2011, between 1.53 am and 7.17 am is considered. During this 324-minutes-acquisition, a raw frame has been recorded every minute. As in the previous subsection, the evolution of signal pixel and background intensities are plotted respectively in red and black curve in Fig. 1.12.(a). The evolution of the exposure time over this long time period is provided in Fig. 1.12.(a) in dotted blue curve (logarithmic scale). This curve

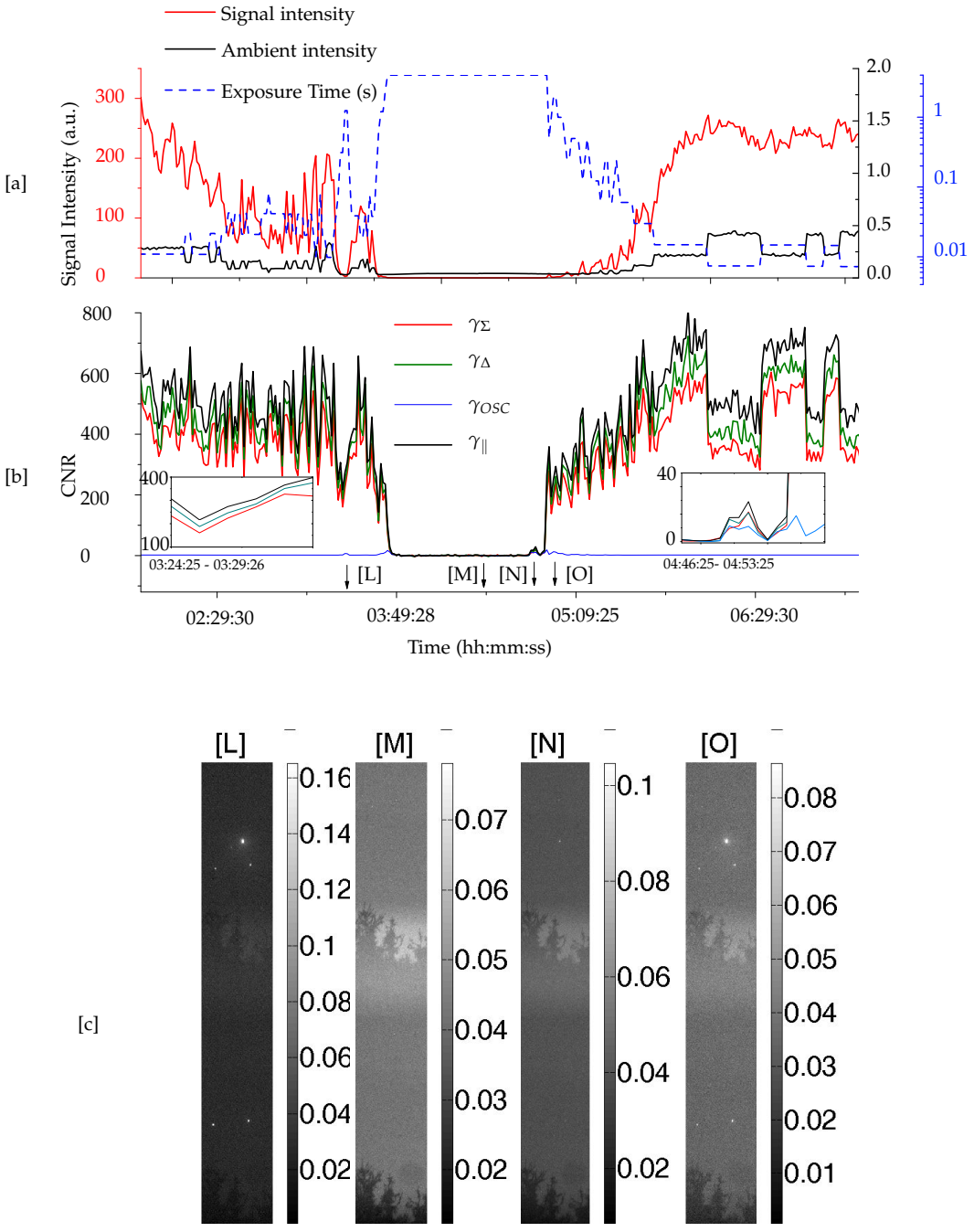

Figure 1.12: The signal contrast for different polarimetric representations from the polarimetric images. It is seen that the OSC does not provide a good way of representing the source because the division adds noise to the OSC image decreasing the contrast of source from surrounding. The inset shows the zoomed out part of the curve where the fog is thinning and the contrasts are comparable.

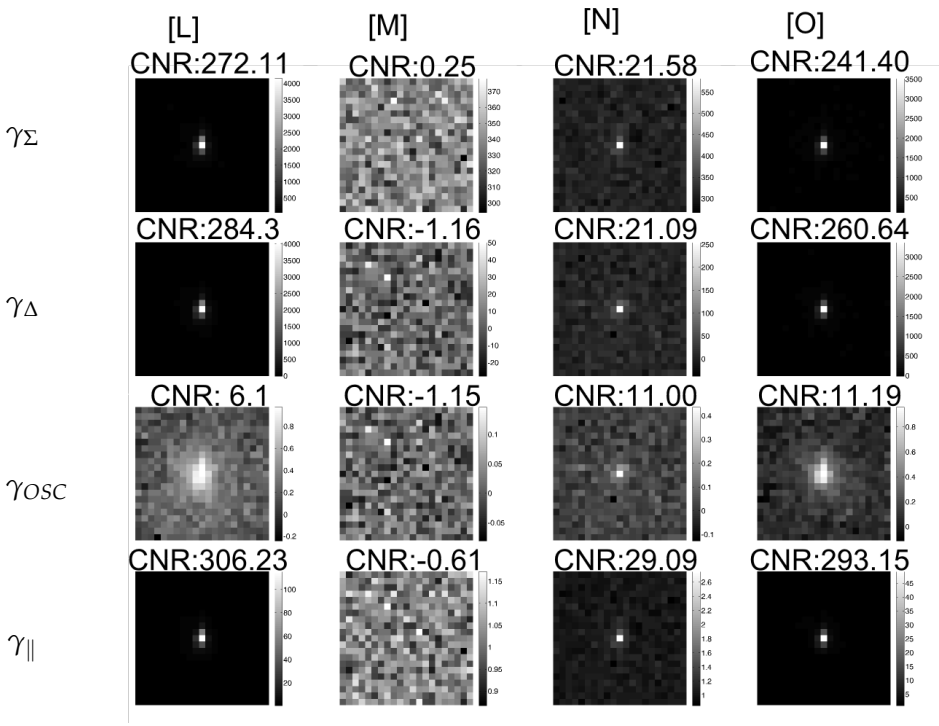

Figure 1.13: Images extracted during night time for times L and M as indicated in fig. 1.12. The OSC image is observed to be noisy and has least signal contrast as a result.

shows the strong variations of the exposure time at night with atmospheric conditions, ranging from 7 ms to a maximum value of 4 s authorized by the camera used. From the observation of these curves, it can be noted that a dense fog cloud has totally obscured the visibility of the source between 3.40 am and 4.55 am, leading to a maximum exposure time in total darkness, as in situation labeled M in Fig. 1.12. On the other hand, the beginning and the end of the acquisition correspond to almost clear sky conditions (as in situations labeled L and O). The strong signal intensity variations observed in clear sky conditions are mainly due to atmospheric turbulence which causes flicker of the position of the signal pixel on the images, and can also be partly due to an imperfect smoothing of the source modulation at 100 Hz. In the conditions of the experiment, one other situation labeled N has retained our attention since it corresponds to one of the rare instants of fog setting/rising, in which the source is partly visible. The raw images corresponding to these four situations are also plotted in Fig. 1.12.(c). The display dynamics has been expanded for situations L and O so that the background becomes visible.

As in Fig. 1.10, the CNRs associated to the four signal representations are plotted in Fig. 1.12.b across the whole dataset. The contrast images obtained at each particular situation analyzed L, M, N and O are given in Fig. 1.13. These experimental results first confirm that OSC is not a relevant signal representation due to noise amplification occurring with normalization. The corresponding CNR is indeed always close to zero, and the noise amplification can be clearly observed in Fig. 1.13. This effect is particularly enhanced in night conditions since background values are very close to or equal to zero (since the exposure time is limited in clear sky to prevent saturation of the source pixel, see Fig. 1.12.(a)), thus

leading to non-numerical values in the final image, which are not taken into account in the computation of CNR.
The comparison of the three other signal representations considered in this section is more informative. It can first be noted that between 3.40 am and 4.55 am, none of the representations allows the source to be significantly detected over the background, due to total absorption of the emitted light when propagating though dense fog. In clear sky conditions however (situations L and O) or partially reduced visibility (situation N), it can be observed that simple intensity image and polarimetric difference image share comparable CNR values. This confirms the fact that γ_Δ only outperforms a simple intensity image in the presence of significant background contribution, as observed above in daytime conditions. In night time conditions, the very dark background is strongly affected by camera dark noise and a difference image could, in some configurations of noise realization, lead to a degradation of the CNR with respect to an intensity detector. Only the polarization filtered image $\gamma_\parallel$ allows improving the CNR values by a factor comprised between 10% and 35%, which can be explained from the noise reduction induced by the spatial averaging of the background in the expression of $\gamma_\parallel$.
These results, which seem to soften the interest of polarimetric imaging for vision enhancement though turbid atmosphere in night conditions, actually reveal the limitations of the present setup used for these experiments. These nocturnal acquisitions indeed allowed us to identify two ways of improvement for our detection system, which are (a) the minimization of the dark noise, and most importantly (b) the increase in detector dynamics. Reducing the dark noise would limit the levels of noise in dark background in night-time conditions for polarimetric signal representations, as stated above. Moreover, it can be observed in Fig. 1.12.(b) that between 6.00 am and 7.10 am, strong variations in all the CNR values occur, following the same abrupt "steps" at each modification of the exposure time. This is a confirmation that in these situations, the dark image background is perturbed with camera dark noise. Indeed, this noise contribution is independent of the exposure time and is thus artificially doubled relatively to the signal pixel value when exposure time is divided by two, hence leading to a strong decrease in terms of CNR. This also confirms that adapting the exposure time cannot increase the dynamics of a detector when the illumination variations across the scene exceed the sensor dynamics. It would thus be highly beneficial to use a high dynamics sensor to improve these results and potentially increase the range of environmental conditions for which polarimetric imaging could be highly advantageous for vision enhancement through turbid atmosphere over long distances. In light of this, a 16-bit dynamics, low-noise camera was bought and used for further experiments that are presented in the next chapter.

1.8 Discussion

The above results provide a quantitative comparison of commonly used polarimetric image representations in outdoor foggy conditions. Such a study is indeed necessary before a polarimetric imaging scheme can be employed for actual transport applications. The com-

parative results indicate that the best representation that maximizes the contrast of a polarized light source through fog may depend on the foggy conditions itself. This opens an opportunity to theoretically and experimentally explore the existence and form of a 'universal' polarimetric representation that maximizes contrast of the polarized source though any foggy conditions. In addition, the results indicate that the OSC image underperforms compared to a difference image (in case of thin fog) or a polarization filtered image (in case of dense fog). Thus, in the next chapter, a linear combination of the two polarimetric images will be studied to derive a contrast maximizing polarimetric representation using both experiments and information theoretical tools.

2

Optimal contrast enhancement and detection of polarized sources through fog

In the previous chapter, the design, setup and the preliminary results of a long-range polarimetric imaging experiment were discussed. Various common polarimetric image representations were analyzed and it was shown that the representation that maximizes the contrast of a polarized source through fog differs for different visibility conditions. For example, the orthogonal-states contrast (OSC) image was shown to under-perform with respect to a difference image or sometimes even a simple polarization filtered image. In light of the conclusions drawn from the preliminary results presented in the previous chapter, certain questions arise naturally. Is there an 'universal' polarimetric representation that maximizes the contrast of the polarized light beacon through fog, irrespective of the visibility conditions? If so, what are the parameters that comprise this contrast maximizing representation and what is its analytical form? Can it be rigorously derived and extended to a generic polarimetric imaging scheme? Finally, is it possible to quantitatively characterize the quality of the representation and compare its performance with respect to a standard camera?

This chapter deals with addressing these questions using information theory with realistic models inferred from experiments, validating the theory with experimental results and using the theory to propose real-time, automatic detection schemes for polarized light beacons through fog. In section 2.1, first, a generalized polarimetric imaging scheme is considered and a noise model is proposed. Using the noise model, an optimal polarimetric representation is derived. Then, in section 2.2, the efficiency of the optimal representation with respect to an intensity camera is theoretically predicted. Then, in section 2.3, the theoretical prediction are validated by comparing with the experimental results. For

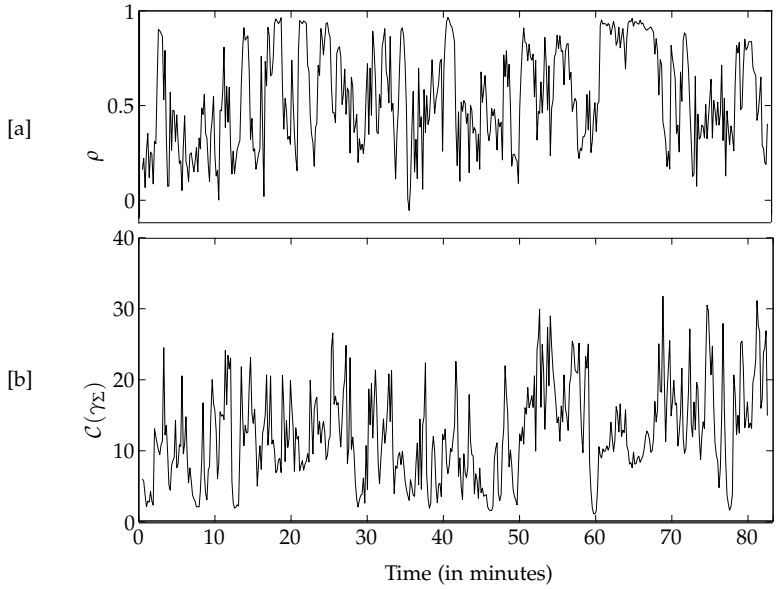

Figure 2.1: [a] The time evolution of the background correlation coefficient between the two polarimetric images estimated in the neighborhood of the source pixel. [b] The time evolution of the CNR of the intensity-summed image γ_Σ

this purpose an experimental data set taken during 24-01-2014 between 1:00 p.m. and 2:20 p.m. (at a time interval of 1 frame every 10 seconds) was utilized. This data set, referenced throughout the chapter was chosen because it encompasses most of the foggy weather conditions from clear sky, to thin fog to thick fog, with no apparent structure in the time evolution of the visibility as indicated by the time evolution of the CNR of the intensity-summed image in black solid lines in Fig. 2.1. Finally, in section 2.4 and 2.5, real-time implementation and detection strategies of the optimal representations are presented, followed by concluding remarks in section 2.6.

Before proceeding into core of the chapter, let us introduce and recall some of the notations which are relevant for a clear understanding of the analysis that follows. In the experiment detailed in the previous chapter, a highly polarized source with degree of polarization $P = 1$ embedded in a fully unpolarized background with degree of polarization $\beta = 0$, was imaged using a snapshot polarization sensitive camera. The polarization camera effectively produces a two-dimensional image at each time frame $I_P = [I_\parallel, I_\perp]^T$ where the i^{th} pixel (in lexicographic order) in image I_P can be written as $\boldsymbol{x_i} = [x_{i,\parallel}, x_{i,\perp}]^T$ constituting a random variable $\boldsymbol{X_i}$. The pixel marker indicated by the subscript i can be dropped without loss of generality. The expectation value of a function that depends on the random variable, over an ensemble of pixels, is then denoted by angle brackets as $\langle . \rangle$. Further, from each frame a region-of-interest (ROI) is extracted from the full-field image according to the ROI defined in section 1.7.1 of chapter 1.

In imaging scenarios with incoherent light and considerably high intensities, the Poisson noise in photons reaching the detector can be approximated by a Gaussian distribution

with the variance equal to the mean intensity. Consequently, the random variable $\boldsymbol{X}$ is hypothesized to follow a multi-dimensional Normal distribution as

$$P(\boldsymbol{x}) = \frac{1}{\sqrt{2\pi\,|\Gamma|}}\; exp\left[-\frac{1}{2}(\boldsymbol{x}-\langle\boldsymbol{x}\rangle)^T\Gamma^{-1}(\boldsymbol{x}-\langle\boldsymbol{x}\rangle)\right], \tag{2.1}$$

where, $\Gamma = \left\langle(\boldsymbol{x}-\langle\boldsymbol{x}\rangle)(\boldsymbol{x}-\langle\boldsymbol{x}\rangle)^T\right\rangle$ is a 2×2 covariance matrix and $\langle\boldsymbol{x}\rangle$ is the mean intensity. In the most general case, the covariance matrix may not be diagonal and the distribution may be correlated. Especially, in a snapshot polarimetric camera, where simultaneous polarimetric images are taken, the pixels that receive the light from objects in the unpolarized/partially background may be correlated. This correlation may arise due to slight visibility of background objects or due to non-uniform fog densities around the source. For pixels in the immediate background region, denoted by $\mathcal{B}$ and defined in the ROI in Fig. 1.8b, an empirical correlation coefficient can be computed using

$$\widehat{\rho} = \sum_{i\in\mathcal{B}} \frac{(X_i^{\parallel} - \langle X^{\parallel}\rangle_{\mathcal{B}})(X_i^{\perp} - \langle X^{\perp}\rangle_{\mathcal{B}})}{\widehat{\sigma_{\mathcal{B}}}(X^{\parallel})\widehat{\sigma_{\mathcal{B}}}(X^{\perp})}, \tag{2.2}$$

where, $\widehat{\sigma_{\mathcal{B}}}$ represents the empirical standard deviation of the intensities of the pixels in background region $\mathcal{B}$. The time evolution of the estimated background correlation coefficient for the data set considered in this chapter, is plotted in Fig. 2.1. Clearly, there is finite correlation between the backgrounds of the two polarimetric images and the time evolution also is related to the visibility. This, will be apparent in the following sections in the chapter when the theory is developed and compared with the experiments.

2.1 Generalized imaging scheme and optimal representation

A generalized two-channel polarimetric imaging scheme can be applied in various scenarios. For example, in underwater imaging in a reflection mode, a polarized source may illuminate an object embedded in a turbid medium. In this case, the illuminated object of interest and the backscatter from the background may have arbitrary degree of polarization. Taking into account various other situations, a generalized polarimetric imaging scheme is presented which provides limits of this imaging modality adapted to the situation.

2.1.1 Correlated noise model

Let us consider a polarimetric imaging situation where the source with mean intensity s and a DOP of $P \in [0,1]$ and is embedded in a background with mean intensity b and DOP of $\beta \in [0,1]$. Then, the mean intensity $\langle\boldsymbol{x}\rangle$ and the covariance (Γ) of the polarimetric pixel $\boldsymbol{X}$ can be modeled and parametrized as

$$\langle \boldsymbol{x} \rangle = \begin{pmatrix} s\frac{1+P}{2} + b\frac{1+\beta}{2} \\ s\frac{1-P}{2} + b\frac{1-\beta}{2} \end{pmatrix} \tag{2.3}$$

$$\Gamma = \left\langle (\boldsymbol{x} - \langle \boldsymbol{x} \rangle)(\boldsymbol{x} - \langle \boldsymbol{x} \rangle)^T \right\rangle = \begin{pmatrix} \frac{1+\beta}{2}\epsilon^2 + \sigma^2 & \rho\frac{\sqrt{1-\beta^2}}{2}\epsilon^2 \\ \rho\frac{\sqrt{1-\beta^2}}{2}\epsilon^2 & \frac{1-\beta}{2}\epsilon^2 + \sigma^2 \end{pmatrix}, \tag{2.4}$$

where ρ is the correlation coefficient, σ^2 and ϵ^2 are the noise variances due to the detector and due to optical fluctuations, respectively. According to the origin of the optical fluctuations, ϵ^2 can be set proportional to the background intensity b or independent from it, nevertheless, without loss of generality, the optical noise will be denoted by ϵ^2 in the remainder of the chapter. For a low-noise detector, it can be safely assumed that the noise variance of the detector is much smaller than the noise fluctuations introduced by light and its interaction with the intervening turbid medium, i.e, $\sigma^2/\epsilon^2 \ll 1$. Thus, in following analysis, the detector noise is neglected, i.e., σ^2/ϵ^2 is set to 0, but a full analysis including the detector noise can be found in the theoretical article reported by us [7]. At this point, it can be noted that the total intensity $x_T = x_\parallel + x_\perp$, when detected by a simple intensity camera, can be characterized by a mean $\langle x_T \rangle = s + b$ and variance $var(x_T) = \epsilon^2 + \sigma^2$, when imaged through a simple intensity camera.

2.1.2 Maximum likelihood estimation and optimal representation

Given the above model, the log-likelihood function for a set of N independent realizations of the random variable $\boldsymbol{X}$, at the considered pixel, can be written as

$$ln\left[P(\boldsymbol{x})\right] = \sum_{i=1}^{N} - ln\left[2\pi\left|\Gamma\right|\right] - \frac{1}{2}(\boldsymbol{x}_i - \langle \boldsymbol{x} \rangle)^T \Gamma^{-1} (\boldsymbol{x}_i - \langle \boldsymbol{x} \rangle). \tag{2.5}$$

Finding the expression of the estimator $\hat{s}_{ML}$ that maximizes the log-likelihood function with respect to the source intensity s provides one with the maximum likelihood (ML) estimator for the source intensity. If the maximum likelihood (ML) estimator is unbiased, then it is known to be unique and minimum variance estimator for the exponential family of distributions, i.e, it reaches the Cramer-Rao minimum variance bound for large N [82]. The ML estimator for the source intensity s, in this case, turns out to be of the form

$$\hat{s}_{ML} = \frac{1}{Z}\left(U\frac{1}{N}\sum_{i=1}^{N} x_{i,\parallel} + V\frac{1}{N}\sum_{i=1}^{N} x_{i,\perp} + C \right), \tag{2.6}$$

where U, V and Z are given by (see Appendix B.1)

$$U = -\sqrt{1-\beta^2}(1-P)\rho + (1-\beta)(1+P) \tag{2.7a}$$

$$V = -\sqrt{1-\beta^2}(1+P)\rho + (1+\beta)(1-P) \tag{2.7b}$$

$$C = b\left(\beta^2 + \rho\sqrt{1-\beta^2}(1-P\beta) - 1 \right) \tag{2.7c}$$

$$Z = 1 - \beta^2 - \sqrt{1-\beta^2}\rho(1-P^2) + (P-\beta)^2 \tag{2.7d}$$

As shown in the calculations in Appendix B.1, the estimator is unbiased, i.e., $\langle \hat{s} \rangle = s$. The ML estimator derived here shows that an optimal representation is, indeed, a linear combination of the two polarimetric images. In the imaging scenario considered for the experiment presented in the previous chapter, the DOP of the source and the background are known to be $P = 1$ and $\beta = 0$, whereas, the correlation coefficient has to be estimated over the neighborhood of the pixel under consideration. Considering a single realization of polarimetric pixel with $P = 1$ and $\beta = 0$, the ML estimator for the experimental condition at hand can be written as $\hat{s}_{ML} = x_{\parallel} - \rho x_{\perp} - b(1-\rho)/2$. A contrast maximizing representation can be obtained from the above ML estimator for the contrast measure (CNR) defined in Eq. (1.10). The contrast-to-noise ratio (CNR) is defined such that the mean background intensity (defined by blue pixels in the ROI illustrated in Fig. 1.8b) in the ROI is subtracted from the mean source intensity obtained from any representation. Consequently, the CNR is invariant under any constant offset. Thus, an optimal, CNR maximizing polarimetric representation based on the ML estimator, for the pixels withing a ROI can be simply written as [1]

$$\gamma_{ML} = W_{ML} I^P = I_{\parallel} - \rho I_{\perp}, \tag{2.8}$$

where, in notation consistent with previous chapter, $W_{ML} = [1, -\rho]$. The simple linear form of the polarimetric representation, derived from maximum likelihood principle, is quite fortunate as it requires computation that is well within the real-time constraint as will be seen in section 2.4. The linear form also confirms the results presented in the previous chapter, where the polarization difference image (γ_{Δ}) and the polarization filtered image ($\gamma_{\parallel}$) were able to out perform OSC image (γ_{OSC}). Revisiting the preliminary results presented in the previous chapter, it was shown that the polarization filtered image performed well during low fog situation and the difference image had the best contrast performance during thin fog. The ML representation suggests that the background noise correlation between the two polarimetric channels (ρ), in the vicinity of the source pixel, is the parameter that influences the best polarimetric representation and reduces to a polarization filtered image when $\rho \to 0$ and to a difference image when $\rho \to 1$. Sorting a time series data in increasing order of background correlation in the pixels surrounding the source pixel, it can be observed in Fig. 2.4 that ρ qualitatively indicates the visibility conditions. With increase in visibility of the background structure the correlation coefficient is seen to increase as well. It seems logical now to infer that the difference image produces best contrast in high correlation frames due to its ability to cancel out correlated background noise. When the correlation is low, the difference image only brings additional noise that deteriorates the contrast of the source. Thus, the weighing of the $I_{\perp}$ image with the correlation coefficient provides an adaptive, contrast-maximizing, universal polarimet-

[1] In practice, a correlation map is generated such that each pixel in the map corresponds to the background correlation coefficient. This map is then multiplied pixel-wise to the full-field $I_{\perp}$ before subtracting from the full-field $I_{\parallel}$. The pixel notation are dropped in the Eq. (2.8) to not to distract the reader.

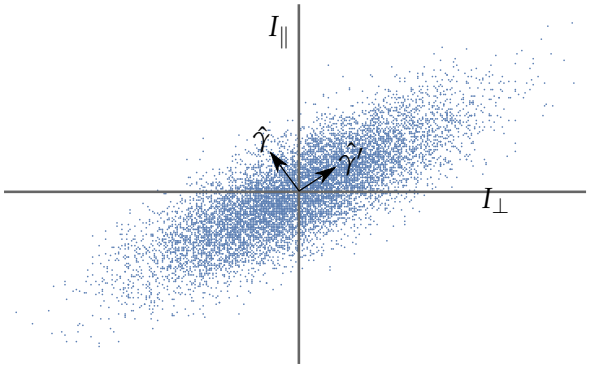

Figure 2.2: Density plot of a two-dimensional correlated Gaussian random variable akin to the noise model adopted to model the background pixels in a polarimetric camera. The data appropriately rotated to lie on the axis $\hat{\gamma}$ will show minimum variance. For the sake of simplicity, the data plotted here for illustration corresponds to a centered two-dimensional random variable.

ric representation which will be tested on real experimental data in section 2.3.

2.1.3 Comparison with background noise-variance minimizing representation

The CNR defined in Eq. (1.10) is a measure of deviation of the source intensity from the distribution of the background intensities of its neighborhood pixels. Thus, in order to find a representation that maximizes the contrast of a source over the background, an alternative approach is to consider a representation that minimizes the variance in the background.

For a correlated two-dimensional Gaussian random variable X, the 2D density plot of random variable can be illustrated as in Fig. 2.2 (with assumption of centered random variables in Fig. 2.2 for the sake of simplicity). In our case, for partially correlated background, one might expect a similar density plot of the data outcomes. Searching a variance minimizing representation effectively amounts to retaining the projection of the data on the axis $\hat{\gamma}$, where the variance is minimum. This problem is similar to the Principal Component Analysis (PCA) approach, and consists of retaining the principal direction that exhibits lowest variance.

The well-known solution to this variance minimization problem consists in projecting the data along the direction given by the eigenvector of the covariance matrix associated to the smallest eigenvalue. Assuming that there is no additive detector noise for the sake of simplicity ($\sigma = 0$), the smallest eigenvalue of Γ given in Eq. (2.4) reads

$$\lambda_1 = \frac{1}{2}\left(1 - \sqrt{\Delta}\right), \text{ with } \Delta = \beta^2 + \rho^2 - \rho^2\beta^2,$$

and the corresponding eigenvector is

$$w_1 = \begin{pmatrix} \frac{\sqrt{\Delta}-\beta}{\rho\sqrt{1-\beta^2}} \\ -1 \end{pmatrix}.$$

As a result, the variance minimizing representation will be obtained by setting $\gamma_{PCA} = W_{PCA}X$, with $W_{PCA} = w_1^T/||w_1||$, which can be rewritten as $W_{PCA} = [\cos(\theta_{PCA})\ \sin(\theta_{PCA})]$, with $\theta_{PCA} = \arctan\left[\rho\sqrt{1-\beta^2}/(\beta-\sqrt{\Delta})\right]$, illustrating the fact that this operation amounts to rotating and project the data onto the lowest-variance direction.
It can be observed from the above equation that the alternative representation derived here by minimizing the noise variance is proportional to the weighing vector $[1 \quad \rho\sqrt{1-\beta^2}/(\beta-\sqrt{\Delta})]$, which clearly shows that it generally differs from the ML representation derived in the previous section. Let us analyze more precisely the case of fully polarized source ($P = 1$), and fully unpolarized background ($\beta = 0$) for the sake of illustration. In this case, it can be checked that $\gamma_{PCA} = \gamma_\Delta/\sqrt{2}$ whatever the value of ρ, and that it corresponds to the representation with minimum variance in the background (the variance is equal to $(1-\rho)/2$ in the case considered). In the context of the experiments conducted ($P = 1$ and $\beta = 0$), this variance minimizing representation is, therefore, equal to the ML representation (up to a multiplicative factor of $\sqrt{2}$) only for fully correlated fluctuations, (i.e., for $\rho = 1$). However, eventhough it ensures minimum variance in the background of the image, γ_{PCA} does not maximize the CNR of a polarized source, and therefore does not correspond to the optimal contrast maximizing representation provided by γ_{ML}. More precisely, it can be checked that in the considered case, the ratio $CNR(\gamma_{ML})/CNR(\gamma_{PCA}) = \sqrt{2/(1+\rho)}$.
As a result, a variance-minimization approach does not guarantee an optimal representation for enhancing the contrast of a source. With some hindsight, this seems logical, as γ_{PCA} does not take into account any property (here full polarization) of the source. For example, the difference image performs well when the background noise is highly correlated on the two images, whereas when the correlation is close to 0, the difference image brings additional noise in background and no information about the source (since $I_\perp$ does not contain any information about the source).

2.2 Performance gain with polarimetric imaging

Using the above noise model for the simplified polarimetric imager, the gain in using polarimetric imaging for contrast imaging can be analyzed. In the context of the imaging scheme considered in this part of the thesis, the parameters s and P represent the information about the source. The polarimetric image provides us with raw data from where the information about the source can be extracted. The total informational content available in the data to estimate the parameters can be classically quantified by the Fisher information (FI) (see Appendix A). The mathematical object, Fisher information, is generally a matrix and is closely related to the maximum precision (or minimum achievable variance) in estimation of parameters given the data set and the probability model. In fact, the inverse of the Fisher information matrix (FIM) gives us a covariance matrix which called the Cramer-Rao bound (CRB). According to the Cramer-Rao theorem, the Cramer-Rao bound (CRB) is the minimum achievable covariance bound on the parameters under consideration [82, 83]. For example, given a probability density function (PDF), $P(\boldsymbol{x}, \boldsymbol{\eta})$ parametrized

by an N dimensional vector $\boldsymbol{\eta} = [\eta_1, \eta_2, ..., \eta_N]$, an $N \times N$ Fisher information matrix (FIM) can be obtained by computing

$$\mathcal{F}_{kl} = -\left\langle \frac{\partial^2 \, ln\,[P(X)]}{\partial \eta_k \partial \eta_l} \right\rangle, \tag{2.9}$$

where $\langle . \rangle$ is the expectation taken over ensembles. The above expression can be easily computed for a multivariate Gaussian distribution, whose mean $\boldsymbol{\mu}$ and covariance Γ are a function of the parameter vector $\boldsymbol{\eta}$. The general expression given in [84] and briefed in Appendix A.3 is

$$\mathcal{F}_{kl} = -\left\langle \frac{\partial \, ln\,[p(x)]}{\partial \eta_k} \times \frac{\partial \, ln\,[p(x)]}{\partial \eta_l} \right\rangle = \frac{\partial \mu}{\partial \eta_k}^T \Gamma^{-1} \frac{\partial \mu}{\partial \eta_l} + \frac{1}{2} tr\left[\Gamma^{-1} \frac{\partial \Gamma}{\partial \eta_k} \Gamma^{-1} \frac{\partial \Gamma}{\partial \eta_l} \right] \tag{2.10}$$

The Fisher information of estimation of the source intensity (s) is calculated easily from the above expression as the covariance matrix does not depend on s and, thus, $\partial\Gamma/\partial s = 0$. The Fisher information is given as

$$\mathcal{F}(s) = \frac{1}{\epsilon^2(1-\rho^2)} \left[1 + \frac{(P-\beta)^2}{1-\beta^2} - \frac{\rho(1-P^2)}{\sqrt{1-\beta^2}} \right]. \tag{2.11}$$

2.2.1 Gain in contrast performance

Using the above formulation, the gain in using polarimetric imaging for contrast imaging can be theoretically analyzed with respect to a simple intensity camera (IC). For example, when imaged with an intensity imager, the Fisher information (FI) for the estimation of the source intensity s under a Gaussian hypothesis, is simply $\mathcal{F}_{IC} = 1/(\epsilon^2 + \sigma^2) \sim 1/\epsilon^2$ (since $\langle x_T \rangle = s + b$ and var(x_T) = $\epsilon^2 + \sigma^2$). Since the FI quantifies the information content in estimation of a parameter (in this case, s), a gain in using polarimetric imaging for estimation of the source intensity can be defined as the ratio of corresponding Fisher informations as

$$\mathcal{G} = \frac{\mathcal{F}(s)}{\mathcal{F}_{IC}} = \frac{1}{(1-\rho^2)} \left[1 + \frac{(P-\beta)^2}{1-\beta^2} - \frac{\rho(1-P^2)}{\sqrt{1-\beta^2}} \right] \tag{2.12}$$

Let us analyze the information gain in using polarimetric imaging and deduce the conditions where a polarimetric imager is superior than an intensity camera in estimating the source intensity through fog. In a general imaging situation, the correlation coefficient of the background fluctuations is not under experimental control and may vary from scene to scene depending on the visibility conditions. Therefore, it is of interest to first map out conditions on P and β for which a minimum gain of $\mathcal{G}_{min}$ can always be expected, irrespective of the visibility conditions, i.e., the irrespective of the value of $\rho \in [0, 1]$. The conditions are derived in Appendix B.2 and are given below.

$$(1+P)^2 \geq 2\mathcal{G}_{min}(1+\beta), \quad P > \beta \tag{2.13a}$$

$$(1-P)^2 \geq 2\mathcal{G}_{min}(1-\beta), \quad P < \beta \tag{2.13b}$$

The above conditions are plotted and labeled in Fig. 2.3 in black solid lines for $\mathcal{G}_{min} = 1, 1.5, 1.9$. Let us look at the conditions where at least a unity gain is expected for any value of ρ which is shown in Fig. 2.3 as unshaded white region. The shaded area in gray, which is bounded by the two $\mathcal{G}_{min} = 1$ contours, shows a region of ambiguity. The gain in this region may or may not be unity depending on the value of ρ. To show the dependency of gain on ρ within this gray region, the region of ambiguity for three values of correlation coefficient is shown in color. For example, if the correlation values in the experiment always lie close to zero, say $\rho = 0.001$, then the region of ambiguity is much smaller and shown in orange shaded region (with orange dashed strokes). For $\rho = 0.001$, beyond this orange shaded region, the gain is always greater than or equal to unity. Similarly, the region of ambiguity for $\rho = 0.5$ (shaded in green with green dotted strokes) and for $\rho = 0.95$ (shaded in blue and bounded by blue dashed strokes) are also shown in Fig. 2.3.

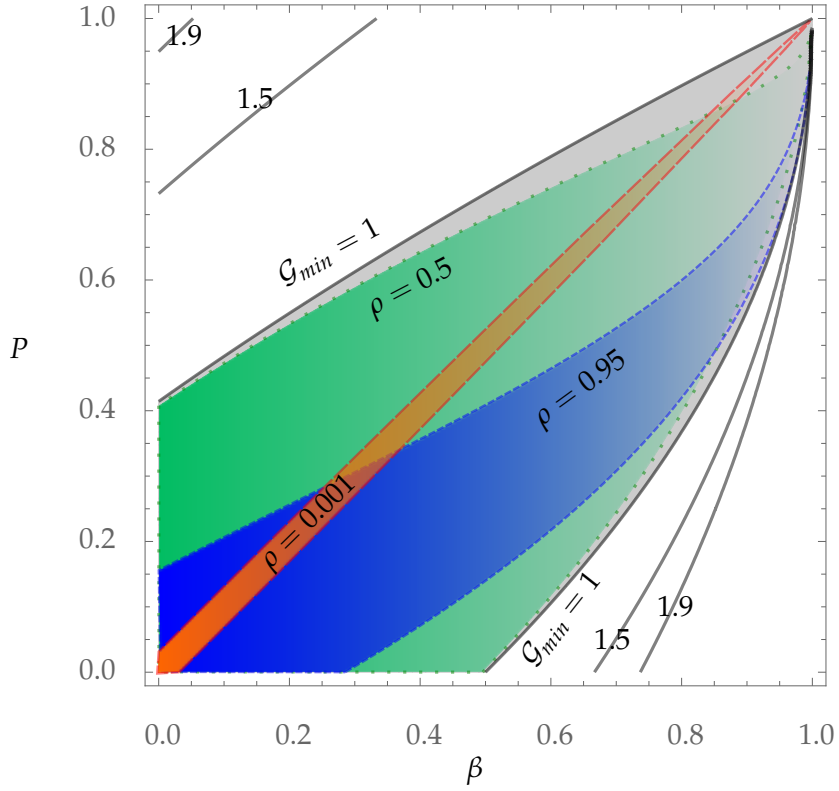

Figure 2.3: The shaded areas show the region of ambiguity where the gain is less than or equal to unity. The unshaded region (white) represents the conditions where the polarization sensitive imaging provides a gain greater than unity, when compared to a simple intensity camera for all values of the correlation coefficient ρ. The shaded area in green (under green dotted contour) shows the region of ambiguity when the correlation coefficient value is 0.5, i.e., $\rho = 0.5$. Similarly, regions shaded in blue (under blue dashed line) and orange (under orange solid line) show the unity gain condition for $\rho = 0.95$ and $\rho = 0.001$, respectively.

As a general remark, within the region of ambiguity, the contrast in DOP ($|P - \beta|$) is not enough for polarization sensitive imaging to provide any additional gain with respect to

an intensity camera. In the extreme cases, where the DOP contrast between source and background, i.e., $|P - \beta| \sim 1$ a minimum gain of 2 can always be expected, irrespective of the value of ρ. It is also observed that the minimum gain contours are asymmetric and a minimum gain of $\mathcal{G}_{min} > 2$ can be achieved in situation when the background is highly polarized and the source is unpolarized ($\beta \gg P$).
In the other case where the background is unpolarized (i.e., $\beta = 0$), a gain greater than unity can always be expected for all values of correlation coefficient ρ only when $P > (\sqrt{2} - 1) \sim 0.414$. The experimental conditions at hand, which requires detection of polarized light beacons through fog, are well within this condition with $P = 1$ and $\beta = 0$. According to the above theoretical analysis, a minimum gain of 2 times can always be expected by using a polarimetric camera instead of a simple intensity camera. A quantitative comparison of this will be presented in later sections, where theoretical predictions are tested alongside experimental data.
In summary, using information theory it was derived that the optimal representation for contrast enhancement of the source is a linear combination of the two polarimetric images. The local background noise correlation coefficient was identified as the parameter that dictates the weights of the linear combination. In light of this, the OSC image representation can be outrightly discarded. The underperformance of the widely used OSC image representation was also established in the experimental results shown in the previous chapter. Thus, it will not be further considered in the context of contrast imaging.
In the next section, the theoretical predictions are put to test using real experimental data.

2.3 Contrast maximizing representation

To check the performance of the optimal polarimetric representation γ_{ML} provided in Eq. (2.8), an experimental data set taken during 24-01-2014 between 1:00 p.m. and 2:20 p.m. (at a time interval of 1 frame every 10 seconds) was utilized. This data set was obtained with a higher dynamics/lower noise camera (Andor NEO sCMOS 5.5 Mpixels, 16-bit, 0.015e-/pixel/s dark noise at -30°C sensor temperature) compared to the Balser camera used for the data in the previous chapter. The imaging system was re-calibrated with this low-noise, high-dynamics camera. The data-set was chosen such that the rapid change in visibility conditions encompassed all the foggy situations (from no fog to thin fog to thick fog) with source intensity and visibility varying in time without any apparent order. A frames from the time series data are shown in Fig. 2.4, where the frames are sorted in increasing order of the background correlation-coefficient in the neighborhood of the source. The figure, shows that a finite background correlation does exist and also qualitatively increases with visibility of the background structure.
The ROIs extracted from the dataset were used to form a time series data of the two-dimensional polarimetric image $I_P = [I_\parallel, I_\perp]^T$. Then, the two images may be used to form a generic linear representation $\gamma = \boldsymbol{W} I_P$ with weighing vector $\boldsymbol{W} = [u, v]$. For example, the intensity-summed image (γ_Σ) can be obtained with $\boldsymbol{W} = [1, 1]$. Before the ML representation can be compared, a numerical contrast-maximizing representation is

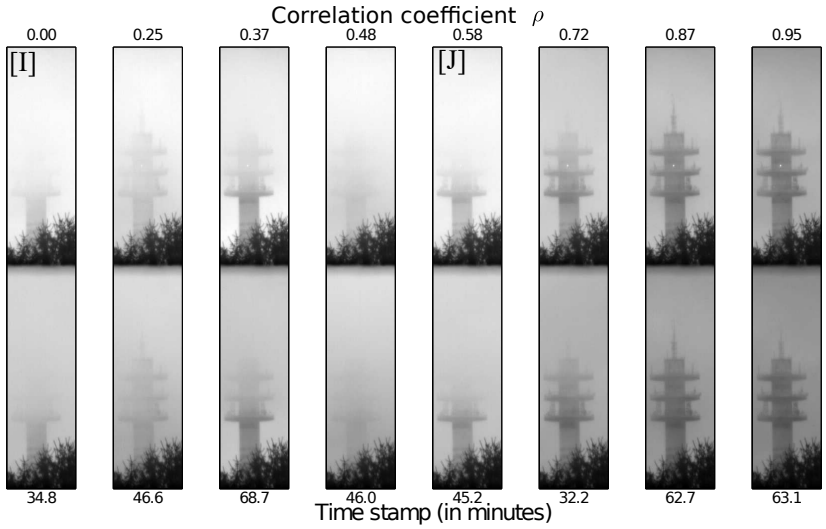

Figure 2.4: Examples of raw images from the polarimetric camera, showing the tower and the source with varying conditions of fog density and visibility. The time stamp of acquisition and measured correlation coefficient of noise at the source pixel location are respectively indicated below and above each image.

sought to set a standard. Since, the optimal representation is a linear combination, it is possible to obtain an optimal weighing vector $\boldsymbol{W}_{CS}$ which maximizes the CNR given in Eq. (1.10) by numerically searching over all possible weights. First, such a computational search over the domain of the weighing vector was performed over the experimental data and the procedure is detailed below.

2.3.1 Computational search

Given the contrast measure described before in Eq. (1.10), each time frame of the polarimetric image was used to obtain a linear representation $\gamma = \boldsymbol{W}^T I_P$. A contrast maximizing linear representation was obtained by searching for the appropriate weighing vector $\boldsymbol{W}$ that maximizes the contrast function $\mathcal{C}(\gamma)$ as

$$\boldsymbol{W}_{CS} = \underset{u,v}{argmax}[\mathcal{C}(\gamma)] \tag{2.14}$$

Because of the small size of the ROI, it was possible to use a straightforward method to find the contrast-maximizing linear representation within limited computation time (around 1 second, using Matlab on a standard laptop). For the entire data set, five different image representations mentioned in the Table 2.1 were obtained and their respective CNRs were calculated.

Representation	Symbol	$\boldsymbol{W}$	$g^{\Sigma} = \mathcal{C}(\gamma)/\mathcal{C}(\gamma_{\Sigma})$
Intensity-summed	γ_{Σ}	$[1, 1]$	1
Pol. filtered	$\gamma_{\parallel}$	$[1, 0]$	$\sqrt{2(1+\rho)}$
Pol. difference	γ_{Δ}	[1, -1]	$\sqrt{(1+\rho)/(1-\rho)}$
Computational	γ_{CS}	$[1, v_{CS}]$	-
Max. Likelihood	γ_{ML}	[1, -ρ]	$\sqrt{2/(1-\rho)}$

Table 2.1: Polarimetric representations and gains in CNR. It may be recalled that CNR was defined in Eq. (1.10) such that it (and hence the CNR gain) remains independent of scalar multiplication to the weight vector $\boldsymbol{W}$.

Two example frames corresponding to time stamp 34.6 minutes (labeled as I) and 45.2 minutes (labeled as J), with different visibility conditions are shown in Fig. 2.5a. It is easily observed that in the first row of images, the visibility of the source is low and the $\gamma_{\parallel}$, γ_{CS} and γ_{ML} present similar contrast values. However, the second row, with intermediate visibility of the source, the representations γ_{CS} and γ_{ML} remain close to each other and outperform other representations. The map of the 2D search performed over values of $u \in [0, 1]$ and $v \in [-1, 1]$ is shown in Fig. 2.5b, with the standard image representations marked in colors. Since the CNR remains insensitive to scaling of the intensity values, an equivalent 1D search over $v \in [-1, 1]$ can be performed by setting $u = 1$. The map of the 1-D search performed to obtain the numerical contrast-maximizing representation γ_{CS} in both the cases are also shown in Fig. 2.5c. The colored dots in the figure correspond to the other polarimetric representations. The weights obtained from the computational search (black dots) are close to the values of the correlation coefficient used for the ML representation (shown in blue dots).
Since, the intensity-summed image provides a representation similar to that of an image obtained from an intensity camera, a normalized contrast function was defined. The contrast gain obtained from any representation γ is written with respect to the contrast obtained from the intensity-summed image as

$$g^{\Sigma} = \frac{\mathcal{C}(\gamma)}{\mathcal{C}(\gamma_{\Sigma})} \tag{2.15}$$

The contrast gain obtained at each time frame for representations γ_{ML} (in blue cross) and γ_{CS} (in black solid lines) are plotted in Fig. 2.6 along side the contrast gain obtained using a difference image (γ_{Δ}) and a polarization filtered image ($\gamma_{\parallel}$).

- It is clearly seen that the time-evolution of the normalized contrasts shows no apparent order, suggesting rapid change in the fog and the visibility conditions. The contrast values obtained for the intensity-summed image γ_{Σ} shown in dotted black curve in the bottom shows that contrast varies from close around zero to 20 in an apparent random fashion.

- The curve in green (filled) shows the gain in contrast obtained when using the polarization filtered image $\gamma_{\parallel}$. The contrast gain remains almost constant around 2

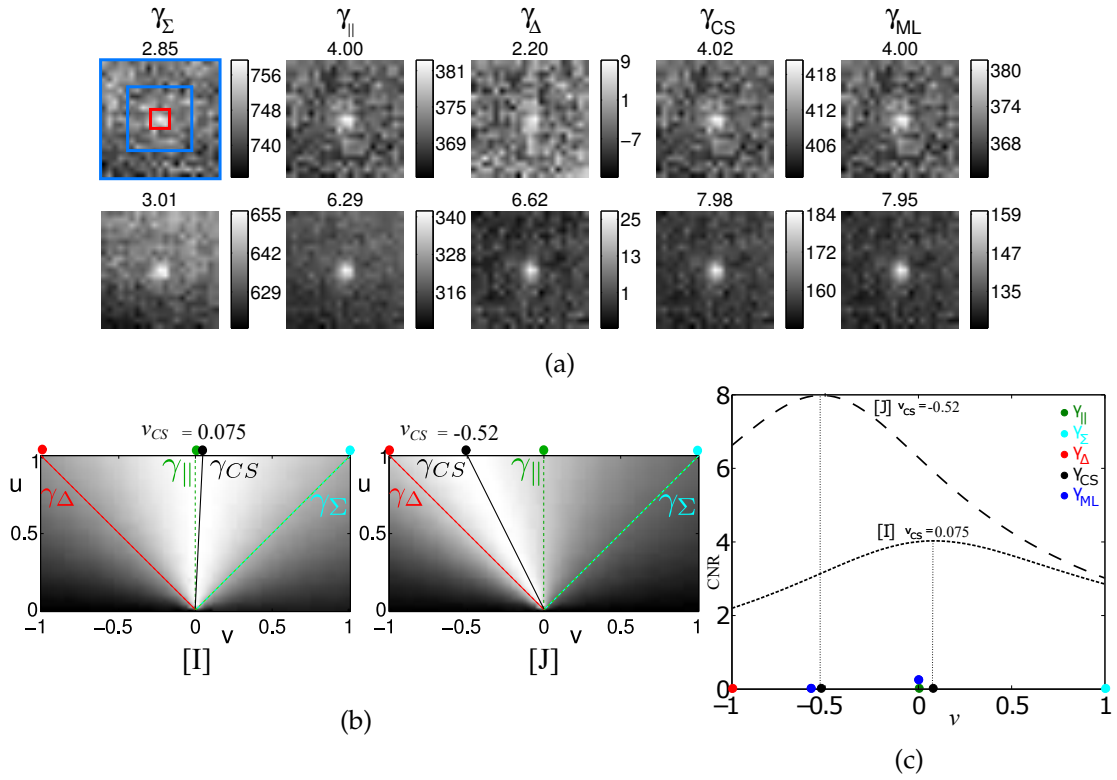

Figure 2.5: (a) Comparison of the contrasts obtained for three representations of the polarimetric images for frames labeled as [I] and [J] in Fig. 2.4. The source region, $\mathcal{S}$ is bounded by the 3×3 pixels red square and $\mathcal{B}$ is the background region between the two blue squares of sizes 11×11 pixels and 21×21 pixels. (b) CNR-maximizing 2D search over values of $u \in [0,1]$ and $v \in [-1,1]$ for the two frames [I] and [J]. In a well-calibrated imaging system, the search can be performed equivalently over v, keeping $u = 1$. (c) CNR-maximizing 1D search over values of v keeping $u = 1$ for the two frames.

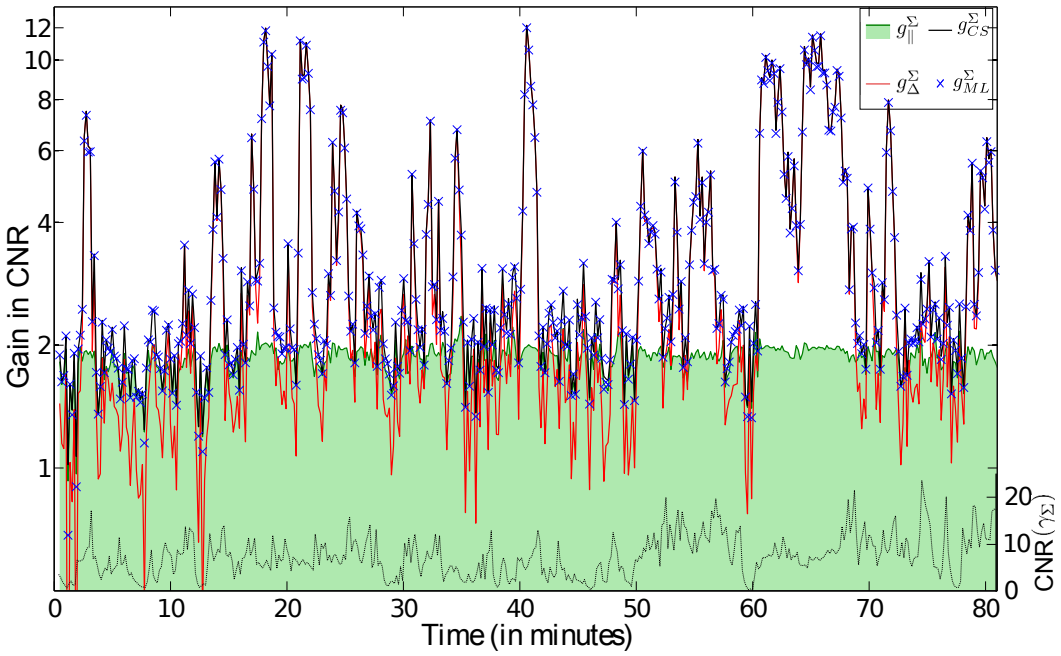

Figure 2.6: Gain in contrast (log scale) reached by the difference image γ_Δ (red solid lines) and γ_{CS} representation (black solid line) with respect to the intensity-summed image γ_Σ. The blue crosses show the gain obtained with γ_{ML} representation, which can be seen to follow the maximum attainable contrast. The green filled curve shows the gain of the $\gamma_\|$ image with respect to the intensity-summed image. (Results reported by us in [1])

irrespective of the visibility conditions.

- The curve in red shows the gain in contrast obtained from the difference image γ_Δ. The gain varies with the highest observed gain around 12 times. It is observed that the gain obtained by γ_Δ is not always the best as inferred in the previous chapter. In fact the g_Δ^Σ can be smaller than the $g_\|^\Sigma$ as indicated by the plot in Fig. 2.6.

- The plot in black shows the gain in contrast of obtained representation γ_{CS}. The plot shows that in all conditions, the black curve keeps the best of both the green and red curves. This clearly indicates that there indeed exists a contrast maximizing linear representation that is adaptive and differs from the difference image or the polarization filtered image in general.

- Finally, the contrast gain obtained from the γ_{ML} is shown as blue crosses and shown to closely follow the contrast maximizing representation.

The ML representation is adaptive to the visibility conditions and has the potential to provide fast, real-time detection maps of the polarized source of light through fog when using a simplified polarimetric camera. Let us now compare the experimental results with the theoretical predictions. It can be noted that for a generic representation $\gamma = WI_P$, the variance is $var(\gamma) = u^2 var(I_\|) + v^2 var(I_\perp) + 2uv\ covar(I_\|, I_\perp)$. Thus, a theoretical gain in contrast of γ with respect to the intensity-summed representation may be obtained as

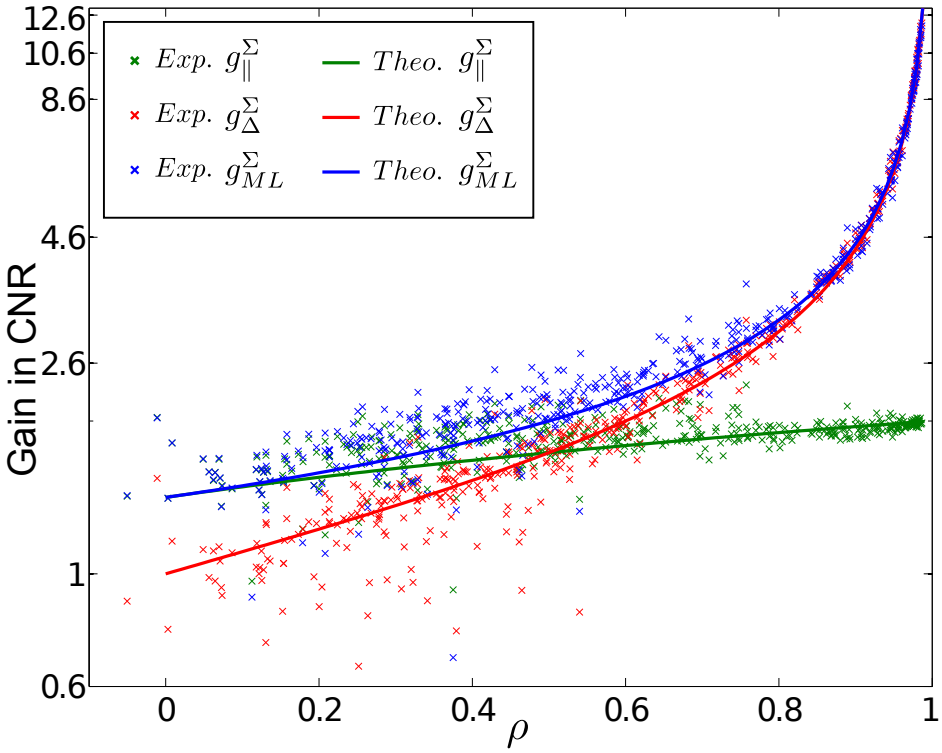

Figure 2.7: The experimentally obtained gain in CNR (scattered points) for each representation as a function of correlation coefficient between the immediate backgrounds in the two polarimetric images is plotted in log scale. For comparison, the corresponding theoretically derived functional forms of the expected gain in each representation (with respect to the intensity-summed image) are plotted in solid lines. The theoretical gains are also listed in Table 2.1.

$var(\gamma_\Sigma)/var(\gamma)$. A straight forward calculation shows that the gains are simple functions of the correlation coefficient ρ and tabulated in Table 2.1. Plotting the theoretical gain (in solid lines) alongside the experimental contrast gains (in symbols) in Fig. 2.7 reveals the order in the apparent noisy data. The experimental and theoretical contrast gains show fair agreement inducing further confidence in the theoretical model. A maximum contrast gain of about 12 times is seen in experiments in this particular dataset. In this high gain region where the background correlation is nearly 1, the visibility of the source is already quite high. But this can be used to efficiently reject the background revealing the polarized source in high contrast. Such scenarios can be very useful in aircraft landing and taxiing applications.

2.3.2 Intermediate conclusion

It was shown experimentally that the two polarimetric channels acquired along two orthogonal polarization directions can have intensity fluctuations that are significantly correlated (refer Fig. 2.1.a). Using the above theoretical noise model, the influence of the background noise correlation on the optimal polarimetric image representation was shown.

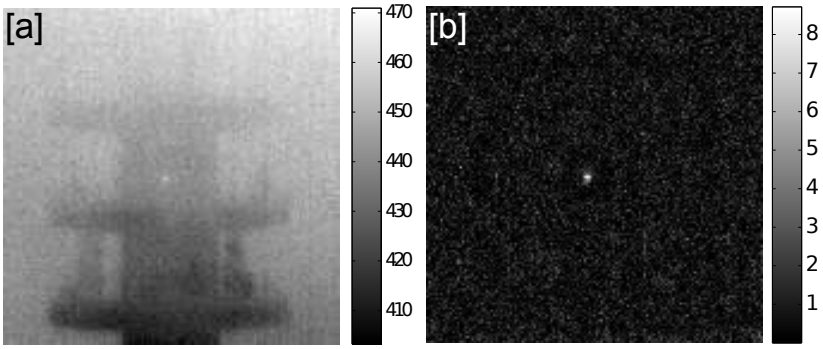

Figure 2.8: Comparison of the intensity-summed image obtained with a standard camera (left, [a]) with a processed CNR map of γ_{ML} (right, [b]) that can be provided as a final contrast enhanced image to the end-user or to a higher-level image processing unit.

The optimal representation that maximizes the contrast of a polarized source through fog was shown to be a weighted linear combination of the two polarimetric channels. A sample contrast map obtained using the ML representation presented in Fig. 2.8 shows the efficiency of background rejection in such an imaging and processing scheme. In the following section, further light is shed upon the implementation methods and detection strategy that has been used to achieve a real-time full-field polarimetric contrast imaging with inexpensive hardware.

2.4 Implementation

The analysis presented above was performed for a small 21 $\times$ 21 pixels ROI around the source whose location in the field of view was known, a priori. However, in a real situation the location of the source and the number of sources may be unknown and they need to be detected. Since, the ML representation is an adaptive representation which depends on the background statistics around the considered pixel, it has to be evaluated locally (i.e., in the neighborhood of the pixel under consideration), for each pixel in the image and at each frame. This is also necessary if the source and the imager are in relative motion, as in the case of aircraft landing application.

More precisely, for the computation of the ML representation, an intermediate image is required which maps the local correlation coefficient of the background noise in the immediate neighborhood of each pixel. A straightforward method to achieve this consists of applying a moving window similar to the mask of the ROI shown earlier in Fig. 1.8b to calculate the correlation coefficient in the background pixels in region B, whose shape and size is adapted to the expected imaging scenario. For instance, in our case, punctual polarized sources are to be detected over long distances. Hence, the window shape and size are restricted to the ROI defined in chapter 1, with a central target region of 3 $\times$ 3 pixels (denoted by S) and an outer background region B that spans a square region of 21 $\times$ 21 pixels minus a central exclusion square of 11 $\times$ 11 pixels.

Such a small moving window over the full-field of image can be time consuming and,

hence, not suitable for real-time imaging. In light of this, two strategies were identified to reduce the moving window into a 2D convolution operation and compute the correlation coefficient with good accuracy and minimum computation time.

As established in the previous section, the two optimal representations (γ_{CS} and γ_{ML}) could provide the same contrast-maximized image for visual aide, but the preference of one representation over other can be strongly influenced by their ease of implementation and computational time.

Let us look at the common computations required for producing γ_{ML} and γ_{CS} for the entire field of view for a single frame. In both cases, the local statistics of the polarimetric images need to be calculated. In case of γ_{CS}, the local CNR has to be calculated at each step of the weight $v \in [0, 1]$ to obtain an optimal weight v_{CS} and only retain the maximum CNR value at each pixel to produce a CNR map of the entire polarimetric image. Thus, in this case, mean of local background and target plus standard deviation of the background is required to be calculated N times (with N being the number of samples of $v \in [0, 1]$ to search for optimal weights). To ensure a reliable computation of v_{CS}, a fine sampling of the v values is required, hence leading to a high number of statistics calculations to identify maximum CNR at each pixel[2]. Meanwhile, computation of γ_{ML} requires calculation local background and target means, local background standard deviations and local background covariance for estimation of the local correlation coefficient, a sum total of five such calculation as against at least 3N such calculations in case of γ_{CS}.

Clearly, the ML representation provides an easy to implement closed-form expression, and in practical situations is also faster than computing γ_{CS}. This is of major interest in the widespread context of automated detection of sources of unknown number and locations. Moreover, it gives us extra essential computational time to implement automated adapted size and shape search over the ROI mask.

The estimation of local statistics can be accelerated in computation time, by noticing that they break down to performing simple convolution of the entire image with the ROI. To illustrate this, the computation of local statistical first moment (mean) and local covariance, is presented here. Denoting the two polarimetric images as $I_{\parallel}$ and $I_{\perp}$, the mean background intensity can be calculated by defining a background region in binary ROI mask. Let us denote this ROI mask as M_{roi} which consists of ones where the mean is to be calculated and zeros where the pixels must be excluded. It can be noted, the mean map μ can be calculated easily as $\mu_{\parallel} = (I_{\parallel} * M_{roi})/\Sigma M_{roi}$, where $f * g$ represents a 2D convolution of images f and g and ΣM_{roi} represents the sum over all pixel values in the M_{roi}. The local covariance image can be calculated $cov(I_{\parallel}, I_{\perp}) = ((I_{\parallel} - \mu_{\parallel}) \times (I_{\perp} - \mu_{\perp}) * M_{roi})/(\Sigma M_{roi} - 1)$. In a similar fashion, the local variances and the correlation coefficient can be calculated

[2]In case of γ_{CS}, it is necessary to record the maximum CNR value at each pixel by searching over all weighing vectors. This is easily implemented without having to store all CNR maps produced at each step of v, by noting that $\text{Max}(a, b) = (a + b + |a - b|)/2$. This can be implemented by looping over the weights of the linear combination (i.e., over v) and estimating the local statistics and then the CNR at each pixel. Then, with only one previous CNR image in the memory and simple pixel-wise arithmetic on each pixel provides the maximum CNR value at each pixel. At the end of the loop the final image contains maximum CNR values at each pixel calculated over then entire search.

easily using convolution.
There are two computationally efficient ways of computing the 2D convolution. They are briefly mentioned below.

Convolution by using fast Fourier transforms Noting that a convolution is simply as multiplication in the Fourier domain, the local statistics can be calculated rapidly with efficient fast Fourier transforms (FFT) routines. Since 2D-FFT on images can be implemented on a hardware level, on GPUs or even with C/C++ on conventional computers, reaching real-time speeds is easily accessible even with large image sensors. With an FFT implementation, the relative efficiency in speed processing between γ_{CS} and γ_{ML} has been evaluated, and is reported in Fig. 2.9.a. This figure shows that a speed up of around 12 times can be obtained using the ML representation. The speed-up with respect to a brute-force, moving window calculation is not considered here, since they do not scale well with the field of view.

Convolution by method of integral images Convolution can also be computed using the method of integral images [85]. In this method, an image is transformed into an integral image according to the following procedure: The i^{th}, j^{th} pixel of the integral image F^{int} of an image f is the addition of the all the pixel values from coordinate $0,0$ to i,j, i.e. $F^{int}_{i,j} = \sum_{k=0,l=0}^{i,j} f_{k,l}$. This operation need only be performed once for the image. Then, as an illustration, the local mean at pixel i,j over a neighborhood of size $2d+1 \times 2d+1$ in image f can be calculated at each pixel as $\mu_{i,j} = [2d+1]^{-2}(F^{int}_{i+d,j+d} + 2F^{int}_{i-d,j-d} - F^{int}_{i-d,j+d} - F^{int}_{i+d,j-d})$. This method is then easily extended to arbitrary ROI masks, where the local statistics are calculated by using simple arithmetic operations. The advantage of this method is that it scales linearly with the image size. Owing to its fastness it widely used in face detection algorithms implemented on smart-phones [86].
Using this method to estimate the local statistical parameters, a further four-fold increase in speed has been obtained, as can be seen in Fig. 2.9, resulting in an overall speed up of about 40 times with respect to the computational search. The benchmarking was done using Matlab program but the speed-up ratios are expected to remain the same using low level programming. With low level programming and various computational optimization approaches it is, indeed, possible to reach real-time video requirements, because of the simple form of the optimal image representation. Further, in the perspective of the application considered in this thesis (i.e., visual aide for aircraft landing in obscured weather conditions), the speed-up offered by integral images method would allow for automated ROI size and shape adaptation to the increase in apparent size of the runway lights with the approach of the airplane.

2.5 Detection

Fast real-time computation opens opportunities for implementation of auto-detection and location estimation of polarized sources in an image. In the context of the application

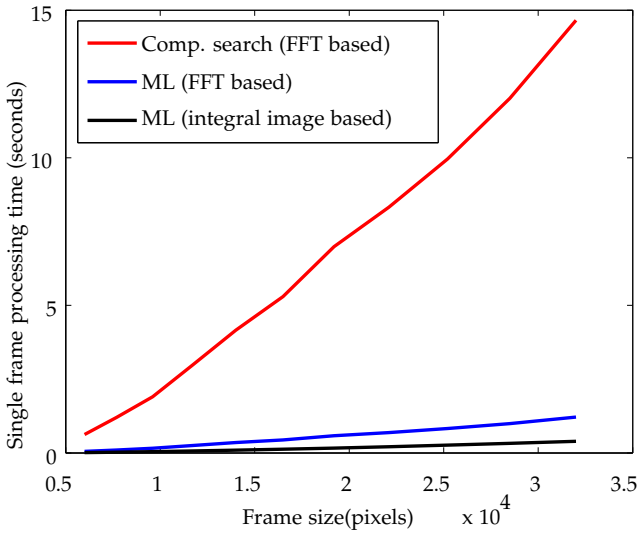

Figure 2.9: Processing time of one frame for providing the optimal representation contrast map using computational search (red curve) or ML representation (blue curve) using FFT methods, or ML representation using integral image method (black curve).

considered, auto-detection could lead to automatic scene rendering and computation of flight parameters like distance of landing, altitude, orientation and slope using only vision. Using such polarimetric camera and image processing scheme, a CNR map can be created for any polarimetric representation representation as $\mathcal{C}(\gamma)$. The CNR map is insensitive to scaling and offset in intensity values and simply provides an estimate for local SNR. Thus, for Gaussian random variables, the computed CNR values would follow a Chi-distribution with unitary mean and variance [87]. This is easily checked in Fig. 2.10.a, where the histogram of the $\mathcal{C}(\gamma_{ML})$ for a frame where the source is indiscernible from the background is plotted alongside the Chi-distribution (in orange). The plot shows the characteristics of the background CNR values that may be expected in any frame. A visible polarized beacon, can then be discriminated from the background by applying an appropriate threshold. Since, the CNR values are well-behaved and follow Chi-distribution, a CNR threshold can be easily chosen for an acceptable probability of false alarm (PFA). For example, to choose a false alarm rate of 5%, one must choose the CNR threshold at 1.96. However, it should be noted that the CNR map may have negative values if the central pixel has lower value than its surrounding. As in our case, the true positive will always have a higher value from its surrounding, this information can already be used to discard 50% of the pixels as background. Thus, the CNR threshold of 1.96 finally provides a 2.5% false alarm rate tolerance. Lets define a symbolic function $\mathcal{T}(\gamma)$ for a given polarimetric representation γ as the thresholded map of $\mathcal{C}(\gamma)$ with a threshold of 1.96. The figure Fig. 2.10.b, then shows the thresholded CNR map corresponding to various representations. The false alarms in the CNR map of γ_{ML} is not better than γ_{Σ}, but is lowest among the other polarimetric representations. As a naive strategy for further reduction of the false alarms, one may question the possibility of taking advantage of the various other

polarimetric representations which are easily computed as well. Of course, the assumption behind this approach is that the CNR false alarm maps for each representation (which are Chi-distributed random values) are independent. Under this strategy, a pixel-wise logical AND operation on the thresholded maps would produce a composite thresholded map $\mathcal{T}' = \mathcal{T}(\gamma_{ML})\ AND\ \mathcal{T}(\gamma_{\Delta})\ AND\ \mathcal{T}(\gamma_{\Sigma})$, where the false positive count can be expected to be further reduced. This AND operation is implemented on the thresholded maps and the result is shown in Fig. 2.10.b, seemingly, indicating significant reduction in false alarms. However, this technique does not guarantee at all that the probability of detection of source(s) is preserved or even similar to the probability of detection obtained with γ_{ML} detection map only. As a consequence, to draw any conclusion on this point, a joint and complete study of the detection efficiency remains a perspective to this work and would include an analysis of the receiver-operating-characteristic (ROC) curves, with either synthetic data or with data acquisitions with multiple sources. In the context of this experiment, with a single source spanning over very few pixels, the available data did not allow for such a study.

An alternative approach, which may be adopted to provide visual aid in bad weather, is a color composite CNR map. In this case, a color composite map ($\mathcal{T}_{col}$) can be produced by setting red = $\mathcal{T}(\gamma_{ML}) \times \mathcal{C}(\gamma_{ML})$, green = $\mathcal{T}(\gamma_{\Delta}) \times \mathcal{C}(\gamma_{\Delta})$ and blue = $\mathcal{T}(\gamma_{\Sigma}) \times \mathcal{C}(\gamma_{\Sigma})$. Such a visual aid may be useful to distinguish between, polarized sources and intensity unpolarized false alarms. For instance, for the same detected intensity at the detector end, a true polarized beacon may show higher red channel than blue channel, where as a intense unpolarized (or partially polarized) light may exhibit higher blue channel, thereby enabling visual discrimination of false detection based on the comparison of contrasts of various polarimetric representations. The color composite map $\mathcal{T}_{col}$ is implemented and shown in row [b] of Fig. 2.11 where four frames with various foggy conditions are considered and ordered by increasing visibility of source from left to right as shown in the intensity images in row [a] of the figure. It can be observed from the colors of background pixels in $\mathcal{T}_{col}$ that the false alarm pixels in each threshold map are mostly independent.

In airplane landing/taxiing applications, this approach could visually help in discriminating the source from pixels that are intense and have a low degree of polarization like, water or reflecting surfaces, or unpolarized airport lights. Once again, these preliminary considerations would require a thorough and rigorous study through the computation of ROC curves in order to be validated.

2.6 Conclusions

The initial motivation of imaging polarized beacons through fog in real-time has led to a co-designed two-channel polarimetric imaging system, complete with an optimal estimation procedure and automatic detection scheme capable of working in real-time. Data in real conditions of degraded weather was gathered by setting up an original outdoor experiment to simulate various conditions that may be encountered in a real-life application scenario, thus, putting more value into the imaging system to be adopted in real-life situa-

tions. In order to help in potential transition into industry, various factors were taken into account, like inexpensive adhesive polaroid sheets and conventional incandescent lamp for source and portable, robust and modular polarimetric camera system. In addition, the real experiment was able to provide testable data for the signal processing and detection schemes that were developed specifically for the imaging scenario under consideration. Using information theory, an optimal contrast maximizing polarimetric representation was derived that adapts to any weather condition. Moreover, a theoretical gain in using such a polarimetric system was also derived and was shown to agree well with the experimental results, thereby, adding confidence to the theoretical model and various inferences derived from it. The experimental conditions for attaining minimum gain in a general two-channel polarimetric imaging scheme were also mapped out to provide instant knowledge of the efficiency using the polarimetric camera over an intensity camera. In fact, a maximum contrast gain of 12 times was reported with the experimental conditions at hand. Finally, the simplicity of the derived optimal representation paves way for fast computation on minimum hardware and adds towards the goal of real-time imaging. In addition, fast implementation of the image processing algorithms were envisaged and an automatic detection scheme based on the gathered knowledge was proposed. The accuracy of the detection scheme even in very low visibility conditions and the overall study of polarimetric imaging through fog over long distances, makes this entire imaging scheme ready to be taken forward into testing stage for real-applications.

This concludes the first part of the thesis, where a snapshot polarimetric camera used to perform an end-to-end study of the polarization contrast imaging through fog in real atmospheric conditions. In the next part, a new imaging modality is considered which concerns light modulated at high frequency for ballistic photon discrimination through turbid media.

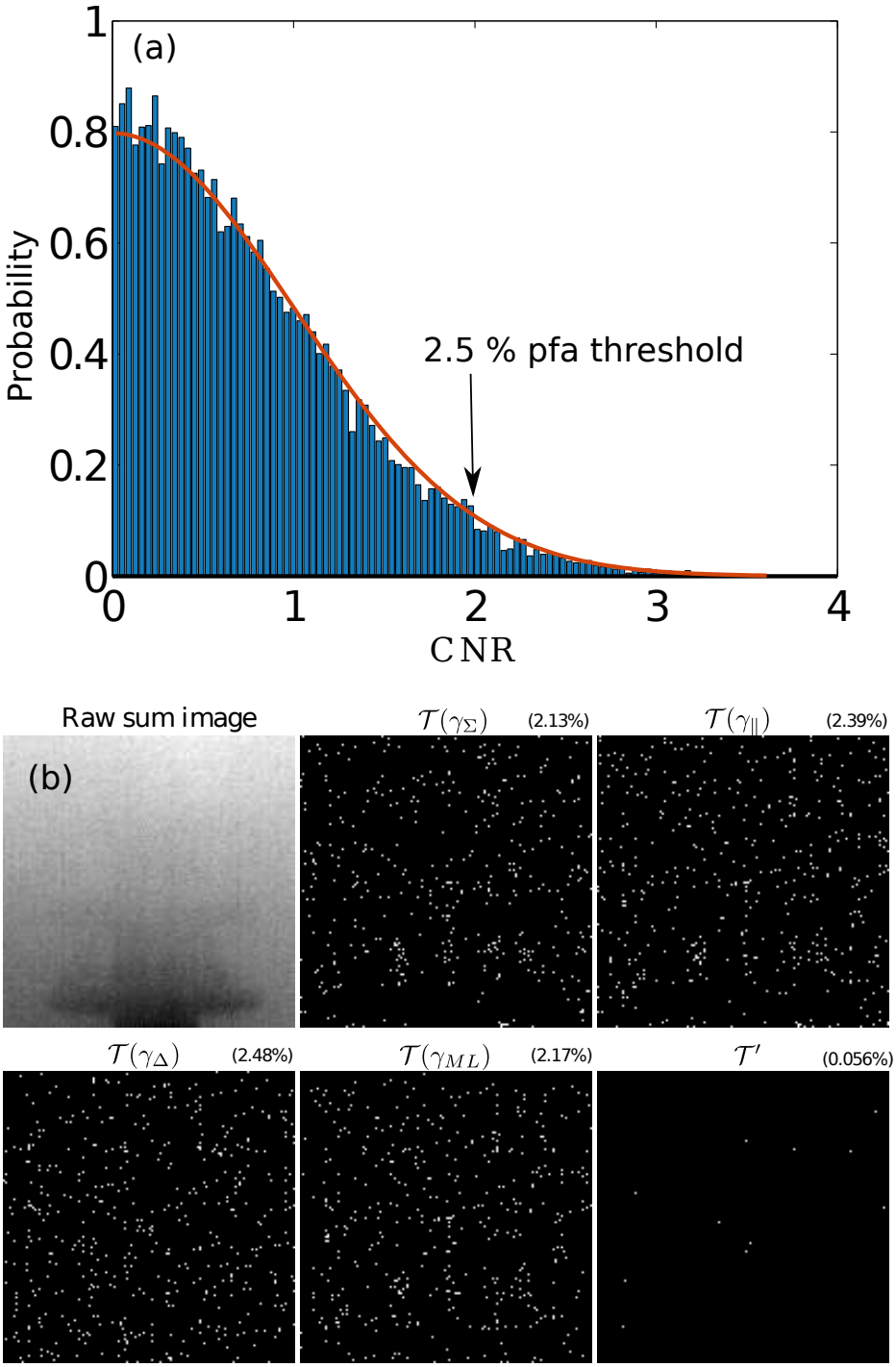

Figure 2.10: (a) The histogram obtained from the CNR image closely follows the Chi-distribution (in orange line) as is expected for Gaussian noise. (b) Shows the thresholded CNR images with 2.5% false alarm tolerance for various representations as indicated on each image. The bottom right image shows the result of the AND operation on the $\mathcal{T}(\gamma_{ML})$, $\mathcal{T}(\gamma_\Delta)$ and $\mathcal{T}(\gamma_\Sigma)$ false alarm reduction that is obtained by AND operation on the $\mathcal{T}(\gamma_{ML})$, $\mathcal{T}(\gamma_\Delta)$ and $\mathcal{T}(\gamma_\Sigma)$. The composite thresholded detection map shows a reduction of the number of false detections in the scene, but may simultaneously reduce the probability of detection of the source. Concluding on the interest of such composite test is a perspective to this work, as it would require computation and analysis of the ROC curves to evaluate on a fair basis the capabilities of detection of all the considered tests.

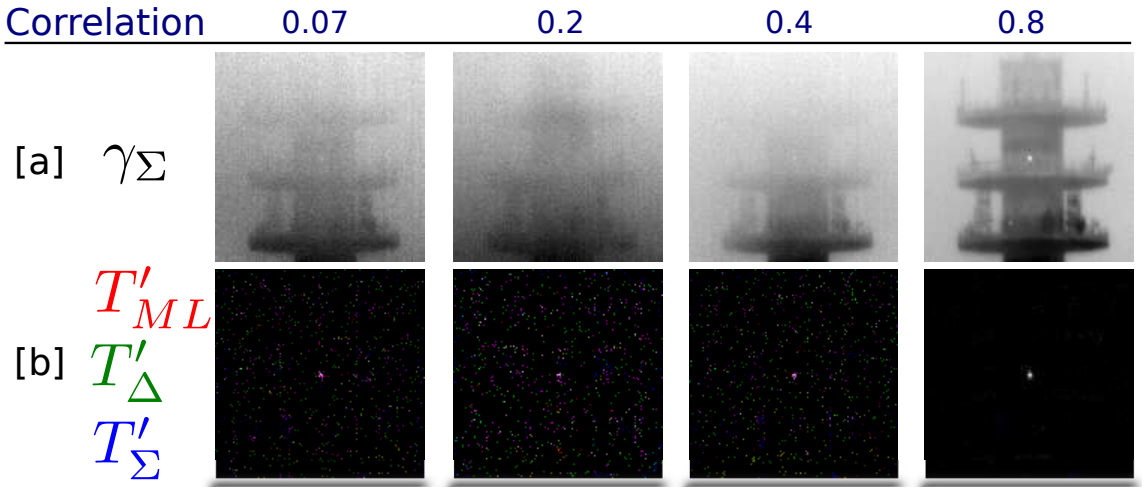

Figure 2.11: Row [a] shows the raw summed image (γ_Σ) with increasing order of background correlation (indicated above each column). Row [b] shows the composite color detection map $\mathcal{T}_{col}$ that is color coded such that Red = $\mathcal{C}(\gamma_{ML})\mathcal{T}(\gamma_{ML})$, Green = $\mathcal{C}(\gamma_\Delta)\mathcal{T}(\gamma_\Delta)$ and Blue = $\mathcal{C}(\gamma_\Sigma)\mathcal{T}(\gamma_\Sigma)$.

Part ii

Intensity modulation imaging

3

Light transport through diffusive media

The transport of light through turbid medium was briefly discussed in the introduction section of this thesis in terms of ballistic, snake and diffuse components of light. In this section, a detailed description is provided, emphasizing the theoretical models that have been successfully used to analytically describe the photon transport in turbid media. Focus will be on simple approximations that work efficiently and are relatively easy to handle analytically.

In the classical regime, when the wavelength of light is much smaller than the scattering length scales, light can be considered as non-interacting classical particles flowing down the flux distribution in a random medium. This radiative transport of light is best described by the Boltzmann transport equation which is usually intractable analytically [8, 88, 89]. Owing to this constraint, simulation have been performed using Monte-Carlo techniques to solve the Boltzmann transport equation with high accuracy [8]. Monte-Carlo simulations are only limited by time of computation and computational memory, but they remain out of scope with respect to this thesis as only analytically tractable results are focused upon. Functional expansion of the Boltzmann transport equations provide approximate solutions with limited range of accuracy but, in highly scattering media, these approximations provide an efficient and tractable means to model light transport.

The first order spherical harmonic solution of the Boltzmann equation for radiative transport is called the P-1 approximation, which under further suitable approximations turns out to be the standard diffusion equation (SDE) for photon transport. The diffusion approximation provides the most analytically tractable set of equation to model light transport. However, the diffusion model has its own limitations, which will be provided in subsequent sections. The limitations are surpassed by its efficiency and fairly accurate representation of light transport, especially, in boundary-less highly scattering media. In

turbid media with water in some form as the dominant constituent, transport of near infrared light (usually in the range of 650 nm- 900 nm, for biomedical applications) provides a suitable candidate to be studied under the SDE. Consequently, the diffusion model of light transport has found wide popularity in biomedical imaging [8]. The accuracy of using SDE has been validated with the Monte-Carlo simulations of radiative transport and have proved efficient within its validity regime [11].
Given the wide usage, efficiency and analytical tractability, the diffusion theory is used to theoretically model the diffuse photons traversing in a turbid medium. In the course of this thesis, the transport of modulated light in turbid media is theoretically analyzed and optimal use of quadrature demodulation scheme is derived. Several novel deductions will be presented that are relevant not only to imaging through fog, but for the biomedical applications as well.
A brief introduction to the derivation of SDE from the Boltzmann equation is first required to understand the validity regime of the diffusion theory. In light of this, the next section is intended to provide an overview of the radiative transport model and point towards the assumptions used to obtain the diffusion model of photon transport.

3.1 Radiative transport model and diffusion approximation

In the macroscopic regime, photons can be treated as classical non-interacting particles. Neglecting optical non-linearities in the medium and some fundamental properties of light like coherence and polarization, a macroscopic transport equation can be derived by applying conservation of energy or continuity of radiance (L with units W m^{-2} sr^{-1}). In a scattering medium having macroscopic and temporally stationary optical properties such as absorption coefficient μ and scattering coefficient μ_s, the rate of change of energy in an infinitesimal volume (dV) is the sum of rate of all losses and gains in the energy. Let us enumerate all the sources of losses and gains of photons within a volume element of differential length ds in the photon propagation direction $\hat{s}$.

Loss due to divergence In case of a diverging source, the energy diverging out of the volume element is

$$dP_{div} = \frac{\partial L(\boldsymbol{r}, \hat{s}, t)}{\partial s} dV d\Omega = \nabla.[L(\boldsymbol{r}, \hat{s}, t)\hat{s}] dV d\Omega.$$

Loss due to attenuation The source of attenuation of the photon flux is absorption of photons and scattering of photons out of the volume element,

$$dP_{attn} = (\mu_t ds)[L(\boldsymbol{r}, \hat{s}, t) dV d\Omega],$$

where $\mu_t = \mu + \mu_s$ is total attenuation coefficient, taking into account both the attenuation due to absorption (μ) and attenuation due to scattering (μ_s).

Gain due to incoming scattered light Scattered light can enter the volume element from all directions. To incorporate this, a phase function $f(\hat{s}', \hat{s})$ must be introduced that represents the probability of light propagating in direction $\hat{s}'$ to be scattered to direction $\hat{s}$. The phase function usually depends on the angle between $\hat{s}'$ and $\hat{s}'$, therefore, a scattering anisotropy parameter can be introduced such that $g = \int_{4\pi} L(\boldsymbol{r}, \hat{s}, t) f(\hat{s}'.\hat{s}) d\Omega$. The energy gain can then be written as

$$dP_{sca} = (\mu_s dV) d\Omega \int_{4\pi} L(\boldsymbol{r}, \hat{s}', t) f(\hat{s}'.\hat{s}) d\Omega'.$$

Gain due to the source The energy incident into the volume element from a source is

$$dP_{src} = S(\boldsymbol{r}, \hat{s}', t) dV d\Omega,$$

where S is the source power per unit volume per unit solid angle.
Thus, the change in energy in the volume element $dP = \frac{\partial L(\boldsymbol{r}, \hat{s}, t)/c}{\partial s} dV d\Omega = -dP_{div} - dP_{attn} + dP_{sca} + dP_{src}$, leading to the time-dependent Boltzmann transport equation [8, 88, 89]

$$\frac{1}{c} \frac{\partial L(\boldsymbol{r}, \hat{s}, t)}{\partial s} = -\hat{s}.\nabla L(\boldsymbol{r}, \hat{s}, t) - \mu_t L(\boldsymbol{r}, \hat{s}, t) + \mu_s \int_{4\pi} L(\boldsymbol{r}, \hat{s}', t) f(\hat{s}'.\hat{s}) d\Omega' + S(\boldsymbol{r}, \hat{s}', t). \quad (3.1)$$

The expression equates the angular rate of change in the photon flux density (or radiance) L at a point $\boldsymbol{r}$ and traveling in the direction $\hat{s}$ at time t, to the losses and the influx of photons due to absorption, scattering and the source. In the expression, c is the velocity of the particles in the medium and $\mu_t = \mu + \mu_s$ is the total attenuation constant. The linear transport equation presented above does not take into account the coherence and polarization effects. The coherence and polarization effects have been take in into account in literature [90], but they remain out of scope of the analysis conducted in this second part of the thesis. Further, for transport applications or even biomedical imaging through turbid media, it is preferable to use incoherent, light sources like LED sources or super luminescent sources.
As mentioned before, this equation is difficult to solve analytically and numerical and computational methods are generally employed to solve the problem. An approximate solution can be obtained by reducing the integro-differential equation into a set of differential equations by approximating the angular dependency of radiance and the phase function with a finite series expansion into spherical harmonics. Employing the following series expansions [8]:

$$L(\boldsymbol{r}, \hat{s}, t) = \sum_{l=0}^{N} \sum_{m=-l}^{l} \psi_{l,m}(\boldsymbol{r}, t) Y_{l,m}(\hat{s}) \quad (3.2)$$

$$S(\boldsymbol{r}, \hat{s}, t) = \sum_{l=0}^{N} \sum_{m=-l}^{l} q_{l,m}(\boldsymbol{r}, t) Y_{l,m}(\hat{s}) \quad (3.3)$$

$$f(\hat{s}', \hat{s}) = (1/4\pi) \sum_{l=0}^{\infty} (2l+1) g_l P_l(\hat{s}'.\hat{s}) = \sum_{l=0}^{N} \sum_{m=-l}^{l} g_l Y^*_{l,m}(\hat{s}') Y_{l,m}(\hat{s}) \quad (3.4)$$

The functions $Y_{l,m}$ are the spherical harmonic functions and P_l is the Legendre Polynomial of order l. g_0 in the phase function is set to one while g_1 is the average cosine of the scattering angle. Truncating the series expansion at $l = N$ provides the so called P-N approximation as known in the neutron transport literature [91].
Restricting ourselves to the P-1 approximation, the radiance $L(\boldsymbol{r}, \hat{s}, t)$ can be written in terms of the photon fluence $\boldsymbol{\Phi}$ and the current density $\boldsymbol{J}$ as [8]

$$L(\boldsymbol{r}, \hat{s}, t) = \frac{1}{4\pi}\boldsymbol{\Phi}(\boldsymbol{r}, t) + \frac{3}{4\pi}\boldsymbol{J}(\boldsymbol{r}, t).\hat{s}, \tag{3.5}$$

and the source can be written in terms of its moments as

$$S(\boldsymbol{r}, \hat{s}, t) = \frac{1}{4\pi}S_0(\boldsymbol{r}, t) + \frac{3}{4\pi}\boldsymbol{S_1}(\boldsymbol{r}, t).\hat{s}, \tag{3.6}$$

These first-order expansions are then substituted in the linear transport equation and integrated over all directions to reveal

$$\frac{1}{c}\frac{\partial \boldsymbol{\Phi}(\boldsymbol{r}, t)}{\partial t} + \mu\boldsymbol{\Phi}(\boldsymbol{r}, t) + \boldsymbol{\nabla}.\boldsymbol{J}(\boldsymbol{r}, t) = S_0(\boldsymbol{r}, t), \tag{3.7}$$

and the first directional moment is obtained by substituting the first-order expansions in the linear transport equation, multiplying with $\hat{s}$ and integrating over all directions to obtain

$$\frac{1}{c}\frac{\partial \boldsymbol{J}(\boldsymbol{r}, t)}{\partial t} + (\mu + \sigma)\boldsymbol{J}(\boldsymbol{r}, t) + \frac{1}{3}\boldsymbol{\nabla}\boldsymbol{\Phi}(\boldsymbol{r}, t) = \boldsymbol{S_1}(\boldsymbol{r}, t), \tag{3.8}$$

where $\sigma = \mu_s(1 - g)$ is the reduced scattering coefficient and $g = g_1$ is the anisotropy factor. By decoupling Eq. (3.7) and Eq. (3.8) one obtains the P-1 equation as

$$\begin{aligned}\left[\frac{3D}{c^2}\frac{\partial^2 \boldsymbol{\Phi}(\boldsymbol{r}, t)}{\partial t^2} + \frac{3D\mu}{c}\frac{\partial \boldsymbol{\Phi}(\boldsymbol{r}, t)}{\partial t}\right] + \frac{1}{c}\frac{\partial \boldsymbol{\Phi}(\boldsymbol{r}, t)}{\partial t} + \mu\boldsymbol{\Phi}(\boldsymbol{r}, t) - D\nabla^2\boldsymbol{\Phi}(\boldsymbol{r}, t) \\ = S_0(\boldsymbol{r}, t) + 3D\left[\frac{1}{c}\frac{\partial S_0(\boldsymbol{r}, t)}{\partial t} - \nabla\boldsymbol{S_1}(\boldsymbol{r}, t)\right]\end{aligned} \tag{3.9}$$

In the above equation $\boldsymbol{S_1}$ is the first moment in the expansion of the source, showing dipole like anisotropy in the source and $D = [3(\mu + \sigma)]^{-1}$ is the diffusion constant. Under certain further assumptions, i.e., when the terms in the square brackets are neglected, the above equation reveals itself as the standard diffusion equation (SDE) for the flux $\boldsymbol{\Phi}$. These approximations, that also provide the validity conditions for application of the SDE to photon transport in turbid media, are

- Assuming that $3D\mu = \mu/(\mu + \sigma) \ll 1$, one has the condition that $\sigma \gg \mu$, which implies that the medium must be highly scattering. In such a medium the photons go through multiple scattering events before being absorbed. With this assumption the second term in the first square brackets can be ignored.

- The contribution of the dipole nature of the source $\boldsymbol{S_1}$ is neglected by assuming an isotropic source. However, in most cases where the source is not isotropic, it is

justified by considering a collimated source of light as a virtual isotropic point source placed one mean free path inside the medium.

- To diminish the contributions of the terms $\frac{3D}{c^2}\frac{\partial^2 \mathbf{\Phi}(\boldsymbol{r},t)}{\partial t^2}$ and $\frac{3D}{c}\frac{\partial S_0(\boldsymbol{r},t)}{\partial dt}$, the time evolution of the source and the flux must be slower than $[3D/c]^{-1}$. For a sinusoidally modulated source, this implies that the angular frequency of oscillation $\omega < [3D/c]^{-1} = (c/(\mu+\sigma))$ ($\sim c/\sigma$, when $\sigma \gg \mu$). The condition can be derived mathematically in the Fourier domain by taking the source as $exp\,[-i\omega t]$ and replacing the time derivatives with $-i\omega$.

Using the above approximations, one arrives at the diffusion equation which describes the space-time evolution of the fluence rate and is written as

$$\frac{1}{c}\frac{\partial \mathbf{\Phi}(\boldsymbol{r},t)}{\partial t} + \mu \mathbf{\Phi}(\boldsymbol{r},t) - D\nabla^2 \mathbf{\Phi}(\boldsymbol{r},t) = S_0(\boldsymbol{r},t). \tag{3.10}$$

Near-infrared light through tissues remain within the above validity conditions. Owing to this, the diffusion approximation is widely used in medical diagnostics.

3.1.1 Temporally sinusoidal source

Frequency domain analysis of the photon diffusion equation was studied by Fishkin and Gratton [92]. For a sinusoidal excitation of angular frequency ω, modulation index M and mean intensity I_0, the source power instantaneous power is $S(t) = P_0 + MP_0\ exp\,[-i\omega t]$. In that case, the diffuse photons behave as scalar density waves oscillating at the same frequency as the source. The amplitude is damped as the wave travels through the medium and gains additional phase. For a homogeneously scattering medium and an intensity modulated point source at the origin, the oscillating component of the density waves and the DC component is derived as [92, 93, 94]

$$\begin{aligned} \Phi_{AC}(\boldsymbol{r},t) &= \frac{cMP_0}{4\pi Dr}\ exp\,[ikr]\ \ exp\,[-i\omega t]\,, \\ \Phi_{DC}(\boldsymbol{r},t) &= \frac{P_0\ exp\,[-r/\delta]}{4\pi Dr}, \end{aligned} \tag{3.11}$$

where the complex wave number k is defined by [1]

$$\begin{aligned} k &= i\sqrt{\frac{-\mu + i(\omega/c)}{D}} \\ &= \sqrt{\frac{\mu}{D}}\left[\sqrt{\frac{\sqrt{1+(\omega/\mu c)^2}+1}{2}} + i\sqrt{\frac{\sqrt{1+(\omega/\mu c)^2}-1}{2}}\right] \end{aligned} \tag{3.12}$$

The complex wavenumber implies that the scalar photon density wave is exponentially attenuated with well defined wavelength, amplitude and phase. In the following sections,

[1] It is worth noting that this is not the only solution for the frequency domain analysis, but it is the physically relevant solution [95]

these well-known results are used in consistent manner to obtain dimensionless parameters that are relevant in describing modulated light transport through a diffusive medium. The well studied diffusion theory described here is applied to the imaging scheme considered in this thesis to obtain novel results in the context of ballistic photon filtering and estimation of scattering parameters, as detailed in the following chapter.

3.2 Diffusion model and imaging through turbid media

The diffusion model arises when the photons are allowed to perform a random walk, diffusing from high photon density regions to low photon density regions. The theory has proved efficient when modeling light in a predominantly scattering medium and when detection is carried out sufficiently away from a point source. Let us now identify some parameters that are important for describing transport in a scattering medium. The scattering length (l_s) is defined as the mean distance traveled by a photon before a scattering event and is the inverse of the scattering coefficient μ_s. The inverse of the reduced scattering coefficient ($\sigma = \mu_s(1-g)$) is denoted by l_σ and is the mean distance traveled by photons before isotropically scattering in all directions. The anisotropy factor g is the mean cosine of the scattering phase function, as introduced above [8, 96]. Few more important length scales emerge which are relevant in the context of transport of photons in the medium. The transport mean free path (MFP) is the inverse of the total attenuation due to absorption and scattering and is denoted by $l = [\mu + \mu_s]^{-1}$. It describes the mean distance traveled by photons before they loose their directional information. Further, a transport (or reduced) mean free path, $l_* = [\mu + \sigma]^{-1}$ arises through the transport equations and can be interpreted as the attenuation length of quasi-ballistic photons. The diffusion theory also includes two other constants: the diffusion length (D) defined as $D = l_*/3$ and the optical penetration depth (δ), which is the inverse of the effective attenuation coefficient ($\sqrt{\mu/D}$) in diffused medium. Finally, the absorption coefficient (μ) is associated with an absorption length. For ease of reading, the corresponding definitions are tabulated in Table 3.1.

In addition, for the analysis in the following sections, various dimensionless constants will be used that are given in the right side of Tab 3.1. The dimensionless parameters $R_\delta = r/\delta$ and $R = r/l$ correspond to the equivalent optical attenuation of diffused light and equivalent optical attenuation of ballistic light, respectively, for various values of r, δ and l. Similarly, $R_* = r/l_*$ is a dimensionless equivalent attenuation of quasi-ballistic light. The parameter q is related to the angular frequency of modulation and is given in Eq. (3.13) and the non-trivial form of the reparameterization simplifies the complex wave number k as shown in Eq. (3.12).

$$q = \sqrt{\frac{1 + \sqrt{1 + \left(\frac{\omega}{\mu c}\right)^2}}{2}} \tag{3.13}$$

Meaning (units)	Symbol	param.	Defn.
MFP (m)	$l = 1/(\mu + \mu_s)$	R	r/l
Transport MFP (m)	$l_* = 1/(\mu + \sigma)$	R_*	r/l_*
Diffusion length (m)	$D = [3(\mu + \sigma)]^{-1}$	–	–
Optical penetration depth (m)	$\delta = \sqrt{D/\mu} = [3\mu(\mu + \sigma)]^{-1/2}$	R_δ	r/δ
Effective scattering length (m)	$l_\sigma = 1/\sigma$	–	–
Distance of propagation (m)	r		
Angular modulation frequency (rad/s)	ω	q	$\sqrt{\frac{1+\sqrt{1+(\omega/\mu c)^2}}{2}}$
Effective (real) refractive index	n		
Speed of light in medium (m/s)	c	–	–

Table 3.1: Symbols, definitions and derived variables

3.2.1 Imaging scheme

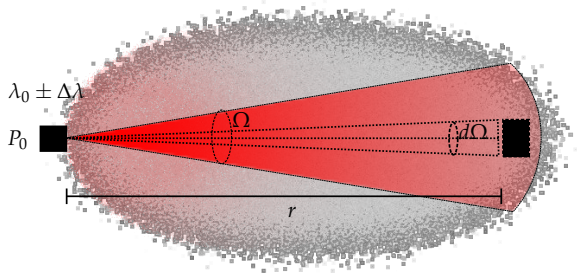

Figure 3.1: Imaging scheme: A directional source of light with power, P_0, forward cone solid angle, Ω, having a limited spectral width ($\lambda \pm \Delta\lambda$) is detected at a distance r by a detector that subtends an angle $d\Omega$ from the source.

The imaging scheme considered here includes a directional point source of light with a forward cone solid angle Ω and that subtends a solid angle of $d\Omega$ at the detector which is placed at a distance r from the source. First a non-modulated source of power P_0 is considered. The case of sinusoidally varying intensity-modulated source is addressed in the next section. For the sake of simplicity, the source is considered to have limited spectral range $\lambda_0 \pm \Delta\lambda$, so that the above diffusion parameters can be considered as constant over the spectral range of the source. The schematic in Fig. 3.1 illustrates the scenario. In the presence of an intervening scattering medium, the net intensity of ballistic photons reaching the detector of collection area $d\Omega r^2$ is proportional to the total power P_0 emitted by the source, and is given by the Beer's law as $I_B = \xi P_0\, e^{-(\mu+\mu_s)r} \frac{d\Omega r^2}{\Omega r^2} = \xi P_0\, e^{-(\mu+\mu_s)r} \frac{d\Omega}{\Omega}$. The scaling factor ξ represents the overall detector efficiency on the considered spectral range including optical losses, detection geometry and quantum efficiency of detector. Similarly, according to the steady state solution of the diffusion theory, the diffuse photon intensity reaching the detector is also proportional to the total power emitted by the source such that $I_D = \xi P_0\, e^{-r/\delta} \frac{d\Omega r^2}{4\pi D r} = \xi P_0\, e^{-r/\delta} \frac{d\Omega}{4\pi} \frac{r}{D}$ [94, 97]. The expressions of the intensities of ballistic

and diffused light show that there are clearly two important length scales to be considered, namely, the transport MFP (l_*) and the optical penetration depth (δ). Considering only the above two classes of photons, it is possible to obtain an order of magnitude value of the ratio (α) of ballistic photons to diffuse photons reaching the detector as

$$\alpha = \frac{I_B}{I_D} = \Omega' \frac{D}{r}\, e^{-r(\mu+\mu_s-1/\delta)} = \Omega' \frac{e^{R_\delta - R}}{3R_*}, \tag{3.14}$$

where dimensionless variables R,R_*, R_δ and $\Omega' = 4\pi/\Omega$ are used.

3.2.2 Modulated light in diffused media

The propagation of sinusoidally modulated light through a scattering medium has been modeled using diffusion theory and it has been shown that the transport of modulated light behaves as photon density waves whose properties are dependent on the properties of the medium [94, 92, 98, 99]. Considering an intensity modulated source of light having modulation angular frequency ω and modulation index M, the instantaneous power emitted reads $p(t) = P_0(1 + M\ cos\,[\omega t])$. The ballistic light that follows Beer-Lambert's law, is only attenuated and reaches the detector with instantaneous detected intensity $i_b(t) = I_B(1 + m_B\ cos\,[\omega t])$, with $I_B = \xi P_0\ exp\,[-R]\, d\Omega/\Omega$ as established above and without any change in received modulation index, $m_B = M$.

However, as shown in previous sections, the time dependent solution of the photon diffusion theory shows that the modulated light traversing through a scattering medium is received at the detector with a complex wavenumber and, thus, reduced modulation index and additional phase [94]. Then, the instantaneous diffuse light intensity received at the detector is $i_d(t) = I_D(1 + m_D\ cos\,[\omega t + \Delta\phi])$, with $I_D = \xi P_0\ exp\,[-R_\delta]\, d\Omega/(4\pi D)$. The reduced modulation index m_D and the phase $\Delta\phi$ can be obtained from the complex wave number given in Eq. (3.12). For the sake of conciseness, their derivations are not given here but their expressions are identically reported in [94, 97]:

$$\begin{aligned} m_D =& M\ exp\left[-r\sqrt{3\mu(\mu+\sigma)}\left(\sqrt{\frac{1+\sqrt{1+(\omega/\mu c)^2}}{2}}-1\right)\right] \\ =& M\, e^{-R_\delta(q-1)}, \end{aligned} \tag{3.15a}$$

$$\Delta\phi = r\sqrt{3\mu(\mu+\sigma)}\sqrt{\frac{-1+\sqrt{1+(\omega/\mu c)^2}}{2}} = R_\delta\sqrt{q^2-1}. \tag{3.15b}$$

where the parameter q has been defined in Eq. (3.13), is related to the angular frequency of modulation and ranges between $[1, \infty)$ when $\omega \in [0, \infty)$. Although the physical interpretation of the parameter q is not straightforward, it will be seen later that the term qR_δ can be identified as a dimensionless, frequency-dependent, effective attenuation of the diffused light. Further, in the following sections, $\beta = m_B/m_D$ will denote the ratio of the modulation indices of ballistic light to diffuse light.

It is quite straightforward to see that using the above equations, the parameters R_δ and q can be estimated when the modulation index and phase of the diffuse light are accurately detected. The model can indeed be inverted as will be shown in the next chapter.
Thus, the above formulation provides a simple analytical method for estimating of the scattering and absorption parameters of the scattering medium using only diffuse light and a modulated light source, provided the assumptions and conditions for the derivation are fulfilled. In practice, especially in diffuse optical imaging, the modulation frequency is scanned to obtain corresponding values of modulation index and phase. Then, a non-linear fit of the theoretical prediction with the data provides the estimates for the scattering and absorption properties of the medium [94]. The effect of scattering media on modulation index and phase can also be exploited to attain discrimination of ballistic photons that retain the modulation index and phase. These application scenarios can be analyzed from an information theoretical point of view for a well-defined detection technique. The detection of the modulation index and the phase can be performed in various ways. Generally in a demodulation scheme, the amplitude, phase and mean intensity are recorded and then the modulation index can be easily estimated. Quadrature demodulation is one of the simplest and the most widely used scheme for demodulation. It avoids, in particular, the necessity of signal synchronization or phase tracking of the incoming signal which brings additional noise contributions. In the following section a quadrature detection scheme is shown and its noise model is derived.

4

Intensity modulation imaging efficiency

Intensity modulated light is another modality that can be used in the field of imaging through turbid media. In the previous chapter, modulated intensity passing thorough a nebulous medium has been shown to alter the transport properties of diffused photons as a function of the modulation frequency and scattering properties of the medium itself. Such a scheme can be used to image through scattering media by two basic ways: (i) by estimation and mapping of scattering and absorption inhomogeneities in the medium itself or (ii) by ballistic photon discrimination imaging, where the low SNR ballistic photons are selectively imaged and distinguished from diffuse photons. The former methodology has been widely used in the field of biomedical imaging [4], where the scattering and absorption inhomogeneities with tissue properties are estimated to aid in medical diagnostics [100, 101], especially in mammography [102] and brain imaging [103]. This field has seen maturity and transition in recent years from research to applications. However, noise and resolution still remain primary limitations of this methodology. In such cases the time dependent solution to diffusion theory is used to model the transport of pulsed light [5, 104] or modulated light [99, 94, 10, 105] through the scattering media. The precision of estimation of the parameters is crucial in this case. In practice, intensity modulated light with diffusion theory are widely used in frequency-domain photon migration, where an intensity modulated light with modulation frequencies of a few hundred MHz is transmitted through a diffusive medium. As established in the previous chapter, modulated light traveling through the diffusive medium forms a macroscopic density wave with the wave number dependent on the scattering and absorption properties of the medium. As a result, the detected modulated light has reduced modulation index and an additional phase, both of which depend on the scattering properties of the medium and its thickness. Using the analytical expressions for the modulation index and phase predicted by the diffusion

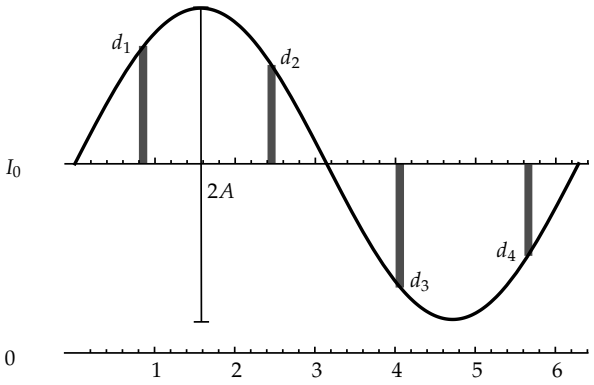

Figure 4.1: Illustration of the optical signal received at the detector. As an example, four samples are shown here to form the quadrature components which, consequently, can be used for estimation of amplitude and phase of the signal.

theory, the parameters of the intervening medium can be estimated by using a single or multiple modulation frequencies. Similarly, the change in modulation index and phase of the diffuse light can be used to discriminate them from ballistic photons which retain the spatio-temporal information of the modulated source. In this context modulated light and lock-in detection has an obvious advantage of background rejection but the efficiency of ballistic photon filtering has not been studied well. In this thesis, the above two modalities will be studied with a goal of identifying optimal experimental design parameters and performance metric for imaging through turbid media using intensity modulated light and quadrature demodulation.

4.1 Quadrature demodulation

Demodulation of light at radio frequencies and higher poses practical challenges like phase synchronization, timing jitters etc. One of the demodulation techniques which is robust to such noises and provides demodulation without a need of a synchronization signal is the quadrature demodulation. It is well known and widely used in electronics and telecommunications fields like radar and radio broadcasting. The quadrature demodulation scheme is, especially, important when the the source and detector are far apart and a synchronization signal may not be available. For example, when using modulated light for assisting in aircraft landing and taxiing, the source on the ground and an on-board camera should be preferably independent and be able to demodulate without synchronization. In a quadrature detection scheme, both the received amplitude and the relative phase of the signal can be estimated without need of a synchronized source. It is necessary to have the prior knowledge of the frequency of the source so that the input signal can be multiplied with a sine and cosine wave of the same frequency to obtain the quadrature components. Considering the detected light modulated at an angular frequency of ω (rad.s^{-1}) and modulation index M, the instantaneous intensity is written as $i(t) = I_0(1 + M\ cos\ [\omega t])$, for the average detected intensity I_0. Multiplication of this signal with a sine wave of the same

frequency with a relative phase $\Delta\phi$ and integrating/summing over a integer multiple of the time period of oscillation, one obtains $V = A\ sin\,[\Delta\phi]$. $2A = MI_0$ is the peak-to-peak amplitude of oscillation of the detected signal (see Appendix D for detailed calculations) as shown in Fig. 4.2 . In a synchronized detection scheme where the source modulation can be taken as a reference to nullify the phase term, it is possible to retain only the amplitude of modulation. However, practical complications may arise due to drifting of phase which is usually addressed by phase locking methods. In some cases, when the source is located far away from the detector, the reference is not available. To avoid these limitations and complications, one may resort to the well-known quadrature demodulation scheme where the signal may also be multiplied with a cosine of the same frequency. Integrating over an integer number of time periods, one obtains $U = A\ cos\,[\Delta\phi]$. The U and V are represent the in-phase and quadrature components of the signal respectively. The amplitude can be retrieved by squaring and adding the quadrature components as $A = \sqrt{U^2 + V^2}$, and the relative phase difference between the source and the detector can also be obtained by $\phi = tan^{-1}\,[V/U]$.

The obvious advantage of using such modulation-demodulation scheme is to improve the SNR of the modulated signal which is embedded in an illuminated constant background. The background rejection is achieved by means of spectral filtering of the wide band background noise. Considering a source with mean intensity I_0, angular frequency ω and modulation index M embedded in a background with noise power spread uniformly over a spectral range of $[0, B_0]$, with $B_0 > \omega$. For a quadrature detection system with bandwidth of detection of B_Q around the central angular frequency ω, the SNR enhancement of the signal with respect to the constant background is B_0/B_Q. The efficiency of background rejection is also inversely proportional to the central frequency used, consequently, higher modulation frequencies are favorable to attain enhanced background noise rejection. The efficiency of lock-in detection for such SNR enhancement by means of background noise rejection is well established and widely used.

In case of a modulated light signal through a highly scattering medium, the ballistic and diffuse light will be modulated at the same frequency, thus, both the components of the light source will be equally discriminated form the constant background. Irrespective of the modulation frequency, this provides an SNR enhancement of ballistic and diffuse signal from the source by a factor of B_0/B_Q. However, resolution and visibility enhancement due to ballistic filtering is not guaranteed at any modulation frequency. The purpose of the following sections is to address the feasibility of discriminating ballistic photons from the diffuse photons in an experimental scheme utilizing a modulated-source and quadrature-demodulation. Further, this part of the thesis also aims at identifying the operating frequencies at which one can obtain ballistic photon filtering using modulated light. Therefore, it is first necessary to derive a noise model for a generic quadrature detection scheme.

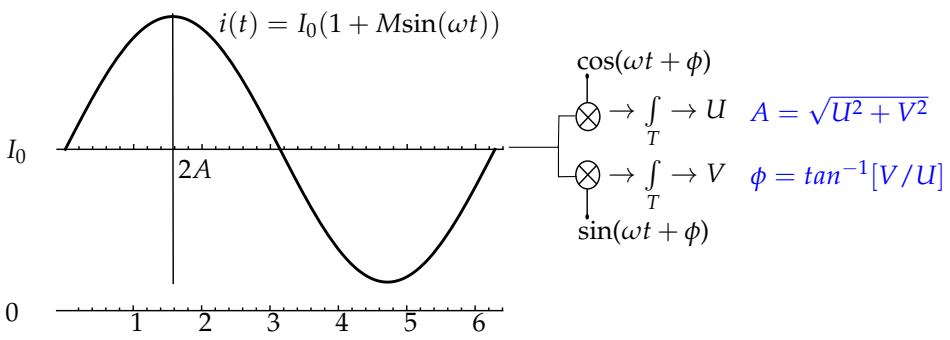

Figure 4.2: Schematic of a quadrature demodulation scheme.

4.2 Noise model for quadrature demodulation

Let us consider a quadrature detection system that receives a sinusoidal signal with instantaneous intensity $i(t) = I_0(1 + \ cos\,[\omega t])$. To obtain a noise model for the quadratures, let us consider that the signal is sampled N times within a period of oscillation, such that the mean sampled intensity is $d_i = I_0(1 + M\ cos\,[\omega t_i])$. Further, the quadrature components (U, V) are obtained by weighing the sampled data with cosine and sine waves of the same frequency and then summing over a integer number of time periods, i.e., $U = \sum_{i=1}^{N} d_i\ cos\,[\omega t_i + \phi] = A\ cos\,[\phi]$ and $V = \sum_{i=1}^{N} d_i\ sin\,[\omega t_i + \phi] = A\ sin\,[\phi]$, for $N \geq 2$. This applies for a continuous demodulation system, which can be considered in the limit of $N \rightarrow \infty$. From the obtained variables U and V, the amplitude $A = MI_0/2$ and phase ϕ of the demodulated signal are respectively given by $A = \sqrt{U^2 + V^2}$ and $\phi = \tan^{-1}[V/U]$. The above strategy is used along with knowledge of photon noise to derive the noise distribution of the amplitude and phase that is produced by the detection system. The reasoning is summarized below :

- Note that, the photon count within an infinitesimal sampling window may follow Poisson distribution with mean and variance equal to the instantaneous mean intensity at the sampling window. Therefore, the photon count variance at time t_i is d_i.

- The sampled data d_i is the weighted by sine and cosine waves of same frequency and summed over to produce the quadrature components U and V which follow a compound Poisson distribution. Thus, the weighted noise propagates as shown in Appendix C.3 and the variance of the quadrature components is $var(U) = var(V) = I_0/2$.

- For large values of I_0 as encountered in imaging problems, the compound Poisson distribution can be approximated as a Normal/Gaussian distribution with variance equal to the mean. Thus, it can be inferred that U and V are distributed as $\mathcal{N}[A\ cos\,[\phi]\,, \Lambda^2]$ and $\mathcal{N}[A\ sin\,[\phi]\,, \Lambda^2]$, respectively, with $\Lambda^2 = I_0/2$ and with $\mathcal{N}[\bar{x}, var(x)]$ denoting the normal distribution with mean $\bar{x}$ and variance $var(x)$.

- Knowing the distribution of the quadrature components, it is then possible to derive

the joint probability density function (PDF) of the random variables, $Z = \sqrt{U^2 + V^2}$ and $\Psi = \tan^{-1}(V/U)$, by applying the appropriate change of variables to the Gaussian distribution, as given in the Appendix C.1. The expected values of the random variables Z, Ψ and their variance form the parameter vector $\boldsymbol{\theta}' = [A, \phi, \Lambda^2]$, where $2A = MI_0$ is the peak-to-peak amplitude as shown in the schematic of Fig. 4.2. Then, the joint PDF of the amplitude and phase is

$$P_{Z,\Psi}(z, \psi | A, \phi, \Lambda^2) = \frac{z}{2\pi\Lambda^2}\, exp\left[-\frac{1}{2\Lambda^2}(z^2 + A^2 - 2zA\, cos\,[\psi - \phi])\right]. \tag{4.1}$$

The noise term which only includes the photon noise can be used to provide physical limits of using quadrature demodulation with light. The noise variance term can be extended to include detector noise. The noise in detector can be attributed to thermal fluctuations (or dark noise) and electronic read-out noise. Consequently, the noise in the detected quadrature components can be written as $\Lambda^2 = I_0/2 + \Lambda^2_{Thermal} + \Lambda^2_{ro}$. In the analysis that will follow, these noise contributions are largely ignored to provide idealized situation that corresponds to physical limits of the system.

The noise model derived here is generic and is used in fields like NMR imaging [106]. In recent years, quadrature demodulation cameras have also found commercial use, especially in 3D imaging. Such demodulation cameras will be reviewed in the next chapter alongside the description of the development of a novel full-field quadrature demodulation camera. This generic noise model can be directly applied to such cameras that obtain amplitude and phase information [107]. In the rest of this chapter, this noise model is reparameterized and various useful insights are gained in the context of imaging through turbid media using modulated light.

4.2.1 Fisher information

The joint PDF of the amplitude and phase received at the quadrature detector end can provide insight into the precision with which the received data can be used to estimate the mean amplitudes and phase. The Fisher information (FI) provides such a metric to quantify the precision of estimation from a dataset given a noise model. The definition and importance of Fisher information (FI) has been provided in Appendix A and has been illustrated in the first part of the thesis. In the multiple parameter case, the Fisher information matrix (FIM) provides insight into mutual dependencies of estimators and is directly related to the covariance lower bound on unbiased estimation of unknown parameters through the Cramer-Rao bound. In further sections the FIM will be used to derive various optimal operating points and quantify the efficiency of detection systems. In light of this, the expected FIM with respect to the three parameters that define the PDF in Eq. (4.1) is derived.

The expected FIM for a parameter vector ($\boldsymbol{\eta}$), is defined as $\mathcal{F}(\boldsymbol{\eta})_{ij} = -\left\langle \frac{\partial^2\, ln[P(x|\boldsymbol{\eta})]}{\partial\eta_i \partial\eta_j} \right\rangle$, where $\langle . \rangle$ denotes the expectation value. We present below the FIM for the detection procedure described above with respect to the parameter vector $\boldsymbol{\theta}' = [A, \phi, \Lambda^2]$. It is straightforward

to calculate the FIM (using the defination given in Eq. (.28) in Appendix A) for the given noise model. The FIM then reads

$$\mathcal{F}(\boldsymbol{\theta}') = \begin{pmatrix} \frac{1}{\Lambda^2} & 0 & 0 \\ 0 & \frac{A^2}{\Lambda^2} & 0 \\ 0 & 0 & \frac{1}{\Lambda^4} \end{pmatrix}. \tag{4.2}$$

The above FIM is diagonal, which shows that the three parameters in $\boldsymbol{\theta}'$ can be estimated independently, i.e., without joint estimation errors. Moreover, the precision in estimation of the phase increases with the amplitude of the signal. The detection technique described in the preceding section is derived for a single detector, but can be extended to multiple pixel, full-field lock-in detectors as will be studied in the next chapter in the context of lock-in imaging. In this detection scheme, the recorded amplitude and phase of the diffuse light through a scattering media can be modeled by the diffusion theory as presented in chapter 4. Using this model, the noise model of the detection can be reparametrized as shown below and consequently, estimation precision of the parameters can be calculated.

4.3 Ballistic photon filtering

The importance of ballistic photon discrimination imaging and the various strategies used to attain it, were discussed in the introduction chapter. In the context of using intensity modulated light to attain ballistic photon filtering, it is first necessary to distinguish it from SNR enhancement of the source that is achieved by spectral filtering of the background noise. As mentioned in the previous section, background rejection can be achieved even at relatively low frequencies of modulation. However, the question arises, can intensity modulation provide imaging of objects embedded in a turbid medium whose resolution is hampered by the diffused photons? In an imaging scenario, where the source is imaged through a turbid medium without any background illumination, is it possible to extract the spatial information of the source? These questions will be answered in this section by tying together information theoretical tools with diffusion theory of photon transport.
In an imaging scenario through turbid media in absence of ambient background, there are pixels that receive only diffuse photons forming the set denoted by $\mathcal{D}$, and there are pixels that receive a few ballistic photons over the diffused light, forming the set denote here by $\mathcal{B} \oplus \mathcal{D}$. In scenarios where ballistic photons lie a few standard deviation away from the background diffused light, ballistic photons imaging can always be achieved using an idealistic intensity camera with infinite dynamics and low noise properties. In which case a simple thresholding at the maximum diffuse light intensity may produce ballistic photon filtering. However, with real detectors, due to limited dynamics and sensitivity, the only way to attain ballistic photon imaging using intensity imager is by increasing the photon budget enough for the detector to be able distinguish the small intensity increase due to ballistic photons. Again, it is not always possible to increase the photon budget by means of indefinitely increasing the source intensity or the exposure time, due to constraints like real-time imaging, eye-safe source power, source power consumption or simply when the

Table 4.1: Expressions of intensity, modulation index and relative phase for the ballistic and diffuse components of the detected light.

Detection	Ballistic photons	Diffuse photons	Ratio (Ballistic/Diffuse)
Relative phase ($\Delta\phi$)	0	$R_\delta\sqrt{2(q^2-1)}$	–
Modulation index	$m_B = M$	$m_D = Me^{-R_\delta(q-1)}$	$\beta = e^{R_\delta(q-1)}$
Intensity	$I_B = \xi\frac{d\Omega}{\Omega}P_0\ e^{-R}$	$I_D = \xi\frac{d\Omega}{4\pi}3P_0R_*\ e^{-R_\delta}$	$\alpha = \Omega'\frac{e^{R_\delta - R}}{3R_*}$

ballistic photon counts are so small that the source intensity has to be increased by many orders of magnitude. As a result, various strategies mentioned in the introduction section use physical properties of light, other than intensity, to discriminate ballistic photons.
The diffuse photons in an intensity modulation scheme have been shown to propagate as photon density waves, and their modulation index and phase are physically affected by the scattering parameters of the intervening medium. This effect, which was established in the previous chapter, can be exploited to attain physical discrimination of ballistic photons that retain the original information of the source like modulation index and phase. In the remainder of this section, the efficiency of attaining ballistic filtering, given the noise model of a quadrature demodulation scheme, is derived.

4.3.1 Information metric for ballistic filtering efficiency

Let us first recall the expressions of the intensity, phase and modulation index of ballistic and diffuse light components through the Table 4.1. As established in the previous chapters, the diffuse light gradually loses the information about the source while the ballistic light retains it. The received amplitude and phase data at each pixel can then be used to estimate certain parameters of the source. Intuitively, if the estimation is carried out by taking the pixels that only receive diffuse light, one would obtain lower precision of estimation as compared to the case where the estimation is carried out over pixels that receive ballistic light over the diffuse light. Following this argument, a metric of ballistic filtering efficiency can be defined as the ratio of Fisher information content for estimation of the modulation index M carried in data contained in pixels $\mathcal{B}\oplus\mathcal{D}$ to that contained in $\mathcal{D}$. As a result, a gain in ballistic filtering efficiency can be defined as $\mathcal{G}_{bf} = \mathcal{F}^M_{\mathcal{B}\oplus\mathcal{D}}/\mathcal{F}^M_{\mathcal{D}}$.
Since, $M = 2A/I_0$, the FI in estimation of M can be calculated by recalling that for reparameterization $\eta' \to \eta$, $\mathcal{F}(\eta) = \mathcal{F}(\eta')(\partial\eta'/\partial\eta)^2$, leading to the gain in ballistic filtering efficiency

$$\mathcal{G}_{bf} = \frac{\frac{1}{\Lambda^2_{\mathcal{B}\oplus\mathcal{D}}}\left(\frac{\partial A_{\mathcal{B}\oplus\mathcal{D}}}{\partial M}\right)^2}{\frac{1}{\Lambda^2_{\mathcal{D}}}\left(\frac{\partial A_{\mathcal{D}}}{\partial M}\right)^2}, \tag{4.3}$$

where, $\Lambda^2_{\mathcal{D}} = I_D/2$, $\Lambda^2_{\mathcal{B}\oplus\mathcal{D}} = I_{\mathcal{B}\oplus\mathcal{D}}/2$, $A_{\mathcal{D}} = m_D I_D/2$ is the amplitude detected at pixels in region $\mathcal{D}$. The amplitude detected at the pixel $\mathcal{B}\oplus\mathcal{D}$ can be calculated by adding the instantaneous intensity received at those pixels and integrating over integer number of time periods of oscillation. The calculation is shown in Appendix C.6 and turns out to be

$A_{\mathcal{B}\oplus\mathcal{D}} = (m_D I_D/2)\sqrt{1+\alpha^2\beta^2+2\alpha\beta\ cos\left[\Delta\phi\right]}$. Recalling that, α is the ratio between mean ballistic light intensity and mean diffused light intensity and β is the ratio of modulation index retained by the ballistic light to modulation index retained by diffuse light, the expression for the gain $\mathcal{G}_{bf}$ can be written as

$$\mathcal{G}_{bf} = \frac{1}{1+\alpha}\left(1+\alpha^2\beta^2+2\alpha\beta\cos\Delta\phi\right) \tag{4.4}$$

The above expression is a general expression for quantifying ballistic filtering gain and depends on the additional phase due to the diffused light ($\Delta\phi = \phi_D - \phi_B$) and the ratios α and β. The quantities can be either obtained from rigorous simulation of the radiative transport equation using Monte-Carlo methods or analytically derived using a model for ballistic and diffuse light. In the analytical model developed in this and previous chapter, the ratios α and β are obtained by using Beer's law and diffusion theory as described in the previous chapter. Using the expression for α provided in Table 4.1, the analytical expression of the gain then is derived as

$$\mathcal{G}_{bf} = \frac{1+\frac{\Omega'^2\ e^{\tau}\left(1+6\frac{R_*}{\Omega'}e^{-\tau/2}\ cos\left[\sqrt{-1+q^2}R_\delta\right]\right)}{9R_*^2}}{1+\alpha} \tag{4.5}$$

where the variable $\tau = 2(qR_\delta - R)$ is introduced for the sake of conciseness and its physical meaning will be apparent in further sections.

4.3.2 Modulation frequency condition for ballistic filtering gain

The presence of q in both the exponential and cosine term in Eq. (4.5) makes the derivation of the unity gain condition difficult. For convenience, but without loss of generality, an isotropically emitting light source is considered for the analysis of the Eq. (4.5) by setting $\Omega' = 1$ (in the same notation as chapter 4). The Eq. (4.5) can be expanded out as a function of the normalized angular modulation frequency ($\omega/\mu c$), ratio of reduced scattering coefficient to absorption coefficient (σ/μ) and a normalized source detector distance $r\mu$. A contour plot of $ln\left[\mathcal{G}_{bf}\right]$ as a function of σ/μ and $\omega/\mu c$ with constant $r\mu = 2$ is shown in Fig. 4.3a (The conditions, $r\mu = 2$, corresponds to a situation where the detector is placed at a distance two times the absorption length $1/\mu$).
A detailed analysis of the figures shows that:

- The figure is roughly linearly divided into two halves by an oscillating contour of unity gain. Within this oscillating contour, which arises due to dependency of the phase of the diffuse density wave on the scattering parameters of the medium, the gain can be lower than unity. On the lower right side of the oscillating unity contour, i.e, for highly scattering media and low modulation frequencies, the gain remains only marginally greater than unity. The amplitude and oscillating frequency of the oscillating term depends on $r\mu$ which can also be inferred from the cosine term in Eq. (4.5).

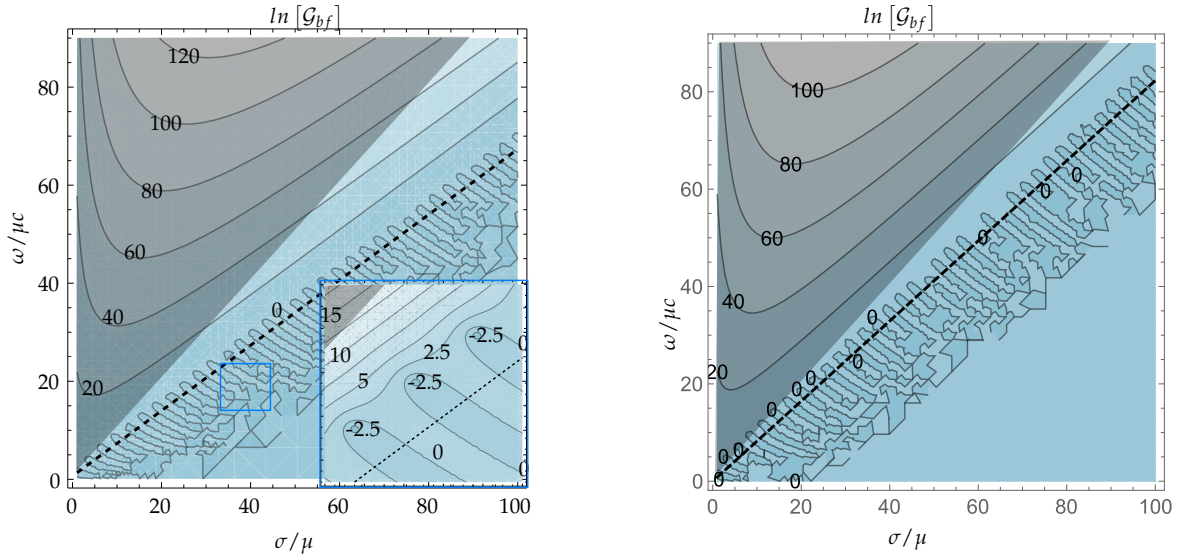

(a) (b)

Figure 4.3: (a) Contour plot of $ln\left[\mathcal{G}_{bf}\right]$ as a function of σ/μ and $\omega/\mu c$ for $r\mu = 2$ and isotropically scattering medium with $g = 0$. The minimum angular frequency condition to attain ballistic photon filtering is shown in black-dashed line and the shaded region indicates the region where diffusion approximation is not strictly valid. The inset shows the oscillating region near the transition boundary (b) Contour plot of $ln\left[\mathcal{G}_{bf}\right]$ as a function of σ/μ and $\omega/\mu c$ for $r\mu = 2$ and scattering medium with $g = 0.1$, showing that the minimum frequency is close to the limits of validity of diffusion equation.

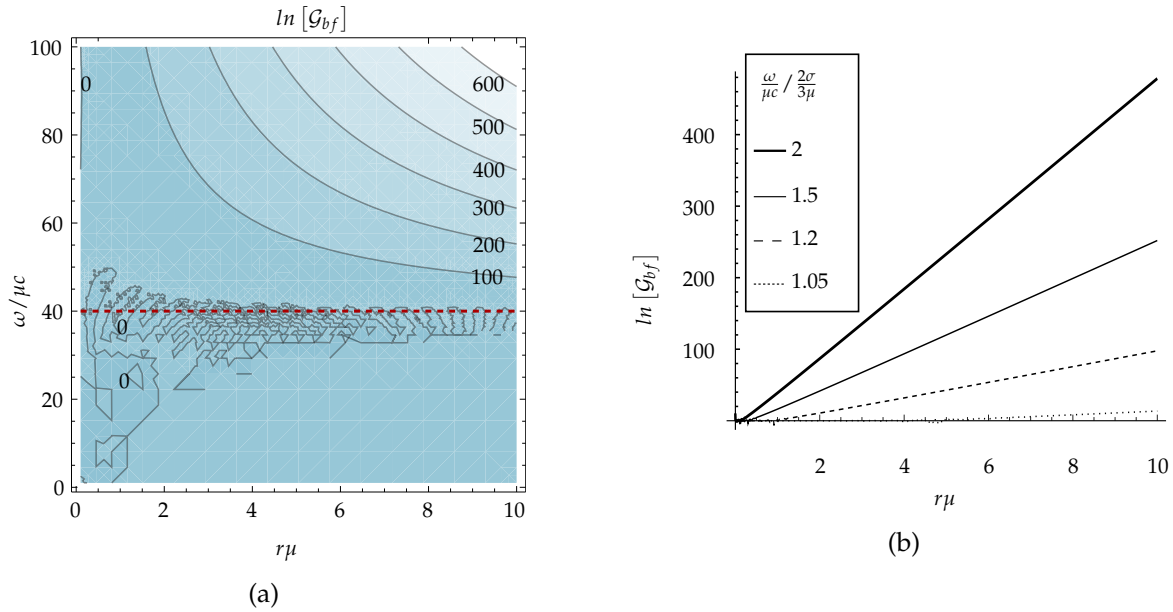

(a) (b)

Figure 4.4: (a) The contour plot of the ballistic filtering gain as a function of $\omega/\mu c$ and $r\mu$ for constant $\sigma/\mu = 60$. The black dotted line shows the minimum frequency condition $2\sigma/3 = 40$. (b) The exponential increase of the gain with increase in $r\mu$ is shown through the linear plot.

- The gain exponentially increases when the angular frequencies lie above the roughly linear oscillating contour. This indicates that there exists a minimum frequency of modulation above which a significant gain in ballistic photon filtering can be expected.

- The gain increases with the increase in $r\mu$ (and Ω') as can be inferred from the analytical expression for the gain, but they do not significantly affect the condition on modulation frequency for attaining significant gain. The dependency of the gain on $r\mu$ is shown in Fig. 4.4, where the gain is plotted for a constant $\sigma/\mu = 60$ (for highly scattering medium) as contour plot with respect to $r\mu$ and $\omega/\mu c$ in Fig. 4.4a and as a log plot of the gain, for various multiples of the minimum derived frequency. It may be inferred that the gain increases roughly exponentially, with $r\mu$, however, it is essential to keep in mind that for large values of the $r\mu$, the number of detected photon may be low due to absorption. The dependency on Ω' confirms that a highly directional source may provide better ballistic filtering efficiency. Similarly, for a fixed detection field of view, a large source-detector distance may also allow better spatial filtering of the directional ballistic light from the isotropic diffuse light, which is highly interesting for landing assistance applications.

- The minimum modulation frequency for significant ballistic photon filtering can be approximately derived by noting that the gain expression exponentially increases and the amplitude of the cosine term exponentially decreases when $\tau > 0$. Rewriting this condition reveals the condition on the angular frequency through q as $qR_\delta > R$. Interestingly, such a condition suggest that qR_δ behaves as a frequency dependent attenuation for the diffuse light in the case of intensity modulated light and that a significant ballistic filtering can be achieved when the attenuation of the diffuse light is greater than the attenuation of the ballistic light.

- The above inequality, $q > R/R_\delta = \left(1 + \sigma/\mu(1-g)\right)/\sqrt{3(1+\sigma/\mu)}$, leads to a condition on the minimum operating frequency to attain ballistic filtering. Recalling that the diffusion equation remains valid when $\sigma/\mu \gg 1$, the expression for minimum angular frequency can be written as

$$\frac{\omega}{c} > \frac{2}{3}\frac{\sigma}{(1-g)^2} \tag{4.6}$$

  As a result, for a highly scattering medium, the minimum frequency required to attain significant ballistic filtering is largely dependent on the reduced scattering coefficient and not on the absorption coefficient, μ, or the source-detector distance, r.

- For the analysis to be valid, the anisotropy factor g cannot be arbitrarily high. An increase in g increases the minimum required frequency, meanwhile, the diffusion equation is valid when the angular frequency is limited by the transport mean free path time l_*/c, i.e., $\omega < (\mu + \sigma)c$. Using Eq. (4.6) and the limit of validity, it is easy to check that $g < 1 - \sqrt{2/3} = 0.1835$. The contours of the gain for $g = 0.1$ is

plotted in Fig. 4.3b and shows that the minimum frequency contour is close to the limits of validity of the diffusion equation, emphasizing that the analysis is valid for highly scattering and nearly isotropically scattering medium. But nonetheless, such a simple rule on modulation frequency can be analytically derived.

The condition on modulation frequency for attaining ballistic filtering given in Eq. (4.6), is plotted as black dashed line on the contour maps in Fig. 4.3 and seems to provide a simple and well-approximated condition for attaining significant ballistic filtering. As a result, Eq. (4.6) can be considered a simple rule of thumb for achieving ballistic filtering in the context of intensity modulation and quadrature demodulation scheme. It must be noted that Ω' and $r\mu$ are set as constants in Fig. 4.3a) as they only affect the value of gain but do not change the condition for efficient ballistic filtering.

The above derived condition may be refined by a finer approximation for the minimum frequency that can be derived by allowing the amplitude of the cosine term in the gain expression to be much smaller than unity, i.e. $6R_* \; exp\left[R - qR_\delta\right] < 1$. This condition leads to an offset to the previous condition as $q > R/R_\delta + \; ln\left[6R_*\right]/R_\delta$. The effect of the additional offset term is small but can provide insight into the influence of the source-detector distance r on the condition for attaining ballistic filtering. Noting that the function $ln\left[x\right]/x > 1/x$ for $x \gg e$, a close approximation can be made to obtain a condition $\omega/c > (2/3)\sigma + 4/r$ that depends on r. Thus, r provides an inversely proportional offset for the minimum angular frequency. The above simplifications provide simple rules of choosing a minimum modulation frequency to attain ballistic filtering, however, in real life applications where precision is of importance, the precise solutions may be used to calculate the operating frequency.

Identification of this minimum modulation frequency for ballistic filtering is important from a practical point of view as it is easier to design electronic or electro-optic devices that work at low modulation and demodulation frequencies. The expression derived above can also serve conversely to provide the range of visibilities that can be handled by a ballistic filtering device working at any fixed modulation-demodulation frequency.

4.3.3 Maximum expectable gain

The above analysis takes into account only the photon noise to provide minimum operating frequency to attain gain in efficiency of filtering ballistic photons from diffuse photons. The gain values derived above are clearly unrealistic because all other limitations of detection procedure are ignored. In a realistic scenario, the detection process may introduce further detector noise and the detection may be limited by the detector dynamics. However, it is still of interest to analyze the evolution of the maximum expectable gain in such a detection scheme, considering it as an upper limit on gain.

In highly scattering media, where fewer ballistic photons are received at the detector end, then $\alpha \ll 1$ and the gain term can be simplified into

$$\mathcal{G}_{bf_{max}} \sim 1 + \frac{\Omega'}{9R_*^2} e^{\tau}, \tag{4.7}$$

where τ appears to be the exponent of the asymptotic gain. The expression of such an exponent is given by

$$\tau = 2r\mu\Big[q\sqrt{3(1+\frac{\sigma}{\mu})} - \big(1+\frac{\sigma}{\mu(1-g)}\big)\Big]. \tag{4.8}$$

The above expression fairly retrieves the gain values $ln\left[\mathcal{G}_{bf}\right]$ plotted in Fig. 4.3a in high gain regions. As noted above, the value of the maximum expectable gain depends on ω and σ but also on r and μ. As noted before, the gain values increase linearly with Ω' and exponential increase may be observed with increase in the modulation frequency. Nearly exponential increase may also be observed with increase in r and the absorption coefficient μ. Presumably, the gain may only be limited by the detector's noise properties, dynamics and the available photon budget.

4.3.4 Limitations and validity of the diffusion approximation

It is of importance to keep in mind the limitations of the diffusion equation in the above analysis and the one that follows in further sections. The diffusion approximation is valid for highly scattering medium, where the reduced scattering coefficient is greater than the absorption coefficient and when the detector is placed further than one transport mean free path from the source. The source and detector are placed within the medium far from any boundaries. The diffusion equation also breaks down for very high modulation frequencies, where the photon density waves arrive faster than they diffuse within the time scales of the transport mean free time (l_*/c). This validity condition that was mentioned in the previous chapter reads as $\omega < c(\mu + \sigma)$.

4.3.5 Typical experimental conditions and predictions

Let us apply the prediction of the above theoretical formulation to some practical situations. Ballistic filtering may have applications in the field of transport safety, where imaging of beacons of light through fog may provide aide to an aircraft pilot or driver on the road. It may have application in automated navigation as well. Currently, there are time-of-flight (ToF) cameras that can demodulate a modulated signal at a maximum of 40 MHz [108]. The ToF cameras will be briefly reviewed in the next chapter. Using 10 MHz as a benchmark, according to the above theory, it is possible to attain ballistic filtering when reduced scattering length is greater than 3.2 m, for effective refractive index $n \sim 1$ and remains valid when the absorption length is much greater than 32 m. These numbers remain valid for near infrared light where the absorption coefficient of water vapor can be of the order of 0.02 m^{-1}. Thus, the scattering length is close to the transport mean free path l_*. This clearly, indicates that ballistic photon imaging may be used in navigation situation in degraded weather conditions, especially for airplane landing and taxiing. When dealing with imaging through degraded weather, the visibility is quantified using Koschmieder visibility formula that defines visibility as $V = 3.9 * l_*$ [109, 110]. With the above calculations, ballistic filtering can be obtained using a 10 MHz modulation when the visibility

$V > 12.5$ m. To put this into perspective, a visibility value of $V < 100$ m is considered as no visibility when reported during bad weather conditions [111]. Therefore, an intensity modulated imaging scheme can prove to be very effective when used as a means of attaining vision though fog. In light of these calculation, this thesis also deals with developing a full-field demodulation camera that is designed to be cost effective, modular and portable. This will be discussed in detail in the next chapter.
Similarly, for tissues where the absorption coefficient is typically $0.05\ \mathrm{cm}^{-1}$ and a scattering coefficient $5\ \mathrm{cm}^{-1}$, the minimum frequency required for ballistic photon filtering through a thick sample will be of the order of 100 GHz. This frequency lies 3 order of magnitude above the frequencies used for diffuse optical tomography in the present day. But as we will see in chapter 6, demodulation at such frequencies can indeed be envisaged with novel imaging systems.

4.4 Maximum precision in estimation of scattering parameters

In biomedical imaging, the absorption and scattering inhomogeneities in tissues can provide valuable information to aide in medical diagnostics. Since the transport properties of modulated diffuse light is dependent on the scattering parameters of the intervening medium as recalled in chapter 4, this opens an opportunity to estimate the scattering parameters of the tissue using a forward model provided by the analytical expression via the diffusion equation. For example, simple expressions for the estimation of the dimensionless parameters R_* and R_δ introduced in the previous chapter can be obtained by inverting the relation (given in Table 4.1) between modulation index and phase to the parameters R_δ and q as

$$R_\delta = \frac{\Delta\phi^2 - 2\ ln\left[\beta\right]^2}{4\ ln\left[\beta\right]}, \tag{4.9a}$$

$$q = \frac{\Delta\phi^2 + 2\ ln\left[\beta\right]^2}{\Delta\phi^2 - 2\ ln\left[\beta\right]^2}. \tag{4.9b}$$

However, noise due to detector and photons themselves may significantly affect such an estimation procedure. Therefore, the information theoretical formalism developed in the previous sections is used again to gain insight into the maximum achievable precision in estimation of scattering parameters using a quadrature demodulation scheme.

4.4.1 Precision in amplitude and phase detection

In biomedical applications, the amplitude and the phase data obtained from a set of detectors is used to estimate the scattering properties of the tissues. The quality of amplitude and phase data affect the performance of estimation. In this regard, previously reported studies have explored the effect of modulation index on the SNR of detected amplitude and phase [112] in experiments and simulations. In these studies, the effect of modulation index were limited to certain range of absorption and scattering coefficient and they fail to

provide a general analytical expression for enhancement of signal quality. Using the formulation developed in the preceding sections it is possible to first analyze the evolution of quality of detected signal with respect to the change in modulation frequency. After which we can move forward to determining the precision in estimation of scattering parameters from diffused light in an intensity modulation scheme.

The Fisher information for the estimation of the amplitude and phase was derived in Eq. (4.2) and it provides the inverse of minimum expectable variance in estimation of parameters from data. From this minimum-variance bound, best expectable SNR for amplitude and phase can be derived as

$$SNR^D_{Amp} = \sqrt{\frac{A^2}{[\mathcal{F}(A)]^{-1}}} = \sqrt{\frac{A^2}{\Lambda_D^2}} = \sqrt{\frac{3}{2}}\sqrt{M^2 S_0 R_* e^{(1-2q)R_\delta}}, \tag{4.10}$$

$$SNR^D_{Ph} = \sqrt{\frac{\Delta\phi^2}{[\mathcal{F}(\Delta\phi)]^{-1}}} = \sqrt{\Delta\phi^2 \frac{A^2}{\Lambda_D^2}} = \sqrt{\frac{3}{2}}\sqrt{M^2 S_0 R_* R_\delta^2 \left(q^2-1\right) e^{(1-2q)R_\delta}}, \tag{4.11}$$

with $\mathcal{F}(A) = [\mathcal{F}(\theta')]_{1,1}$ and $\mathcal{F}(\Delta\phi) = [\mathcal{F}(\theta')]_{2,2}$. The SNR of both amplitude and phase depend on q and hence on the angular frequency of modulation ω. In case of biomedical imaging where the SNR of the signal is considered to affect the estimation of the scattering parameters of the tissues, it is important to study the evolution of the quality of signal obtained. For this purpose, the frequency dependence of the expected SNRs of amplitude and phase of Eq. (4.10) and Eq. (4.11) are plotted in Fig. 4.5 and Fig. 4.6 for various values of μ and σ. The plotted SNRs are normalized to $\sqrt{M^2 S_0/2}$ to show the frequency dependence by plotting against $\omega/\mu c$. The quantity $\sqrt{M^2 S_0/2}$ can be interpreted as the signal-to-noise ratio of the light from the source in absence of any intervening medium. [1]

The expected SNR of the amplitude that is plotted in decibels shows a cutoff. It can be analytically shown that the cutoff frequency $\omega_{cut} = (\mu c/2)(1+(1/R_\delta))^2$ and remains close to $(\mu c/2)$ when the effective attenuation of the diffuse light increases due to increase in source-detector distance, absorption or scattering.

Similarly, the expected SNR of phase and its dependency on the modulation frequency is plotted in Fig. 4.6. Interestingly, the SNR has a peak between a band of frequency depending upon the scattering parameters of the medium. This suggests that there lies an optimum modulation frequency band where the SNR of the detected phase is maximum, potentially leading to better reconstruction of the absorption and scattering maps of tissues. In biomedical applications, the modulation angular frequencies used are chosen close to absorption rate μc. This is usually justified by citing the fact that for smaller frequencies the change in phase due to diffusion is too small to be detected while at much higher frequencies, the change in phase becomes comparatively insensitive to change in frequency, thereby not bringing any further improvement in the estimation of the scattering parameters of the medium. Such intuitive arguments try to take into account a few

[1] It may be noted that in Fig. 4.5, the normalized SNR is shown to be greater than unity in some cases, this arises due to the factor $\sqrt{3}$ in Eq. (4.10) and Eq. (4.11), due to the three dimensional isotropic geometry considered. Of course, the greater than unity, normalized SNR, is due to the nature of normalization with $\sqrt{M^2 S_0/2}$.

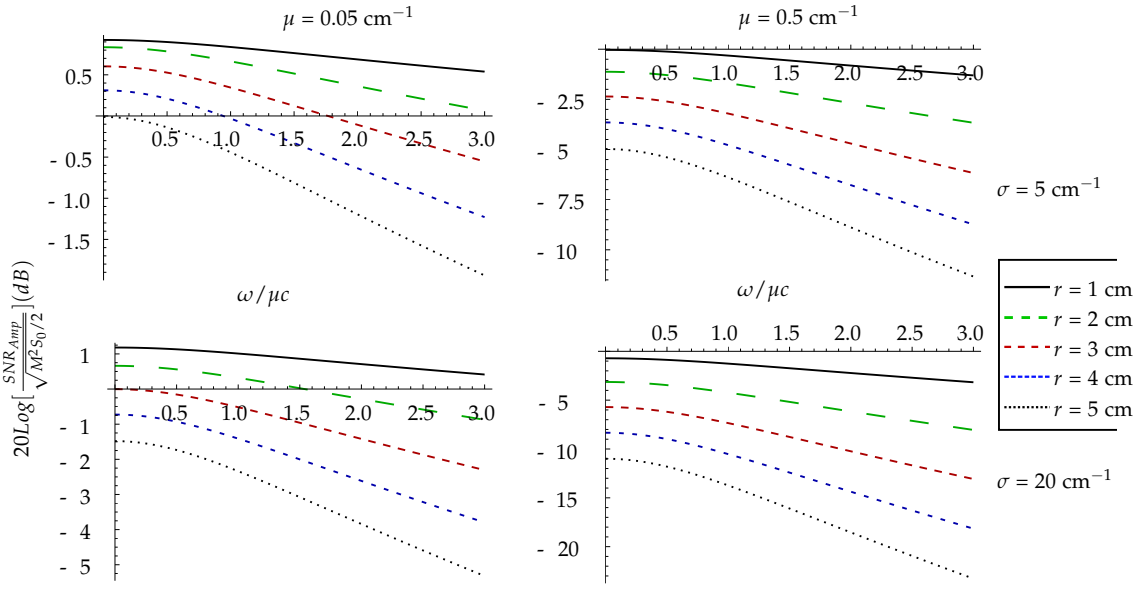

Figure 4.5: The theoretical evolution of normalized SNR (dB) of detected amplitude as a function of the modulation frequency for various values or absorption coefficient (μ) and reduced scattering coefficient (σ).

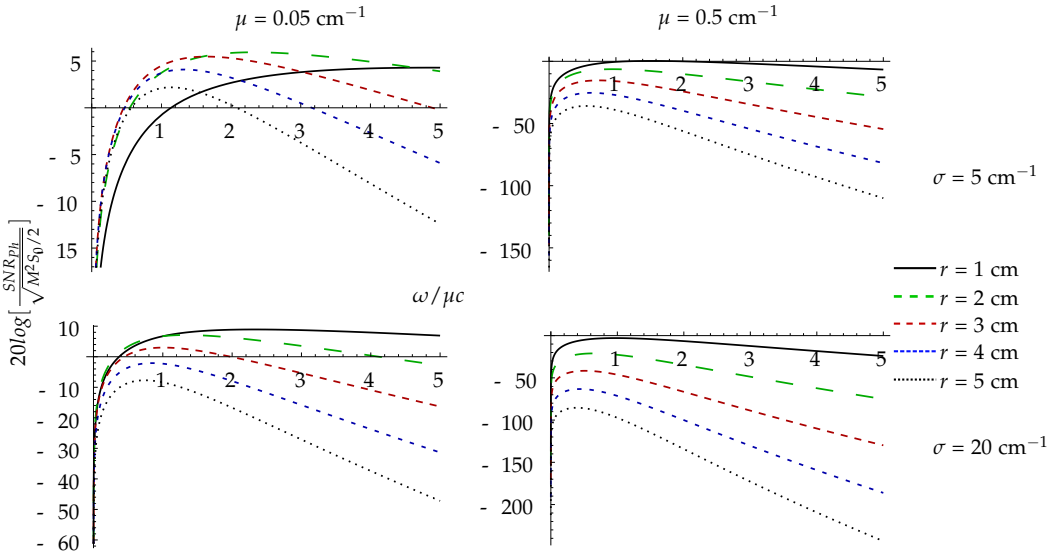

Figure 4.6: The theoretical evolution of normalized SNR (dB) of detected phase as a function of the modulation frequency for various values or absorption coefficient (μ) and reduced scattering coefficient (σ).

competing factors to obtain an operating frequency but they are not exhaustive. However, some previous studies present existence of an optimal frequency of modulation for which the SNR of the amplitude and phase signal is maximum [112]. These findings remain qualitative in agreement with the theoretical ones presented in this section.
To further compare the previous results with the theoretical predictions presented here, the plots from [112] are presented alongside the predictions of our theoretical model in Fig. 4.7 and Fig. 4.8. In these figures the SNR values are normalized to the SNR obtained at 100MHz.
The qualitative agreement of the theoretical results with previously reported observation validates the model. To study the existence of an optimal frequency for the estimation of the scattering parameters, a rigorous information theoretical analysis is performed in the following sections by extending the noise model derived in the previous sections.

4.4.2 Reparametrization of noise model using diffusion theory

The FIM in estimation of the amplitude and phase was derived from the noise model developed in section 4.1. Ballistic filtering efficiency was then quantified by calculating the Fisher Information in estimation of the modulation index M. The noise model is dependent on the parameter vector $\boldsymbol{\theta'} = [A, \Delta\phi, \Lambda^2]$ was established to be a function of scattering parameters through the diffusion equation for photon transport. Considering the effect of diffused light only, one obtains the FIM with respect to the new set of parameters $\boldsymbol{\theta} = [M, R_\delta, R_*]$. The FIM provides means to deduce insight into the precision of estimation of each respective parameters and their interdependency on other parameters. The FIM with respect to the new parameters can be obtained in a straightforward way from the FIM presented in Eq. (4.12) through the Jacobian matrix, $J_{\mathcal{D}}$, of the transformation $\boldsymbol{\theta'} \rightarrow \boldsymbol{\theta}$ in the presence of diffuse light only, as denoted by the suffix $\mathcal{D}$. The Jacobian matrix is calculated such that the i^{th}, j^{th} component of the matrix is $\left[J_{\mathcal{D}}\right]_{i,j} = \frac{\partial\theta'_i}{\partial\theta_j}$. Given the modulation index, phase and the intensity expected for diffuse light from the diffusion model (summarized in Table 4.1), the amplitude, phase and variance can be written as $A_D = m_D I_D/2$, $\Delta\phi = R_\delta\sqrt{2(q^2-1)}$ and $\Lambda_D^2 = I_D/2 = 3S_0R_*\ e^{-R_\delta}/2$, where $S_0 = \xi d\Omega P_0/4\pi$. The Jacobian is then calculated to obtain the FIM with respect to parameter vector $\boldsymbol{\theta}$ using the transformation $\mathcal{F}_{\mathcal{D}}(\boldsymbol{\theta}) = J_{\mathcal{D}}^T\mathcal{F}(\boldsymbol{\theta'})J_{\mathcal{D}}$. The Jacobian matrix is provided in the Appendix C.4 and the resulting Fisher information matrix (FIM) reads

$$\mathcal{F}(\boldsymbol{\theta}) = \begin{bmatrix} \frac{3}{2}e^{(1-2q)R_\delta}R_*S_0 & -\frac{3}{2}e^{(1-2q)R_\delta}MqR_*S_0 & \frac{3}{2}e^{(1-2q)R_\delta}MS_0 \\ -\frac{3}{2}e^{(1-2q)R_\delta}MqR_*S_0 & 1+\frac{3}{2}e^{(1-2q)R_\delta}M^2\left(-1+2q^2\right)R_*S_0 & -\frac{1}{R_*}-\frac{3}{2}e^{(1-2q)R_\delta}M^2qS_0 \\ \frac{3}{2}e^{(1-2q)R_\delta}MS_0 & -\frac{1}{R_*}-\frac{3}{2}e^{(1-2q)R_\delta}M^2qS_0 & \frac{2+3e^{(1-2q)R_\delta}M^2R_*S_0}{2R_*^2} \end{bmatrix}. \tag{4.12}$$

4.4.3 Lower bound on estimation precision

The above re-parameterization allows us to study the variance bound in estimation of $\boldsymbol{\theta}$ with respect to the frequency of modulation represented by the variable q. According to

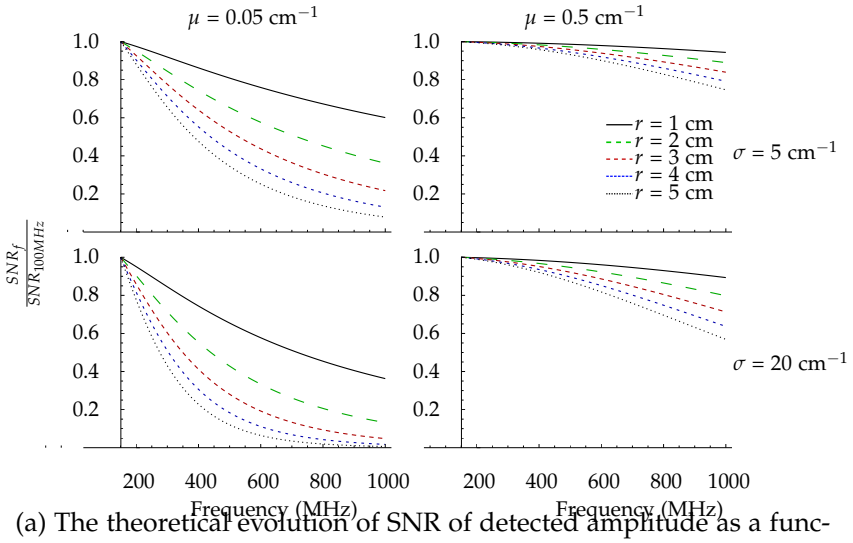

(a) The theoretical evolution of SNR of detected amplitude as a function of the modulation frequency normalized for SNR value of amplitude at 100 MHz, for various values or absorption coefficient (μ) and reduced scattering coefficient (σ).

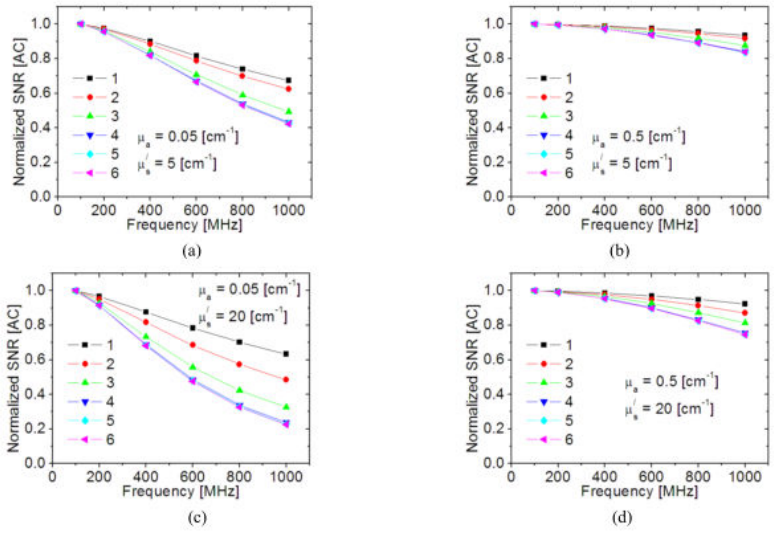

Fig. 2. Normalized SNR values for the AC signal as a function of source-modulation frequency for six different source-detector pairs (see Fig. 1 for reference). The 4 graphs show 4 sets of optical properties. The absorption coefficient μ_a increases with a column, while the reduced scattering coefficient μ_s' increases with a row.

(b) The figure, reported by A.H. Hielscher et. al in [112] (reproduced here with due permission), shows the evolution of SNR of phase as a function of frequency obtained using Monte-Carlo simulations.

Figure 4.7

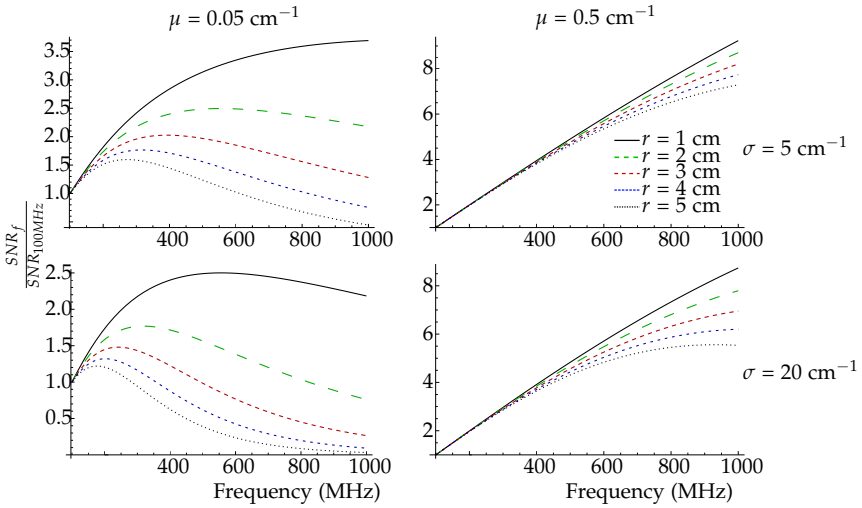

(a) The theoretical evolution of SNR of detected amplitude as a function of the modulation frequency normalized for SNR value of amplitude at 100 MHz, for various values or absorption coefficient (μ) and reduced scattering coefficient (σ).

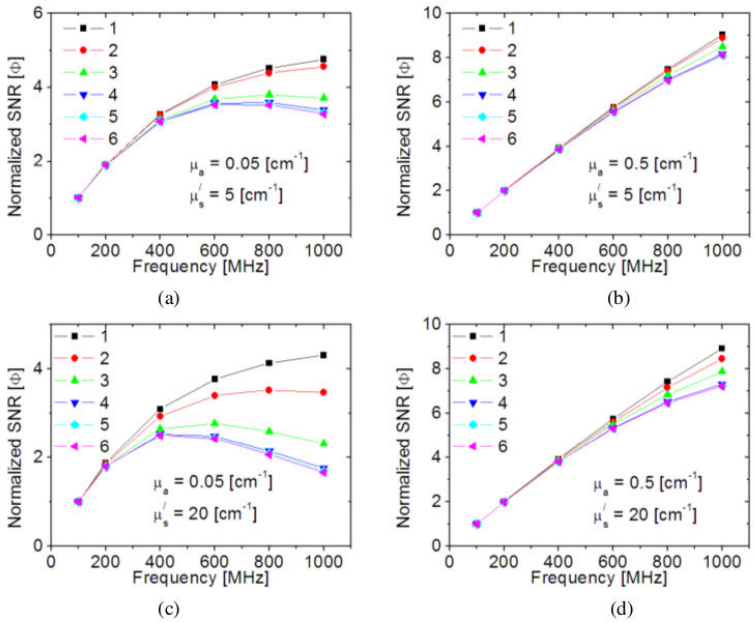

Fig. 3. Normalized SNR of phase shifts at various frequencies. The absorption coefficient μ_a goes higher in the column direction, while the reduced scattering coefficient μ_s' goes higher in the row direction.

(b) The figure, reported by A.H. Hielscher et. al in [112] (reproduced here with due permission), shows the evolution of SNR of phase as a function of frequency obtained using Monte-Carlo simulations.

Figure 4.8

the Cramer-Rao theorem, for any unbiased estimator $\hat{\boldsymbol{\theta}}$ of the parameter vector $\boldsymbol{\theta}$, one has $w\left\langle(\hat{\boldsymbol{\theta}}-\left\langle\hat{\boldsymbol{\theta}}\right\rangle)(\hat{\boldsymbol{\theta}}-\left\langle\hat{\boldsymbol{\theta}}\right\rangle)^T\right\rangle w^T \geq w\mathcal{F}(\boldsymbol{\theta})^{-1}w^T$. Thus, the Cramer-Rao bound (CRB) provides a minimum covariance bound that can be reached by an efficient estimation technique. Generically, it is not guaranteed that such an efficient estimator always exists, however, Maximum Likelihood (ML) estimators are known to be asymptotically unbiased and efficient for large collection of data [82].

Let us now derive and analyze the lower covariance bound to reveal some simple conclusions and rules for the estimation problem. The lower bound can be calculated by inverting the FIM $\mathcal{F}_{\mathcal{D}}(\boldsymbol{\theta})$ as $CRB_{\mathcal{D}}(\boldsymbol{\theta}) = \mathcal{F}_{\mathcal{D}}(\boldsymbol{\theta})^{-1}$

$$CRB_{\mathcal{D}}(\boldsymbol{\theta}) = \begin{pmatrix} M^2 + \frac{4e^{(-1+2q)R_\delta}q}{3(1+q)R_*S_0} & \frac{2e^{(-1+2q)R_\delta}}{3M(1+q)R_*S_0} & -MR_* + \frac{2e^{(-1+2q)R_\delta}}{3M(1+q)S_0} \\ \frac{2e^{(-1+2q)R_\delta}}{3M(1+q)R_*S_0} & \frac{2e^{(-1+2q)R_\delta}}{3M^2(-1+q^2)R_*S_0} & \frac{2e^{(-1+2q)R_\delta}}{3M^2(-1+q^2)S_0} \\ -MR_* + \frac{2e^{(-1+2q)R_\delta}}{3M(1+q)S_0} & \frac{2e^{(-1+2q)R_\delta}}{3M^2(-1+q^2)S_0} & R_*^2 + \frac{2e^{(-1+2q)R_\delta}R_*}{3M^2(-1+q^2)S_0} \end{pmatrix} \tag{4.13}$$

and the determinant of the CRB (consequently, the determinant of FIM) which provides the total information content in a given data for the joint estimation of $[M, R_\delta, R_*]$, is calculated to be

$$det\left[CRB_{\mathcal{D}}(\boldsymbol{\theta})\right] = \frac{4}{9}\frac{e^{2(2q-1)R_\delta}}{M^2S_0^2\left(q^2-1\right)} \tag{4.14}$$

It is clearly seen that the variances and covariance bounds are functions of the frequency of modulation (represented by q). The minimum variance of R_* ($[CRB_{\mathcal{D}}(\boldsymbol{\theta})]_{3,3}$) increases with its mean value and has an additional frequency dependent term, while the variance of R_δ ($[CRB_{\mathcal{D}}(\boldsymbol{\theta})]_{2,2}$) decreases with the R_*. The estimation variance of the parameters R_δ and R_* share the same functional dependence on the modulation frequency, through $e^{(-1+2q)R_\delta}/(-1+q^2)$. A simple calculus shows that this function reaches a minimum at $q_{opt} = \left(1+\sqrt{1+4R_\delta^2}\right)/2R_\delta$, indicating the existence of an optimal angular frequency ω_{opt} around which the parameters can be estimated with minimum variance.

This optimal angular frequency depends only on R_δ and is given by the following expression

$$\frac{\omega_{opt}}{\mu c} = \frac{\sqrt{2}\left[1+\left[1+4R_\delta^2\right]^{\frac{1}{2}}+R_\delta^2\left(3+\left[1+4R_\delta^2\right]^{\frac{1}{2}}\right)\right]^{\frac{1}{2}}}{R_\delta^2}, \tag{4.15}$$

whose evolution is plotted in Fig. 4.9.a and the reference angular frequency μc is denoted as ω_a. In the next subsection the properties and evolution of the optimal frequency ω_{opt} obtained for the estimation of scattering parameters is analyzed.

Alternatively, when all the parameters are to be estimated simultaneously, it is convenient to minimize the determinant of the CRB given as shown in Eq. (4.14). The generalized CRB is also a function of the modulation frequency with a slightly different functional form compared to the functional dependencies of marginal variances. Minimizing this term with respect to q provides another optimal frequency for the joint estimation of the parameters M, R_* and R_δ. It can be shown that the optimal frequencies in both cases are close to each other, both quantitatively and qualitatively. However, in the next section the

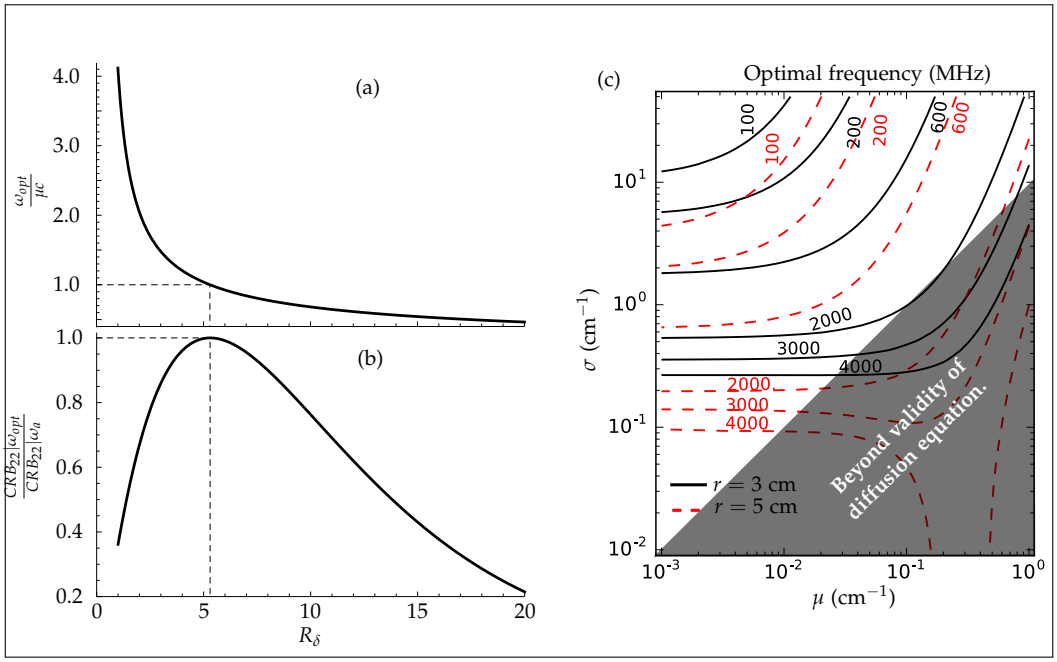

Figure 4.9: (a) Ratio of the optimal frequency ω_{opt} to commonly used operating frequency $\omega_a = \mu c$ as a function of the normalized optical attenuation R_δ. (b) Loss in precision in the estimation of R_δ using modulation angular frequency ω_a as opposed to ω_{opt} as a function of R_δ. (c) Contours of optimal frequency of modulation as a function of absorption coefficient μ and reduced scattering coefficient σ and the detection distance r for an intervening medium having refractive index 1. The frequencies can be scaled down by a factor of n for a medium with refractive index n.

variance maximizing optimal frequency is analyzed and its properties and evolution are studied.

4.4.4 Optimal operating frequency

The expression of the variance-minimizing optimal angular frequency ω_{opt} has a non-trivial form that depends on the normalized optical attenuation $R_\delta = r/\delta$, which represents the inverse of an overall visibility factor for the diffuse photons. The existence of an optimal operating point has interesting consequences, especially in the context of diffused optical imaging, where the SNR of the images is an important limiting factor. To compare the losses incurred by choosing a non-optimal operating frequency, a standard frequency used in biomedical applications, $\omega_a/\mu c = 1$, is considered [97].

A comparison of the performances of estimation provided by the two frequencies, ω_{opt} and ω_a is attained by taking the ratio of the variances in the estimation of R_δ obtained when using ω_{opt} against ω_a. The ratio is plotted in Fig. 4.9.b as function of R_δ. The figure provides a quantitative study of the loss in precision in using ω_a as opposed to using ω_{opt}. The precision of estimation are equal only when $R_\delta = 5.3$, at which point $\omega_{opt} = \omega_a$, as indicated by the dashed lines in the figures. For example, taking typical

values of scattering parameters valid in tissues, such that $\mu = 0.1$ cm^{-1} and $\sigma = 10$ cm^{-1}, the two operating points are the same only for a detector placed as distance of 3 cm. As illustrated in Fig. 4.9.a, for a detection carried out at a distance higher than 3 cm, the optimal frequency is in fact smaller which may reduce the cost and complexity of the electronics required at high frequencies while providing better results. On the other hand, if the detection is carried out closer than 3 cm, higher operating frequencies are suggested as compared to standard operational frequency.

Similarly, since R_δ is a function of σ, μ and r, the dependency of the optimal modulation frequency on these three parameters can be analyzed from the contour plot shown in Fig. 4.9.c. Firstly, for fixed values of σ and μ, the optimal operating frequency decreases with increase in r. Secondly, for fixed values of r and μ, the optimal frequency is seen to decrease with the increase in σ. The above two dependencies can be interpreted by noticing that longer distance of travel or higher scattering coefficient would allow for a larger amount of multiple scattering events leading to greater modification of the phase and the modulation index of the diffused light, for a given coefficient μ.

Finally, the optimal frequency is seen to increase with the increase in μ, for fixed values of r and σ. An increase in absorption would lead to smaller amplitude of modulation at the detector. To compensate for this loss that occurs at a rate of μc, the photon density arrival rate should be increased leading to a increase in optimal frequency of operation. It can also be noticed that the change of optimal operating frequency is more sensitive to a change in absorption coefficient than to a change in σ or r. The above conclusions can also be easily obtained by noticing that equation Eq. (4.15) can be approximated to $\omega_{opt} = c[r\sqrt{3(1+\sigma/\mu)}]^{-1}$, for sufficiently large value of R_δ. It is interesting to notice at this level that the above analytical deductions about the existence of an optimal operating frequency and its evolution with scattering parameters are qualitatively in very good agreement with previous numerical simulations and experimental studies presented in [112, 113, 93] which was also compared directly in section Fig. 4.7 and Fig. 4.8.

More generally, the above results show that the analysis based on a diffusion model for the propagation of photons coupled with an information theoretical approach, makes it possible to account for several competing phenomena involved in light diffusion. For example, taking the modulation index as a parameter, the phase increases while the detected modulation index decreases with the increase in the modulation frequency with quite different functional dependencies. The interplay of these contribution to the detection allow for an optimum frequency that minimizes the variance of estimation. Moreover, the information theoretical analysis is able to provide the functional dependence of the optimal operating frequency with respect to properties of the medium under consideration and practical indications concerning the optimal experimental parameters for the estimation task considered. The conclusion obtained appears to be more specific than the usual rule of thumb used in similar experiments, as it reveals the optimal operating frequency and provides insight into the various competing phenomena that produce it.

4.5 Summary and conclusion

In this chapter a noise model for the quadrature detection scheme was derived and the analytical expression for precision in estimation of amplitude and phase was obtained through the FIM. The diffusion theory of transport of modulated light through turbid media was used to parametrize the noise model by the scattering parameters of the medium. The formulation was used to obtain performance metric and optimal operating points and for two application scenarios, namely, ballistic photon filtering and estimation of scattering parameters of a scattering medium.

In the case of ballistic photon imaging using intensity modulated light, we proposed to define a metric for ballistic filtering efficiency as the ratio of Fisher information for the estimation of the source modulation index calculated in pixels that receive both ballistic and diffused light to that of pixels that only receive diffuse light. It was shown that the effective attenuation of intensity modulated diffuse light was a function of the frequency of modulation as qR_δ and can be tuned by changing the modulation frequency and attain ballistic filtering. However, due to photon noise in quadrature detection schemes, a significant gain in ballistic photon filtering can be obtained only above a certain minimum modulation frequency. This minimum operating frequency was derived and appeared to be essentially a linear function of the scattering coefficient of the intervening medium only: it was shown that a significant gain in ballistic filtering can be expected when the angular frequency of modulation $\omega > 2\sigma c/3$. The theoretical expression of the expected gain at any frequency was also derived and its evolution with respect to physical parameters at hand was discussed.

In the case of estimation of scattering parameters using only diffused light, the evolution of the SNR of amplitude and phase of the detected modulated signal was derived and compared with previous experiments and simulations to reveal fair agreement. The Cramer-Rao lower bound on the estimation of scattering parameters was derived and was shown to reach a minimum at an optimal modulation frequency. The derived optimal frequency of modulation that achieves minimum variance of estimation depends on the optical penetration depth and the distance of propagation. The evolution of this optimal operating frequency was analytically shown to be increasing with higher absorption coefficient and decreasing with increase in distance of detection and/or the scattering coefficient of the medium. The loss in estimation precision incurred when using a non-optimal operating frequency was quantified. The derivation of the optimal operating frequency paves way for better design of diffuse optical imaging setups that are used in medical instruments.

In this approach, diffusion theory of photon transport and noise model of a quadrature demodulation scheme were tied together using information theoretical tools to provide minimum-variance operating points and derivation of expected gains by taking into account various competing phenomena in the system. The calculations indeed provides knowledge about physical limitations on photons detection in the modulation scheme considered, however, it must be noted that the analysis is valid within the applicability of the diffusion theory. The diffusion approximation breaks down at large angular modula-

tion frequencies close to $\omega/c = \mu + \sigma$. The extremely high values of gain presented in this chapter are only limited by physical photon noise that is carried forward to the detection scheme. The properties of the detector, like detection noise and detector dynamics were ignored so far to limit the calculations and to focus on the physical limits and optimal operation of such a scheme. However, in real life application, additive detector noise and source phase noise must be taken into account. Incorporating such additional noise factors in our approach is a clear perspective to this work, which will indeed limit the attainable gain values to more realistic values.

5

All-optical full-field high-frequency demodulation camera

This chapter details the practical considerations that must be taken into account for the development of a full-field intensity demodulation imaging system. An ideal full-field demodulation camera should be able demodulate at any frequency, at least in giga-hertz range and obtain amplitude and phase information from an unsynchronized modulated source. However, usually, for operations at high frequencies electronic limitations like frequency jitter and faithful reproduction of sinusoids are the main bottlenecks. Various methodologies have been applied to attain full-field demodulation and it is helpful to first review the ones important in the context of this thesis. Then, a proposal and proof of concept of a novel and versatile full-field demodulation camera is presented and its advantages and disadvantages are listed.

5.1 Full-field demodulation cameras

A first class of high speed demodulating imaging system are scanning, single pixel LIDARs (Light detection and ranging), which have been used since many decades as demodulation imagers and are still in active use in both military and civil applications. These will be excluded from the discussion as they are not relevant in the context of full-field demodulation cameras. Instead, attention will be given to recent full-field cameras like time-of-flight (ToF) cameras and modulated gain intensifiers, describing their advantages and disadvantages which eventually sets the need for a novel all-optical full-field demodulation camera as proposed in the thesis.

5.1.1 Modulated gain intensifier cameras

Intensified cameras (iCCDs) are used widely, especially, when the photon budget available for imaging is too small to be detected by standard CCD or CMOS cameras. To obtain a high gain in photon detection, the intensifier camera uses a micro channel plate (MCP) between a photo cathode plate and phosphor screen. The photo-electrons emitted from the photo cathode are accelerated towards the MCP by high electric field. The initial photo electrons may produce multiple secondary electrons from the MCP to achieve a gain of the order of 10000 [114]. The electron multiplication depends on the voltage applied across the MCP, making it a voltage controlled gain camera [115]. The voltage controlled gain can act as a fast shutter that may be used to demodulate multiple pixels at the same time. Such demodulation is actively used in certain areas of research in biomedical imaging [116] and 3D imaging [115]. However, the use of intensified cameras for full-field demodulation has a number of limitations. Firstly, they are prone to noise due to electron multiplication from only a few photons. Secondly, a high voltage of the order of 4 kV - 8 kV [117, 118] is usually required for satisfactory operation. In general, high voltage modulation at radio frequencies and higher is problematic electronically and can be achieved only for narrow range of frequencies. Further, they are bulky and cannot be used in situations which require portability. Clearly, they are suitable for low photon budget imaging and time gated imaging at nanosecond time windows, but they are not designed for full-field demodulation. Owing to these limitations, novel camera have been developed in recent years, specifically, designed for demodulation at radio frequencies.

5.1.2 Time of flight cameras

One of the recent interesting developments in full-field demodulation is the invention of ToF cameras. A ToF camera provides a compact and inexpensive means of correlating source signal with an internal reference signal to estimate the intensity, amplitude and phase received at each pixel for frequencies typically at 5-30 MHz [108, 119]. The system consists of a synchronized source, usually in the near infrared range (with wavelength, $\lambda \sim$ 850 nm) and an array of detectors that sample the received signal at four different phases with respect to the modulated source. In most cases the camera is used in a reflection mode where modulated light from the synchronized source is reflected from a scene and then recorded. Depending on the distance (d) of the objects in the scene, each pixel receives light with a phase ϕ_d with respect to the phase of the source modulation, given by

$$\phi_d = \frac{4\pi f}{c} d, \tag{5.1}$$

where, f is the frequency of the modulated light from the source and c is the velocity of light in the medium. The relative phase, amplitude of modulation and the average intensity are estimated at each (super) pixel using a 'four-bucket sampling' method. The camera includes a source with instantaneous intensity $s(t) = S_0(1 + \ cos\,[\omega t])$ which is reflected from the objects in the scene and received as $r(t) = A\ cos\,[\omega t + \phi_d] + B$. The received signal is sampled four times within a period, with the sampling windows separated by $\pi/2$

phase, producing the samples $C_0, C_{\pi/2}, C_\pi$ and $C_{3\pi/2}$. Using the four samples, the relative phase, amplitude and the mean intensity at each pixels are estimated as given below

$$A' = AS_0 = \sqrt{[C_{3\pi/2} - C_{\pi/2}]^2 + [C_0 - C_\pi]^2}, \tag{5.2}$$

$$\phi_d = tan^{-1}\left[\frac{C_{3\pi/2} - C_{\pi/2}}{C_0 - C_\pi}\right], \tag{5.3}$$

$$B' = BS_0 = \frac{1}{4}(C_0 + C_{\pi/2} + C_\pi + C_{3\pi/2}). \tag{5.4}$$

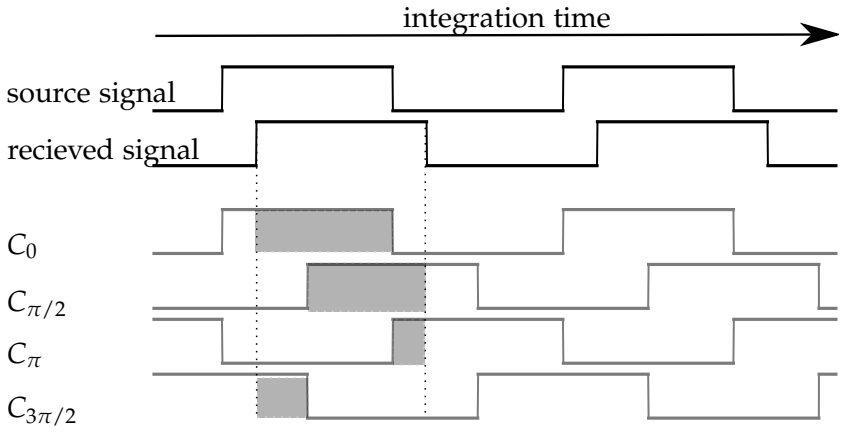

Figure 5.1: The timing diagram showing the signal, the received signal and the four samples collected withing a period [2].

The four samples are recorded in a fashion shown in the timing diagram in Fig. 5.1. To attain measurement of the four signals, a super-pixel containing four detectors are fabricated on the camera sensor, such that each detector in the super pixel is run with a $\pi/2$ phase. The ToF camera requires electronic clocking that is taken care by embedded electronics [2]. The four samples are recorded by the ToF camera by taking four frames which are equally spaced in time within a time period of the modulation.
The ToF camera has many advantages. It is relatively inexpensive, especially due to its mass production and demand in 3D imaging and gesture recognition in media and entertainment industry [119], it is very portable and is of the size of a consumer video camera along with its board and can be further miniaturized to fit in a phone [119]. Under a gaussian noise assumption, the depth measurement variance can be approximately written as [120, 121, 122, 123]

$$\sigma = \frac{c}{4\pi f\sqrt{2}} \frac{\sqrt{A' + B'}}{m_d A'} \tag{5.5}$$

where, m_d is the demodulation amplitude and depends on the sensors. From Eq. (5.5), it is clearly seen that the high offset values reduce the depth resolution. At high frequencies, the depth resolution may seem to increase but in fact it is limited by the electronic (de)modulation depth m_d, which attenuates due to the physical properties of silicon detectors in use. This limits the performance of the ToF cameras. Owing to this, the maximum modulation frequency used by the ToF cameras are limited to 80 MHz but for efficient

usage, typically, 5-40MHz is used. Other main limitations are its resolution and detector dynamics. Since, ToF cameras have different architecture and fabrication from conventional cameras, given the cost and complexity of production only low resolution formats are in use. Typically, a resolution of 320 $\times$ 240 pixels, being the most commonly used format [108] and have poor dynamics.

5.1.3 Software demodulation

Another low-frequency methodology for full-field demodulation is implemented by recording several frames within a period of modulation with a high frame rate camera. Then, given the modulation frequency, the time series of each pixel can be multiplied with a sine and cosine during processing to provide a software based demodulation at each pixel. The software processing in this technique can be accelerated by using graphic cards or embedded electronics to attain real-time processing times [34]. However, the maximum modulation frequency has to be at least 2-4 times smaller than the frame rate of the camera to obtain full-field demodulation, and may be limited to around 1kHz when using very high frame rate and expensive cameras.

5.1.4 Need for high frequency demodulation camera

As mentioned in the previous chapter, the typical modulation frequencies required for ballistic photon imaging and frequency domain diffuse imaging ranges from hundreds of MHz to around 1 GHz. The above mentioned state-of-the-art techniques for full-field demodulation barely reach these frequency without sacrificing on quality of signal. These limitation pave way for a technological advancement in full-field demodulation camera to fill the gap in the high frequency full-field demodulation area. Owing to this, in the following sections, a novel and versatile demodulation camera is proposed and a working prototype is described in detail. The proposed imaging system, does not require rethinking of the detection system as it uses active optical components and conventional intensity camera for its operation.

5.2 All-optical full-field quadrature demodulation

As in the case of the polarimetric imaging system described in the chapter 1, the goal of the full-field quadrature demodulation camera (ffQDC) proposed in this chapter, is to provide a stand-alone modular device which could be inserted in front of any conventional camera. Depending on the application area, a user could choose between inexpensive web-cameras and HD cameras to EMCCDs and low-noise, high dynamics cameras.
At the heart of the imaging system proposed here lies an electro-optic modulator. An electro-optic modulators (EOM) is widely used in optical telecommunication, where optical carriers are used to transfer information over fiber-based high speed and long distance transmission lines. Based on a specific arrangement of a birefringent electro-optic crystal, an all-optical, full-field quadrature demodulation camera has been developed during the

course of this thesis. This novel setup has been patented in 2016. This allows one to minimize electronic components and to attain demodulation on a simple intensity camera like a CCD or CMOS sensor array.
An electro-optic modulator is usually a birefringent crystal whose relative refractive index of the extraordinary axis with respect to ordinary axis can be modified by applying an electric field across its faces. If the polarization state of the incoming beam is linear and parallel to one of the eigen-axes of the crystal, this induces an optical phase delay for the beam due to the voltage dependent change in refractive index. However, when the polarization axis of the incoming beam is not aligned with the extraordinary axis of the crystal, a phase delay between the transverse electric field components of the beam produces an elliptically polarized light in the outgoing beam. This technique has been used as Pockel cells to attain intensity modulation of light to attain Q-switching in lasers [124]. Let us understand the working of an EOM using Jones calculus to derive its transfer function.

5.2.1 Electro-optic effect

Some optically transparent materials change their optical properties by application of electric field across their faces. The electric-field induces distortion in the dielectric permittivity of the crystal, accordingly, changing its refractive index differently for different axes. The refractive index which is a function of the applied electric field can be expanded in terms of Taylor series and written as

$$n(E) = n + a_1 E + \frac{1}{2} a_2 E^2 + ..., \tag{5.6}$$

$$n(E) = n - \frac{1}{2} r n^3 E - \frac{1}{2} \xi n^3 E^2 + ..., \tag{5.7}$$

where, for convenience, electro-optic coefficients $r = -2a_1/n^3$ and $\xi = -a_2/n^3$ are generally used. In case of birefringent material like Lithium Niobate (LiNbO3) (LNB) and Lithium Tantalate (LiTaO3) (LTA), the refractive index is changed proportional to the applied electric field. For Pockels effect [124], where the change in refractive index is linearly proportional to the electric field, the second and higher order terms are negligible. Thus, the refractive index in this case can be written as $n(E) = n - \frac{1}{2} r n^3 E$. For the most commonly used crystals for Pockels effect, like LNB, LTA, KDP, the coefficient r remains in the range 10^{-12} to 10^{-10} m/V. Such low values of the coefficient, produces a small change in refractive index of the material, in the order of 10^{-5}, but may induce an optical phase shift of 2π when the length of the material is 10^5 times the wavelength of light. The Pockels effect has been used to modulate the optical phase or polarization of light. In an anisotropic medium, the relative refractive index of the extra-ordinary axis with respect to the ordinary axis can be modulated with the electric field. When the direction of polarization of the input light is aligned at 45° with respect to the extraordinary axis of the crystal, the two components of light propagate along the ordinary and extraordinary axis, respectively. The phase of the component of the light in the plane of the extraordinary axis is retarded as compared to the one in the plane of the ordinary axis to produce a change in the state of polarization of the exiting beam. Thus, the crystal behaves as an electrically

Table 5.1: Optical components and their matrix representation for Jones calculus.

Component	Jones representation
Horizontal Polarizer (P_h)	$\begin{bmatrix} 0 & 0 \\ 0 & 1 \end{bmatrix}$
Vertical Polarizer (P_v)	$\begin{bmatrix} 1 & 0 \\ 0 & 0 \end{bmatrix}$
Quarter-wave plate (Q)	$\begin{bmatrix} 1 & 0 \\ 0 & -i \end{bmatrix}$
EOM[$\Delta\phi$]	$\begin{bmatrix} 1 & 0 \\ 0 & e^{-i\Delta\phi} \end{bmatrix}$
Rotation operator ($\mathcal{R}[\theta]$)	$\begin{bmatrix} cos\,[\theta] & sin\,[\theta] \\ -\,sin\,[\theta] & cos\,[\theta] \end{bmatrix}$

tunable waveplate. Using the relation of the refractive index with the electric field, the phase gained by light of wavelength λ_0 traveling through this medium can be written as

$$\phi = \phi_0 - \frac{\pi r n^3 V L}{d\lambda_0} = \phi_0 + \pi \frac{V}{V_\pi}, \tag{5.8}$$

where, L is the length of the crystal, V is the voltage applied over the faces of the crystal of thickness d and $\phi_0 = 2\pi nL/\lambda_0$. For a phase retardation of π, the voltage required is called half-wave voltage and is given by $V_\pi = \frac{d}{L}\frac{\lambda_0}{rn^3}$. Then, the change in phase is simply given by

$$\Delta\phi = \pi \frac{V}{V_\pi} \tag{5.9}$$

5.2.2 Intensity modulation and quadrature phase

To attain intensity modulation without using a Mach-Zehnder type configuration, the EOM is placed between two cross polarizers such that the axis of the EOM is oriented at 45° with respect to the input polarization as shown in the schematic in Fig. 5.2. As will be seen in the further sections, such an optical configuration of the EOM is capable of providing simultaneous modulation in a quadrature phase using a single EOM and other passive optical components. The optical transfer function of the intensity modulation a setup can be calculated by using the Jones matrix for various optical components as tabulated in Table 5.1.

The transfer function of a light passing through the configuration shown in the schematic in Fig. 5.2 can be written as

$$P_h.\left(\mathcal{R}\left[\frac{-\pi}{4}\right].EOM[\Delta\phi].\mathcal{R}\left[\frac{\pi}{4}\right]\right).P_v.I_{in} = \frac{1}{2}(1 - \ cos\,[\Delta\phi]), \tag{5.10}$$

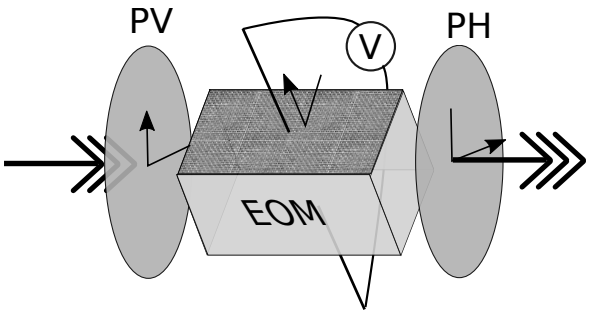

Figure 5.2: Electro optic modulator in an intensity modulation configuration. The EOM is placed between cross polarizers with optical axis of the EOM aligned at 45° with respect to the input polarizer PV.

where, $I_{in} = [1,1]^T$ and represents unpolarized light and $R[\theta]$ is the rotation matrix as given in Table 5.1. It must be noted that the Jones formulation does not account for unpolarized light, thus the input Jones vector $I_{in} = [1,1]$, which actually represents light polarized in 45 degrees, is used to indicate light with equal contributions in the two orthogonal axes with respect to the input polarizer P_h.

Thus, the transfer function is a cosine function of the phase induced in the EOM by the input voltage. When a ramp voltage of $V_\pi \omega t/\pi$ is applied, the transfer function is oscillatory with an angular frequency of ω. The cosine transfer function is shown in Fig. 5.4 in orange. Indeed, this optical configuration of the EOM, used as fast shutter, is not efficient because of requirement of large V_π as compared to a Mach-Zehnder type modulator architecture, which can achieve high frequency modulation requiring voltages as low as 2 V [125]. However, this configuration allows to attain quadrature demodulation using a electro-optic crystal. As will be seen in later sections that the imaging system based on a single electro-optic crystal, allows for modular and portability design of the imaging system with minimum mechanical constraints.

5.2.3 Electro-optic shuttering with quadrature phase

A simple modification to the optical configuration described above can provide the quadrature component of the modulated light. Construction of an optical setup such that the transfer function is in quadrature with the above described configuration can be achieved by simply introducing a quarter-wave plates (QWP) before the exit polarizer. The transfer function can be calculated to be

$$P_h.Q.\left(\mathcal{R}\left[\frac{-\pi}{4}\right].EOM[\Delta\phi].\mathcal{R}\left[\frac{\pi}{4}\right]\right).P_v.I_{in} = \frac{1}{2}(1 - \ sin\,[\Delta\phi]), \tag{5.11}$$

Interestingly, this equation shows that a phase delay of $\pi/2$ in the optical range due to the presence of the quarter-wave plates (QWP) can be transferred to a $\pi/2$ phase delay in the RF modulation with such an optical apparatus, as shown in Fig. 5.4.

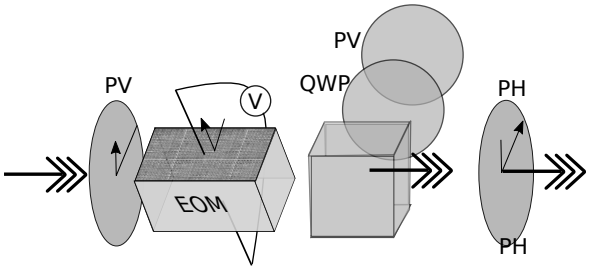

Figure 5.3: Electro optic modulator in a quadrature intensity modulation configuration. A beam splitter BS splits the beam after passing through the EOM. One of the arms is passed through polarizer PH and other is passed through a quarter-wave plate QWP and then a polarizer PH. For a ramp excitation of the EOM the two arms output modulated light in quadrature phase with respect to each other.

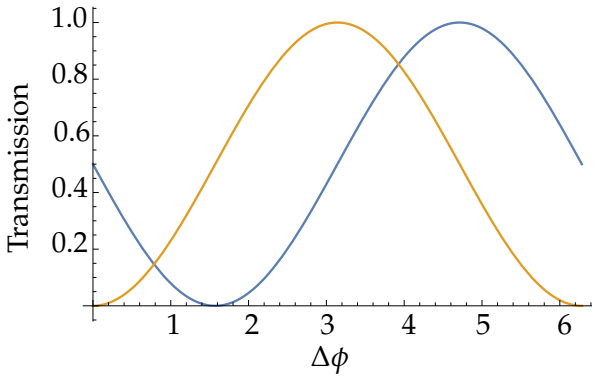

Figure 5.4: Transfer functions of two optical arms in quadrature with respect to each other.

5.2.4 Electro-optic shuttering and quadrature demodulation

The above optical scheme that produces in-phase and quadrature modulation can be used as a electro-optic shuttering mechanism to attain demodulation at high frequencies. An intensity modulated beam of light passing through such a configuration will be down converted to an intermediate frequency corresponding to the beat note between the modulation frequency of the source and the modulation of the EOM after passing through a low pass filter.

In the context of full-field demodulation, a conventional camera with exposure time longer than the time period of modulation can replace a low pass filter, which is the case when using high frequencies modulation. The intermediate frequency can be made arbitrarily small by tuning the frequency of the source or the detector. The low frequency modulation can then be sampled by a conventional, low frame-rate intensity camera. Then, demodulation can be achieved by obtaining at least 3 or more frames per cycle, similar to the case of the ToF cameras. However, in this case multiple frames need to be used to obtain the mean intensities, amplitudes and phases at all pixels of the camera. It is possible to obtain all optical quadrature demodulation using only a single frame by additional optics.

5.2.5 All-optical quadrature demodulation

As described in the previous chapter, a quadrature demodulation scheme requires the incoming signal to be multiplied with a sine and cosine wave of the same frequency as the modulation frequency of the signal. Then, an integrator is used as low pass filter to obtain quadrature components of the signal, form where the amplitude and the relative phase is estimated. A generic schematic of such a demodulation scheme is shown in the Fig. 5.5.

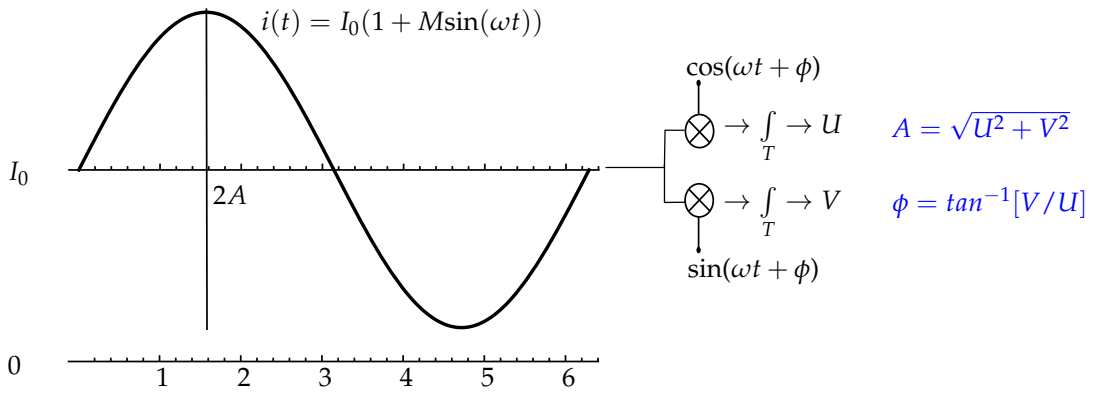

Figure 5.5: Schematic showing the demodulation scheme.

An all-optical quadrature detection scheme can be realized by using such a scheme as shown in the schematic in Fig. 5.3. The all-optical, full-field demodulator requires the incoming modulated to be split into two optical arms, each passing through optical components with different transfer function given by $\mathcal{T}_1 = T(1 - cos\,[\Delta\phi])$ and $\mathcal{T}_2 = T(1 - sin\,[\Delta\phi])$, where, T is the DC intensity transfer function for the optical arms. The transfer functions of the two optical arms are plotted in Fig. 5.4 for $T = 1/2$.

Let us consider such an optical demodulation system as shown in the schematic in Fig. 5.3. An incoming beam of light which is modulated in intensity as $S(t) = S_0(1 + M\,cos\,[\omega t + \phi])$ is divided into two optical arms with transfer functions $\mathcal{T}_1$ and $\mathcal{T}_2$. When the EOM is asynchronously modulated at the same angular frequency of ω and imaged with a conventional camera the light signal is integrated over a period the exposure time of the camera, acting as a low-pass filter. With exposure time much longer than the time period of modulation, i.e., $2\pi/\omega$, the central high frequency component and the high frequency sideband is averaged out leaving only the near DC component. After a simple calculation (shown in Appendix D) the intensity retrieved at the two arms are $U = S_0T(1 - (M/2)\,cos\,[\phi])$ and $V = S_0T(1 + (M/2)\,cos\,[\phi])$. After rejecting a the background term S_0T, the amplitude and the relative phase are estimated as $A = \sqrt{U^2 + V^2}$ and $\phi = tan^{-1}\,[V/U]$, where $A = TS_0M/2$.

The quadrature demodulation based on the above mentioned scheme can be implemented only when the EOM can be driven to explore at least 2ϕ phase with a ramp voltage with a peak-to-peak voltage of $2V_\pi$. This is evident from the Fig. 5.4, where it can be observed that a faithful sinusoidal transfer functions in both the arms, simultaneously, can only be obtained when the EOM is driven linearly in time with $2V_\pi$ peak-to-peak voltage. Generally, this voltage is in hundreds of volts depending on the dimensions of the crystal as

discussed in subsection 5.2.1. Indeed, the crystal width are limited on the lower end by lowest acceptable field of view and multimode propagation of the light along the crystal. Attaining high voltage ramps at high frequency is electronically challenging and this, puts additional constraints on the dimensions. Furthermore, in this scheme, the background DC offset term S_0T can be eliminated by estimating the background, either with spatial estimation techniques or by detuning the source and detector in frequency and obtaining at least two frames. These, consideration will be discussed by the end of the chapter.
Nonetheless, an imaging setup based on the schematic in Fig. 5.3 can be envisaged where an image is passed through the EOM and then split either by a beam splitter or a Fresnel prism to go through separate optical paths. Keeping in mind modularity and cost of such an imaging system, a novel imager is proposed in the following section.

5.3 Full-field quadrature demodulation camera

5.3.1 Description

An imaging system based on the principle described in the previous section is presented here. This requires an image to be passed through an EOM, which is set up in an intensity modulation configuration. The schematic shown in Fig. 5.6a represents a 3D view of the proposed full-field demodulation camera. The final design and choice of optical components in the system are in accordance with our preference of portability, modularity and cost of the imaging system and a pictures of prototypes imaging system are shown in Fig. 5.6b.
The imaging system consists of a polarizer P_v placed at the entrance of the light. The polarization axis of P_v is aligned vertically. Light from infinity then passes through an EOM whose optical axis is aligned at 45° with respect to the polarizer P_v. The clear face of the EOM also acts as an aperture for the pair of objectives $L1$ and $L2$ that collimate the incoming beam of light. The collimated beam is then angularly separated into two beams by a Fresnel bi-prism (FP). One of the beam is them passed through a polarizer P_h to form an image U on the intensity camera through objective $L3$. The other beam is passed through a quarter wave plate (QWP) and then a polarizer P_h to form another image V on the CMOS camera. The matched pixels in images U and V are expected to be in quadrature with respect to each other as per the theory described in the previous section. The two pixel-registered images U and V can be seen as a two dimensional image X such that the i^{th} pixel in X can be written as $x_i = [u_i, v_i]$. In case of perfect pixel-to-pixel registration in the two images, equal gain in each pixel and perfect quadrature phase difference between the two images, an amplitude and phase image can be reconstructed such that the i^{th} pixel in the amplitude map A is $z_i = \sqrt{u_i^2 + v_i^2}$ and the corresponding phase value at the pixel is $\phi_i = tan^{-1}[v_i/u_i]$, forming a phase map Φ. It must be noted that the refractive indexes of EOM are dependent on the wavelength of light used. Thus, for the above scheme to work, the light entering the imaging system has to be narrow band. This, can be achieved by using a narrow band filter or by using coherent light. However, even when using

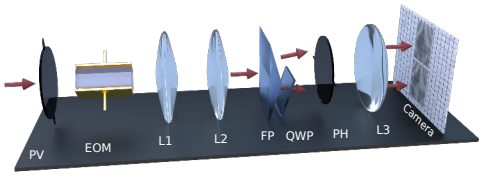

(a)

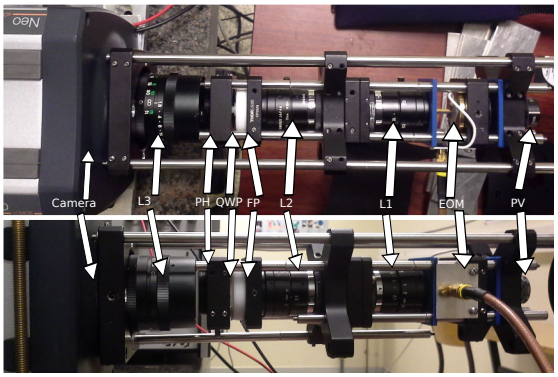

(b)

Figure 5.6: Design and schematic of the full-field intensity demodulation camera. P_v is an input polarizer with polarization axis aligned vertically. The EOM is placed such that the optical axis is aligned at 45° with respect to the polarizer P_v. Two objectives $L1$ and $L2$ are placed to obtain a collimated beam of input light to pass through a Fresnel bi-prism (FP) which divides the input beam of light into two beams. One of the beam passes through polarizer P_h to form an image U on the intensity camera via objective $L3$. The other beam of input light passed through a quarterwave plate (QWP) and polarizer P_v to form an image V on the CCD through objective $L3$.

coherent light for imaging, various imperfections may arise due to the optical asymmetry encountered by the two image-forming optical arms. Further imperfection in intensity and phase may arise from slight mismatch between the orientation of optical axes of various optical components. At last, the effective AC and DC gain at each pixel of the camera may not be same. All these factors have to be taken into account while calibrating the imaging system, as the faithful estimation of amplitude and phase at each pixel and the quality of the spatial information provided by the final images will depend on these factors. In the following subsections these constraints and imperfections are detailed and a calibration process is described.

5.3.2 Coherent Imaging through EOM

Dimensions of electro-optic crystal A fundamental limitation for realizing a quadrature demodulation scheme based on the methodology described in the previous section is the dimension of the EOM to be used. The length of the EOM provides the total phase shift encountered by light. To realize a quadrature demodulation, it is imperative to have a phase shift of at least 2π. This introduces a stringent constraint on the minimum ratio of breadth-to-length of the crystal that may be used, given by, $rn^3V(L/d) = 2\lambda_0$. Finally, the maximum voltage that can be applied on the faces of the EOM depends on the available electronics that can produce a fair high voltage saw-tooth wave at radio frequencies. Using an LNB crystal with electro-optic coefficient of 30.8 pm/V at 633 nm, refractive index of 2.20, with maximum peak-to-peak voltage of 295 Volts and an operating wavelength of 633 nm, $(L/d) \sim 20$. The ratio of the length and the breadth is also responsible for field of

view through the crystal and the internal reflections from the sides of the crystal that may occur due to long length of the crystal. In the prototype developed here, a LNB crystal from MolTech GmbH was used with r = 30.8 pm/V, L = 40 mm and d = 2 mm.

Isogyres Light entering an electro-optic crystal undergoes multiple reflections from the faces of the crystal. In case of illumination with coherent light, the multiple reflections of the incoming light interfere to form patterns which are known as isogyres [126, 127]. A raw image taken from the imaging system when illuminated uniformly with coherent light at 632 nm is shown in Fig. 5.7. The two images are marked as U and V. Firstly, in each image the isogyre pattern is clearly visible. This indicates that due to interference from multiple reflections in the electro-optic crystal, all the pixels are not in the same phase and may undergo modulation with different phases. As mentioned before, it is indeed possible to attain demodulation of signal by using only one in-phase image, but it will require multiple frames to sample the low frequency intermediate signal with the usual low frame rate intensity camera. Further, due to the presence of isogyres, the effective region of interest will be limited to the central area, thus, limiting the field of view drastically. This introduces practical limitations on the in-phase full-field demodulation, which can only be achieved with multiple frames. However, in this thesis the in-phase demodulation is ignored and only quadrature demodulation is focused upon, because of its clear advantages, from a practical point of view.

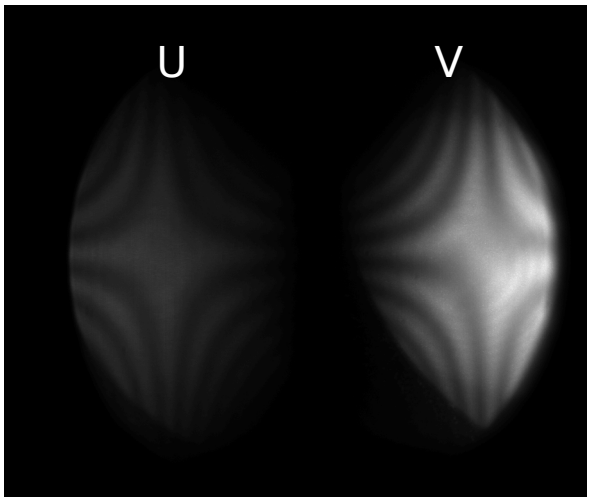

Figure 5.7: Raw frame from the imager showing isogyre patterns formed on the intensity camera when using uniform coherent illumination.

In the proposed quadrature demodulation scheme, this limitation is overcome by noticing that each corresponding pixel in the two images remain in quadrature. Thus, even though not all pixels in each individual image are in phase but the amplitude and phase information at each pixel is preserved when taking into account both the in-phase (U) and quadrature image (V). As shown in Fig. 5.7, the difference in isogyre patterns in the two images already indicates that corresponding pixels in the two images are not in phase. This fact will be clear by end of this section, as the discussion will continue on establishing

that the corresponding pixels in the two images are in fact in quadrature. However, first it is important to calibrate the system for intensity and amplitude mismatch and attain a good pixel-to-pixel registration in the two images to allow efficient extraction of the two quadrature images for estimation of amplitude and phase of the detected signal at each pixel. The calibration methods utilized here are described in the following subsection.

5.3.3 Calibration

The calibration of such a system is of utmost importance. As in the case of polarimetric camera in the first part of the thesis, the calibration of the full-field demodulation camera comprises the camera calibration and then the optical calibration.

Camera calibrations

Dark noise Fixed pattern noise or dark noise in a detector system arises predominantly due to thermally induced electron emission from each pixel in the camera. When no light is absorbed by the pixels, a certain amount of the electrons are emitted nonetheless. The camera used in our case is the same as used for polarimetric imaging in the previous part, a Andor Neo camera, with high dynamics and low noise properties. The dark noise/fixed pattern noise at each pixel is obtained by averaging over several frames when there is no light falling on the camera. An average over 500 dark frames were performed to obtain the mean of dark noise fluctuations at each pixel and produce a map I_{dark}.

Pixel gain non uniformity The pixel gain non-uniformity of an intensity camera is also recalled here. The emission of electron per photon received may vary from pixel to pixel due to unavoidable manufacturing defects. At a uniform illumination of the entire camera sensor, some pixels may have gain higher or lower than other, this non-uniformity can be mapped and used to correctly scale the intensities detected by the camera as I_{gain}. Finally, the corrected image is given by $I_{corrected} = (I - I_{dark})/I_{gain}$.

Pixel registration In any imaging system that creates two images using different set of pixels, one of the first calibration steps is to obtain pixel-to-pixel registration between the two images. In general the two images formed on the same camera sensor may undergo different optical aberrations and asymmetric geometric distortions over the entire image. These effects can be corrected as described in the chapter 2 using non-linear interpolation, which require a fair amount of computation time and need graphical processing units or FPGA to attain real-time processing times. In this case, only a linear pixel registration method was utilized that remains fairly accurate to a central region of about 50×50 pixels. The pixel registration was obtained by placing a known image with a background of periodic dots and attain maximum overlap between the images. The linear translation coefficients were stored as calibration parameters for further use. Using this linear translation parameters, a pixel-to-pixel registration of the two images is performed to extract two images of the same scene, one that is in-phase (from here on denoted by U) and one

in quadrature (denoted by V). The matched pixels in the two images can then be expected to the in quadrature phase with each other. However, a perfect pixel registration may not guarantee the two images to be in perfect quadrature due unavoidable misalignments in the optics. These optical calibration are discussed next.

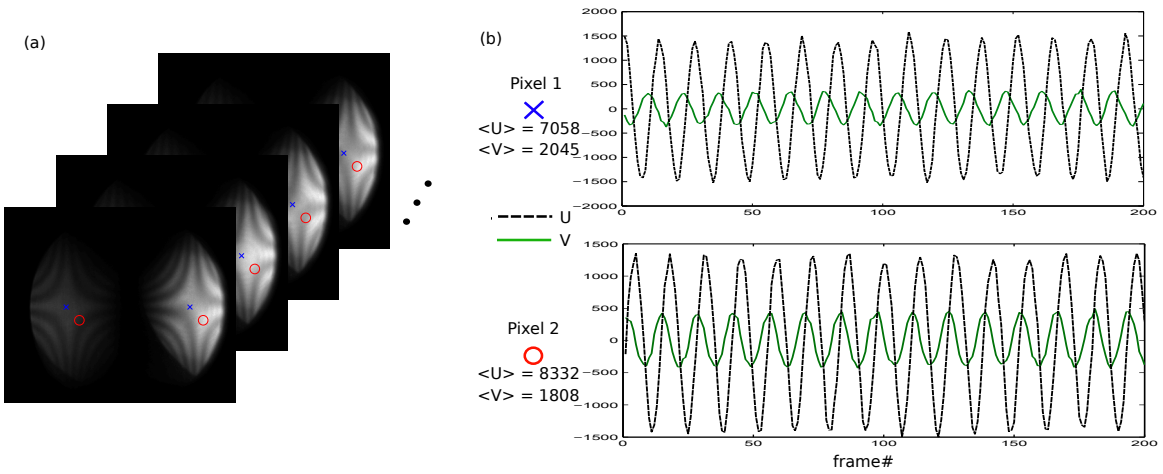

Figure 5.8: (a) A time series of raw images (2560 $\times$ 2160 pixels) were recorded with a slow linear ramp with peak to peak voltage of $2V_\pi$ = applied to the EOM. The isogyre patterns move on each image but the corresponding pixels remain in quadrature. (b) Pixel 1 labeled by a blue cross and pixel 2 labeled by a red circle are chosen. The time series of these pixels and their corresponding quadrature counterparts are plotted for the raw pixel data. The solid green line shows the time series of the in-phase pixel (u) and the dotted black line shows the time series of the quadrature pixel (v). The time series are subtracted from their mean values which are also indicated next to them.

Optical calibration

Intensity, amplitude and quadrature phase normalization The optical calibration of a full-field intensity modulation camera is of utmost importance. Various key parameters play a role that must be estimated to attain proper intensity demodulation. The calibrations specific to the proposed camera are related to normalization of intensity, amplitude and deviation from quadrature phase. The two raw images U and V formed on the same sensor may have differences in average intensity at each pixel and may undergo difference in amplitude, due to various optical components and the influence of the EOM which creates isogyre patterns. The differences may arise due to the differences in optical transfer function seen by each image. The difference in optical transfer function in the two image forming optical arms may arise due to the additional QWP in one of the arms and due to imperfect alignment of optical components. Such a difference is clearly observed from raw data plotted in Fig. 5.8.b

The two images formed on the camera undergo different optical transfer functions, an asymmetry that arises due to the passage of one of the arm of the optical beam passing through an additional QWP. The intensity mismatch discussed above is further affected

by the isogyres formed by the EOM for coherent light. Even in the case of perfect pixel-to-pixel registration, along with perfect intensity mismatch correction, there might still be deviation from quadrature phase due to imperfect alignment of QWP, EOM, polarizers or due to small imperfection in pixel-registration. These imperfections may result in transfer functions of the two optical arms at ith pixel as

$$\mathcal{T}_{1i} = T_{1i}(1 - \ cos\left[\Delta\phi_i\right]), \tag{5.12}$$

$$\mathcal{T}_{2i} = T_{2i}(1 - \ sin\left[\Delta\phi_i + d\phi_i\right]). \tag{5.13}$$

The intensity gain mismatch and phase orthogonality of the two images, thus, need to be calibrated. Several calibration methods exist for correcting the intensity and quadrature phase of a quadrature demodulator, especially for their application in RADARs, and have been reported in [128, 129]. Here, the calibration procedure described in [130] is followed. This method produces single step fast calibration for both intensity mismatch and phase orthogonality mismatch.

The two quadrature images (U and V) form a two-dimensional image. The ith pixel of the two-dimensional image can be written as $X_i = [u_i, v_i]$. When the imaging system is allowed to image a uniformly illuminated scene with non-modulated light source and the EOM is excited with a slow ramp, one obtains the transfer function of the two arms at each pixel. To calibrate our system, an integrating sphere (Labsphere CSTM-US-800C-100R Uniform Light Source System). and a coherent source at 633 nm was used. The EOM was modulated with a ramp from -147.5 V to 147.5 V, which provides a 2π excursion at each pixel with the selected EOM in use. Several cycles of the modulation were recorded. The time series at the i^{th} pixel can be written as a random variable

$$X_{i,t} = \begin{bmatrix} u_{i,1} & v_{i,1} \\ u_{i,2} & v_{i,2} \\ : & : \\ u_{i,j} & v_{i,j} \\ : & : \end{bmatrix} = S_0 \begin{bmatrix} T_{1i}(1 - \ cos\left[\Delta\phi_{i,j}\right]) & T_{1i}(1 - \ sin\left[\Delta\phi_{i,j} + d\phi_i\right]) \end{bmatrix} \tag{5.14}$$

The mean is then $\langle X_{i,t} \rangle = S_0[T_{1i}, T_{2i}]$ and the covariance of the random vector $X_{i,t}$ is $\Gamma_i = \left\langle (X_{i,t} - \langle X_{i,t} \rangle)^T (X_{i,t} - \langle X_{i,t} \rangle) \right\rangle$ and can be written as

$$\Gamma_i = T_{1i}^2 S_0^2 \begin{bmatrix} \left\langle \ cos\left[\Delta\phi_i\right]^2 \right\rangle & \frac{T_{2i}}{T_{1i}} \left\langle \ cos\left[\Delta\phi_i\right] \ sin\left[\Delta\phi_i + d\phi_i\right] \right\rangle \\ \frac{T_{2i}}{T_{1i}} \left\langle \ cos\left[\Delta\phi_i\right] \ sin\left[\Delta\phi_i + d\phi_i\right] \right\rangle & \frac{T_{2i}^2}{T_{1i}^2} \left\langle \ sin\left[\Delta\phi_i + d\phi_i\right]^2 \right\rangle \end{bmatrix} \tag{5.15}$$

$$= \frac{T_{1i}^2 S_0^2}{2} \begin{bmatrix} 1 & \frac{T_{2i}}{T_{1i}} \ sin\left[d\phi_i\right] \\ \frac{T_{2i}}{T_{1i}} \ sin\left[d\phi_i\right] & \frac{T_{2i}^2}{T_{1i}^2} \end{bmatrix} \tag{5.16}$$

Clearly, from the above expression, the diagonal elements of the covariance matrix provides the information of the intensity mismatch between the two optical arms, while the off-diagonal elements contain the information about the deviation from quadrature phase between the two optical arms. Using the covariance matrix it is, thus, possible to correct

for these imperfections by realizing that in the case of perfect quadrature detection the covariance matrix must be diagonal with equal diagonal components. This can be also intuitively inferred from the fact that the quadrature components are orthogonal and hence de-correlated. To obtain a correction at each pixel, it is easy to see that the two-dimensional quadrature pixel X_i must be rotated and scaled in such a way that the covariance matrix Γ_i is diagonalized with equal diagonals. This can be easily performed by estimating the covariance matrix at each pixel and solving for its eigenvalues and eigenvectors. The matrix formed by eigenvector as column vectors provide us the scaling and rotation information required to obtain the correction. However, a faster and numerically stable method to obtain the scaling and rotation matrix is through singular-value decomposition (SVD) which is performed on the time-series data at each pixel, without estimating the respective covariance matrix. The calibration process is described below along with its application on the real setup.

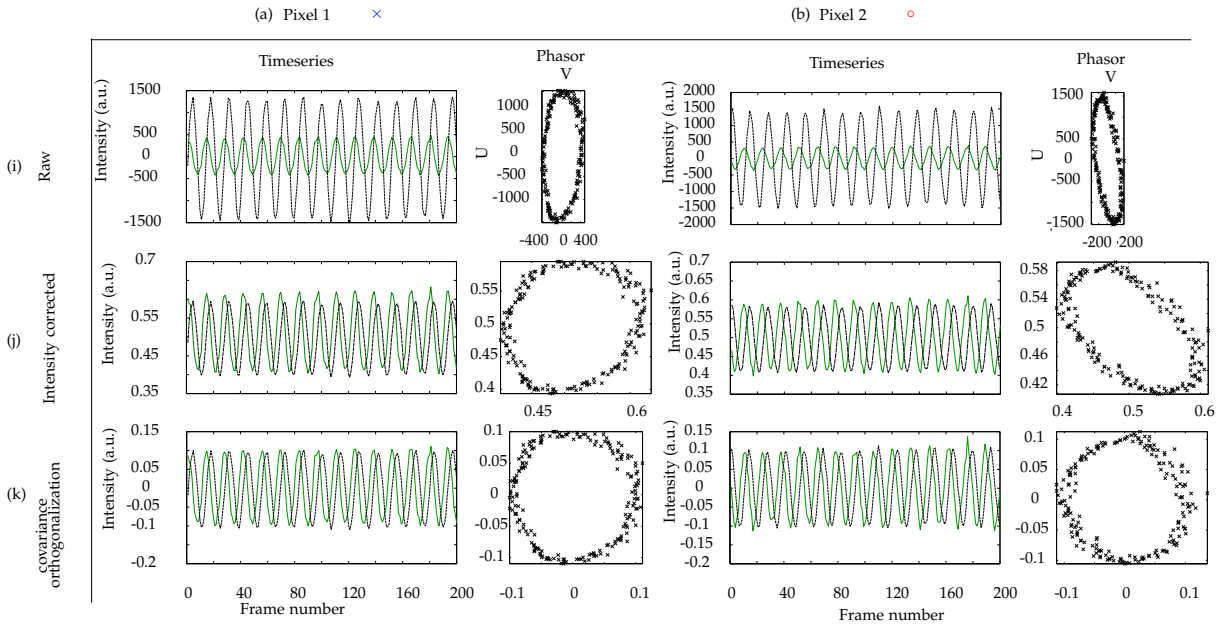

Figure 5.9: The figure shows the time series data and the corresponding phasor diagram for two pixels, one marked as × and shown in column (a) and other marked as ○ and shown in column (b). Row (i) Shows the time series for the raw, uncalibrated images of the quadrature components u_i (black dashed) and v_i (green solid). Row (j) shows the same time series when only the intensity mismatch is corrected for. Row (k) shows the time series and phasor diagram for the calibrated imaging system, where both the intensity and the deviation from quadrature has been corrected using a covariance matrix orthogonalization method.

In Fig. 5.9.i the raw time series of the in-phase and the quadrature component are shown in black and green solid lines, for two pixels in columns (a) and (b). The two pixels are labeled by symbols × and ○. The phasor diagram of the time series is also shown next to the time series data.

The time series shown is obtained when the camera is set up to image a uniformly illu-

minated un-modulated source of coherent light. Uniform illumination was obtained by using a integrating sphere and a 633 nm laser source. A slow ramp modulation of 0.2 Hz and peak to peak voltage of 295 V was induced on the EOM to produce 2 π sinusoidal transmission on the two optical arms that produce the quadrature images. The camera was operated at a 200 ms exposure and frames were recoded at each 250 ms to sample at least 20 points per cycle.

The intensity mismatch between the quadrature components are clearly seen in the row (i) of the Fig. 5.9. A simple correction can be performed to eliminate the intensity mismatch between the two optical arms by dividing each frame with the time average at each pixel. Such a correction is shown in the row (j) of the Fig. 5.9, which fairly rescales the intensities and amplitudes of the in-phase and quadrature components but does not correct for the deviation from quadrature phase as shown by the phasor diagram for pixel 2 (labeled by ○) in the second column of the figure. The deviation from quadrature phase at pixel 2 may arise from an improper pixel registration due to asymmetric geometric distortions in the two images or due to the isogyres.

To correct for both the intensity and phase within a single procedure, the 200 $\times$ 2 time series data (real numbers) $\Delta X_{i,t} = X_{i,t} - \langle X_{i,t} \rangle$ at each pixel is decomposed using SVD as $\Delta X_{i,t} = A\Sigma B^T$, such that A is a 200 $\times$ 200 unitary matrix, Σ is a 200 $\times$ 2 diagonal matrix and B^T is a 2 $\times$ 2 real unitary matrix. The diagonal values of Σ are called the singular values. The singular values are extracted to form the 2 $\times$ 2 diagonal matrix Σ'. Then the covariance matrix at ith pixel can be written $\Gamma_i = \Delta X_{i,t}^T \Delta X_{i,t} = (A\Sigma B^T)^T (A\Sigma B^T) = B\Sigma^T \Sigma B^T$. As mentioned before, the intensity and phase correction can be obtained by applying a scaling and rotation of the data through the matrix R_i to obtain $Y_i = R_i X_i$ such that the covariance of the resulting transformed data is the identity matrix. The covariance matrix of the transformed data is $\Gamma_i^Y = Y_i^T Y_i = R_i^T X_i^T X_i R_i = R_i^T \Gamma_i R = (R^T B \Sigma'^T)(\Sigma' B^T R_i) = I$, where I is the identity matrix. Thus, the expression for the transformation matrix is obtained by solving $(R_i^T B \Sigma'^T)(\Sigma' B^T R_i) = I$. It can be checked (see Appendix D.2) that the unique solution is $R_i = B\Sigma'^{-1} B^T$. The 2 $\times$ 2 matrix R_i is composed of a scaling via the matrix Σ'^{-1} to correct for intensity mismatch and a rotation through the matrix B to correct for the deviation from quadrature phase.

The transformation matrix R_i can be obtained at each pixel. Since, R_i is symmetric and can be normalized to its first element, only one of the diagonal component and one of the off-diagonal component need to be stored as calibration maps for all the pixel. Finally, each quadrature image from a single frame from the full-field quadrature demodulation camera (ffQDC) is transformed by two simple multiplications and additions at each pixel. The transformed images are obtained by applying R_i at each pixel X_i. The result of such a correction is shown in the row (k) of Fig. 5.9. The phasor diagram next to the time-series shows that the intensity and the phase are well corrected. The quadrature images can now be used to estimate the amplitude and the phase.

Spatial phase variations Each pixel in the image has a different transfer function and the phase relative to the source signal is also different for each pixel. The spatial phase

mismatch pattern is seen as the isogyre patterns. Thus, for accurate recovery of the phase in the final images, a map of this spatial mismatch must be recorded. The relative phase calibration map is obtained by taking a time series of the images, say U, selecting the time series of the central pixel and correlating the time series with every pixel in U to obtain a correlation map Θ. The correlation of each pixel with respect the central pixel contains the information about the phase difference of that pixel with respect to the central pixel. The covariance matrix of a pixel with respect to a central pixel can be derived in a fashion similar to previous analysis for quadrature phase mismatch and it is then easily checked that the correlation coefficient is simply the $cos\left[\Delta\theta_{i,c}\right]$, where $\Delta\theta_{i,c}$ is the phase difference between i^{th} pixel and the central pixel c. The phase difference map is then subtracted from the phase map obtained from the quadrature detection to produce a corrected phase ϕ'.

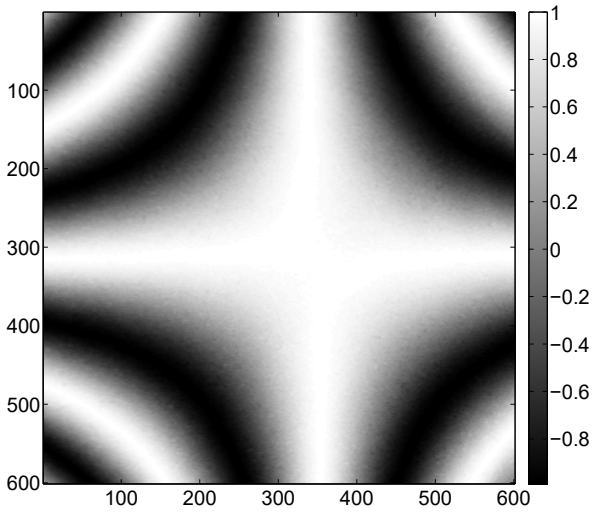

Figure 5.10: The correlation map Θ quantifies the spatial non-uniformity of the phase of the transfer function at each pixel respect to the central pixel.

With the above calibration in place, the ffQDC can be studied for its frequency selectivity as presented in the following subsection.

5.3.4 Quality of detection

The quality of the quadrature detection camera is given by its efficiency to enhance signals from a specified frequency and reject signals modulated at other frequencies. In the case of a full-field demodulation imaging, if the ffQDC is operated at a frequency of f_c, only the pixels that receive light from a source modulated at the same frequency as the ffQDC (f_c) will be selectively enhanced and other pixels which receive constant illumination or modulated illumination from sources with frequencies other than f_c will be diminished. To quantify the frequency response of the ffQDC, the source was kept at a central frequency f_c and the demodulation frequency of the imaging system was detuned and the amplitude was estimated at each pixel. This was performed for various exposure times of the camera and the amplitudes were plotted against the detuning. The plot for a single pixel is shown in Fig. 5.11.

The plots show that there is indeed a frequency width (denoted as Δf) around the central frequency beyond which the detected amplitude diminishes. The frequency width (Δf) does not seem to change with the change in central frequency (f_c), however, with increase in the exposure time the width decreases. This indicates that the frequency sensitivity of the ffQDC can be enhanced by increasing the exposure time, which is coherent with the fact that the exposure time here acts as an integrator in a filter circuit. These factors are considered in detail below.

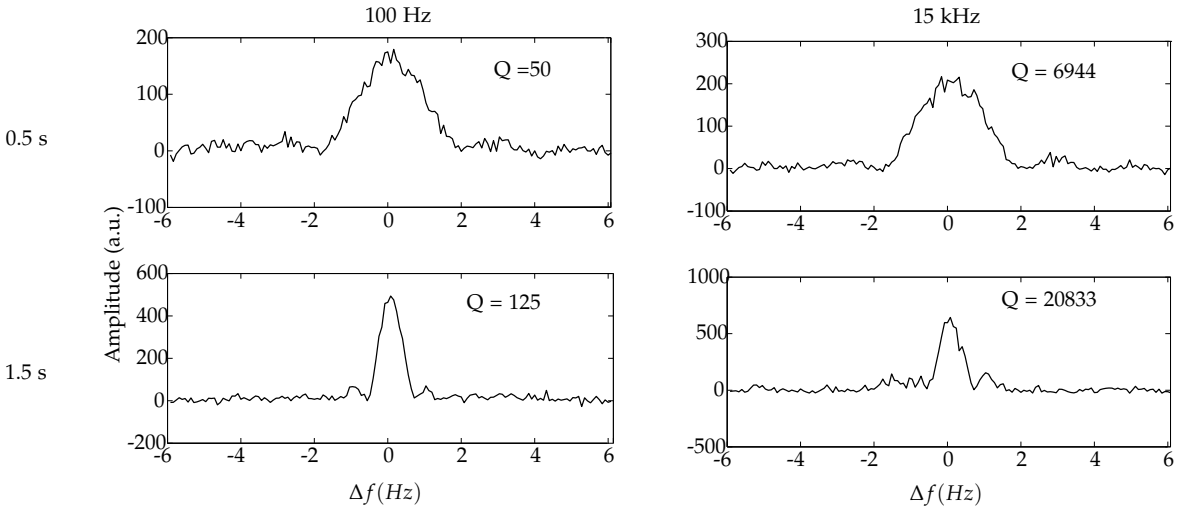

Figure 5.11: The plots show the amplitude estimated at a single two-dimensional pixel of the ffQDC, when the camera is detuned in frequency with respect to a central source frequency. The plots show the frequency response of the camera at central frequencies 100 Hz and 15 kHz. Two different exposure times of 0.5 s and 1.5 s were utilized at each frequency to show that width of detection decreases with increase in exposure time thereby increasing the frequency selectivity of the camera. The quality factor $Q = f_c/\Delta f$ is indicated in each plot as well.

The shape of the frequency response resembles a Sinc function (cardinal sine) because the detected sinusoidal signal is convoluted with a square window of the exposure time of the camera. A detailed calculation in Appendix D.1 shows that the frequency response at each pixel of the ffQDC is

$$A(\Delta f, \epsilon) = I_0 M \, sin\left[\pi \Delta f \epsilon\right] / (\pi \Delta f), \tag{5.17}$$

where I_0 is the mean detected intensity, ϵ is the exposure time, and M is the modulation index of the source.

Effect of central frequency The central frequency does not have a significant effect on the frequency response curve. The detuning from the central frequency is responsible for the decrease in estimated amplitude. This is apparent from the fact that the detuning creates an intermediate frequency which, in turn, is DC filtered by the camera exposure time. Further, theoretical calculations provided in Appendix D.1, show that the central frequency comes in the denominator for estimation of the amplitude and those terms can

be ignored when operating at high central frequencies.

Effect of exposure time In the case of this demodulation camera, the CCD/CMOS sensor acts as an integrator and a low-pass filter due to a long exposure time. With the increase in exposure time, the high frequency components are more efficiently rejected. This can be inferred from Eq. (5.17) and is also indicated by the Fig. 5.11. To further confirm this, the full-width at half maximum (FWHM) was obtained at each exposure and the trend observed is shown in Fig. 5.12.
The quality factor of demodulation, given by the $Q = f/\Delta f$ is increases with increase in both the central frequency and the exposure time. The quality factor is the dimensionless quantity that quantifies the frequency sensitivity of the entire imaging system.

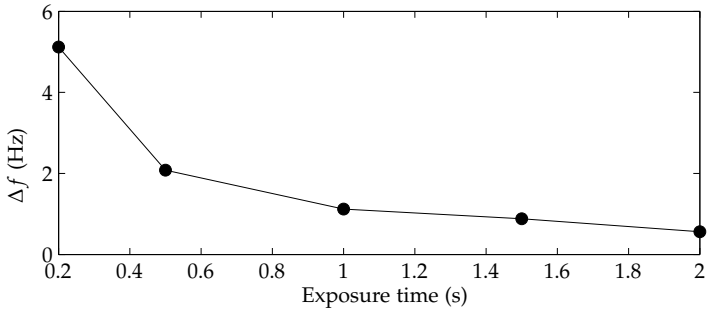

Figure 5.12: The plot shows the full-width at half-maximum (Δf) of the frequency response of the ffQDC as a function of the exposure time.

5.3.5 Preliminary images

To test the working of a calibration process, a simple mask with letter 'e' was imaged with an illuminated background as shown in Fig. 5.13 labeled as 'intensity image'. The final amplitude and phase images with proper calibration are expected to show uniform illumination of the background instead of the isogyre patterns. In Fig. 5.13, the estimated amplitude and phase images obtained before and after the calibration step are shown. It is observed that the amplitude image after calibration shows no pattern corresponding to the isogyres, indicating that the pixels in the two quadrature images have been well-balanced and in quadrature with respect to each other providing a smooth amplitude. The phase image, however, is not without ambiguity as each pixel has a different transfer function.

5.3.6 Background subtraction with four optical arms

In case of the above imaging scheme where only two images (in-phase and quadrature images) per frame is recorded, the estimation of background with only one frame is a challenge. The intensity image, amplitude and the phase can be retrieved faithfully, with at least three images. A robust method is to record four images of the scene at phases 0, $\pi/2$, π and $3\pi/2$. A simple modification to the above mentioned setup can provide these four images on a single frame of the camera. This is achieved by introducing a Wollaston

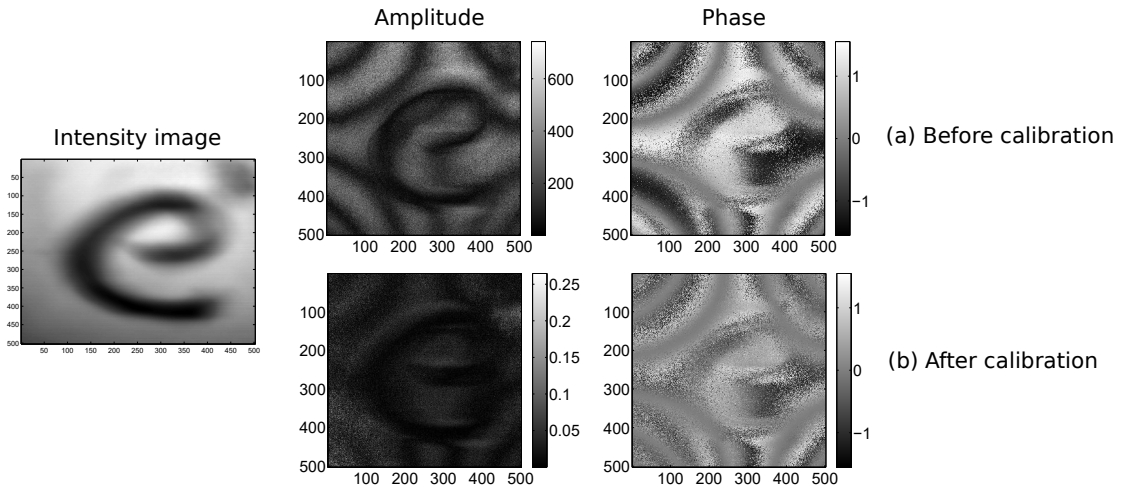

Figure 5.13: Preliminary results with the quadrature demodulation camera without DC offset subtraction.

prism after the quarter wave plate and before the objective L3 in Fig. 5.6b. The resulting setup is shown in Fig. 5.14.

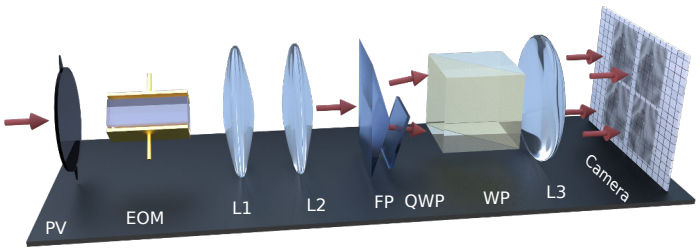

Figure 5.14: Schematic of the Wollaston prism-based four-image demodulation camera.

This Wollaston-prism based variant of the camera produces a four images and the four optical arms have transfer function given by

$$\mathcal{T}_1[\Delta\phi] = P_h.\left(\mathcal{R}\left[\tfrac{-\pi}{4}\right].EOM[\Delta\phi].\mathcal{R}\left[\tfrac{\pi}{4}\right]\right).P_v.I_{in} = T_0(1 - cos\,[\Delta\phi]), \quad (5.18)$$

$$\mathcal{T}_2[\Delta\phi] = P_h.Q.\left(\mathcal{R}\left[\tfrac{-\pi}{4}\right].EOM[\Delta\phi].\mathcal{R}\left[\tfrac{\pi}{4}\right]\right).P_v.I_{in} = T_0(1 - sin\,[\Delta\phi]), \quad (5.19)$$

$$\mathcal{T}_3[\Delta\phi] = P_v.\left(\mathcal{R}\left[\tfrac{-\pi}{4}\right].EOM[\Delta\phi].\mathcal{R}\left[\tfrac{\pi}{4}\right]\right).P_v.I_{in} = T_0(1 + cos\,[\Delta\phi]), \quad (5.20)$$

$$\mathcal{T}_4[\Delta\phi] = P_v.Q.\left(\mathcal{R}\left[\tfrac{-\pi}{4}\right].EOM[\Delta\phi].\mathcal{R}\left[\tfrac{\pi}{4}\right]\right).P_v.I_{in} = T_0(1 + sin\,[\Delta\phi]), \quad (5.21)$$

producing four images I_1, I_2, I_3 and I_4 corresponding to phases 0, $\pi/2$, π and $3\pi/2$, respectively, as shown in the raw frame in Fig. 5.15. The frame taken when a modulated coherent source at 632 nm casts a 'T' shaped shadow on a background. The background is structured and is illuminated with unmodulated ambient light. The modulation frequency

is set at 1 kHz and the EOM is driven with a ramp with frequency 1kHz, without any synchronization with the source.

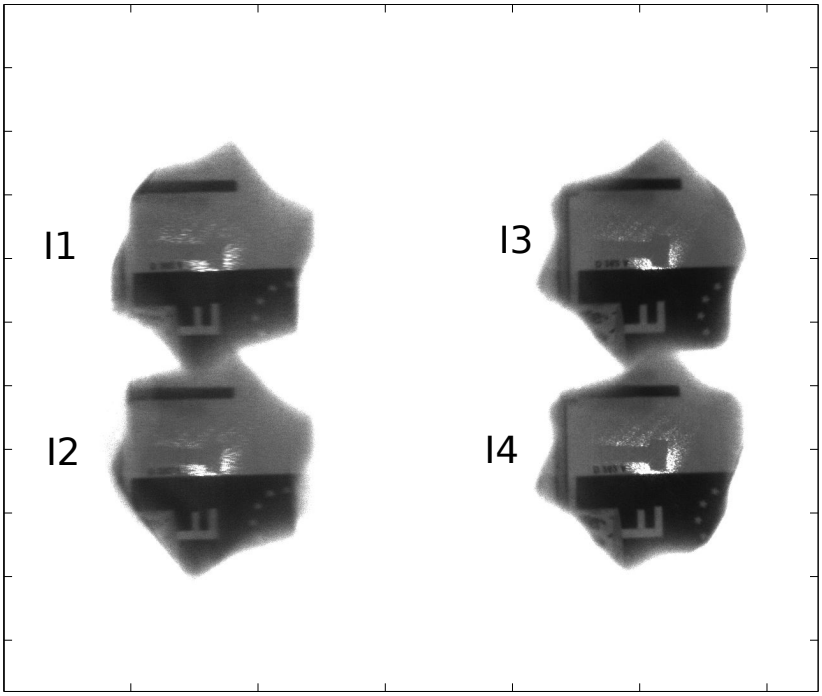

Figure 5.15: A single frame taken from the camera and calibrated for intensity mismatch. The frame shows four images of the same scene, which are at phases 0, $\pi/2$, π and $3\pi/2$.

With the four images extracted from the single frame using calibration methodology discussed before, the amplitude, phase and intensity can easily be calculated as (see Appendix D for details)

$$A = \frac{1}{2}\sqrt{(I_1 - I_3)^2 + (I_2 - I_4)^2}, \tag{5.22}$$

$$\phi = tan^{-1}\left[(I_2 - I_4)./(I_1 - I_3)\right], \tag{5.23}$$

$$I = \frac{1}{4}(I_1 + I_3 + I_2 + I_4). \tag{5.24}$$

The background rejection and selective imaging of modulated light is demonstrated in Fig. 5.16. It is worth reminding that these 1 kHz demodulation images are obtained from a single frame with a conventional camera working at 200 ms exposure time.

5.4 Intensity modulated imaging through turbid media

In chapter 4 it was derived that to attain ballistic photons imaging in an intensity (de) modulation imaging scheme, a minimum frequency of modulation is required, which depends on the reduced scattering parameter. The minimum frequency in a general case can be in MHz range or above. With the full-field demodulation camera described here, these frequencies are reachable. A clear perspective of the work is design of modulation circuit capable of providing high voltage ramp at 10 MHz (and even few Ghz) without

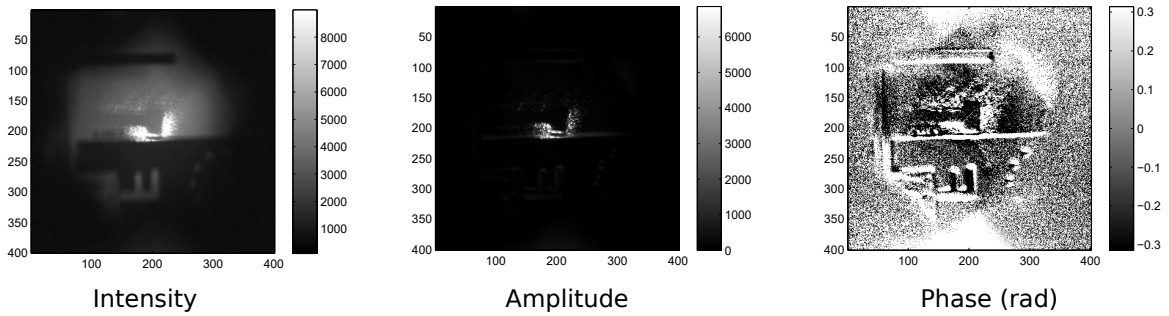

Figure 5.16: Intensity, amplitude and phase images estimated from a single frame of the camera. A modulated coherent source illuminates the central region around the 'T' shaped shadow. The background is illuminated with ambient light.

Table 5.2: Components used in the construction of the full-field quadrature demodulation prototype.

Components	Specification
Polarizers (PV, PH) (Thorlabs, LPVISB050)	500 - 720 nm
Quarter-wave plate (QWP) (Adhesive sheet)	–
Fresnel bi-prism (NewLight photonics inc.)	base 20×20×1.0 mm, apex angle: 160°
Lithium Niobate crystal (LNB) (MolTech GmbH)	2×2×40 mm, Gold electrode coating

any modification to optical module of the imaging system. Working frequency of that the order of MHz a full-field, real-time ballistic photon imaging may be demonstrated using the proposed ffQDC.

5.5 Summary

A novel, full-field demodulation camera was developed in this chapter to fill the technological gap that exists today in the context of high frequency full-field demodulation. In the context of this thesis, the invention of this camera arises from the initial motivation of developing imaging systems for seeing through fog and tissues which require high frequencies of modulation as shown in chapter 5. The use of EOM in an intensity modulation mode increases the potential of such an imaging system to be used at various frequencies up to GHz range. Simple optical elements were used to obtain two simultaneous images of the entire scene which are in quadrature phase with respect to each other. The proposed imaging system is thus well suited for even transport application where it is necessary to obtain real-time imaging. The specification of various components used in the construction of the device are mentioned in Table 5.2 and the advantages and limitations are listen in the following sections.

5.5.1 Advantages

Modularity and Portability The proposed ffQDC is designed to be modular. As seen in Fig. 5.6a, the imaging system consists of an optical module placed in front of a conventional intensity camera and an objective. This modularity opens up possibilities of adapting the camera to specific purposes. For example, the intensity camera can be replaced with a low-noise high gain camera if the photon budget is small or a small mobile phone camera to maximize portability and dissemination. It can be replaced with a camera with high response in near-infrared wavelengths to be used in biomedical imaging or even a thermal camera (with suitable electro-optics crystal) may be used for defense related applications. Further, the EOM module is placed such that it can be removed for the setup or controlled at a fixed voltage to operate as an intensity camera. The dimensions of the whole camera remains relatively small as well. For instance, the prototype developed during the thesis is about 25 cm $\times$ 10 cm in dimensions. The dimensions can be further reduced by using custom optics where the lenses, Fresnel prism, polarizers and quarter-wave plate can be designed as a single unit.

Synchronization and Noise On of the main advantages of a quadrature detection scheme is that it requires no synchronization with an external source of light. This is ideal for scenarios like transport through degraded weather conditions where a beacon of modulated light can be placed to delimit the secured pathway and the demodulation camera may aide in navigation. For example, in the case of aircraft landing, modulated light sources can be placed on the runway and an on-board demodulation camera may provide visual aide to the pilot during foggy weather. The long distances involved in such applications require that the source and detector are independent and not synchronized.

Frequency tunability The use of an EOM as a voltage controlled shutter has the potential to be operated at the ultra high frequency range of the order of GHz. This opens up application in various domains like 3D imaging at microscopic scales. Although, the EOM requires peak voltages of the order of hundred volts, it is an order of magnitude less than what is required by gain modulated intensifier cameras that was reviewed in section 5.1.1. Moreover, it offers possible frequency tunability without any change of the optical components of the camera.

Limited electronics The proposed ffQDC operates with minimum electronics. The electronics requirements other than the conventional camera are: one synthesizer and high voltage amplifier capable of producing high frequency ramp waveform at peak-to-peak voltages. The imaging system does not require any dephasors or any specific hardware pixel architecture as in the case of ToF cameras.

5.5.2 Limitations

The dependencies of various parameters of the camera on each other is the source of the limitations of the proposed camera which are mentioned below.

Background intensity In the two channel version of the proposed imaging system, the background offset removal remains a challenge when using only single acquisition frame. Although, this is overcome by detuning the source and reference, it does require at least two frames for background estimation. This, in turn, requires fast (60-100 fps) cameras to attain realtime full-field demodulation. However, this limitation in non-existent in the four-channel version of the proposed camera, where a single frame can be used for background offset estimation and cancellation.

High voltage ramp at high frequencies To obtain a 2 π excursion using the EOM and the polarizers, the operating voltage and the dimensions of the EOM are coupled with each other. In our system where a 2 mm $\times$ 2 mm clear aperture was used a peak-to-peak voltage of a around 295 V was required. Obtaining a fair reproduction of a ramp at high frequencies and high voltage is out of the scope of the thesis, but remains technologically attainable.

Field of view The field of view in the proposed imaging system is reduced because two (or four) images share the pixels on the same camera. Further, depending on the angle of the Fresnel prism, the common scene in the two images may be smaller than each image itself. These consideration are taken into account so far and further improvements to the system can be envisaged. Some of the improvement areas are described in following subsection.

Symmetric wave excitation of EOM It is necessary to attain 2 π excursion on the EOM in the intensity modulation mode to attain quadrature demodulation. This can be inferred directly from the transmission curves of the two arms as shown in Fig. 5.4. To attain a sinusoidal transfer function on both the optical arms, a ramp waveform needs to be applied across the faces of the EOM. Usually, it is difficult to generate high voltage ramp waveforms at high frequencies, due to the frequency cut-off of electronics components. Temporally symmetric waveforms are easier to generate (such as triangles) and harmonic (sinusoidal) excitation at high radio frequencies is mostly favorable from the electronics stand point. As a result, the effect of sinusoidal and other symmetric excitation of the EOM was checked theoretically, as shown in Appendix E. This calculation shows that the more the excitation will be asymmetric, the less the effective efficiency of the optical modulation will be, reaching zero efficiency for perfectly symmetric waveforms.
In summary, it is not possible to excite the EOM with symmetric waveforms to achieve quadrature demodulation. However, high frequency sinusoidal excitation can be used over a very low frequency ramp that explored the whole 2π phase excursion of the EOM.

This method considerably reduces the efficiency of detection and is only studied as a laboratory technological alternative to applying high frequency ramp voltage on the EOM.

Monochromatic illumination The demodulation possible due to the EOM is sensitive to the wavelength of light. This restricts the usage to a narrow band illuminating source of light.

5.5.3 Improvements

Compound optical component design On of the obvious improvements over the prototype device is the replacement of all the optical components as a single optical mount. The polarizers, prism, the quarter-wave plate, the lenses and even the EOM can be designed as a single component that can be attached to any existing camera to convert it into full-field intensity demodulator with only simple additional electronics. Such an integrated design may help the system to be more portable and robust than the prototype version.

Three-cameras The use of the Fresnel bi-prism keeps the system modular and versatile, but reduces the field of view. To improve upon this design, a three way prism beam splitter along with three separate camera sensors may be used. The three-way beam splitter may replace the Fresnel bi-prism and the three emerging optical arms may go through transfer function proportional to $(1 + \ cos\,[\phi])$, $(1 - \ cos\,[\phi])$ and $(1 + \ sin\,[\phi])$ of the phase applied to the EOM. The arms with phase difference of π can be used to estimate the mean intensity at each pixel. The mean intensity can be subtracted from the quadrature components to estimate the amplitude and the phase in real-time. However, the camera sensors need to be synchronized with each other.

Use of polarimetric camera Recent development in polarimetric cameras have produced division of focus sensors where a super pixel consisting of (at least) four pixels is used. Each pixel in the super pixel is aligned with an array of liner, circular or elliptical polarizers [63]. With a small modification to such cameras, they can replace the Fresnel bi-prism, quarter wave plate and the end polarizers to produce a compact demodulation camera.

Polymer based EOM Finally, a recent class of electro-optic polymers [131] may replace the EOM crystal all together to obtain full-field demodulation with less power consumption and compact design.

5.5.4 Potential applications

Despite the listed drawbacks and limitations, the development of a robust, exploitable prototype using the proposed ways of improvement is a promising perspective to this thesis. Indeed, an EOM-based, all optical, full-field intensity demodulation camera that does not require synchronization with the source is novel and applications in many fields of science and technology can be envisaged.

Ballistic imaging through turbid media As presented in chapter 5, a full-field demodulation camera may be used to attain ballistic filtering where the minimum operating frequency depends on the scattering parameters of the medium. The minimum frequency may range from 100 kHz to 1000 MHz depending on the intervening medium. For applications in navigation in degraded weather conditions, it is essential to have real-time imaging capabilities, portability and no synchronization. The proposed camera is well-suited for such applications. Aircraft landing and taxiing in foggy weather is a major limitation in some small airports that do not have category III instrument landing systems. In such cases the pilot has to rely on vision and visual aide. A further concern in light fog situation is the timing between consecutive landings. A small decrease in the timing between landings of two aircrafts can have a major impact on the traffic flow in airports. A lot of effort is being made to reduce this time to ensure steady flow of aircraft traffic. Such a demodulation camera can indeed aide in vision in degraded weather conditions or just to enhance the visibility of the runway indicators.

Biomedical imaging through tissues Another major use of such a camera can be estimation absorption coefficients in tissues by using diffused light. Hitherto, fiber optics and fast photo detectors are used to demodulate light and produce scattering inhomogeneity maps within tissues, but with low resolution. A full-field demodulator may help in obtaining such maps in real-time. The portability of the system ensures that it can be used in remote locations where access to technology is limited.

3D imaging Although, the ToF camera is suitable for 3D imaging, it is limited by its resolution, sensitivity and maximum operating frequency. The resolution of the proposed camera is only limited by the resolution of the intensity camera which can be easily replaced due to the modularity of the system. High resolution 3D ranging, may be used in both consumer applications and defense related applications.

Vibration analysis In aircraft industries, space industry and heavy machinery industry, high frequency vibrational stress is one of the problems. A full-field demodulation camera can be used to attain the vibrational modes by sweeping the frequencies of the source and the detector.
The varied potential applications and robustness of the invented imaging system makes it a lucrative device for transition from research to industry.

Conclusion

The thesis presents a rigorous study of imaging of active light sources through turbid media, especially, through fog. The work spans across various domains from designing of experiments and engineering novel imaging systems to applying photon transport theory and information theory to attain optimal imaging through fog.

In the first part of the thesis, where a Wollaston prism-based snapshot polarimetric camera is used to image polarized beacon through fog, a contrast gain with respect to an intensity camera of at least 2 times and maximum of about 12 times was reported experimentally using an optimal polarimetric representation. The imaging system was studied end-to-end from calibration of the polarimetric imager, acquisition control to its use in an original outdoor experiment for data collection in real atmospheric conditions. Alongside, analytical expressions were derived to quantify the gain in precision that can be expected while using such of the polarimetric imaging system. The information theoretical analysis was also extended to include generic experimental conditions which may be helpful in polarimetric imaging scenarios other than the one considered in this thesis. Finally, it is concluded that such a simple two-channel polarimetric camera can be used to detect polarized beacons of light through fog with high efficient. The simplicity, efficiency and robustness of the imaging system makes it suitable to be used in real-life situations, for example in case of visual aide to pilot in degraded weather conditions.

In the second part of the thesis, the possibility of attaining efficient imaging of intensity modulated sources through turbid media was explored. A modulation/demodulation scheme is known to provide SNR enhancement by background rejection and, thus, is inherently capable of isolating active modulated sources through fog, even at low frequencies of modulation, making it comparable with the polarimetric camera by design. However, it was noticed that an intensity modulation scheme can have further advantages. By using a diffusion model for photon transport and a noise model for a generic quadrature detection scheme, it was shown that it is possible to discriminate ballistic photons from diffuse photons using intensity (de)modulation imaging. Again, using the noise model parameterized by the diffusion theory of photon transport, a minimum modulation frequency for achieving ballistic photon imaging for any given photon budget was analytically derived. It was deduced that in for imaging through fog or other dense turbid media, modulation frequencies of the order of MHz and above is required. To fill the technological gap for real-time full-field demodulation at such frequencies, a novel demodulation camera was proposed and patented. The camera that was developed in-house is potentially capable of imaging in GHz range in real-time. Eventually, the prototype of the camera and its variation was designed, built and calibrated. Using the imaging system in a real experiment scenario remain a clear perspective of the work, which would complete the research ideology behind this thesis.

Even though, the thesis had a well-defined goal, the techniques developed herein apply to a wider field, especially, in biomedical imaging. Some of the results presented in the thesis apply directly to medical imaging, hopefully, making the work of wide interest. The

results presented in this thesis, pave way for transition of these advanced imaging systems into real-life situations.

Appendices

A Fisher information and Cramer-Rao bound

A.1 Observation and expectation

In any measurement system, the observed data is not devoid of unpredictable fluctuations. The resulting error in measurement can arise either due to the detection system or the physical process underlying the experiment itself. The nature of these fluctuations and the distribution followed by the random processes depend on the design of the experiment. Generically, an experiment is designed around determining some quantities of interest according to a theoretical model. An experimenter expects to observe smooth functions as predicted by the theory but instead the measurements are noisy and vaguely correspond to smooth functions. The statistical approach addresses this by distinguishing between observations and expectations. The goal of statistical methods is to design the experiment and process the observed data such that the parameters of interest can be deduced as efficiently as physically possible.

Let us consider an experiment that produces a observed random vector $\boldsymbol{y} = [y_1, y_2, .., y_M]^T$ and N independent experiments are performed to produce the data $\boldsymbol{y}_1, \boldsymbol{y}_2, .., \boldsymbol{y}_N$. The quantity of interest may be given by theory as parametric function of the observed data, such that the expectation value (denoted by $\langle . \rangle$) of this function is given by $\langle g(\boldsymbol{Y}, \boldsymbol{\theta}) \rangle$. The parameter vector, $\boldsymbol{\theta} = [\theta_1, \theta_2, .., \theta_K]$, is generally unknown and their expectation values must be determined from the observed data. The observation, which is a random variable, $\boldsymbol{Y}$ may be assigned a suited PDF that should be determined from the experimental design. The theoretical expected dependency of the measurement on the parameters $\boldsymbol{\theta}$ may serve as the noise model to parametrize the PDF, which will be denoted here as $p(\boldsymbol{Y}|\boldsymbol{\theta})$. Then, the expectation of any function $f(\boldsymbol{Y})$ can be mathematically presented as

$$\langle f(\boldsymbol{y}) \rangle = \int_{-\infty}^{\infty} f(\boldsymbol{y}) p(\boldsymbol{Y}|\boldsymbol{\theta}) d\boldsymbol{y} \tag{.25}$$

where, the integration can be replaced by summation in the context of discrete values, wherever applicable.

A.2 Distinguishability and Information

Let us introduce the concept of information content in observables. The concept of information can be introduced in various ways leading to interpretations that may differ from one another. For an intuitive and simple description, one can resort to the concept of distinguishability. The following brief derivation is inspired from [132]. Starting with the question, how well can two random variables with well defined parametric probability distributions be distinguished from each other, the relative difference (Δ_a) between $p(\boldsymbol{Y}|\boldsymbol{\theta})$ and $p(\boldsymbol{Y}|\boldsymbol{\theta} + \boldsymbol{d\theta})$ can be simply written as

$$\Delta_a = \frac{p(\boldsymbol{Y}|\boldsymbol{\theta} + \boldsymbol{d\theta}) - p(\boldsymbol{Y}|\boldsymbol{\theta})}{p(\boldsymbol{Y}|\boldsymbol{\theta})} = \frac{\partial \, ln \, [p(\boldsymbol{Y}|\boldsymbol{\theta})]}{\partial \theta_a} d\theta_a \tag{.26}$$

The expectation value of the relative difference quickly vanishes, i.e. $\langle \Delta \rangle = 0$. However, the covariance takes the form

$$\left\langle \Delta_{ab}^2 \right\rangle = \int_{-\infty}^{\infty} d\boldsymbol{y}\ p(\boldsymbol{Y}|\boldsymbol{\theta}) \frac{\partial\ ln\left[p(\boldsymbol{Y}|\boldsymbol{\theta})\right]}{\partial \theta_a} \frac{\partial\ ln\left[p(\boldsymbol{Y}|\boldsymbol{\theta})\right]}{\partial \theta_b}\ d\theta_a d\theta_b \tag{.27}$$

It may be noted that the term $\frac{\partial\ ln[p(\boldsymbol{Y}|\boldsymbol{\theta})]}{\partial \theta_a}$ is the Fisher score with respect to parameter θ_a [133] and the non-vanishing covariance $\left\langle \Delta_{ab}^2 \right\rangle$ can yield a measure of distinguishability through the matrix $\mathcal{F}(\boldsymbol{\theta})$ such that $dl^2 = \left\langle \Delta_{ab}^2 \right\rangle = \mathcal{F}_{ab}(\boldsymbol{\theta})\theta_a\theta_b$. The matrix, which was emphasized in the works of Ronald Fisher, is called the FIM and is defined such that the a^{th}, b^{th} component of the matrix is

$$\mathcal{F}_{ab}(\boldsymbol{\theta}) = -\left\langle \frac{\partial\ ln\left[p(\boldsymbol{Y}|\boldsymbol{\theta})\right]}{\partial \theta_a} \frac{\partial\ ln\left[p(\boldsymbol{Y}|\boldsymbol{\theta})\right]}{\partial \theta_b} \right\rangle \tag{.28}$$

Fisher information has been interpreted as the amount of information brought forward by the observable random variable $\boldsymbol{Y}$ to estimate the parameters $\boldsymbol{\theta}$ of the distribution that describes the measurement.

A.3 Reparametrization

Usually, when solving an estimation problem, a theoretical model may present another vector of parameters $\boldsymbol{\theta'}$ that are related to $\boldsymbol{\theta}$. In this case, the FIM for a change in parameters $\boldsymbol{\theta} \rightarrow \boldsymbol{\theta'}$ can be achieved simply by obtaining the Jacobian matrix of the transformation defined by $J_{ab} = \frac{\partial \theta_a}{\partial \theta'_b}$. Then, the transformed FIM is $\mathcal{F}(\boldsymbol{\theta'}) = J^T\ \mathcal{F}(\boldsymbol{\theta})\ J$.

A.4 Fisher information matrix for multivariate Gaussian PDF

The log-likelihood function of a multivariate Gaussian distributed random variable is

$$ln\left[p(x)\right] = -\frac{N}{2}\ ln\left[2\pi\right] - \frac{1}{2}\ ln\left[|\Gamma|\right] - \frac{1}{2}(x-\mu)^T\Gamma^{-1}(x-\mu), \tag{.29}$$

where, μ and Γ are functions of $d-$dimensional parameter vector $\boldsymbol{\theta} = \theta_{i=1,2,...d}$. Then, using matrix identities $\partial(\ ln\left[|A|\right]) = tr\left[A^{-1}\partial A\right]$ and $\partial(A^{-1}) = -A^{-1}\partial A A^{-1}$ [134], and noting that for positive symmetric matrix Γ, $(x-\mu)^T\Gamma^{-1}\partial\mu = \partial\mu\Gamma^{-1}(x-\mu)^T$, the Fisher score with respect any parameter θ_k is calculated as

$$\frac{\partial\ ln\left[p(x)\right]}{\partial \theta_k} = -\frac{1}{2}tr[\Gamma^{-1}\frac{\partial\Gamma}{\partial\theta_k}] + \frac{1}{2}(x-\mu)^T\Gamma^{-1}\frac{\partial\Gamma}{\partial\theta_k}\Gamma^{-1}(x-\mu) - \frac{\partial\mu^T}{\partial\theta_k}\Gamma^{-1}(x-\mu) \tag{.30}$$

Then, the FIM is the covariance matrix of the Fisher score, thus, the $(k,l)^{th}$ component of

the FIM is calculated by keeping in mind $\langle x-\mu\rangle = 0$, as

$$\begin{aligned}
\mathcal{F}_{kl} &= -\left\langle \frac{\partial\, ln\,[p(x)]}{\partial\theta_k} \times \frac{\partial\, ln\,[p(x)]}{\partial\theta_l} \right\rangle \\
&= \frac{\partial\mu}{\partial\theta_k}^T \Gamma^{-1}\frac{\partial\mu}{\partial\theta_l} + \frac{1}{4}tr\left[\Gamma^{-1}\frac{\partial\Gamma}{\partial\theta_k}\right] tr\left[\Gamma^{-1}\frac{\partial\Gamma}{\partial\theta_l}\right] \\
&- \frac{1}{4}tr\left[\Gamma^{-1}\frac{\partial\Gamma}{\partial\theta_k}\right]\left\langle (x-\mu)^T\Gamma^{-1}\frac{\partial\Gamma}{\partial\theta_l}\Gamma^{-1}(x-\mu)\right\rangle \\
&- \frac{1}{4}\left\langle (x-\mu)^T\Gamma^{-1}\frac{\partial\Gamma}{\partial\theta_k}\Gamma^{-1}(x-\mu)\right\rangle tr\left[\Gamma^{-1}\frac{\partial\Gamma}{\partial\theta_l}\right] \\
&+ \frac{1}{4}\left\langle (x-\mu)^T\Gamma^{-1}\frac{\partial\Gamma}{\partial\theta_k}\Gamma^{-1}\frac{\partial\Gamma}{\partial\theta_l}\Gamma^{-1}(x-\mu)\right\rangle
\end{aligned}$$

Then, noting that for a random variable y with $\langle y\rangle = 0$ and covariance Γ, $\langle y^TAy\rangle = tr\,[A\Gamma]$ [134] and $\langle y^TAyy^TBy\rangle = tr\left[A\Gamma(B+B^T)\Gamma\right] + tr\left[A\Gamma^{-1}\right] tr\left[B\Gamma^{-1}\right]$ [134, 84], one obtains,

$$\mathcal{F}_{kl} = -\left\langle \frac{\partial\, ln\,[p(x)]}{\partial\theta_k} \times \frac{\partial\, ln\,[p(x)]}{\partial\theta_l} \right\rangle = \frac{\partial\mu}{\partial\theta_k}^T \Gamma^{-1}\frac{\partial\mu}{\partial\theta_l} + \frac{1}{2}tr\left[\Gamma^{-1}\frac{\partial\Gamma}{\partial\theta_k}\Gamma^{-1}\frac{\partial\Gamma}{\partial\theta_l}\right] \tag{.31}$$

The above derivation is given here because of its rarity in literature. An equivalent derivation is reported in [84].

B Polarimetric imaging

B.1 Maximum-likelihood estimator of the source intensity

The log-likelihood function for a set of N polarimetric pixels, under the Gaussian hypothesis is written as

$$\mathcal{L}(x) = ln\,[P(x)] = \sum_{i=1}^{N} - ln\,[2\pi\,|\Gamma|] - \frac{1}{2}(x_i - \langle x\rangle)^T\Gamma^{-1}(x_i - \langle x\rangle). \tag{.32}$$

Then, the ML estimator $\hat{s}_{ML}$ is derived by solving $\partial\mathcal{L}(x)/\partial s = 0$, which reduces to (since Γ is independent of s)

$$\frac{\partial L(x)}{\partial s} = -\sum_{i=1}^{N}\frac{1}{2}\left[\left(\frac{\partial\langle x\rangle}{\partial s}\right)^T\Gamma^{-1}(x_i - \langle x\rangle) + (x_i - \langle x\rangle)^T\Gamma^{-1}\frac{\partial\langle x\rangle}{\partial s}\right] = 0. \tag{.33}$$

Consequently, one obtains the estimator $\hat{s}_{ML} = (1/Z)(U\frac{1}{N}\sum_{i=1}^{N}x_{i,\parallel} + V\frac{1}{N}\sum_{i=1}^{N}x_{i,\perp} + C)$, where U, V, C and Z are given by

$$U = -\sqrt{1-\beta^2}(1-P)\rho + (1-\beta)(1+P) \tag{.34a}$$

$$V = -\sqrt{1-\beta^2}(1+P)\rho + (1+\beta)(1-P) \tag{.34b}$$

$$C = b\left(\beta^2 + \sqrt{1-\beta^2}\rho - P\beta\rho\sqrt{1-\beta^2} - 1\right) \tag{.34c}$$

$$Z = 1 - \beta^2 - \sqrt{1-\beta^2}\rho(1-P^2) + (P-\beta)^2 \tag{.34d}$$

Noting that, $\langle x_{\parallel} \rangle = s(1+P)/2 + b(1+\beta)/2$ and $\langle x_{\perp} \rangle = s(1-P)/2 + b(1-\beta)/2$, it can be checked that $\langle \hat{s}_{ML} \rangle = s$. Hence, the estimator is unbiased.

B.2 Polarimetric efficiency

The gain is given by

$$\mathcal{G} = \frac{\mathcal{F}(s)}{\mathcal{F}_{IC}} = \frac{1}{(1-\rho^2)} \left[1 + \frac{(P-\beta)^2}{1-\beta^2} - \frac{\rho(1-P^2)}{\sqrt{1-\beta^2}} \right]$$

Solving the above equation for ρ to attain a gain $\mathcal{G} = k$ gives,

$$\rho = \frac{(1-P^2)\left(1 \pm \sqrt{1 + \frac{4k[(1-\beta^2)(k-1)-(P-\beta)^2]}{(1-P^2)^2}}\right)}{2\left(\sqrt{1-\beta^2}k\right)} \tag{.35}$$

A gain greater than equal to k can be expected, independent of the value of ρ, when the term inside the square root is less than zero. This computes the bounding region where a gain can be expected irrespective of the value of ρ, which yields

$$(1+P)^2 \geq 2k(1+\beta), \quad P > \beta \tag{.36a}$$

$$(1-P)^2 \geq 2k(1-\beta), \quad P < \beta \tag{.36b}$$

Thus, for $\beta = 0$, the minimum value of P for which a gain greater unity can always be expected is given by $P > \sqrt{2} - 1$.

C Intensity modulated light and quadrature demodulation

C.1 Joint PDF of amplitude and phase

Let us consider quadrature components $[U, V]^T$ as joint Gaussian random variables with mean $[A\ cos\,[\phi]\,, A\ sin\,[\phi]]^T$ and covariance matrix $\Sigma = \text{Diag.}\left([\Lambda^2, \Lambda^2]\right)$. Then, the joint distribution of the random variables U and V is

$$\begin{aligned} &P_{U,V}(u, v|A, \phi, \Lambda^2) = \\ &\frac{1}{2\pi\Lambda^2}\ exp\left[-\frac{(u - A\ cos\,[\phi])^2 + (v - A\ sin\,[\phi])^2}{2\Lambda^2}\right]. \end{aligned} \tag{.37}$$

For a change of variables, such that $Z = \sqrt{U^2 + V^2}$ and $\Psi = \tan^{-1}[V/U] \implies U = Z\ cos\,[\Psi]\,, V = Z\ sin\,[\Psi]$, changed PDF can be obtained by noting that

$$\begin{aligned} P_{Z,\Psi}(z, \psi|A, \phi, \Lambda^2) &= P_{U,V}(u, v|A, \phi, \Lambda^2) \left| J_{u,v}^{z,\psi} \right| \\ &= \frac{z}{2\pi\Lambda^2}\ exp\left[-\frac{1}{2\Lambda^2}(z^2 + A^2 - 2zA\ cos\,[\psi - \phi])\right], \end{aligned} \tag{.38}$$

where, $J_{u,v}^{z,\psi}$ is the Jacobian of the transformation $\{u, v\} \to \{z, \psi\}$ and $|.|$ is the determinant.

C.2 Moments of the pdf

$$\langle z \rangle = \int_0^\infty \int_0^{2\pi} z P_{Z,\Psi}(z,\psi|A,\phi,\Lambda^2) d\phi dz = \tag{.39}$$

$$\langle z^2 \rangle = \int_0^\infty \int_0^{2\pi} z^2 P_{Z,\Psi}(z,\psi|A,\phi,\Lambda^2) d\phi dz = A^2 + 2\Lambda^2 \tag{.40}$$

$$\langle z\ cos\,[\psi] \rangle = \int_0^\infty \int_0^{2\pi} z\ cos\,[\psi]\ P_{Z,\Psi}(z,\psi|A,\phi,\Lambda^2) d\phi dz = A \tag{.41}$$

$$\langle z\ sin\,[\phi] \rangle = 0 \tag{.42}$$

C.3 Noise variance

At each time slice t_i the photons received at the detector can be modeled as having Poisson noise with variance equal to the mean. Then, the optical noise variance at each slice is $I(t_i) = I_0(1 + M\ cos\,[2\pi t_i/T])$. The quadrature components are obtained by weighing each slice with sine and cosine of same frequency. Thus, the total noise variance will propagate as

$$\begin{aligned}
\text{var}(V) &= \sum_{i=0}^{nT} sin\,[2\pi t_i/T + \phi_r]^2\, I(t) \\
&= \frac{I_0}{2} + I_0 M \sum_{i=0}^{nT} (\ sin\,[2\pi t_i/T + \phi_r]\ (\ sin\,[4\pi t_i/T + \phi_r] + \ sin\,[\phi_r])) \\
&= \frac{I_0}{2}
\end{aligned}$$

Similarly, one shows $\text{var}(U) = \frac{I_0}{2}$.

C.4 Jacobian matrix of the transformation $\theta' \to \theta$ for diffuse light only

The Jacobian matrix for $\boldsymbol{\theta'} = [A, \phi, \Lambda^2] \to \boldsymbol{\theta} = [M, R_\delta, R_*]$

$$J_{\mathcal{D}} = \begin{bmatrix} \frac{3}{2}e^{-qR_\delta}R_* S_0 & -\frac{3}{2}e^{-qR_\delta}MqR_* S_0 & \frac{3}{2}e^{-qR_\delta}MS_0 \\ 0 & \sqrt{-1+q^2} & 0 \\ 0 & -\frac{3}{2}e^{-R_\delta}R_* S_0 & \frac{3}{2}e^{-R_\delta}S_0 \end{bmatrix}. \tag{.43}$$

C.5 Fisher information $\mathcal{F}_{\mathcal{D}}(\boldsymbol{\theta})$

In the presence of diffused light only, the FIM for a change of coordinates $\boldsymbol{\theta'} \to \boldsymbol{\theta}$ is simply calculated by $\mathcal{F}_{\mathcal{D}}(\boldsymbol{\theta}) = J_{\mathcal{D}}^T\ \mathcal{F}(\boldsymbol{\theta'})\ J_{\mathcal{D}}$ as,

$$\mathcal{F}(\boldsymbol{\theta}) = \begin{bmatrix} \frac{3}{2}e^{(1-2q)R_\delta}R_* S_0 & -\frac{3}{2}e^{(1-2q)R_\delta}MqR_* S_0 & \frac{3}{2}e^{(1-2q)R_\delta}MS_0 \\ -\frac{3}{2}e^{(1-2q)R_\delta}MqR_* S_0 & 1 + \frac{3}{2}e^{(1-2q)R_\delta}M^2\left(-1+2q^2\right)R_* S_0 & -\frac{1}{R_*} - \frac{3}{2}e^{(1-2q)R_\delta}M^2 q S_0 \\ \frac{3}{2}e^{(1-2q)R_\delta}MS_0 & -\frac{1}{R_*} - \frac{3}{2}e^{(1-2q)R_\delta}M^2 q S_0 & \frac{2+3e^{(1-2q)R_\delta}M^2 R_* S_0}{2R_*^2} \end{bmatrix}. \tag{.44}$$

C.6 Amplitude detected at ballistic and diffused regions

Diffused region $\mathcal{D}$ When the detector (or a pixel) receives only diffused light, the quadrature components detected are given by

$$\begin{aligned} u_D &= \int I_D(1 + m_D\ cos\left[\omega t - \phi_D\right])\ cos\left[\omega t + \delta\phi\right] dt \\ &= \frac{I_D m_D}{2}\ cos\left[\phi_D + \delta\phi\right] \end{aligned}$$

$$\begin{aligned} v_D &= \int I_D(1 + m_D\ cos\left[\omega t - \phi_D\right])\ sin\left[\omega t + \delta\phi\right] dt \\ &= \frac{I_D m_D}{2}\ sin\left[\phi_D + \delta\phi\right]. \end{aligned}$$

Ballistic + Diffused region $\mathcal{B} \oplus \mathcal{D}$ When the detector (or a pixel) receives both contributions of diffused light and ballistic light, the quadrature components detected have the following expressions (with phases taken with respect to ϕ_B, i.e. $\phi_B = 0$, without loss of generality)

$$\begin{aligned} u_{\mathcal{B}\oplus\mathcal{D}} = &\int \left[I_D(1 + m_D\ cos\left[\omega t - \phi_D\right]) + I_B(1 + m_B\ cos\left[\omega t\right])\right] \\ &\times\ cos\left[\omega t + \delta\phi\right] dt \\ &= \frac{I_D m_D}{2}\ cos\left[\phi_D + \delta\phi\right] + \frac{I_B m_B}{2}\ cos\left[\delta\phi\right] \end{aligned}$$

Similarly,

$$v_{\mathcal{B}\oplus\mathcal{D}} = \frac{I_D m_D}{2}\ sin\left[\phi_D + \delta\phi\right] + \frac{I_B m_B}{2}\ sin\left[\delta\phi\right].$$

Amplitudes As a consequence of the above derivations, the amplitudes estimated on detectors that receive only diffused light and detectors that receive both ballistic and diffused light respectively read

$$A^2_{\mathcal{D}} = \frac{I_D^2 m_D^2}{4}$$

$$\begin{aligned} A^2_{\mathcal{B}\oplus\mathcal{D}} =& \frac{I_D^2 m_D^2}{4} + \frac{I_B^2 m_B^2}{4} + \frac{I_D I_B m_D m_B}{2}\ cos\left[\phi_D\right] \\ =& \frac{I_D^2 m_D^2}{4}\left(1 + \alpha^2\beta^2 + 2\alpha\beta\ cos\left[\phi_D\right]\right). \end{aligned}$$

D All-optical full-field quadrature demodulation camera

Using an EOM, polarizers and quarterwave plate a quadrature demodulation scheme can be envisaged. Four optical arms can be designed such that they have the tranfer functions as given below

$$\mathcal{T}_1[\Delta\phi] = P_h.\left(\mathcal{R}\left[\tfrac{-\pi}{4}\right].EOM[\Delta\phi].\mathcal{R}\left[\tfrac{\pi}{4}\right]\right).P_v.I_{in} = T_0(1 - cos\,[\Delta\phi]) \quad (.45)$$

$$\mathcal{T}_2[\Delta\phi] = P_h.Q.\left(\mathcal{R}\left[\tfrac{-\pi}{4}\right].EOM[\Delta\phi].\mathcal{R}\left[\tfrac{\pi}{4}\right]\right).P_v.I_{in} = T_0(1 - sin\,[\Delta\phi]) \quad (.46)$$

$$\mathcal{T}_3[\Delta\phi] = P_v.\left(\mathcal{R}\left[\tfrac{-\pi}{4}\right].EOM[\Delta\phi].\mathcal{R}\left[\tfrac{\pi}{4}\right]\right).P_v.I_{in} = T_0(1 + cos\,[\Delta\phi]) \quad (.47)$$

$$\mathcal{T}_4[\Delta\phi] = P_v.Q.\left(\mathcal{R}\left[\tfrac{-\pi}{4}\right].EOM[\Delta\phi].\mathcal{R}\left[\tfrac{\pi}{4}\right]\right).P_v.I_{in} = T_0(1 + sin\,[\Delta\phi]), \quad (.48)$$

where, $I_{in} = [1, 1]^T$ and T_0 is arbitrary constant scaling factor.
Given a sinusoidally modulated signal $i(t) = I_0(1 + M\,cos\,[\omega t + \phi])$ passing through the arm 1 which is excited with ramp voltage to attain a sinusoidal shuttering having transfer function $\mathcal{T}_1[\omega t]$, the intensity received at the camera is

$$\begin{aligned} I_1'(t) &= i(t)\mathcal{T}_1[\omega t] \\ &= T_0 I_0\left(1 - \frac{M}{2}\,cos\,[\phi] + M\,cos\,[\omega t + \phi] - cos\,[\omega t] - \frac{M}{2}\,cos\,[2\omega t + \phi]\right) \end{aligned}$$

This signal is integrated over the exposure time of the camera, ϵ, yielding

$$\begin{aligned} I_1 &= \int_0^{\epsilon} I_1'(t)dt \\ &= T_0 I_0\left(\epsilon - \frac{1}{2}M\epsilon\,cos\,[\phi] + \frac{M\,sin\,[\omega\epsilon + \phi]}{\omega} - \frac{M\,sin\,[2\omega\epsilon + \phi]}{4\omega} - \frac{3M\,sin\,[\phi]}{4\omega} - \frac{sin\,[\omega\epsilon]}{\omega}\right) \end{aligned}$$

For sufficiently high angular frequency ω, the intensities recorded by the camera from the four optical components are

$$\begin{aligned} I_1 &= G(1 - \frac{M}{2}\,cos\,[\phi]), \\ I_2 &= G(1 - \frac{M}{2}\,sin\,[\phi]), \\ I_3 &= G(1 + \frac{M}{2}\,cos\,[\phi]), \\ I_4 &= G(1 + \frac{M}{2}\,sin\,[\phi]), \end{aligned}$$

where $G = T_0 I_0 \epsilon$.
The amplitude of the recieved signal is, thus, $A = MG/2$. When only two optical arms (in-phase and quadrature) are used the background offset term bust me estimated or obtained by other means (for example, by detuning in frequency and capturing multiple frames). When the DC term is subtracted from, say, I_1 and I_2 the ampltude and phase are then calculated as

$$A = \frac{1}{T_0}\sqrt{(I_1 - G)^2 + (I_2 - G)^2}$$

$$\phi = tan^{-1}\left[\frac{I_2 - G}{I_1 - G}\right]$$

But, in a practical situation, using the four optical arms, a single frame captured from the camera can provide the information about the amplitude, phase and the mean intensity as

$$A = \frac{1}{2}\sqrt{(I_1 - I_3)^2 + (I_2 - I_4)^2}$$
$$\phi = \ tan^{-1}\left[\frac{I_1 - I_3}{I_2 - I_4}\right]$$
$$G = \frac{I_1 + I_2 + I_3 + I_4}{4}$$

The above, is the basic principle underlying the invention of the all-optical, full-field demodulation camera proposed in chapter 5.

D.1 Frequency response

When the source and the imaging system are detuned with respect to each other with difference $\Delta\omega$, the intensities detected for each arm in the camera can be written as (assuming $\omega \gg \Delta\omega$)

$$\begin{aligned}
I_1 &= G\left(1 - \frac{M\ sin\left[\Delta\omega\epsilon\right]}{2\Delta\omega\epsilon}\right) \\
I_2 &= G\left(1 - \frac{M\ cos\left[\Delta\omega\epsilon\right]}{2\Delta\omega\epsilon} + \frac{M}{2\Delta\omega\epsilon}\right) \\
I_3 &= G\left(1 + \frac{M\ sin\left[\Delta\omega\epsilon\right]}{2\Delta\omega\epsilon}\right) \\
I_4 &= G\left(1 + \frac{M\ cos\left[\Delta\omega\epsilon\right]}{2\Delta\omega\epsilon} - \frac{M}{2\Delta\omega\epsilon}\right)
\end{aligned}$$

Then, the amplitude is estimated from the four components as

$$A(\Delta\omega, \epsilon) = \frac{GM\ sin\left[\frac{\Delta\omega\epsilon}{2}\right]}{\Delta\omega\epsilon/2}. \tag{.49}$$

D.2 Correction matrix for quadrature demodulation camera

Putting $R = B\Sigma^{-1}B^T$ in $R^TB\Sigma^T\Sigma BR = I$, it is checked that $R = B\Sigma^{-1}B^T$ is indeed the solution.

$$R^TB\Sigma^T\Sigma B^TR = B(\Sigma^{-1})^TB^TB\Sigma^T\Sigma B^TB\Sigma^{-1}B^T = B(\Sigma^{-1})^T\Sigma^TB^T = I$$

For real unitary matrix B.

E EOM phase driving limitations and proposed alternative

E.1 Phase driving limitations

When driving an EOM between minimum to maximum phase shift (typically -π / +π), three limitations can be identified and studied:

- Incomplete scan of the phase shift, with a linear ramp (sawtooth) modulation pattern
- Incomplete scan of the phase shift, with a non-monotonous linear (triangle wave) modulation pattern
- Incomplete scan of the phase shift, with a non- linear (sine wave) modulation pattern

We will consider a sine signal modulation pattern $I(t) = I_0\big[1 + m\cos(\omega_0 t + \phi)\big]$. We also assume that two demodulation arms are available simultaneously, with following transmission responses: $T_1(t) = \big[1 + \cos(\Phi(t))\big]/2$ and $T_2(t) = \big[1 - \sin(\Phi(t))\big]/2$. The effects of each of the above limitations are studied in the following sections

Incomplete scan of the phase shift, with a linear ramp (sawtooth wave) modulation pattern

For a ramp (sawtooth wave) modulation pattern, the phase $\Phi(t)$ applied on the transmission modulators can be written

$$\Phi(t) = \alpha[\omega_0 t - \pi], \text{ for } \omega_0 t \in [0, 2\pi], \text{ and with } \alpha < 1$$

for an incomplete scan.

In this case, the demodulated signal $D_1(t) = T_1(t)I(t)$ can be written:

$$\begin{aligned} D_1(t) = \frac{I_0}{2}\big[1 - \sin(\alpha[\omega_0 t - \pi]) + m\cos(\omega_0 t + \phi])\big] + \frac{mI_0}{4}\sin\big(\omega_0 t + \phi + \alpha[\omega_0 t - \pi]\big) \\ - \frac{mI_0}{4}\sin\big(\omega_0 t + \phi - \alpha[\omega_0 t - \pi]\big). \end{aligned} \tag{.50}$$

After integration over one period of the modulation signal ($T = 2\pi/\omega$), one obtains

$$\begin{aligned} \langle D_1(t)\rangle_T &= \frac{\pi I_0}{\omega_0} + \frac{mI_0}{2\omega_0}\sin\phi\sin(\pi\alpha)\big[\frac{1}{1+\alpha} + \frac{1}{1-\alpha}\big] \\ &= \frac{\pi I_0}{\omega_0}\big[1 + \frac{m}{2}\frac{2\alpha}{1-\alpha^2}\mathrm{sinc}(\pi\alpha)\sin\phi\big] \\ &= \frac{TI_0}{2}\big[1 + \frac{m}{2}\eta_1^r(\alpha)\sin\phi\big], \end{aligned} \tag{.51}$$

where $\eta_1^r(\alpha)$ stands for the modulation depth efficiency when $\alpha < 1$.

As for the demodulation signal $D_2(t)$, one gets

$$\begin{aligned} D_2(t) = \frac{I_0}{2}\big[1 + \cos(\alpha[\omega_0 t - \pi]) + m\cos(\omega_0 t + \phi])\big] + \frac{mI_0}{4}\cos\big(\omega_0 t + \phi + \alpha[\omega_0 t - \pi]\big) \\ + \frac{mI_0}{4}\cos\big(\omega_0 t + \phi - \alpha[\omega_0 t - \pi]\big). \end{aligned} \tag{.52}$$

After integration over one period of the modulation signal ($T = 2\pi/\omega$), one obtains

$$\begin{aligned}\langle D_2(t)\rangle_T &= \frac{\pi I_0}{\omega_0} + \frac{\pi I_0}{\omega_0}\mathrm{sinc}(\pi\alpha) + \frac{m\pi I_0}{2\omega_0}\cos\phi\alpha\mathrm{sinc}(\pi\alpha)\big[\frac{1}{1+\alpha} - \frac{1}{1-\alpha}\big] \\ &= \frac{\pi I_0}{\omega_0}\big[1 + \mathrm{sinc}(\pi\alpha) + \frac{m}{2}\frac{-2\alpha^2}{1-\alpha^2}\mathrm{sinc}(\pi\alpha)\cos\phi\big] \\ &= \frac{TI_0}{2}\big[1 + \gamma_2^r(\alpha) + \frac{m}{2}\eta_2^r(\alpha)\cos\phi\big],\end{aligned} \tag{.53}$$

where $\eta_2^r(\alpha)$ stands for the modulation depth efficiency when $\alpha < 1$, and where $\gamma_2^r(\alpha)$ is a spurious bias on the $\phi-$independent demodulation term.

As a result, demodulation of both quadratures might remain operant provided the modulation depths are not too much reduced due to $\alpha < 1$.

Incomplete scan of the phase shift, with a non-monotonous linear (triangle wave) modulation pattern

For a triangle wave modulation pattern, the phase $\Phi(t)$ applied on the transmission modulators can be written

$\Phi(t) = \alpha[\omega_0 t - \pi]$, for $\omega_0 t \in [0, \pi]$, and $\Phi(t) = \alpha[3\pi - \omega_0 t]$, for $\omega_0 t \in [\pi, 2\pi]$, and with $\alpha < 1$

for an incomplete scan, and β denoting the offset set-point of the phase modulation.

In this case, the demodulated signal $D_1(t) = T_1(t)I(t)$ can be calculated, and after integration over one period of the modulation signal ($T = 2\pi/\omega$), one obtains

$$\begin{aligned}\langle D_1(t)\rangle_T &= \frac{\pi I_0}{\omega_0}\big[1 - \sin\beta\mathrm{sinc}(\pi\alpha) + \frac{m}{2}\frac{-8\alpha^2}{1-4\alpha^2}\frac{\cos(\pi\alpha)}{\pi\alpha}\cos\beta\cos\phi\big] \\ &= \frac{TI_0}{2}\big[1 + \gamma_1^t(\alpha,\beta) + \frac{m}{2}\eta_1^t(\alpha,\beta)\cos\phi\big],\end{aligned} \tag{.54}$$

where $\eta_1^t(\alpha,\beta)$ stands for the modulation depth efficiency when $\alpha < 1$, and where $\gamma_2^t(\alpha,\beta)$ is a spurious bias on the $\phi-$independent demodulation term.

As for the demodulation signal $D_2(t)$, one gets after integration over one period of the modulation signal ($T = 2\pi/\omega$)

$$\begin{aligned}\langle D_2(t)\rangle_T &= \frac{\pi I_0}{\omega_0}\big[1 + \cos\beta\mathrm{sinc}(\pi\alpha) + \frac{m}{2}\frac{8\alpha^2}{1-4\alpha^2}\frac{\cos(\pi\alpha)}{\pi\alpha}\sin\beta\cos\phi\big] \\ &= \frac{TI_0}{2}\big[1 + \gamma_2^t(\alpha,\beta) + \frac{m}{2}\eta_2^t(\alpha,\beta)\cos\phi\big],\end{aligned} \tag{.55}$$

where $\eta_2^t(\alpha,\beta)$ stands for the modulation depth efficiency when $\alpha < 1$, and where $\gamma_2^t(\alpha,\beta)$ is a spurious bias on the $\phi-$independent demodulation term.

As a result, not only the modulation depth will be decreased and the result biased, with $\alpha < 1$ and $\beta \neq 0$, but simultaneous demodulation of both quadratures is not operant

anymore with a triangle wave modulation pattern, since the two outputs are functions of a single quadrature of the phase, i.e., $\cos(\phi)$.

With the above consideration, it is necessary drive the EOM for a full 2π phase with a high voltage sawtooth wave. Since high voltage, high frequency sawtooth generation is electronically challenging (if not impossible), the maximum achievable peak-to-peak voltage for a sawtooth constraints the dimensions of the crystal that can be used.

List of publications

Journal articles

1. Panigrahi, S., Fade, J., Ramachandran, H., and Alouini, M., 'Theoretical optimal modulation frequencies for scattering parameter estimation and ballistic photon filtering in diffusing media,' Opt. Express 24, 16066-16083 (2016)

2. Panigrahi, S., Fade, J., & Alouini, M. (2015). Adaptive polarimetric image representation for contrast optimization of a polarized beacon through fog. Journal of Optics, 17, 65703.

3. Sudarsanam, S., Mathew, J., Panigrahi, S., Fade, J., Alouini, M., & Ramachandran, H. (2016). Real-time imaging through strongly scattering media: seeing through turbid media, instantly. Scientific Reports, 6, 25033.

4. Fade, J., Panigrahi, S., & Alouini, M. (2014). Optimal estimation in polarimetric imaging in the presence of correlated noise fluctuations. Opt. Express, 22(5), 4920–4931.

5. Fade, J., Panigrahi, S., Carré, A., Frein, L., Hamel, C., Bretenaker, F., Ramachandran, H., Alouini, M. (2014). Long-range polarimetric imaging through fog. Applied Optics, 53, 3854–65.

Patent

- Panigrahi S., Ramachandran H., Fade J. and Alouini M., 'Optical receiver for full-field optical quadrature demodulation', PCT/FR2016/051086. 10/05/2016.

Conference papers

1. Panigrahi, S., Fade, J., & Alouini, M. (2014). Contrast enhancement in polarimetric imaging with correlated noise fluctuations. In Max ENT (p. 25). Amboise, France.

2. Panigrahi, S., Fade, J., & Alouini, M. (2015). Adaptive polarimetric image representation for contrast enhancement of a polarized beacon embedded in fog. In Journées Imagerie Optique Non Conventionnelle. Paris, France.

3. Panigrahi, S., Fade, J., & Alouini, M. (2015). Noise correlation-based adaptive polarimetric image representation for contrast enhancement of a polarized beacon in fog. In Image and Signal Processing for Remote Sensing XXI, 96430C (October 15, 2015) (Vol. 9643, p. 96430C–96430C–7). Toulouse, France.

4. Panigrahi, S., Fade, J., & Alouini, M. (2015). Optimal contrast enhancement in long distance snapshot polarimetric imaging through fog. In SPIE Optical Engineering + Applications, Polarization Science and Remote Sensing VII (Vol. 96130, p. 96130V). San Diego, United States.

5. Panigrahi, S., Fade, J., Ramachandran, H., & Alouini, M. (2016). Theoretical derivation of optimal operating frequencies for imaging through turbid media using intensity modulated light. In Journées Imagerie Optique Non Conventionnelle 2016. Paris, France.

Poster communications

1. Fade, J., Panigrahi, S., & Alouini, M. (2014, March). Performances optimales d'estimation en imagerie polarimétrique en présence de fluctuations de bruit corrélées.

2. Panigrahi, S., Fade, J., & Alouini, M. (2015, July). Adaptive polarimetric image representation for detection of polarized beacon of light embedded in fog.

3. Panigrahi, S., Fade, J., Carré, A., Hamel, C., Frein, L., Bretenaker, F., Ramachandran, H., Alouini, M. (2014, March). Imagerie polarimétrique à longue distance à travers le brouillard.

Acknowledgment

The smooth completion of the thesis is a result of the help, support and continuous encouragement from friends, family and colleagues. On the professional side, I am grateful to my advisors Mehdi and Julien for their well-balanced guidance. Their expertize in experimental design and theoretical analysis has not only been instrumental in the completion of the thesis but also helped me to grow as a researcher. Additionally, the collaboration with Pr. Hema Ramachandran has led to collaborative journal papers and a patent. Her encouragement and confidence in me has clearly helped me throughout.

I also deeply appreciate and acknowledge the contribution of the technical team in IPR consisting of Ludovic Frein, Steve Bouhier, Cyril Hamel and Anthony Carré. They were closely involved in setting up the polarized source on the tower. The custom electronics requirements for the experiments were fulfilled with help from Ludovic and Steve, whose expertize made it ever so easy. The custom mechanics of experimental setup were designed with a lot of help from Cyril. Anthony's expertize in 3D printing, graphics design and software issues has helped the experiments and presentation of the thesis. Additionally, they always made themselves available and reachable for even informal discussions from the very beginning. I am grateful to all my colleagues for making me feel welcome and comfortable both personally and professionally. I also thank TDF company for their kind approval for using the tower to put the polarized source and carry out the outdoor experiment. I am grateful to members of the jury, especially Pr. Philippe Réfrégier, for helping in improving the quality of the manuscript.

On a personal note, the thesis has also benefited indirectly from my enjoyable stay in Rennes made possible by support of family from back in India and everlasting friends in Rennes. My gratefulness to my mother, father and sister for their unconditional support is unfathomable and is partly expressed by my dedication of this manuscript to them. Finally, the acknowledgment is not complete without mentioning my closest friends: Mélanie, Alice, Benjamin, Nicolas, Noe and Alba who made my life in Rennes quite cherishable. Thanks to the little concert place called Mondo Bizzaro in Rennes that fulfilled my musical needs. I also owe Pr. Deepak Mathur in TIFR who put a lot of confidence in me in the times of need. Finally, I deeply appreciate the direct and indirect contribution of all the people involved in making of this thesis.

Bibliography

[1] Swapnesh Panigrahi, Julien Fade, and Mehdi Alouini. Adaptive polarimetric image representation for contrast optimization of a polarized beacon through fog. *Journal of Optics*, 17(6):065703, 2015.

[2] Ouk Choi Radu Horaud Miles Hansard, Seungkyu Lee. *Time-of-Flight Cameras: Principles, Methods and Applications*. Springer London, 2013.

[3] Diederik S Wiersma. Disordered photonics. *Nature Photonics*, 7(3):188–196, 2013.

[4] Bruce J Tromberg, Natasha Shah, Ryan Lanning, Albert Cerussi, Jennifer Espinoza, Tuan Pham, Lars Svaasand, and John Butler. Non-Invasive In Vivo Characterization of Breast Tumors Using Photon Migration Spectroscopy. *Neoplasia*, 2(1-2):26–40, 2000.

[5] D A Benaron and D K Stevenson. Optical time-of-flight and absorbance imaging of biologic media. *Science (New York, N.Y.)*, 259(5100):1463–6, 1993.

[6] Hema Ramachandran and Andal Narayanan. Two-dimensional imaging through turbid media using a continuous wave light source. *Optics Communications*, 154(5-6):255–260, September 1998.

[7] Julien Fade, Swapnesh Panigrahi, Anthony Carré, Ludovic Frein, Cyril Hamel, Fabien Bretenaker, Hema Ramachandran, and Mehdi Alouini. Long-range polarimetric imaging through fog. *Appl. Opt.*, 53(18):3854–3865, Jun 2014.

[8] L.V. Wang and H. Wu. *Biomedical Optics: Principles and Imaging*. Wiley, 2007.

[9] Diederik S Wiersma, Paolo Bartolini, Ad Lagendijk, and Roberto Righini. Localization of light in a disordered medium. *Nature*, 390(6661):671–673, 1997.

[10] H Jiang, K D Paulsen, U L Osterberg, B W Pogue, and M S Patterson. Simultaneous reconstruction of optical absorption and scattering maps in turbid media from near-infrared frequency-domain data. *Optics letters*, 20(20):2128–30, 1995.

[11] S T Flock, M S Patterson, B C Wilson, and D R Wyman. Monte Carlo modeling of light propagation in highly scattering tissues. I. Model predictions and comparison with diffusion theory. *IEEE Transactions on Biomedical Engineering*, 36(12):1162–1168, 1989.

[12] Michael S. Patterson, Brian C. Wilson, and Douglas R. Wyman. The propagation of optical radiation in tissue I. Models of radiation transport and their application. *Lasers Med. Sci.*, 6(2):155–168, 1991.

[13] Ori Katz, Pierre Heidmann, Mathias Fink, and Sylvain Gigan. Non-invasive single-shot imaging through scattering layers and around corners via speckle correlations. *Nat Phot.*, 8(10):784–790, 2014.

[14] Sina Farsiu, James Christofferson, Brian Eriksson, Peyman Milanfar, Benjamin Friedlander, Ali Shakouri, and Robert Nowak. Statistical detection and imaging of objects hidden in turbid media using ballistic photons. *Applied optics*, 46(23):5805–5822, 2007.

[15] L Wang, P P Ho, C Liu, G Zhang, and R R Alfano. Ballistic 2-d imaging through scattering walls using an ultrafast optical kerr gate. *Science (New York, N.Y.)*, 253(5021):769–771, 1991.

[16] Q Z Wang, X Liang, L Wang, P P Ho, and R R Alfano. Fourier spatial filter acts as a temporal gate for light propagating through a turbid medium. *Opt. Lett.*, 20(13):1498–1500, 1995.

[17] Emmett N. Leith, Brian G. Hoover, Shawn M. Grannell, Kurt D. Mills, Hsuan S. Chen, and David S. Dilworth. Realization of time gating by use of spatial filtering. *Appl. Opt.*, 38(8):1370–1376, 1999.

[18] M Kempe, A Z Genack, W Rudolph, and P Dorn. Ballistic and diffuse light detection in confocal and heterodyne imaging systems. *J. Opt. Soc. Am. A*, 14(1):216–223, 1997.

[19] Megan Paciaroni and Mark Linne. Single-shot, two-dimensional ballistic imaging through scattering media. *Applied optics*, 43(26):5100–5109, 2004.

[20] J C Hebden, R a Kruger, and K S Wong. Time resolved imaging through a highly scattering medium. *Appl. Opt.*, 30:788–794, 1991.

[21] E.M. Sevick, J.R. Lakowicz, H. Szmacinski, K. Nowaczyk, and M.L. Johnson. Frequency domain imaging of absorbers obscured by scattering. *Journal of Photochemistry and Photobiology B: Biology*, 16(2):169–185, 1992.

[22] S. Andersson-Engels, O. Jarlman, R. Berg, and S. Svanberg. Time-resolved transillumination for medical diagnostics. *Opt. Lett.*, 15(21):1179–1181, Nov 1990.

[23] Y. Chen, H. Chen, D. Dilworth, E. Leith, J. Lopez, M. Shih, P. C. Sun, and G. Vossler. Evaluation of holographic methods for imaging through biological tissue. *Appl. Opt.*, 32(23):4330–4336, Aug 1993.

[24] H. Chen, M. Shih, E. Arons, E. Leith, J. Lopez, D. Dilworth, and P. C. Sun. Electronic holographic imaging through living human tissue. *Appl. Opt.*, 33(17):3630–3632, Jun 1994.

[25] J. Moon, P. Battle, M. Bashkansky, R. Mahon, M. Duncan, and J. Reintjes. Achievable spatial resolution of time-resolved transillumination imaging systems which utilize multiply scattered light. *Physical Review E*, 53(1):1142–1155, 1996.

[26] Min Xu and R. R. Alfano. Circular polarization memory of light. *Phys. Rev. E*, 72:065601, Dec 2005.

[27] D. Bicout, C. Brosseau, A. S. Martinez, and J. M. Schmitt. Depolarization of multiply scattered waves by spherical diffusers: Influence of the size parameter. *Phys. Rev. E*, 49:1767–1770, Feb 1994.

[28] Christian Brosseau and Dominique Bicout. Entropy production in multiple scattering of light by a spatially random medium. *Phys. Rev. E*, 50:4997–5005, Dec 1994.

[29] Zeng Nan, Jiang Xiaoyu, Gao Qiang, He Yonghong, and Ma Hui. Linear polarization difference imaging and its potential applications. *Appl. Opt.*, 48(35):6734–6739, Dec 2009.

[30] J. M. Schmitt, A. H. Gandjbakhche, and R. F. Bonner. Use of polarized light to discriminate short-path photons in a multiply scattering medium. *Appl. Opt.*, 31(30):6535–6546, Oct 1992.

[31] Hiromichi Horinaka, Masahiko Osawa, Koji Hashimoto, Kenji Wada, and Yoshio Cho. Extraction of quasi-straightforward-propagating photons from diffused light transmitting through a scattering medium by polarization modulation. *Opt. Lett.*, 20(13):1501–1503, Jul 1995.

[32] Olivier Emile, Fabien Bretenaker, and Albert Le Floch. Rotating polarization imaging in turbid media. *Opt. Lett.*, 21(20):1706–1708, Oct 1996.

[33] Linda Mullen, Alan Laux, Brian Concannon, Eleonora P. Zege, Iosif L. Katsev, and Alexander S. Prikhach. Amplitude-modulated laser imager. *Appl. Opt.*, 43(19):3874–3892, Jul 2004.

[34] Sriram Sudarsanam, James Mathew, Swapnesh Panigrahi, Julien Fade, Mehdi Alouini, and Hema Ramachandran. Real-time imaging through strongly scattering media: seeing through turbid media, instantly. *Sci. Rep.*, 6:25033, 2016.

[35] W. Nicol. On a method of so far increasing the divergency of the two rays in calcareous-spar, that only one image may be seen at a time. *Edinburgh Journal of Philosophy*, 6:83–84, 1828.

[36] G. G. Stokes. On the Composition and Resolution of Streams of Polarized Light from different Sources. *Transactions of the Cambridge Philosophical Society*, 9:399, 1851.

[37] R. Clark Jones. A new calculus for the treatment of optical systemsi. description and discussion of the calculus. *J. Opt. Soc. Am.*, 31(7):488–493, Jul 1941.

[38] E. Wolf. *Introduction to the Theory of Coherence and Polarization of Light*. Cambridge University Press, 2007.

[39] J. C. Maxwell. A Dynamical Theory of the Electromagnetic Field. *Philosophical Transactions of the Royal Society of London*, 155(0):459–512, 1865.

[40] H. Mueller. M.I.T. Course (8.26), Spring. *J. Opt. Soc. Am. 38, 661(A)*, 2:38 , 661(A), 1945.

[41] Philippe Réfrégier and François Goudail. Invariant degrees of coherence of partially polarized light. *Opt. Express*, 13(16):6051–6060, Aug 2005.

[42] E. Collett. *Polarized light: fundamentals and applications*. Optical engineering. Marcel Dekker, 1993.

[43] S. Rahmann and N. Canterakis. Reconstruction of specular surfaces using polarization imaging. In *Computer Vision and Pattern Recognition, 2001. CVPR 2001. Proceedings of the 2001 IEEE Computer Society Conference on*, volume 1, pages I–149–I–155 vol.1, 2001.

[44] Shoji Tominaga and Akira Kimachi. Polarization imaging for material classification. *Optical Engineering*, 47(12):123201–123201–14, 2008.

[45] Albert Le Floch, Guy Ropars, Jay Enoch, and Vasudevan Lakshminarayanan. The polarization sense in human vision. *Vision research*, 50(20):2048–54, 2010.

[46] Samuel Rossel and Rüdiger Wehner. Polarization vision in bees. *Nature*, 323:128–131, 1986.

[47] N J Marshall. A unique colour and polarization vision system in mantis shrimps. *Nature*, 333(6173):557–60, 1988.

[48] N Shashar and T W Cronin. Polarization contrast vision in Octopus. *The Journal of experimental biology*, 199(Pt 4):999–1004, 1996.

[49] CW Hawryshyn. Polarization vision in fish. *American Scientist*, 80(2):164–175, 1992.

[50] Nadav Shashar, Roger T. Hanlon, and Anne deM. Petz. Polarization vision helps detect transparent prey. *Nature*, 393(6682):222–223, 1998.

[51] Christophe Stolz, Mathias Ferraton, and Fabrice Meriaudeau. Shape from polarization: a method for solving zenithal angle ambiguity. *Opt. Lett.*, 37(20):4218–4220, Oct 2012.

[52] S.G. Demos, H. Savage, Alexandra S. Heerdt, S. Schantz, and R.R. Alfano. Time resolved degree of polarization for human breast tissue. *Optics Communications*, 124(5–6):439 – 442, 1996.

[53] Y. Y. Schechner, S. G. Narasimhan, and S. K. Nayar. Instant dehazing of images using polarization. In *Computer Vision and Pattern Recognition, 2001. CVPR 2001. Proceedings of the 2001 IEEE Computer Society Conference on*, volume 1, pages I–325–I–332 vol.1, 2001.

[54] J. Scott Tyo. Design of optimal polarimeters: maximization of signal-to-noise ratio and minimization of systematic error. *Appl. Opt.*, 41(4):619–630, Feb 2002.

[55] Olivier Morel, Christophe Stolz, Fabrice Meriaudeau, and Patrick Gorria. Active lighting applied to three-dimensional reconstruction of specular metallic surfaces by polarization imaging. *Appl. Opt.*, 45(17):4062–4068, Jun 2006.

[56] Steven L. Jacques, Jessica C. Ramella-Roman, and Ken Lee. Imaging skin pathology with polarized light. *Journal of Biomedical Optics*, 7(3):329–340, 2002.

[57] Haitao Luo, Kazuhiko Oka, Edward DeHoog, Michael Kudenov, James Schiewgerling, and Eustace L Dereniak. Compact and miniature snapshot imaging polarimeter. *Applied optics*, 47(24):4413–4417, 2008.

[58] Qizhi Cao, Chunmin Zhang, and Edward DeHoog. Snapshot imaging polarimeter using modified Savart polariscopes. *Applied optics*, 51(24):5791–6, 2012.

[59] Jihwan Kim and Michael J. Escuti. Snapshot imaging spectropolarimeter utilizing polarization gratings. *Proc. SPIE 7086, Imaging Spectrometry XIII*, 708603, 2008.

[60] Michael W Kudenov, Michael J. Escuti, Eustace L Dereniak, and Kazuhiko Oka. White-light channeled imaging polarimeter using broadband polarization gratings. *Applied optics*, 50(15):2283–93, 2011.

[61] Michael W. Kudenov, Michael J. Escuti, Nathan Hagen, Eustace L. Dereniak, and Kazuhiko Oka. Snapshot imaging Mueller matrix polarimeter using polarization gratings. *Optics Letters*, 37(8):1367, 2012.

[62] M W Kudenov, E L Dereniak, L Pezzaniti, and G R Gerhart. 2-Cam LWIR imaging Stokes polarimeter. *Proceedings of the SPIE*, 6972:69720K, 2008.

[63] Wei-liang Hsu, Graham Myhre, Kaushik Balakrishnan, Neal Brock, Mohammed Ibnelhaj, and Stanley Pau. Full-Stokes imaging polarimeter using an array of elliptical polarizer. *Optics Express*, 22(3):3063–3074, 2014.

[64] Arnaud Bénière, Mehdi Alouini, François Goudail, and Daniel Dolfi. Design and experimental validation of a snapshot polarization contrast imager. *Applied optics*, 48:5764–5773, 2009.

[65] Matthieu Dubreuil, Sylvain Rivet, Bernard Le Jeune, and Jack Cariou. Snapshot Mueller matrix polarimeter by wavelength polarization coding. *Optics Express*, 15(21):13660, 2007.

[66] Tsung-Han Tsai and David J Brady. Coded aperture snapshot spectral polarization imaging. *Applied optics*, 52(10):2153–61, 2013.

[67] Viktor Gruev, Rob Perkins, and Timothy York. Ccd polarization imaging sensor with aluminum nanowire optical filters. *Opt. Express*, 18(18):19087–19094, Aug 2010.

[68] Wei-Liang Hsu, Graham Myhre, Kaushik Balakrishnan, Neal Brock, Mohammed Ibn-Elhaj, and Stanley Pau. Full-stokes imaging polarimeter using an array of elliptical polarizer. *Opt. Express*, 22(3):3063–3074, Feb 2014.

[69] Timothy York and Viktor Gruev. Characterization of a visible spectrum division-of-focal-plane polarimeter. *Appl. Opt.*, 51(22):5392–5400, Aug 2012.

[70] S. Bear Powell and Viktor Gruev. Calibration methods for division-of-focal-plane polarimeters. *Opt. Express*, 21(18):21039–21055, Sep 2013.

[71] Fluxdata imaging polarimeter, fd-1665-p.

[72] Julien Fade and Mehdi Alouini. Depolarization remote sensing by orthogonality breaking. *Phys. Rev. Lett.*, 109:043901, Jul 2012.

[73] Julien Fade, Muriel Roche, and Mehdi Alouini. Computational polarization imaging from a single speckle image. *Optics Letters*, 37(3):386–388, 2012.

[74] Philippe Réfrégier, Julien Fade, and Muriel Roche. Estimation precision of the degree of polarization from a single speckle intensity image. *Opt. Lett.*, 32(7):739–741, Apr 2007.

[75] Timothy J. Schulz. Performance bounds for the estimation of the degree of polarization from active laser illumination. *Proc. SPIE*, 5888:58880N–58880N–8, 2005.

[76] Jérémy Vizet, Julien Brevier, Jérôme Desroches, Alain Barthélémy, Frédéric Louradour, and Dominique Pagnoux. One shot endoscopic polarization measurement device based on a spectrally encoded polarization states generator. *Opt. Express*, 23(12):16439–16448, Jun 2015.

[77] Matthieu Dubreuil, Sylvain Rivet, Bernard Le Jeune, and Jack Cariou. Snapshot mueller matrix polarimeter by wavelength polarization coding. *Opt. Express*, 15(21):13660–13668, Oct 2007.

[78] Nicolas Vannier, François Goudail, Corentin Plassart, Matthieu Boffety, Patrick Feneyrou, Luc Leviandier, Frédéric Galland, and Nicolas Bertaux. Active polarimetric imager with near infrared laser illumination for adaptive contrast optimization. *Appl. Opt.*, 54(25):7622–7631, Sep 2015.

[79] M. J. Padgett, A. R. Harvey, A. J. Duncan, and W. Sibbett. Single-pulse, fourier-transform spectrometer having no moving parts. *Appl. Opt.*, 33(25):6035–6040, Sep 1994.

[80] L. Mandel and E. Wolf. *Optical Coherence and Quantum Optics*. Cambridge University Press, 1995.

[81] Maria C. Simon. Wollaston prism with large split angle. *Appl. Opt.*, 25(3):369–376, Feb 1986.

[82] P.H. Garthwaite, I.T. Jolliffe, and B. Jones. *Statistical Inference*. Oxford science publications. Oxford University Press, 2002.

[83] A. van den Bos. *Parameter Estimation for Scientists and Engineers*. Wiley, 2007.

[84] B. Porat and B. Friedlander. Computation of the exact information matrix of gaussian time series with stationary random components. *IEEE Transactions on Acoustics, Speech, and Signal Processing*, 34(1):118–130, Feb 1986.

[85] Franklin C. Crow. Summed-area tables for texture mapping. *SIGGRAPH Comput. Graph.*, 18(3):207–212, January 1984.

[86] P. Viola and M. Jones. Rapid object detection using a boosted cascade of simple features. In *Computer Vision and Pattern Recognition, 2001. CVPR 2001. Proceedings of the 2001 IEEE Computer Society Conference on*, volume 1, pages I–511–I–518 vol.1, 2001.

[87] N.L. Johnson, S. Kotz, and N. Balakrishnan. *Continuous univariate distributions*. Number v. 2 in Wiley series in probability and mathematical statistics: Applied probability and statistics. Wiley & Sons, 1995.

[88] V.V. Tuchin and Society of Photo-optical Instrumentation Engineers. *Tissue Optics: Light Scattering Methods and Instruments for Medical Diagnosis*. Press Monographs. SPIE/International Society for Optical Engineering, 2007.

[89] T. Vo-Dinh. *Biomedical Photonics Handbook*. SPIE press monograph: SPIE. Taylor & Francis, 2003.

[90] BJ Ackerson, RL Dougherty, NM Reguigui, and U Nobbmann. Correlation transfer-application of radiative transfer solution methods to photon correlation problems. *Journal of thermophysics and heat transfer*, 6(4):577–588, 1992.

[91] D.G. Cacuci. *Handbook of Nuclear Engineering: Vol. 1: Nuclear Engineering Fundamentals; Vol. 2: Reactor Design; Vol. 3: Reactor Analysis; Vol. 4: Reactors of Generations III and IV; Vol. 5: Fuel Cycles, Decommissioning, Waste Disposal and Safeguards*. Number v. 2 in Handbook of Nuclear Engineering. Springer, 2010.

[92] J B Fishkin and E Gratton. Propagation of photon-density waves in strongly scattering media containing an absorbing semi-infinite plane bounded by a straight edge. *J. Opt. Soc. Am. A.*, 10(1):127–140, 1993.

[93] Vlad Toronov, Enrico D'Amico, Dennis Hueber, Enrico Gratton, Beniamino Barbieri, and Andrew Webb. Optimization of the signal-to-noise ratio of frequency-domain

instrumentation for near-infrared spectro-imaging of the human brain. *Opt. Express*, 11(21):2717–2729, October 2003.

[94] Bruce J Tromberg, Lars O Svaasand, Tsong-Tseh Tsay, and Richard C Haskell. Properties of photon density waves in multiple-scattering media. *Appl. Opt.*, 32(4):607, February 1993.

[95] D.A. Boas, C. Pitris, and N. Ramanujam. *Handbook of Biomedical Optics*. CRC Press, 2016.

[96] A. Ishimaru. *Wave Propagation and Scattering in Random Media*. An IEEE OUP classic reissue. Wiley, 1999.

[97] Steven L Jacques and Brian W Pogue. Tutorial on diffuse light transport. *Journal of Biomedical Optics*, 13(4):041302, 2008.

[98] Daniele Contini, Fabrizio Martelli, and Giovanni Zaccanti. Photon migration through a turbid slab described by a model based on diffusion approximation. I. Theory. *Appl. Opt.*, 36(19):4587, July 1997.

[99] E. Gratton, S Fantini, M a Franceschini, G Gratton, and M Fabiani. Measurements of scattering and absorption changes in muscle and brain. *Philos. Trans. R. Soc. B Biol. Sci.*, 352(1354):727–735, June 1997.

[100] S R Arridge. Optical tomography in medical imaging. *Inverse Problems*, 15(2):R41–R93, 1999.

[101] M.Q. Brewster and Y. Yamada. Optical properties of thick, turbid media from picosecond time-resolved light scattering measurements. *International Journal of Heat and Mass Transfer*, 38(14):2569 – 2581, 1995.

[102] S. B. Colak, M. B. Van Der Mark, G. W. 'T Hooft, J. H. Hoogenraad, E. S. Van Der Linden, and F. A. Kuijpers. Clinical optical tomography and NIR spectroscopy for breast cancer detection. *IEEE J. Sel. Top. Quantum Electron.*, 5(4):1143–1158, 1999.

[103] Gary Strangman, David a Boas, and Jeffrey P Sutton. Non-invasive neuroimaging using near-infrared light. *Biol. Psychiatry*, 52(7):679–93, 2002.

[104] R Cubeddu, A Pifferi, P Taroni, A Torricelli, and G Valentini. Time-resolved imaging on a realistic tissue phantom: μ(s)′ and μ(a) images versus time-integrated images. *Applied optics*, 35(22):4533–4540, 1996.

[105] B W Pogue and M S Patterson. Frequency-domain optical absorption spectroscopy of finite tissue volumes using diffusion theory. *Physics in medicine and biology*, 39(7):1157–1180, 1994.

[106] Pia Löthgren. Maximum likelihood estimation in signal analysis of MR spectroscopy. Technical report, 2012.

[107] F Mufti and R Mahony. Statistical analysis of signal measurement in time-of-flight cameras. *ISPRS Journal of Photogrammetry and Remote Sensing*, 66(5):720-731, 2011.

[108] Bluetechnix, Sentis M 100.

[109] Helmuth Horvath. On the applicability of the koschmieder visibility formula. *Atmos. Environ.*, 5(3):177–184, 1971.

[110] W E Knowles Middleton and A G Mungall. On the psychophysical basis of meteorological estimates of "visibility". *Eos, Trans. Am. Geophys. Union*, 33(4):507–512, 1952.

[111] Wmo guide to meteorological instruments and methods of observation, 7 2008.

[112] Hyun Keol Kim, Uwe J Netz, Jürgen Beuthan, and Andreas H Hielscher. Optimal source-modulation frequencies for transport-theory-based optical tomography of small-tissue volumes. *Opt. Express*, 16(22):18082–18101, October 2008.

[113] Xuejun Gu, Kui Ren, and Andreas H Hielscher. Frequency-domain sensitivity analysis for small imaging domains using the equation of radiative transfer. *Applied Optics*, 46(10):1624–1632, 2007.

[114] C.C. Davis. *Lasers and Electro-optics: Fundamentals and Engineering*. Cambridge University Press, 1996.

[115] A. D. Payne, A. A. Dorrington, M. J. Cree, and D. A. Carnegie. Characterizing an image intensifier in a full-field range imaging system. *IEEE Sensors Journal*, 8(11):1763–1770, Nov 2008.

[116] Uwe J Netz, Jürgen Beuthan, and Andreas H Hielscher. Multipixel system for gigahertz frequency-domain optical imaging of finger joints. *Rev. Sci. Instrum.*, 79(3):034301, 2008.

[117] Andor ICCD, http://www.andor.com/scientific-cameras/intensified-camera-series.

[118] PrinstonInstruments PI-MAX® 4, http://www.princetoninstruments.com/products/PI-MAX4-emICCD.

[119] PMD tech, http://pmdtec.com/.

[120] Larry Li. Time-of-flight camera–an introduction. *Technical White Paper, May*, 2014.

[121] Faisal Mufti and Robert Mahony. Statistical analysis of signal measurement in time-of-flight cameras. *{ISPRS} Journal of Photogrammetry and Remote Sensing*, 66(5):720 – 731, 2011.

[122] Tobias Möller, Holger Kraft, Jochen Frey, Martin Albrecht, and Robert Lange. Robust 3d measurement with pmd sensors. In *In: Proceedings of the 1st Range Imaging Research Day at ETH*, pages 3–906467, 2005.

[123] B. Buttgen and P. Seitz. Robust optical time-of-flight range imaging based on smart pixel structures. *IEEE Transactions on Circuits and Systems I: Regular Papers*, 55(6):1512–1525, July 2008.

[124] O. Svelto. *Principles of Lasers*. Springer US, 2012.

[125] Peter S. Cross, Richard A. Baumgartner, and Brian H. Kolner. Microwave integrated optical modulator. *Applied Physics Letters*, 44(5), 1984.

[126] Pekka H Äyräs, Ari T Friberg, Matti A J Kaivola, and Martti M Salomaa. Conoscopic interferometry of surface-acoustic-wave substrate crystals. *Appl. Opt.*, 38(25):5399–5407, 1999.

[127] M. Born, E. Wolf, A.B. Bhatia, D. Gabor, A.R. Stokes, A.M. Taylor, P.A. Wayman, and W.L. Wilcock. *Principles of Optics: Electromagnetic Theory of Propagation, Interference and Diffraction of Light*. Cambridge University Press, 2000.

[128] Xinghua Luo, Shougang Chai, and Weidong Chen. Entropy-minimization based i/q channel errors compensation for stepped frequency radar. In *Wireless Communications Signal Processing (WCSP), 2013 International Conference on*, pages 1–4, Oct 2013.

[129] F. E. Churchill, G. W. Ogar, and B. J. Thompson. The correction of i and q errors in a coherent processor. *IEEE Transactions on Aerospace and Electronic Systems*, AES-17(1):131–137, Jan 1981.

[130] D. A. Noon, I. D. Longstaff, and G. F. Stickley. Wideband quadrature error correction (using svd) for stepped-frequency radar receivers. *IEEE Transactions on Aerospace and Electronic Systems*, 35(4):1444–1449, Oct 1999.

[131] A. E. Willner and S. R. Nuccio. Electro-optic polymer modulators. In *Optical Fiber Communication Conference and Exposition (OFC/NFOEC), 2012 and the National Fiber Optic Engineers Conference*, pages 1–3, March 2012.

[132] Ariel Caticha. The basics of information geometry. *AIP Conference Proceedings*, 1641(1), 2015.

[133] R.O. Duda, P.E. Hart, and D.G. Stork. *Pattern classification*. Pattern Classification and Scene Analysis: Pattern Classification. Wiley, 2001.

[134] K. B. Petersen and M. S. Pedersen. The matrix cookbook, 2012. Version 20121115.

Glossary

CCD charged coupled devide. 7, 38

CNR contrast-to-noise ratio. 49, 63

CRB Cramer-Rao bound. 65

DOP degree of polarization. 32, 34, 61, 62, 65, 66

EOM electro-optic modulators. 121, 123, 126, 127, 131, 154

ffQDC full-field quadrature demodulation camera. 13, 121, 134–136, 139–141

FI Fisher information. 65, 97, 99, 108

FIM Fisher information matrix. 65, 97, 108, 111, 114, 150

LCVR liquid crystal variable retarders. 35

LNB Lithium Niobate (LiNbO3). 121, 122, 128

LTA Lithium Tantalate (LiTaO3). 121, 122

MFP transport mean free path. 88

ML maximum likelihood. 62, 63

OSC orthogonal-states contrast. 34, 43, 45, 47, 59

PCA principal component analysis. 24

PDF probability density function. 65, 97, 149

QWP quarter-wave plates. 124, 131

ROI region-of-interest. 8, 49, 50, 60, 63, 74

SDE standard diffusion equation. 83, 84, 86

SNR signal-to-noise ratio. 19–21, 23, 34, 76, 93, 105, 106

SVD singular-value decomposition. 132, 133

ToF time-of-flight. 104, 117, 118, 120, 141

WP Wollason prism. 36–39

Resumé

Imaging through turbid media like fog, tissues, colloids etc. has various applications in real-life situations. The problem of imaging through such scattering media presents a challenge that can be addressed by using novel imaging schemes, information theory and laws of light transport through random scattering media.

The thesis is divided into two parts corresponding to two different imaging modalities, namely, polarimetric contrast imaging and intensity modulated light imaging. In both the cases, advanced imaging systems, capable of imaging in real-time are used and their performances are evaluated both theoretically and experimentally.

In the first part of the thesis, a two-channel, snapshot polarimetric camera, based on a Wollaston prism is used to attain optimal imaging of polarized light source through fog. An original outdoor experiment is setup in the vicinity of the campus Beaulieu in Rennes, France, where a source is placed on a telecommunication tower more than a kilometer away from the imaging system. Data acquired in various weather conditions show that the efficiency of the two-channel polarimetric camera depends on the background noise correlation in the two images. Further, this was confirmed using an information theoretical analysis, which showed that a polarimetric contrast maximizing image representation is a linear combination of the two polarimetric images whose weights depend on the background noise correlation. Based on the derived optimal polarimetric representation, a detection scheme was presented, leading to an end-to-end study of two-channel polarimetric imaging through fog that may be useful in transport applications like aircraft landing/taxiing in degraded weather.

The second part of the thesis deals with intensity modulated light and its potential for ballistic photon imaging through scattering media. First, using the diffusion theory of photon transport and information theory, it was shown that for a given photon budget, ballistic imaging can be achieved for a minimum modulation frequency that depends on the scattering properties of the intervening medium. In real-life situation, the minimum frequency can be in the range of MHz. Real-time imaging at these frequencies is a challenge. Hence, a novel demodulation camera system based on electro-optics was proposed and patented. The imaging system is capable of real-time, full-field demodulation at frequencies of several MHz (potentially, in GHz as well), without requiring a phase synchronized source. A prototype of the imaging system was developed and shown that a demodulation camera based on the proposed design is robust, portable and cost-effective.

Finally, the work presented in this thesis pave way for implementation of advanced imaging systems in real-life situations, varying from biomedical imaging to transport safety.

Resumé

L'imagerie à travers les milieux turbides comme le brouillard, les tissus, les colloïdes, etc. répond à plusieurs besoins de la vie courante. L'imagerie à travers de tels milieux diffusants est un défi auquel peuvent répondre les nouveaux systèmes d'imagerie, la théorie de l'information et l'étude des lois de transport de la lumière dans les milieux aléatoires.
La thèse est divisée en deux parties adressant deux modalités d'imagerie différentes, à savoir : l'imagerie de contraste polarimétrique et l'imagerie modulée en intensité. Dans les deux cas, des systèmes d'imagerie en temps réel sont proposés et mis au point. Leurs performances sont évaluées à la fois théoriquement et expérimentalement.
Dans la première partie de la thèse, une caméra polarimétrique à deux canaux instantanés conçue autour d'un prisme de Wollaston est utilisée pour imager de manière optimale une source de lumière polarisée noyée dans un brouillard. Une expérience en situation réelle a été mise en place à proximité du campus de Beaulieu à Rennes. La source est placée sur une tour de télécommunication située à plus d'un kilomètre du système imageant. Les données acquises dans diverses conditions météorologiques montrent que l'efficacité de cette caméra polarimétrique dépend de la corrélation du bruit de fond dans les deux images initiales. Ceci a été confirmé grâce à une analyse fondée sur la théorie de l'information qui montre que le contraste polarimétriques maximal est obtenu par une combinaison linéaire des deux canaux polarimétriques dont la pondération dépendant de la corrélation du bruit de fond dans les deux canaux. Un système de détection, intégrant cette représentation polarimétrique optimale, a été développé pour explorer de bout en bout les capacités offertes par l'imagerie polarimétrique à deux canaux à travers le brouillard. Ces études trouvent des applications directes dans le transport par temps dégradé, y compris pour l'aide à l'atterrissage d'aéronefs.
Dans la même logique, la deuxième partie de la thèse porte sur l'apport de la modulation d'intensité plein champ pour imager les photons balistiques dans les milieux diffusants. En utilisant de concert la théorie de la diffusion et la théorie de l'information, nous avons pu montrer que, pour un budget de photons donné, il existait une fréquence de modulation minimale pour laquelle le filtrage de photons balistique devient efficace. Cette fréquence dépend des propriétés de diffusion du milieu intermédiaire et se trouve être dans la gamme du MHz en situation réelle. L'imagerie en temps réel à de telles fréquences étant un vrai défi, nous avons proposé un système de démodulation plein champ inédit basé sur l'utilisation d'un cristal électro-optique. Ce système d'imagerie, dont nous avons breveté le principe, est en mesure de démoduler avec une caméra standard une scène en temps réel et en plein champ à des fréquences de plusieurs MHz (voire GHz) sans synchronisation de phase. Un prototype de ce système a été développé permettant de confirmer qu'il était robuste, portable et rentable.
Le travail présenté dans cette thèse ouvre la voie à la mise en œuvre de systèmes d'imagerie de pointe fonctionnant dans des situations réelles, allant de l'imagerie biomédicale, à la sécurité.

Imagerie temp-réel à longue distance à travers le brouillard

Swapnesh Panigrahi

Julien Fade (co-encaderant), Mehdi Alouini (Director de these)

Cette thèse est le résultat d'une collaboration entre l'Institut de Physique de Rennes en France et l'Institut de Recherche Raman (Raman Research Institute) en Inde (Bangalore), financée par le Centre franco-indien pour la promotion de la recherche avancée (CEFIPRA/IFCPAR). Ce projet, qui a pour titre « Imagerie temps-réel à travers le brouillard sur de longues distances », vise à explorer différentes modalités pour l'imagerie de sources de lumière actives à travers le brouillard pour l'assistance à l'atterrissage d'avions et/ou le roulage dans des conditions météorologiques dégradées. La thèse se fonde sur cette motivation initiale et va au-delà pour fournir les limites expérimentales et théoriques à la réalisation d'un tel système. en utilisant des prototypes d'imagerie de pointe et études théoriques des systèmes d'imagerie.

Le transport de la lumière, dans un milieu diffusant aléatoire , est un problème complexe. Néanmoins, ce transport a des propriétés macroscopiques qui peuvent assez bien décrire le système complexe. Dans un milieu présentant un faible diffusion, où la lumière se propage sur de nombreuses longueurs d'onde avant d'être diffusée e, la lumière peut être traitée comme un faisceau de particules classiques se propageant indépendamment les unes des autres. Dans ce cas, la lumière se propageant dans le milieu peut être classée en trois catégories : (i) les photons qui subissent la diffusion vers l'avant et maintiennent l'information de la source et sont appelés photons balistiques ; (ii) les photons qui subissent la diffusion multiple et dans ce processus perdent toutes les informations sur la source, sont nommés lumière diffuse ; (iii) les photons qui subissent en grande partie la diffusion vers l'avant avant d'atteindre la détection, gardant quelques informations sur la source, sont désignés photons quasi-balistiques. Dans le contexte de l'imagerie à travers un milieu turbide, la détection sélective des photons balistiques est intéressante pour de nombreuses applications. Cependant, dans un milieu diffusant, les photons balistiques sont en nombre beaucoup moins important comparé aux photons diffusés, rendant difficile la différenciation, dans un système conventionnel d'imagerie, entre les photons balistiques et les photons diffusés.

Généralement, l'imagerie à travers un milieu turbide tel que le brouillard, les tissus biologiques ou les colloïdes… a de nombreuses applications dans la vie courante. Le problème de l'imagerie à travers de tels milieux représente un défi qui peut être relevé en utilisant de nouveaux systèmes d'imagerie, la théorie de l'information et les théories du transport de la lumière à travers des supports de diffusion aléatoire. À cet effet, cette thèse explore deux modalités d'imagerie, à savoir l'imagerie de contraste polarimétrique et l'imagerie de photons balistiques par modulation d'intensité. Dans les deux cas, les sources actives à localiser/identifier sont affectées par un paramètre physique contrôlé (polarisation

linéaire dans un cas, modulation de l'intensité de la source dans l'autre cas) et des systèmes avancés d'imagerie ont été développés, capables de réaliser une image de contraste en temps réel. De plus, les deux systèmes d'imagerie sont conçus pour être portatifs, peu coûteux, modulaires et facilement améliorables grâce à des extensions, augmentant ainsi leur potentiel pour la transition vers des scénarios en conditions réelles. Les prototypes des systèmes d'imagerie sont établis, testés et leurs performances par rapport aux appareils conventionnels sont évaluées, de manière théorique et expérimentale.

Dans la première partie de la thèse, une caméra instantanée polarimétrique à deux canaux, basée sur un prisme de Wollaston (fig. 1 [a]) est employée pour étudier la représentation optimale de la source lumineuse polarisée à travers le brouillard sur une distance de 1,3 km. On sait que la lumière polarisée a une pénétration optique plus profonde dans un milieu diffusant comparé à une lumière non polarisée. Ce fait peut être exploité pour l'imagerie à travers le brouillard au moyen d'une caméra sensible à la polarisation. En conséquence, une expérience sur le terrain en extérieur a été réalisée à proximité du campus Beaulieu à Rennes, France, où une source est placée sur une tour de télécommunication à plus d'un kilomètre du système d'imagerie polarimétrique. Le système de représentation acquiert deux images simultanées de la même scène dans deux directions orthogonales de polarisation : une dans la direction parallèle à la direction de polarisation de la source et l'autre dans la direction orthogonale. Des données acquises dans diverses conditions atmosphériques ont été employées pour mesurer la performance de diverses représentations polarimétriques standard. Il a été observé que dans des situations de brouillard mince, la différence des deux images prises selon les directions orthogonales fournit le meilleur contraste, tandis que dans des situations de brouillard épais, l'image parallèle à la direction de polarisation de la source était préférable. Ces résultats expérimentaux tendaient à montrer que la représentation optimale devait être adaptative, en fonction des conditions de visibilité.

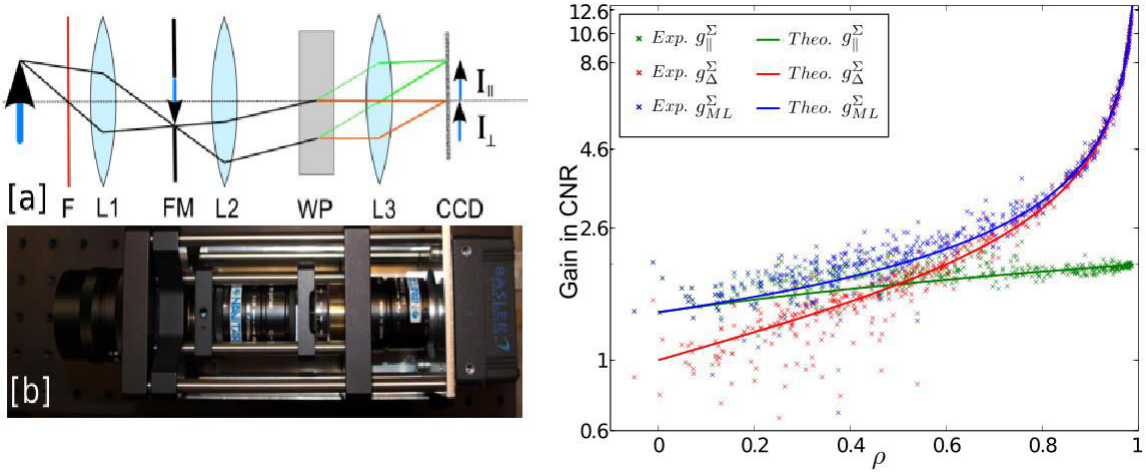

Figure 1

Pour tenir compte des conditions météorologiques, une image de contraste polarimétrique adaptative et universelle a donc été cherchée. Les données expérimentales ont indiqué que

l'efficacité de la caméra polarimétrique à deux voies dépend de la corrélation du bruit de fond gaussien entachant les deux images. Par la suite, il a été confirmé qu'en utilisant un modèle de bruit gaussien corrélé et une estimation au sens du maximum de vraisemblance (maximum-likelihood), le contraste est amélioré en utilisant une représentation optimale qui est une combinaison linéaire des deux images polarimétriques, et dont les poids dépendent de la corrélation de bruit de fond. En utilisant les résultats théoriques et expérimentaux, l'efficacité de contraste de la représentation optimale a été tracée et comparée à d'autres représentations polarimétriques (montrées dans Fig. 1 [c]) et à l'imagerie d'intensité standard. Basé sur la représentation polarimétrique optimale dérivée, les capacités d'amélioration des performances de localisation/détection de sources à travers le brouillard ont été discutées, pour des perspectives applicatives en sécurité des transports comme l'atterrissage d'avions/le roulage sur le sol par temps dégradé.
La deuxième partie de la thèse analyse le potentiel de la lumière modulée en intensité pour l'imagerie de photons balistiques à travers les milieux diffusants. La lumière modulée et sa détection synchrone est connue pour améliorer le rapport signal/bruit pour la détection d'une source lumineuse incluse dans un bruit de fond important. Par ailleurs, la lumière modulée en intensité peut être employée pour discriminer les photons balistiques des photons de diffusion, ouvrant la voie à une amélioration des performances de vision à travers les milieux turbides. Pour identifier l'exigence de fréquence de modulation pour le filtrage de la lumière balistique, la théorie du transport diffusif des photons dans les milieux aléatoires et la théorie de l'information ont été utilisées. Un modèle de bruit d'un système de détection en quadrature a été considéré et paramétré grâce au modèle de la théorie de la diffusion, pour déduire une exigence de fréquence minimale de modulation qui est fonction des paramètres de diffusion du milieu intermédiaire. La fréquence angulaire minimale de modulation a été trouvée $\omega > 2\sigma / 3 (1-g)^2$ (en pointillés sur la Fig. 2 [a]), où σ est le coefficient de diffusion réduit du milieu intermédiaire et g le coefficient d'anisotropie de diffusion.

La thèse étudie les avantages et les inconvénients de l'utilisation de l'imagerie polarimétrique de contraste et de la représentation légère à modulation d'intensité pour voir dans des conditions atmosphériques dégradées. Ceci peut être particulièrement intéressant dans le domaine du transport comme l'atterrissage et le roulement sur le sol d'avions. L'exécution de tels systèmes dans des scénarios réels requiert des études approfondies dans de vraies situations de brouillard, ce qui est présenté dans cette thèse. L'exécution des systèmes avancés de l'imagerie et la quantification de leur efficacité en utilisant la théorie de l'information tiennent compte du développement ultérieur des systèmes pour l'adoption dans l'industrie.

Les résultats quantitatifs de cette étude théorique montrent que les fréquences typiques requises pour l'imagerie à travers le brouillard se situent dans le domaine RF (mégaHertz et au-delà). Obtenir la démodulation optique en mode plein champ (full-field) à de telles fréquences est un défi, qui a été relevé en proposant et en brevetant le principe d'une caméra de démodulation en quadratures tout optique (présenté dans la Fig. 2 [b]), utilisant d'une part un modulateur électro-optique et une division spatiale du faisceau au moyen de composants polarimétriques ad hoc. Le système d'imagerie est capable de créer une image

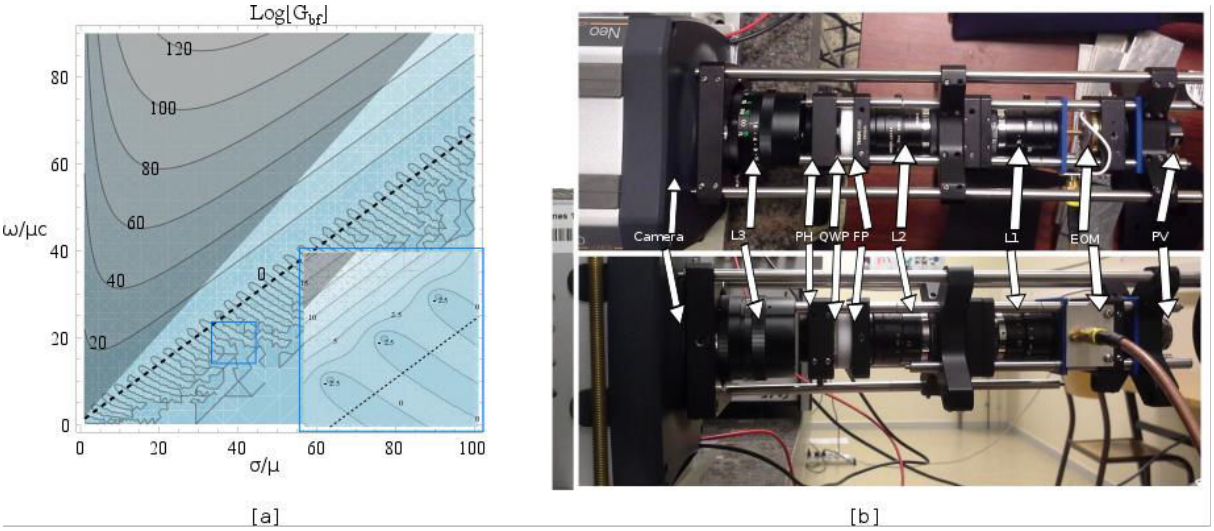

Figure 2

en temps-réel, en mode plein champ et sans exiger une synchronisation de phase avec la source modulée (démodulation en quadratures), et potentiellement jusqu'à des fréquences de la dizaine de gigaHertz dans une version évoluée du montage. Un prototype à basse fréquence (10 kHz) du système d'imagerie a été développé et breveté dans le cadre de cette thèse, et montre qu'une caméra de démodulation basée sur le design proposé peut être robuste, portative et peu coûteuse.

Il existe de nombreuses perspectives pour ce travail qui incluent le développement ultérieur de la caméra de démodulation et des expériences avec la lumière modulée en intensité dans de vraies conditions de brouillard. Néanmoins, le travail présenté dans cette thèse prépare le terrain pour l'exécution de systèmes avancés d'imagerie dans de vraies situations comme le transport, la sécurité ou l'imagerie biomédicale.